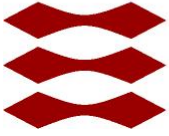


DTU



(2014)

*Metal nanoparticles
for thin film solar cells*

PhD thesis of:

Claudia Gritti

Supervisors:

Andrei Lavrinenko

Radu Malureanu

Beata Kardynal

Aknowledgements

I would like to thank Beata Kardynal, who gave me the possibility to conduct this PhD project, who taught me a lot, made me an independent researcher and have been following me even from distance till the last step of the work. She has also helped me a lot in writing this thesis with full correction of the whole text. Thank you also for your trust in my abilities.

I want to thank then my official supervisors, Andrei Lavrinenko and Radu Malureanu, for their help during this project; in particular, Radu inside the clean room and the optical lab and his support as expert experimentalist; and Andrei, who has given importance to my work even being a bit “outsider” of the Metamaterials group and who encouraged me, in his own way, during tough times.

And thanks to all the Metamaterials group: old and new members, for creating a nice group with guaranteed mutual collaboration and friendly attitude.

I have to be grateful to the people collaborating with me from the research centre FZ-Julich: Stefan Trellenkamp (helping with EBL exposures) and Ulrich Paetzold, directly involved in an important part of this thesis.

I would like to thank all DTU Danchip staff and in particular Peixiong Shi, whose experience with EBL helped a lot; thank you for your constant availability (day and night) and kindness.

Thanks to all DTU Fotonik people who made this path very pleasant creating a nice working atmosphere. In particular I want to thank: Luisa Ottaviano and Irina Kulkova, very kind and collaborative colleagues but also wonderful people and friends. I will also thank all the Nanophotonic Devices group for their support.

Thanks to Letizia Amato for her prompt help in the delivery of this thesis but also for being a great CR-mate.

Outside work environment, I cannot avoid to thank all my friends in Copenhagen, with whom I shared these last 4 years: my irreplaceable Friend Fabio, my buddy Giannis, the Italian family-crew with Sara, David, Nkero and Karis, my dear friend Kamau, all my basketball team and the greek friends.

Finally, a huge thanks to my family, supporting me from Italy and encouraging me all the time, believing in my capabilities and to my home-friends: every time I come back to Italy it is like I never left and they are able to recharge me “full battery”.

As last but not least, I will thank my half-apple, my soul-mate: thank you, Fabri, for everything you have been doing for me, spuring on me to give my best also in the difficult moments, trusting me and giving me self-confidence, supporting, sharing your life with me and simply being as you are.

Contents

List of abbreviations	3
Abstract	5
1. Introduction.....	8
1.1 Photovoltaics and Plasmonics	8
1.2 Motivation and goal	9
1.3 Organization of the thesis	11
2. Localized surface plasmons for thin film solar cells	12
2.1 Localized surface plasmons	12
2.2 State-of-art	14
2.3 Scattering for light trapping	18
2.4 LSPs for electron emission.....	20
2.5 Traps at the LSP resonance energy	22
2.6 Interparticle coupling	24
2.7 Disorder effect.....	26
3. Schottky junction solar cells	30
3.1 GaAs solar cells.....	31
3.1.1 Model and simulations	32
3.1.2 Fabrication of the device	39
3.2 A-Si:H solar cells	48
4. Nanoparticles incorporation and optical characterization.....	50
4.1 Metal choice	51
4.2 Fabrication techniques	52
4.2.1 Electron-beam lithography	52
4.2.2 Electroless plating.....	68
4.3 Indirect absorbance measurements.....	82
4.3.1 First optical characterization setup and first gold order samples	82
4.3.2 Integrating sphere for reflectance and transmittance measurements.....	84
4.3.3 Conclusions.....	101
5. EELS for Ag nanoparticles	102
5.1 STEM and Electron Energy Loss Spectroscopy	102

5.2	EELS for metallic nanoparticles	104
5.3	Dimers: from classic to subnanometer regime plasmon modes.....	105
5.4	EELS measurements of Ag nanoparticles deposited by electroless	109
5.4.1	Sample preparation and data processing.....	109
5.4.2	Results	110
5.4.3	Conclusions.....	121
6.	Solar cells electrical characterization	122
6.1	Short circuit current and quantum efficiency	122
6.2	GaAs Schottky diodes	122
6.3	A-Si:H amorphous solar cells	125
6.3.1	QE spectra.....	125
7.	Conclusions and outlooks.....	130
	Publications	132
	Bibliography.....	135

List of abbreviations

a-Si:H hydrogenated amorphous silicon

AFM atomic force microscope

AZO aluminum zinc oxide

c-Si crystalline silicon

C_{abs} absorption cross section

C_{sca} scattering cross section

CTP charge transfer plasmon

E_g energy gap

EELS electron energy loss spectroscopy

EBL electron beam lithography

FDTD finite difference time domain

FF filling fraction

HMDS hexamethyldisilazane

IR infrared

IPA isopropanol

ITO indium tin oxide

IV (curve) current-voltage characteristic

QE quantum efficiency

LPR localized plasmonic resonance

LSP localized surface plasmon

LSPR localized surface plasmon resonance

NIR near infrared

NP nanoparticle

PECVD plasma enhanced chemical vapor deposition

PV photovoltaics

SEM scanning electron microscope

STEM scanning transmission electron microscope

TCO transparent conductive oxide

TEM transmission electron microscope

SPP surface plasmon polariton

Abstract

Among the different renewable ways to produce energy, photovoltaic cells have a big potential and the research is now focusing on getting higher efficiency and at the same time saving the manufacturing costs improving the performance of thin film solar cells.

The spectral distribution in the infrared wavelength region longer than 800 nm accounts for ~40% of the entire solar energy observed on Earth, and only a few solar cells can efficiently convert solar energy with such a long wavelength. The goal of this work is the harvesting of these NIR photons in order to increase the solar cells efficiency in such spectral range; after an overview of the different technologies available today, the employment of localized surface plasmons (LSPs) through the incorporation of metallic nanoparticles within the photovoltaic device is chosen as a cheap and simple method.

The LSP resonance wavelength and intensity depends on the nanoparticle's size, shape, and local dielectric environment, thus absorption enhancement in a defined wavelength range can be achieved varying these properties (tuning the LSP resonance). Even though scattering enhancement of photons above the gap of the semiconductor is useful to increase light trapping and can come along regardless, we aim, as first target, to absorb forbidden (for the semiconductor) photons by the NPs which can excite hot electrons inside the metal NP and emit them directly into the conduction band of the solar cell semiconductor, without going through the promotion of electrons from the valence band of the semiconductor. The photoemission would extend the spectral response of the photovoltaic device.

Thus, NPs are placed at the metal/semiconductor interface (in order to exploit the localization characteristic of the LSP enhancement) and are used as active nanoantennas absorbing photons with energy smaller than the semiconductor gap but larger than the Schottky barrier height between metal and semiconductor.

The optimization of the fabrication process of GaAs and a-Si:H Schottky solar cells is first conducted and subsequently, the incorporation of Au or Ag nanoparticles at the interface between the semiconductor and a transparent conductive oxide layer (TCO), used to complete the Schottky junction and as top electrode, has followed.

A model representing the device structure with GaAs, ITO and incorporated Au disks or Ag ellipsoids in between, is developed and used for FDTD simulations, in order to identify the set of parameters (NPs size and array periodicity) which could show LSP resonance in the NIR range.

Two techniques are here used to fabricate NPs: electron beam lithography (EBL), to deposit ordered arrays of gold and silver NPs, simple to be compared with modelling; and electroless plating, to grow silver nanocrystals with a cheap technology, producing random distribution of particles. These techniques are studied and optimized aiming to obtain NPs patterns of different size, periodicity and density on the substrates required for the incorporation within the solar cell structure (GaAs, SiO₂, Si₃N₄, AZO/Cr), in order to investigate the LSP resonance and tune it to exploit it below the energy band gap of the semiconductor.

EBL is a difficult technique when working by lift-off on critical size (20-50 nm) nanoparticles. The optimization of the process saw a change from ZEP resist to double layer of PMMA and always requires preliminary exposure dose-tests and final particular attention for lift-off step. EBL resulted to be more suitable for silver NPs, since the deposition of gold (on top of an adhesion thin titanium layer) leads to a variation and non-regularity in the shape of the NPs: truncated cones with varying bottom and top radius. The difference in shape causes broadening of the resonance peak (as demonstrated by simulations).

Electroless plating is a technique, based on chemical reactions, which makes use, in the process chosen for this work, of AgNO_3 powder, diluted in water, and HF at very low concentrations. This kind of deposition is very cheap but precise optimization of recipes, strictly depending on the substrate surface, is needed and limited by the chemistry involved. Thus, the NPs grown with this method are characterized by broad distribution of size and shape of NPs bigger than what can be obtained by EBL.

The nanoparticles, after being deposited on different substrates and eventually coated with TCO, are first optically characterized: reflection and transmission are measured with an integrating sphere and consequent absorption spectra are calculated.

A variety of metal nanoparticles on GaAs and a-Si:H is studied. Only Ag nanoparticles have measurable photon absorption while no effect is seen with Ti/Au nanoparticles. SEM and AFM measurements show that size, shape and height are very variable with Ti/Au nanoparticles fabricated by EBL, within the pattern, and this combined with small density of patterns might be a reason for the unmeasurable absorbance enhancement.

The behavior of ordered Ag NPs fabricated by EBL depends on their size and thickness: 24-34 nm of diameter, array pitch of 100 nm and 15-30 nm of thickness give absorbance enhancement in the visible range between 500 and 600 nm of wavelength. Ag NPs of 20-34 nm size and 30 nm thick, incorporated into a-Si:H solar cell structure (thus covered by TCO) with varying array pitch (60/80/100 nm) show 3 localized surface plasmon resonances (LSPR): around 450 nm, 560 nm and 740 nm. LSPR at 560nm originates from scattering, while LSPRs at 450nm and 740nm, are due to NPs absorption. The tail of the peak at 740nm, falls below the gap of the semiconductor (a-Si:H) and the energy of the photons exciting the LSPs, can be translated in consequent emission of hot electrons.

Random Ag NPs patterns fabricated by electroless plating are characterized by larger size (from 60 nm) and, if, characterized by filling fraction higher than 15%, they give significant absorbance enhancement (20%) in the NIR range regardless the size or shape and already without TCO coating. This enhancement is caused by a huge suppression in transmission and can be exploited to promote photoemission in PV devices.

EELS measurements are conducted on Ag NPs deposited by electroless plating in order to investigate the nature of the absorption enhancement, which is not found on similar ordered patterns. Particular dimers (forming nano-bridges) and elongated particles are the responsible of the plasmonic excitations in the energy range of 0.9-1.5 eV, corresponding to part of the NIR range characterized by absorbance enhancement.

Finally, after optical characterization, the NPs are incorporated within the entire diode structure and electrically characterized.

Spectral responses are measured and in two types of measured GaAs solar cells (with Au and Ag nanoparticles) there was no clear efficiency enhancement in the NIR spectral range. In the case of Au nanoparticles it could be explained in similar way to the absorption data: the effect being broad is too weak. The absence of the expected plasmonic enhancement below the gap in devices with Ag NPs suggests that the energy of absorbed photons does not lead to photoemission but is dissipated through heat. GaAs is known to have very fast surface recombination and possibly it was not reduced well enough with the introduced Si_3N_4 layer.

On the other hand, quantum efficiency of a-Si:H solar cells show enhancement corresponding to the 3 LSPRs found in absorption spectra, but absorption contribute by NPs is enhanced by LSP less effectively than scattering; furthermore, it is also less effective than absorption in semiconductor so really only worth it if the peak can be shifted below the bandgap. Finally, the variability of the enhancement corresponding to the resonances due to absorption is hard to understand, thus possible surface recombination, due to processing variations, might play an important role.

Further developments are needed in the solar cell structure in order to reduce surface recombination and exploit the photoemission below the semiconductor energy gap; nevertheless, promising optical results showed here confirmed the possibility to use nanostructures, in particular randomly distributed, to extend solar cells spectral response to longer wavelengths, through possibly cheap and simple technologies: EBL can be substituted by colloidal solutions implementation and electroless plating is not expensive and results to be effective within a broad set of parameters (size, shape, density). Another application of the studied NPs can be in NIR photodetectors.

1. Introduction

1.1 Photovoltaics and Plasmonics

It is getting more evident, year after year, the impact of the human fossil fuel exploitation on the environment. Many researchers are trying to prove an existing direct correlation between the amount of fossil fuel burnt and the corresponding change in the climate, which is demonstrated to be dangerous unbalancing the ecosystem equilibrium [1]. This is a difficult task since the climate behaves chaotically on a short period scale and more periodic on a long scale.

Nevertheless, many clear negative effects are already part of our knowledge. The amount of CO₂ emitted in the atmosphere has never been so high as now considering the last 650.000 year, as it was demonstrated by the measurements of atmospheric samples contained in ice cores [2]. Moreover, the greenhouse effect was firstly recognized by John Tyndall in the 1860s and its implication in a possible climate change was initially sustained by Svante Arrhenius in the 1896. The greenhouse gases emissions (where CO₂ contributes for about 78% of the total) have been rising since 1970, and it was estimated that in 2013 there were 36 billion tons of CO₂, which correspond to a 61% more than the total emissions in 1990 [3]. About half of the total anthropogenic CO₂ (coming from the combustion of carbon-based fuels) emitted from 1750 and 2010, came from the last 40 years of our history [4].

Undoubtedly, it is necessary to find a new sustainable way to live. The sun is the biggest source of energy available. In one hour it gives to the Earth, more energy than what we need in one entire year. Among the different renewable ways to produce energy, photovoltaic cells have a big potential and the research is now focusing on getting higher efficiency and at the same time saving the manufacturing costs (thin film solar cells).

Plasmonics is the study of the interaction between electromagnetic field and free electrons in a metal. Free electrons in the metal can be excited by the electric component of light to have collective oscillations. The absorption of light can be greatly enhanced in the metal by proper design of metal patterns for surface plasmon excitation; in particular, metallic nanostructures are addressed to take advantage of the enhancement effect caused by localized surface plasmons (LSPs).

In the last 20 years the application of metallic nanostructures within many different fields, like molecular sensing [5], [6], [7] and tagging [8], [9], focusing of light [10], near-field optical microscopy [11], [12], subwavelength photonics [13], optical metamaterials [14] and, in particular, photovoltaics [15], [16], [17], has been strongly appealing. Plasmonics is now considered as a significant approach to enhance the light trapping properties of thin-film solar cells. Metal nanoparticles support surface plasmon modes, which are used to couple light into the optical modes of the underlying or surrounding semiconductor, generating localized surface plasmons. The excitation of the LSP gives rise to pronounced optical absorption, field localization, and scattering effects. The resonance wavelength depends on the nanoparticle's size, shape, and local dielectric environment, thus absorption enhancement in a defined wavelength range can be achieved varying these properties, tuning the surface plasmon resonance. [18]

In this thesis we are focusing the attention on LSPs excited within metallic nanoparticles, which are incorporated into thin film Schottky solar cells.

1.2 Motivation and goal

It is well known that for spherical gold and silver nanoparticles the resonance falls into the visible light spectrum region [15], [16], [19], but it is also worth reminding that plasmon resonances can be red-shifted increasing the particle aspect ratio [20], the size of the nanoparticles [21], or employing particle ensembles (as it will be discussed in Sections 2.3-2.4-2.5). In this work, we are interested in light absorption in the NIR region of the solar spectrum in order to make use of photons that would instead be wasted because of the intrinsic limit (band gap) of the semiconductor.

Figure 1.1 shows the solar radiation spectrum together with the ranges of photon energy absorbed by some of the typical semiconductors (crystalline and amorphous silicon, gallium arsenide), used in PV.

The spectral distribution in the infrared wavelength region longer than 800 nm accounts for ~40% of the entire solar energy observed on earth and only a few solar cells can efficiently convert solar energy with such a long wavelength. It is clear that a significant part of the solar radiation is not used, since not absorbed, by the semiconductor. For c-Si, photons with wavelength longer than 1.1 μm are wasted and it would be advantageous to make use of, at least, photons with wavelengths up to 1.3 μm . GaAs (orange arrow) does not absorb photons from about 880 nm of wavelength and in a-Si:H (blue arrow) even more photons are lost.

The goal of this work is the harvesting of these photons. After an overview of the different technologies available today, the employment of LSPs through the incorporation of nanoparticles within the photovoltaic device is chosen as a cheap and simple method.

Other well exploited methods such as up-conversion methods [22] or two/multi-junction solar cells [23], are complex and technologically demanding.

In this thesis, the nanoparticles are placed at the metal-semiconductor interface and are used as active nanoantennas absorbing photons with energy smaller than the semiconductor gap ($h\nu < E_g$) but larger than the work function W_b ($h\nu > W_b$) [24]. Photon absorption in such a case may result in the photoemission of an electron from the metal NP into the semiconductor (Figure 1.2).

In this way, the localized plasmonic resonance in the nanoparticle will extend the spectral response of the solar cell.

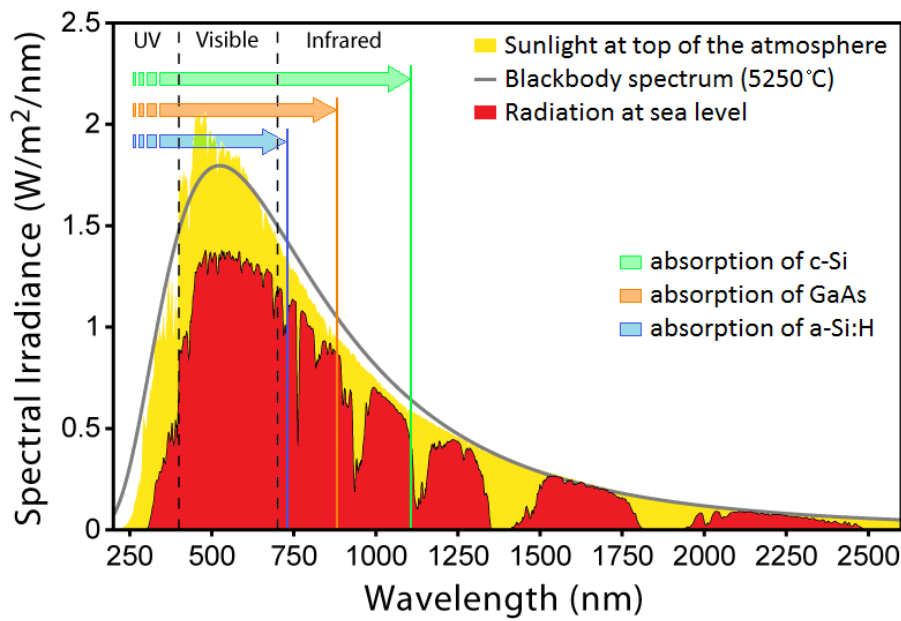


Figure 1.1: Visual representation of the solar radiation spectrum, overlapped with the photon energy bands of absorption by crystalline silicon (c-Si; $E_g=1.1\text{eV}$), gallium arsenide (GaAs; $E_g=1.4\text{eV}$) and amorphous silicon hydrogenated (a-Si:H; $E_g=1.7\text{eV}$)¹.

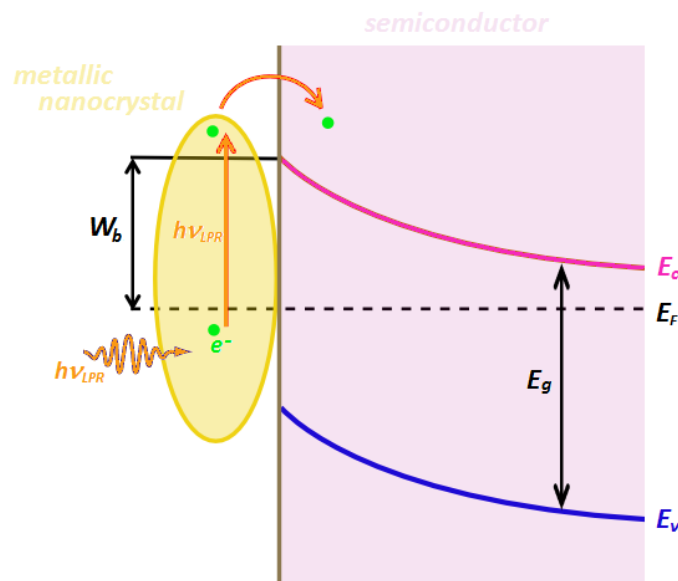


Figure 1.2: Illustration of the mechanism investigated in this thesis. The LPR energy, characterizing the metallic nanoparticles, needs to be larger than the work function (W_b) at the interface and energy gap of the semiconductor (E_g). Once the photon is absorbed by the metallic NP, one electron (green), close to the Fermi level (E_f), can be excited to the conduction band (E_c) of the semiconductor; the necessary energy jump in this case is smaller than the usual jump from the valence band (E_v) to the conduction band within the semiconductor. This mechanism allows the harvesting of photons with lower energy usually not exploited by a typical PV device.

¹ The energy gap value used for a-Si:H is indicative, considering that the band gap could be tuned between 1.55eV and 2.10eV through forced structural relaxation [161], and it corresponds to the value characterizing the real substrate used in this work.

1.3 Organization of the thesis

This thesis is organized as follows:

- ✚ In Chapter 2, we briefly review the fundamentals of LSP resonances in nanoparticles; we give the state-of-art of their application in thin film solar cells for different geometries and consequent phenomena (scattering or photoemission); the review includes single NPs behavior and ensembles of NPs as well.
- ✚ In Chapter 3, the two kind of thin film solar cells (Schottky junction with GaAs and a-Si:H) addressed by this work are presented and their fabrication processed is described.
- ✚ In Chapter 4, the spotlight is pointed on the metallic nanoparticles, explaining the used fabrication technologies (e-beam lithography and electroless plating) and their measured optical properties (SEM characterization and reflectance and transmittance measurements).
- ✚ In Chapter 5, we focus on silver nanoparticles and their EELS characterization.
- ✚ In Chapter 6, the electrical characterization of GaAs and a-Si:H solar cells with and without metallic nanoparticles is shown and motivated.
- ✚ In Chapter 7, conclusions and outlook are draws.

2. Localized surface plasmons for thin film solar cells

2.1 Localized surface plasmons

Localized surface plasmons are non-propagating excitations of the conduction electrons of metallic nanostructures coupled to the electromagnetic field. These modes arise naturally as a solution of the scattering problem of a small, sub-wavelength conductive nanoparticle in an oscillating electromagnetic field. The curved surface of the particle exercises an effective restoring force on the driven electrons, such that a resonance is generated. This results in the field amplification both inside and in the near-field zone outside the particle. Due to the curved surface, plasmon resonances can be excited by direct light illumination, with no need of any phase-matching techniques. [25]

In the regime of interest where the size of the particle d is much smaller than the wavelength λ of the incident electromagnetic field, we can use the quasi-static approximation allowing us to solve the problem for an electrostatic incident field, since the phase of that oscillating field can be considered constant over the volume of the particle. This is strictly true for particle size d smaller than 100 nm.

The nanoparticle is treated here as a homogeneous, isotropic sphere of radius r and dielectric constant ε , and the surrounding medium, also isotropic, is characterized by the dielectric constant ε_m .

Starting from the Laplace equation for the potential, one can show that the applied field (of amplitude E_0) induces a dipole moment inside the spherical particle which is harmonically oscillating and proportional to E_0 [25]. The solution of the problem in terms of polarizability of the particle α leads to

$$\alpha = 4\pi r^3 \frac{\varepsilon - \varepsilon_m}{\varepsilon + 2\varepsilon_m} \quad (2.1)$$

It is clear that the polarizability α experiences a resonant enhancement when $|\varepsilon + 2\varepsilon_m|$ is minimum, which means when the so called *Fröhlich condition* is satisfied:

$$Re[\varepsilon(\omega)] = -2\varepsilon_m \quad (2.2)$$

(assuming $Im[\varepsilon]$ to be small or slowly-varying).

Substituting ε with the Drude value and considering the particle in air, the resonant frequency associated at the *dipole surface plasmon* mode (ω_{sp}) is given by

$$\omega_{sp} = \frac{\omega_p}{\sqrt{3}} \quad (2.3)$$

where ω_p is the plasma frequency.

The resonant behavior of the particle polarizability implies a resonant enhancement of the internal and dipolar fields, which is indeed appealing for different applications, as previously mentioned.

The sphere, once irradiated, is then also radiating because of the induced oscillating dipole, which will then scatter with the incident plane wave. The scattering by the sphere can be described as radiation by a point dipole behaving as:

- ✚ an electric field (magnetic field vanishing), if we are in the near zone of the radiation (really close to the particle)
- ✚ a spherical wave, if we are in the far zone (at a distance from the particle which is bigger than the incident wavelength)

We refer again to the textbook [25] for explicit definitions of the dipolar radiation.

Together with the field enhancement, as consequence of the resonantly enhanced polarizability, the efficiency in scattering and absorption of light by the metal nanoparticle is also increased.

The corresponding cross sections are given by [26]:

$$C_{sca} = \frac{k^4}{6\pi} |\alpha|^2 = \frac{8\pi}{3} k^4 r^6 \left| \frac{\varepsilon - \varepsilon_m}{\varepsilon + 2\varepsilon_m} \right|^2 \propto \frac{r^6}{\lambda^4} \quad (2.4a)$$

$$C_{abs} = k \operatorname{Im}[\alpha] = 4\pi k r^3 \operatorname{Im} \left[\frac{\varepsilon - \varepsilon_m}{\varepsilon + 2\varepsilon_m} \right] \propto \frac{r^3}{\lambda} \quad (2.4b)$$

Both C_{sca} and C_{abs} are highly enhanced at the dipole plasmon resonance (Fröhlich condition) and in particular for small particles, when $\ll \lambda$, the efficiency of absorption dominates over the scattering efficiency.

While absorption and scattering cross sections defined by equations (2.4) are valid for both dielectric and metallic NPs, for metallic particles absorption/scattering is also resonantly enhanced at the Fröhlich condition and this is exactly what we need.

When the nanoparticle is irradiated with a photon that can excite the LSP, the electric field amplitude at the surface of the NP can be increased, through the resonant effect, by almost two orders of magnitude for a low-loss metal such as Ag [27], for instance. The field amplification in the vicinity of the nanoparticles is used to increase optical transition rates, and consequently photon absorption and photocurrent generation. The optical transition rate, W , in a semiconductor is given by the Fermi's golden rule [28]

$$W \propto |E_0|^2 \times |\mathbf{e} \cdot \mathbf{p}_{cv}|^2 \times \int d^3k \delta(E_c(\mathbf{k}) - E_v(\mathbf{k}) - h\nu) \quad (2.5)$$

where E_0 is the electric field amplitude, \mathbf{e} is the field polarization unit vector, \mathbf{p}_{cv} is the momentum operator matrix element between the initial (valence band) and final (conduction band) states, \mathbf{k} is a wave vector, $E_c(\mathbf{k})$ and $E_v(\mathbf{k})$ are the conduction band and valence band dispersion relations, respectively, h is the Planck's constant, and ν is the frequency of the incident photon.

Even though absorption and scattering enhancement of photons above the gap of the semiconductor is useful to increase light trapping and can come along regardless, we aim, as first target, to absorb forbidden (for the semiconductor) photons by the NPs which can excite hot electrons inside the metal NP and emit them directly into the conduction band of the solar cell semiconductor (Figure 1.2), without going through the promotion of electrons from the valence band of the semiconductor.

It is also worth reminding that the enhancement of the field due to plasmonic excitation is occurring within very short distance around the nanoparticles, much smaller than the bulk absorption lengths typical of inorganic semiconductors [18]. Because of this, and also considering the problem of the interface recombination, the NPs need to be placed directly in contact with the active layer of a thin film photovoltaic device. The geometry of the device used as model for this work will be described in Chapter 3.

Going back to equations (2.4), the nanoparticle absorption and scattering cross-sections, which are strongly dependent on the size (r), give a quantification of the relative importance of absorption and scattering processes induced by the nanoparticle, as explained below [18].

For $C_{\text{abs}} \gg C_{\text{sca}}$, the dominant process induced by the nanoparticles is absorption of photons and excitation of LSPs in the metal nanoparticle, accompanied by a large increase in the electromagnetic field amplitude which leads to an increase in electron-hole pair generation; this effect occurs only in a volume, of the semiconductor, within a distance of ~ 10 nm or less from the nanoparticle. The LSP may also decay into single electron excitation, which can be harvested by photoemission.

For $C_{\text{sca}} \ll C_{\text{abs}}$, the dominant process induced by metal nanoparticles is strong forward scattering of incident radiation at wavelengths near and somewhat longer than the LPR wavelength. This forward scattering can increase the electromagnetic field amplitude for a considerable distance, i.e., a micron or more, around the particle, and also increases the overall transmission of electromagnetic energy into the semiconductor material in contact with the NPs, which act in this case as an antireflection coating. This effect increases the electron-hole pair generation rate per unit volume to a more moderate degree than the absorption and LSP excitation process, but within a much larger volume of semiconductor material.

In this thesis we want to fall into the first regime in order to absorb photons that are usually not absorbed by the semiconductor and make use of a very strong and localized field enhancement to excite hot electrons from the metal to the conduction band of the semiconductor, which will create additional photocurrent. We are not really interested here to increase electron-hole pair generation rate in the semiconductor, which would concern photons above the gap.

2.2 State-of-art

In 1980 by McCall *et al.*[29] showed that placing a small metallic sphere nearby a molecule can increase the Raman signal of the latter by many orders of magnitude, due to the local field enhancement coming from the dipole field of the resonant plasma sphere. The local field model of McCall *et al.* was then confirmed by other experimental studies, proving with data that the surface plasma resonance induced by silver nanoparticles enhances Raman scattering, optical absorption, and photoluminescence of a dye [30], [31].

Subsequently, this effect found many potential applications and in 1995 the first photovoltaic device making use of LSP resonance², was developed and measured by Stenzel *et al.* [32]: small metallic clusters of

² Actually, the proposal to use (*propagating*) surface plasmon polaritons to enhance the photoelectric conversion efficiency was described for the first time in 1991 by Hayashi *et al.* [162]: they introduced a 20nm Ag layer into an organic (CuPc) solar cell and they measured an enhancement factor for the short-circuit current of about 7. This was

Ag, Au or Cu were incorporated into an organic solar cell. The efficiency was enhanced because of resonant light absorption in the metal cluster which was accompanied by a strengthened electric field in the vicinity of the particle. The photocurrent enhancement was demonstrated, in accordance with their assumptions, to originate from both local plasmon excitations and interband transitions in the metal clusters.

In contrast to this work, five years later, Westphalen *et al.* [33] incorporated silver particles within a Schottky diode (made by ITO and zinc phthalocyanine-ZnPc, see Figure 2.1a) showing electron photoemission by the metal cluster because of plasmon excitation. In this work there was an evident correlation between the optical absorption of the silver cluster film, made by de-wetting, and the photocurrent of the device (see Figure 2.1b).

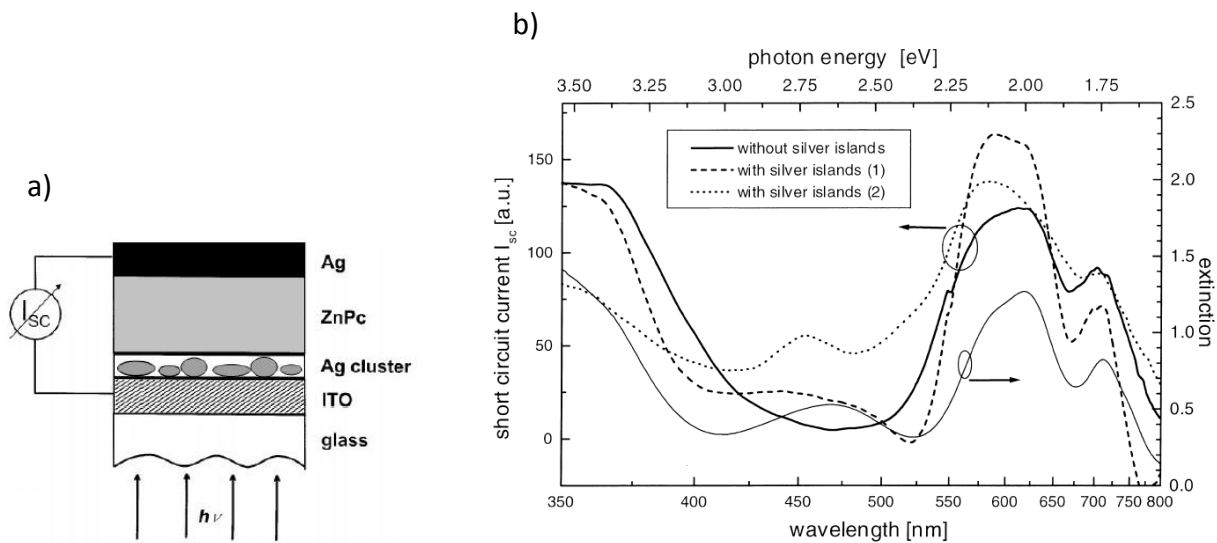


Figure 2.1: a) Representation of the photovoltaic device under study. b) Short circuit current spectra of an ITO/ZnPc-Schottky contact with ((1) and (2)) and without the embedded silver clusters in comparison with the optical extinction spectrum of the silver cluster containing film. The spectra (1) and (2) were obtained at two samples prepared under slightly different tempering conditions. [33]

They also presented a qualitative energy model (Figure 2.2) that explained the experimental data: once the plasmonic oscillation has been generated inside the metal cluster due to the photon absorption at the resonant frequency, it can excite an electron; this “hot” electron can be then driven into the ITO electrode by the electric field of the depletion region; finally the outgoing electron is replaced by another electron coming from the valence band of the semiconductor (ZnPc). A fundamental proof of this model was the fact that the spectral region where the photocurrent increased (450-500 nm) corresponds to wavelengths at which ZnPc does not absorb light.

possible only with the irradiation in longitudinal mode because the transverse mode is lost if not properly matched (f.i. through a periodic grating). In this thesis we are referring to the usage of *localized* surface plasmons (and polaritons): the electron oscillation is spatially confined in a small metallic nanoparticle and, once combined with a photon, the direct consequences are the increase of the absorption and scattering cross section and the near-field enhancement (see chapter 2.1). In contrast to a propagating plasmon polariton, the excitation of the localized plasmon polariton does not depend in general on the illuminating wave field but mainly on the geometrical shape and the material of the nanoparticle as well as its surroundings [90]. These are the features appealing for the photovoltaics.

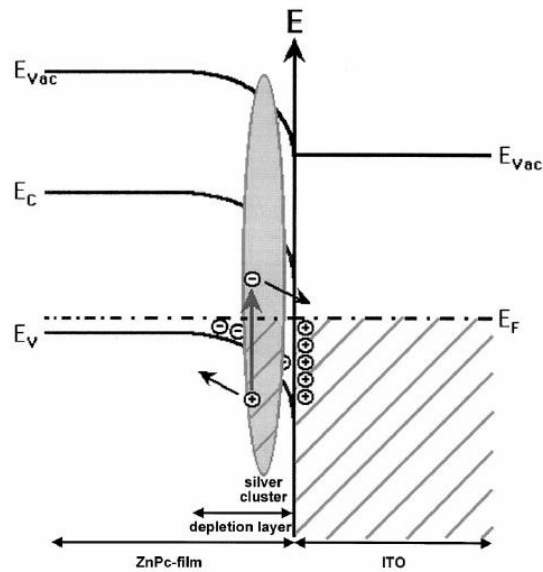


Figure 2.2: Schematic energy model showing photoexcitation, charge separation and transport processes in a silver cluster embedded in the depletion layer of an ITO/ZnPc-Schottky contact. (E_{vac} -vacuum level, E_f -Fermi level, E_v -upper valence band edge, E_c -lower conduction band edge). [33]

Among the first photovoltaic devices with nanocrystals, dye-sensitized TiO_2 thin film solar cells [34] were the most investigated structures, confirming that the enhancement of the optical absorption of the dye by the Ag plasmon resonance effect contributes to the photocurrent. Not only silver islands were taken under study, but also spherical gold nanoparticles, which are appealing for their chemical stability, optical sensitivity and showing unique size and shape-dependent optical properties [35], [36]. In 2007, Furube *et al.* demonstrated electron transfer from gold nanodots into TiO_2 nanoparticles, caused by plasmon excitation [37].

The first real success of plasmonic photoelectric conversion from visible to near-infrared wavelength without deteriorating photoelectric conversion was reported in 2010 by Nishijima *et al.* [38], using electrodes in which gold nanorods (NRs), fabricated by e-beam lithography, were arrayed on the surface of TiO_2 single-crystal electrodes. The dimensions of the NRs were 110 nm by 240 nm by 40 nm, designed to make horizontal and vertical structural periods of 200 and 300 nm, respectively (filling fraction: 44%), and photoelectrochemical measurements were performed using light: non-polarized and polarized along both the long and the short axis of the nanorods.

In Figure 2.3a, the measured extinction spectra are shown: a broad LSP band was observed around the wavelengths of 650 nm (transverse mode) and 1000 nm (longitudinal mode). A good correlation with the internal photoelectric conversion efficiency (IPCE) spectra is shown in Figure 2.3b, where peak values of the photocurrent at 6.3% and 8.4% correspond to the LSP bands in the T-mode and L-mode, respectively. In their research they pointed out that no photocurrent was observed in a device without Au NRs under irradiation of light with a wavelength of 450 nm or longer.

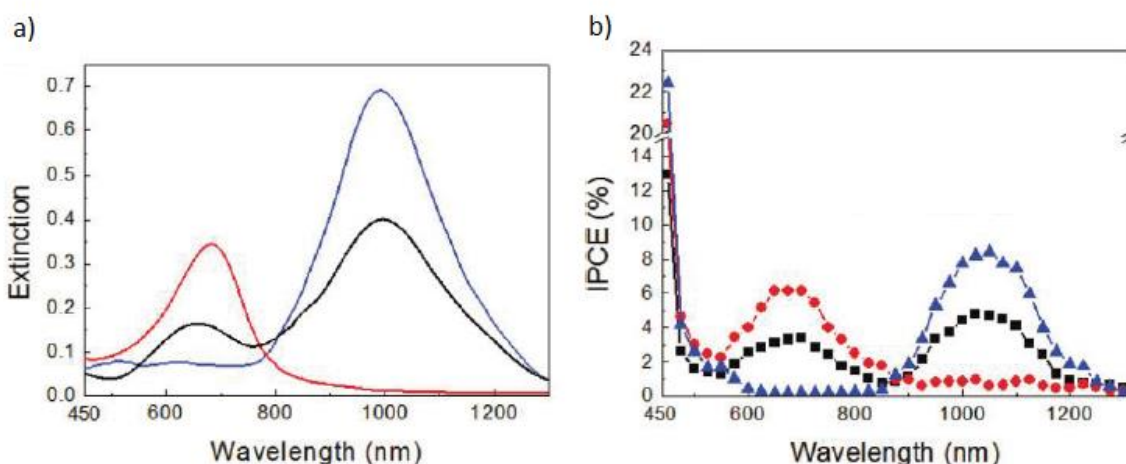


Figure 2.3: a) Extinction spectrum of the Au NRs in water. b) Photoelectric conversion efficiency of the action spectrum measured at each wavelength with monochromatic light. For both graphs: black - under irradiation of non-polarized light, red and blue - minor-axis direction (T-mode) and major-axis direction (L-mode) under irradiation of linearly polarized light, respectively. [38]

This device was a significant step forward in comparison with other previously reported photovoltaic systems [39], [40], [41] because of its wide spectral response which covers the visible and also the infrared radiation (from 800nm to 1300nm), making use of only simple gold nanorods, avoiding the incorporation of different dye-sensitizers and without employing different semiconductors (with different band gaps) like in tandem solar cells.

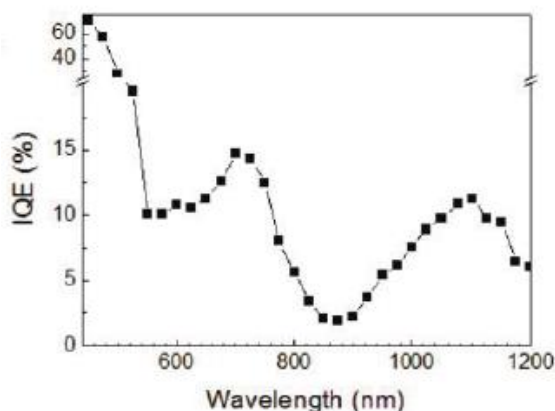


Figure 2.4: Internal quantum efficiency (IQE) values plotted to the wavelength of the monochromatic non-polarized light. [38]

Finally, Nishijima *et al.* reported also the IQE³ spectrum (Figure 2.4), where again local maxima are visible in correspondence of the LSP bands. This is an important point: in a photoelectrochemical cell the IQE does not depend on the wavelength that corresponds to the absorption spectrum of the sensitizer driving the photoelectron transfer [42], therefore this result suggests that the photo-induced electron transfer from Au

³ The photocurrent produced from a monochromatic photon flux can be expressed largely by the internal quantum efficiency (IQE), which is the number of electrons injected into the conduction band of TiO₂ per interacted photon with Au NRs. The IQE is calculated by correcting the IPCE for photons interacted with the Au NRs as $IQE = IPCE/\eta$, where η is the probability of interaction between photons and Au NRs. Therefore, η can be expressed by the following equation: (total photon flux - transmitted photon flux)/total photon flux. [38]

NRs to TiO₂ resulting from the excitation of the LSPs is nonlinearly induced not only by antenna effects but also by electromagnetic field enhancement effects.

2.3 Scattering for light trapping

In thin film solar cells the thickness of the absorbing layer is reduced, in comparison with bulk solar cells, in order to save material costs, but the big drawback is the loss (light escaping from the absorber) due to a very short optical length. Thus, different techniques of light-trapping have been developed in order to reduce both the reflection from the solar cell and the transmission through its active layer. The scattering from metal nanoparticles near their localized plasmon resonance has been shown to be a promising way to enhance light absorption within the thin active film of the solar cells. In 2008 Catchpole and Polman reviewed [16] the experimental and theoretical progress that has been made till that time; the review presented clear evidence of enhancements in photocurrent observed for a wide range of semiconductors and solar cell configurations making use of this light-trapping mechanism.

Plasmonic structures can be implemented in thin film solar cells in three different geometries [15]. First, metallic nanoparticles can be used as sub-wavelength scattering elements to enhance light trapping, increasing the optical path length, within the thin absorbing layer (Figure 2.5a). Second, metallic nanoparticles can be more or less embedded in the semiconductor and used as sub-wavelength antennas in which the plasmonic near-field is coupled to the semiconductor, increasing its effective absorption cross-section (Figure 2.5b). Third, a corrugated metallic film on the back surface of a thin photovoltaic absorber layer can couple sunlight into SPP modes supported at the metal/semiconductor interface as well as guided modes in the semiconductor slab, whereupon the light is converted to photocarriers in the semiconductor (Figure 2.5c).

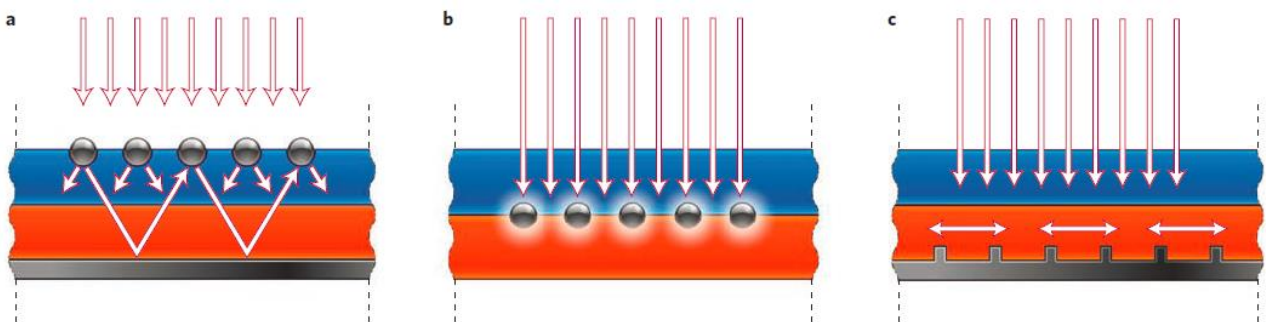


Figure 2.5: a) Light trapping by scattering from metal nanoparticles at the surface of the solar cell. Light is preferentially scattered and trapped into the semiconductor thin film by multiple and high-angle scattering, causing an increase in the effective optical path length in the cell. b) Light trapping by the excitation of localized surface plasmons in metal nanoparticles embedded in the semiconductor. The excited particles' near-field causes the creation of electron-hole pairs in the semiconductor. c) Light trapping by the excitation of surface plasmon polaritons at the metal/semiconductor interface. A corrugated metal back surface couples light to surface plasmon polariton or photonic modes that propagate in the plane of the semiconductor layer. [15]

In these geometries the metallic nanoparticles are exploited for their geometrical optical properties, contributing to the incident photons scattering, or/and like active nanoantennas, leading to the near electromagnetic field enhancement.

Furthermore, Hallermann *et al.* well described some fundamental properties of localized plasmon polaritons in metallic nanoparticles [43], and discussed their use for enhancing thin film solar cells efficiency by increasing light absorption through the strong field enhancement (see Figure 2.6) and the large scattering cross section of plasmons at the resonance wavelength.

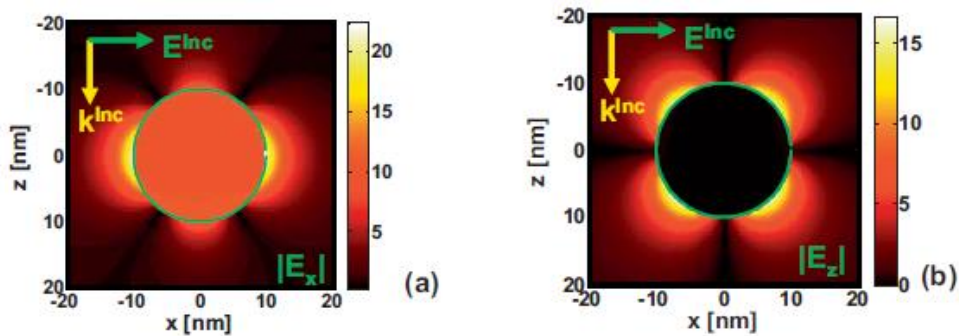


Figure 2.6: Amplitude of the excited localized plasmon polariton at a silver sphere with a radius of 10 nm. The sphere (located at the origin) is embedded in glass ($n = 1.5$) and illuminated with a plane wave ($\lambda = 394.8$ nm) that propagates in the positive z -direction (and whose electric field vector has only an x -component). Field is shown in the plane of $y = 0$ nm in multiples of the incident amplitude; **(a)** shows the amplitude of the electric field's x -component, **(b)** shows the z -component, respectively. [43]

In the same year Nakayama with Atwater's group investigated the effects of plasmonic scattering on absorption and photocurrent collection in p-n GaAs junction solar cells decorated with size-controlled, densely formed high aspect-ratio, Ag nanoparticles on top of the front side [44]. They demonstrated that at wavelengths below surface plasmon resonance, scattered incident light by the nanoparticles yields enhanced absorption in the photovoltaic layers and consequently increased short circuit current density by 8%.

Subsequently, many other scientists focused their research on this phenomenon considering all the possible aspects which could be involved. For instance, the optimization of the design that can maximize the scattering and minimize what is called parasitic absorption⁴ depending on the size [45], [46], [47], [48], [49], [50] of the nanoparticles, the aspect ratio [47], the metal (Au, Ag, Al or Cu) [46], [47], [48], [49], the shape [47], [49], [50], [51], [52] or the used surrounding material [46], [48], [49], which can shift the plasmonic resonance; moreover, the collective effects depending on the density and the interparticle spacing of the particles [46], [53], [54], [55]. Another important studied aspect is the position for their incorporation: on top of/embedded inside/at the rear of the absorbing layer [50], [56], [57], but also as intermediate reflectors in tandem solar cells [58]. Meantime, also the choice of the semiconductor for the solar cell incorporating those nanoparticles (for example a-Si:H or c-Si) [47], [48], needs to be considered. The research related to these features has been conducted either giving evidences of the absorption/photocurrent enhancement with experimental measurements or through analytical or numerical studies with FDTD simulations. Other two parameters found to be important for describing the connection between morphology and optical properties of self-assembled (by solid state de-wetting of thin films) nanoparticles are the surface coverage distribution and the mean surface coverage [50].

⁴ The literature, in general, refers to *parasitic* absorption to indicate the absorption by the nanoparticles of photons which could be directly absorbed by the semiconductor of the solar cell. In order to avoid this (when the plasmonic resonance falls in a wavelength range above the gap of the semiconductor), the preferred geometry of the device incorporates the metal nanoparticles at the rear of the absorbing layer.

Interestingly, the use of the nanoparticles for scattering can be combined with the absorbance enhancement in a wavelength range outside the plasmonic resonance, originating from the Fabry-Perot resonance within the active layer of the thin film solar cell [46]. Finally, for the application of this effect in photovoltaic devices, another aspect cannot be forgotten: the interband transitions, characteristic of the chosen metal for the nanoparticles, which can affect the absorbance of the active layer [45], [47], [59].

Beyond all these aspects, the optimization of the light trapping has also been aimed indulging to very original shapes of nanoparticles [52], [60], [61] or peculiar ensemble geometries [62], [63], [64].

2.4 LSPs for electron emission

As just described, the nanoparticles can scatter the incoming light through the surface plasmon resonance. For frequencies near the resonance, nanoparticles have an optical cross section much larger than their geometrical cross section and that is the reason why they can be used to re-direct efficiently light inside the semiconductor of a solar cell. This resonance could be tuned such that near band gap photons would be absorbed with high probability, while higher energy photons would be unaffected. This was indeed the solution of Kirkengen *et al.* [65] to improve silicon as photovoltaic material: since it is an indirect band gap material, the efficiency would be increased introducing a new mechanism to generate electron-hole pairs near bandgap without phonon assistance. Thus, they did not think about using the nanoparticles as scatterers, to simply increase the indirect absorption (because of a longer optical path inside the wafer), they focused on the possibility of direct absorption of photons in silicon using LSP excitations in the NPs to transfer the momentum.

The demonstration of photoemission came afterwards (2009) from Stiebig's group. Moulin and Luo incorporated small (radius from 20 to 50nm) silver nanoparticles into thin amorphous silicon solar cells (Figure 2.7), in close contact with the active layer [66], [67]. An increased light absorption, coming from a reduced reflection (Figure 2.8a), and a consequent enhanced photocurrent (Figure 2.8b) were found for wavelengths longer than 750 nm, beyond the semiconductor gap limit.

The increased photocurrent in the near infrared range is due to LSPP-induced photoemission of electrons within and in close vicinity of the nanoparticles.

Furthermore, another study experimentally demonstrated the feasibility of Schottky diodes, in which electrons were never generated by absorption in semiconductors but directly excited in metal [68]. Fukuda *et al.* used Au nanorods to excite localized surface plasmons on the Au film forming the Schottky diode (Au/n-Si): their results showed that light illumination excited the free electrons of the Au film and the excitation was enhanced by the LSP resonance of the nanorods placed on top; since the incident photon energy was larger than the Schottky barrier height, the electrons could be transferred into the semiconductor.

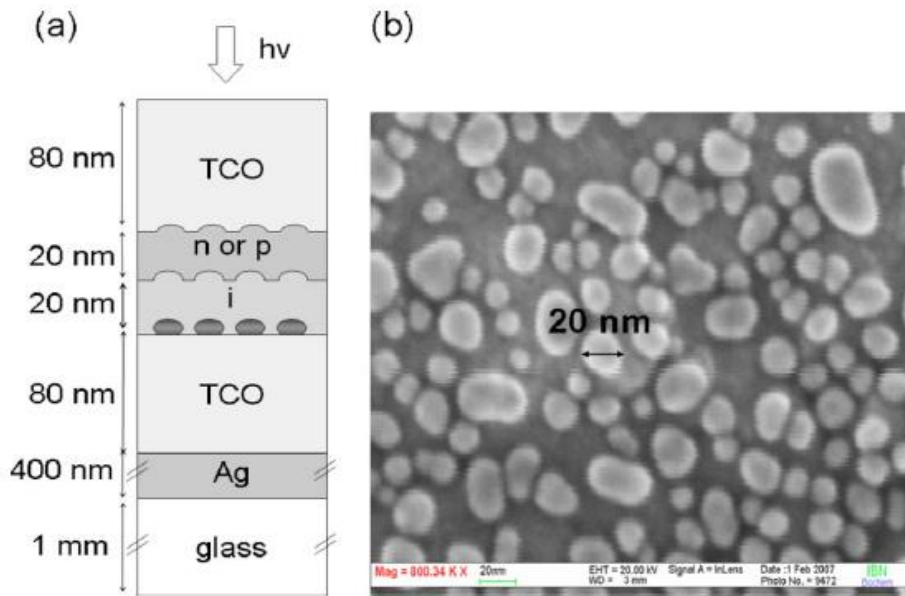


Figure 2.7: a) Schematic drawing of the investigated a-Si:H devices in the Ag/TCO/ i /n/TCO or Ag/TCO/ i / p/TCO configuration. The NPs are positioned at the TCO/ i interface. b) SEM picture of a 2 nm Ag film on glass/Ag/TCO after annealing treatment at 180 °C for 90 min. [66]

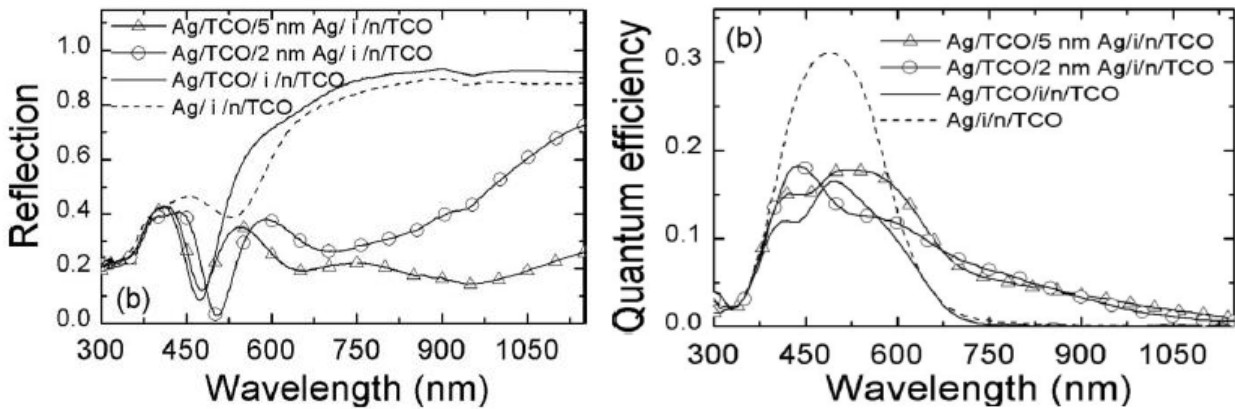


Figure 2.8: Reflection (a) and quantum efficiency (b) measurements of Ag/TCO/(NPs)/i/n/TCO devices with and without nanoparticles resulting from the thermal evaporation of 2 and 5 nm Ag films. [66]

Finally, Halas' group research was also of big inspiration for this thesis: at the beginning of 2011, Knight *et al.* published an experimental study on the application of nanoantennas for photodiodes [69]. They used gold nanorods (50 nm wide and 30 nm thick with varying length, see Figure 2.9a-b) to excite LSPs, which then decay into "hot" electrons injected into the underlying semiconductor (Si), because their energy was enough to overcome the interface barrier (Au/Si). They measured the photocurrent responsivity for nine different antenna lengths (Figure 2.9c), showing the plasmonic resonance shifting within the IR range depending on the length.

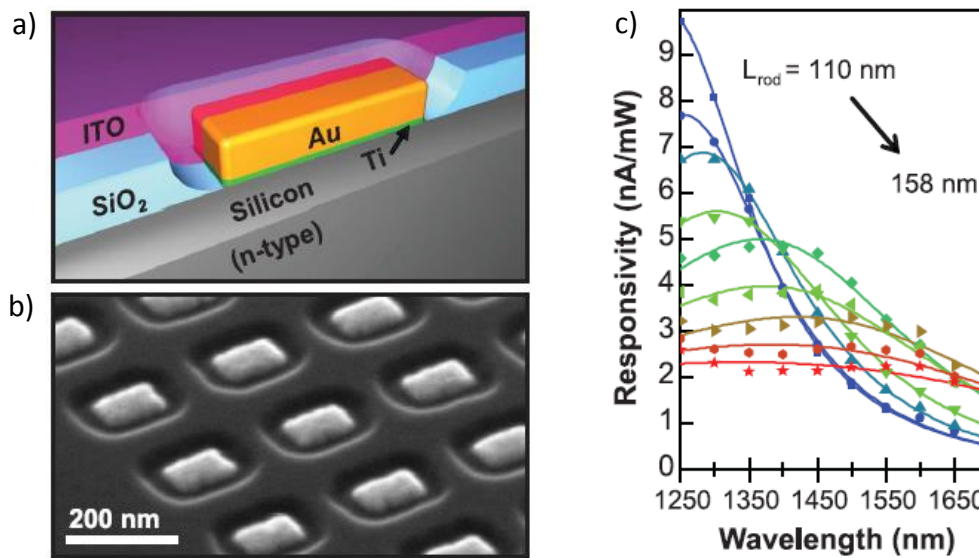


Figure 2.9: a) Representation of a single Au resonant antenna on an n-type silicon substrate (showing the structure of the photodiode). b) Scanning electron micrograph of a representative device array prior to ITO coating. c) Experimental photocurrent responsivity for nine different Au antenna lengths: 110, 116, 122, 128, 134, 140, 146, 152, and 158 nm (points). [69]

Through these devices they investigated hot electron generation by plasmonic antennas but they also admit that further studies and optimization are needed to increase their quantum efficiency, which is here only about 0.01%.

2.5 Traps at the LSP resonance energy

Beside photoemission, LSP resonance can also be used to increase absorption cross section of defect states of the semiconductor, originating the emission of the electrons through an “indirect” mechanism. In 2012 Lükermann *et al.* investigated a-Si:H solar cells with incorporated Ag nanoparticles made by de-wetting (Figure 2.10a) and measured a photocurrent response in the near IR range (below the a-Si:H gap). The observed effect was attributed to the excitation of electrons from defect states (*traps*) to the conduction band of the semiconductor, promoted by the electric field enhancement coming from the LSP resonance of the Ag nanoparticles [70].

A-Si:H is characterized by the presence of traps with energetic position in the range of the LSP resonance energy of the nanoparticles. In Figure 2.10b the NIR peaks in the measured external quantum efficiency spectra are shown: they correspond to different average size of the nanoparticles (redshift with increasing size) and are in good agreement with the calculated relative extinction spectra. The LSP resonances occur at wavelength of 820nm (for average NP size of 10nm), 840nm (23nm) and 875nm (30nm) with a consequent non-zero EQE of about 2.1%, 1.5% and 0.8% respectively.

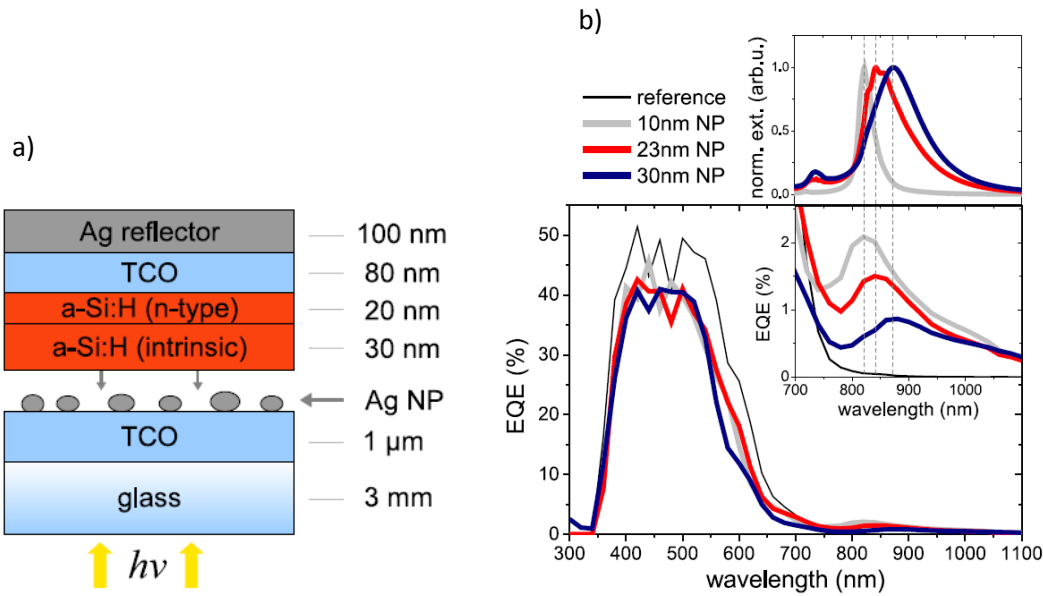


Figure 2.10: a) Schematic design of TCO/Ag NP/a-Si:H p-i-n/TCO solar cells. b) EQE measurements of the PV devices shown in (a). The EQE signal in the NIR range is shown in the inset with an enlarged ordinate scale. The inset on top shows the calculated normalized extinction of Ag NPs with the size distributions used for the real samples in a silicon environment with a refractive index of $n = 4$. Dashed vertical lines indicate the overlap of the calculated LSP resonances with the observed EQE peaks. [70]

As proof of the consistency of the proposed model they varied the boron doping concentration of the a-Si:H (p-type) in order to shift the Fermi level (E_F) towards or below the introduced traps. For medium and high doping concentrations the low energy part of the gap states is already shifted above the E_F leading to a depletion of these states and in such situation the NIR photons cannot promote any electrons to the conduction band, in fact the EQE signal in this range of wavelength decreases with increasing the doping level, till disappearing for really high boron concentration.

In 2013, as confirmation but also overtaking of this work, Moulin *et al.* proposed again a similar structure (Figure 2.11a) as photosensitive device recalling their work of 2009 with a combination of the two effects [71]: the photoexcitation of “hot” electrons in the NPs (as explained in Section 2.3) and the photoexcitation of electrons occupying defect states present in the vicinity of the NPs (as suggested by Lükermann *et al.*), both resulting from the decay of the LSPs excited inside the Ag nanoparticles (of 20 nm size).

In addition, Moulin *et al.* demonstrated that plasmon induced photogeneration of “hot” holes is also able to contribute to a photocurrent and that is why a bifacial symmetrical transparent device (the system shown in Figure 2.11a can be irradiated and characterized also from the back) was prepared in order to compare the quantum efficiency of both processes (hot electrons and hot holes). The photocurrent increase in the NIR range (of about 5%, Figure 2.11c) was also confirmed by the measured absorbance enhancement (of almost 100%, Figure 2.11b).

Another important recent study, made by Vashchenko *et al.* [72], highlighted the existence of the “traps-phenomenon”. They investigated the dark and photo-conductivity of silver nanoparticle ensembles on quartz glass substrates. They measured an increase in the photoconductivity due to the LSP excitation within the Ag NPs and they explained it as an excitation of the electrons from the defect states of the quartz to the conduction band, promoted by the local field enhancement due to the LSPR of the metallic

NPs. They also explained the measured dark current as the movement of the electrons along surface traps by a hopping mechanism.

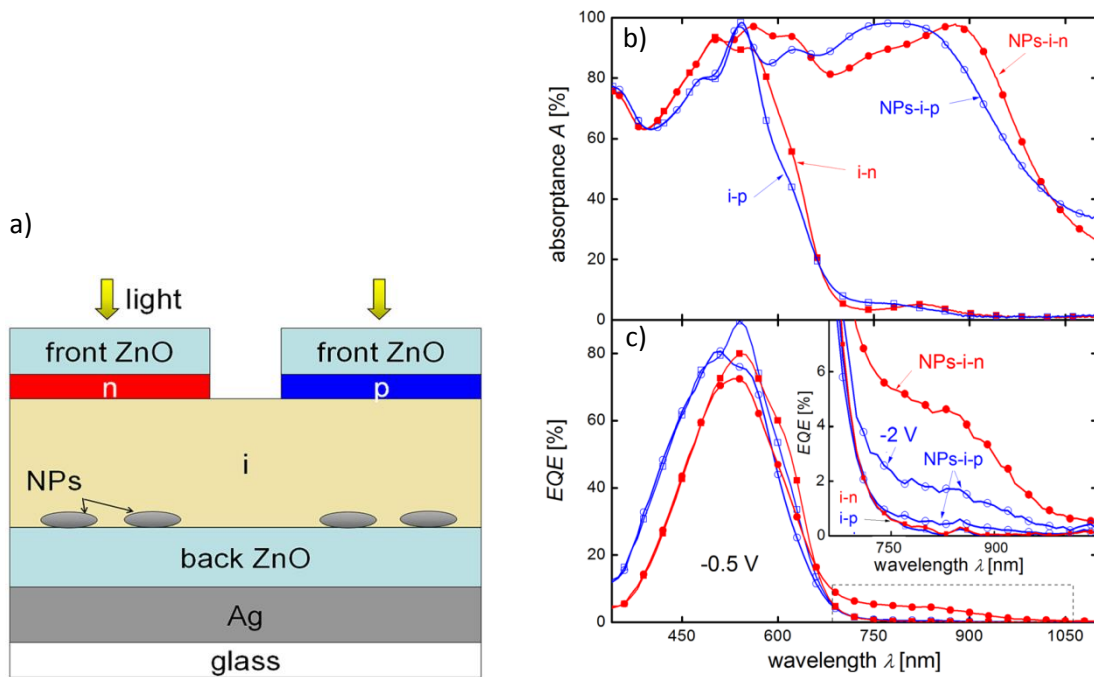


Figure 2.11: a) Schematic drawing of a-Si:H-based photosensitive devices deposited in parallel on the same substrate, with the NPs-i-n and NPs-i-p configurations. b) Absorbance as a function of wavelength and c) external quantum efficiency at 0.5V of i-n and i-p photosensitive devices (filled and open symbols, respectively) with (circles) and without (squares) nanoparticles. The inset in (c) shows an enlargement of the EQE in the long wavelength region (delimited by the dashed box). [71]

2.6 Interparticle coupling

As we mentioned in chapter 2.3, when we talk about nanoparticles and LSP resonance we have to keep in mind that it is strictly dependent on the characteristic of the individual particle: material, size, shape, surroundings, substrate and particle-substrate separation distance. All these features affect the Fröhlich frequency (defined by equation (2.3)) or the peak intensity and width of the resonance. Moreover, in the case of non-spherical shape, the LSP can split into two dipole modes (depending on the polarization) due to the resulting distribution of charge in the asymmetric particle [24], [73], [74], and, also, the presence of tips in the case of sharp and pointed particles can affect their scattering and absorption properties [75], [76].

However, in addition to the study of the single-particle, the collective properties are important for determining the consequent spectral responses of the whole structure, which practically consists of an ensemble of particles.

In chapter 2.1 we showed that a nanoparticle acts as an electric dipole, resonantly absorbing and scattering electromagnetic fields⁵. A particle ensemble can then be treated as an ensemble of interacting dipoles; in

⁵ The dipole approximation is valid only for vanishingly small particles, with $d \ll \lambda$. For particles of larger dimensions, where the quasi-static approximation is not justified, an electrodynamic approach is required and we refer to Mie

this case we expect that the localized modes of the single particles would interact causing consequent shifts of the resonance.



Figure 2.12: Schematic of near-field coupling between metallic nanoparticles for the two different polarizations. [25]

In *ordered* metal nanoparticle arrays, where the distance between the particles d is relatively bigger than the particle size r (such that the dipolar approximation is justified and the particles can be seen as point dipoles), we have 2 regimes:

- ✚ When $d \ll \lambda$: the point dipoles interact via their near-field with a distance dependence of d^{-3} [25] and we have strong field localization (hot spots) in the gaps between adjacent particles [77], [78]. The restoring force acting on the oscillating electrons of each particle, coming from the charge distribution of the neighbours (Figure 2.12), will increase or decrease change (depending on the incident polarization); thus, the interparticle coupling will lead to a shift in the LSP resonance: a blue-shift for the transverse modes and a red-shift for the longitudinal ones.
- ✚ When $d \leq \lambda$: far-field dipolar coupling with a distance dependence of d^{-1} dominates [25] (*radiative* dipolar interaction), which affects both resonance frequency and spectral width [79].

On the other hand, when d is relatively close to r , beside the electromagnetic coupling, also multiple light scattering and interference effects need to be considered because the light scattered by one particle can significantly contribute to the excitation of its neighbors. Such coupling between particles can alter the single scattering and absorption response in a variety of ways depending on the distance between particles as well as their geometrical arrangement. This means that, if we consider a pattern of nanoparticles arranged in a periodic grid, the array will exhibit different optical properties from those of each individual nanoparticle because of the introduction of diffractive orders.

Moreover, with decreasing particle spacing the dipolar coupling between clusters broadens the optical response [20].

Interparticle coupling effects can in fact result in a significant broadband, non-resonant absorption enhancement, as was demonstrated by Rand *et al.* in their study of silver nanoclusters for organic tandem thin-film solar cells [80]: Figure 2.13 shows the increase of the semiconductor (CuPc) absorption at wavelengths longer than then the Ag particles resonance (470 nm), which, they demonstrated, leads to an increase in the efficiency of the 15%.

Theoretical and semi-empirical studies of 2D metal nanoparticles arrays, describing the important relationship between particle size and interparticle spacing, have been analysed in [55]; in [81], a semi-analytical model used to calculate the coupling effects between the dipolar surface plasmon nanoparticles of a periodic structure where d is very close to r is described.

theory: in this case, the excitation of higher order harmonics or multipoles can occur as a result of phase retardation of the applied field inside the material.

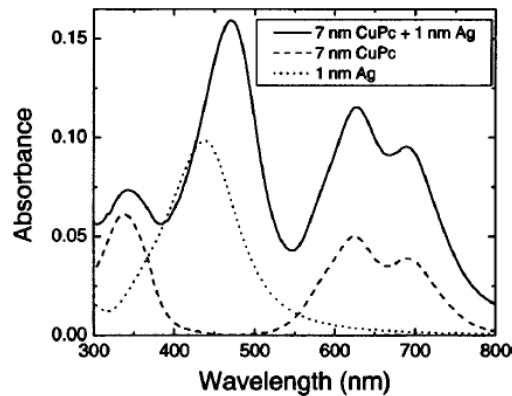


Figure 2.13: Measured absorbance spectra for 1-nm Ag (dotted curve), 7-nm CuPc (dashed curve), and 7-nm CuPc film on 1-nm Ag (solid curve). All films are deposited on quartz substrates. [64]

In general, for periodic arrays of nanoantennas, three coupling regimes exist depending on the interparticle spacing [82]: the *radiative* regime occurs when the array pitch is large enough that the incident radiation at LSP resonant wavelength diffracts above (or below) the substrate; in this case the polarizability of the single particle is slightly affected by the others and this kind of coupling can actually improve the quality (narrower and more intense peaks) of the LSP resonance [83], [84], [85]. The *evanescent* regime occurs when the pitch is so small that the coming light at LSP resonant wavelength diffracts in-plane, creating modes propagating through the structure but evanescently decaying normal to the substrate [86]. As the array pitch is reduced, this transition first occurs for diffractive modes in air, and then in the substrate [87]. In this regime the LSP resonances blue-shift and get narrower showing then an asymmetric band consistent with a Fano lineshape [88]. Finally, when the interparticle spacing gets even smaller, a transition to a third regime, often called *near-field* coupling [82], is observed: here the LSP resonance redshifts, becomes more symmetric and radically broadens. This last regime occurs when the extension of the resonant mode extends beyond the physical antenna end overlaps that of its neighbor [89].

In order to better understand the electrodynamic interactions in near-field coupling regime, two nanoparticles placed at short distance from each other (*dimers*) have been intensively studied [20], [90], [91].

2.7 Disorder effect

Ordered metal nanoparticles ensembles are simple to study the collective effects of the ensembles from an analytical point of view. Setting a constant lattice pitch gives the possibility to simulate the system making use of a unit cell and its regular periodic repetition. These studies can then be compared with experimental measurements made on real samples usually fabricated by electron beam lithography (EBL, see Section 4.2.1).

EBL technology is quite expensive and thus of limited use in thin film solar cells. Alternative cheap technologies make use of colloidal solutions [92] or self-assembly techniques [93], which give rise to random distribution of the particles in space. It is, thus, important to consider the disorder effect and the consequent differences in the optical properties of the disordered particle ensembles.

By comparing ordered patterns with random ones (obtained keeping the same surface coverage but moving each particle from its position in the array by a random x and y offset [47]) Temple *et al.* pointed out a first difference in the extinction spectra (Figure 2.14).

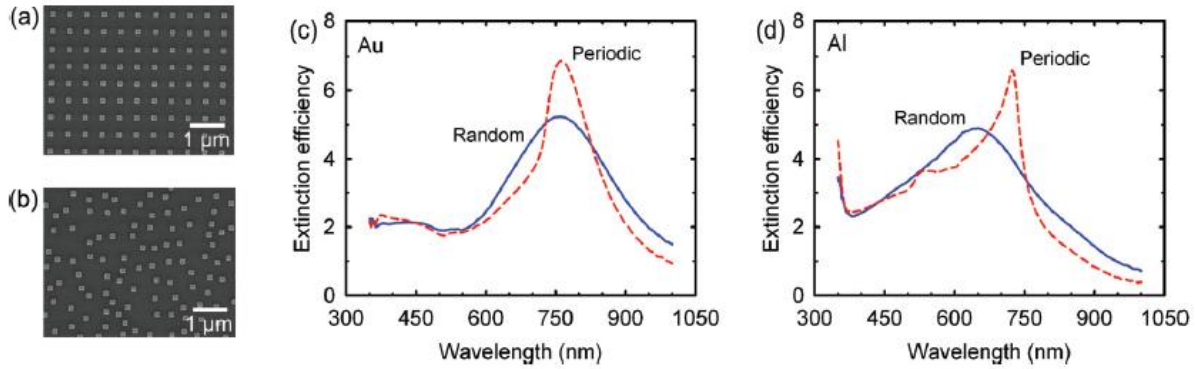


Figure 2.14: SEM images of (a) periodic arrays and (b) random arrays of square particles with a side length of 150 nm. (c) Extinction spectra of Au arrays, (d) extinction spectra of Al arrays. [47]

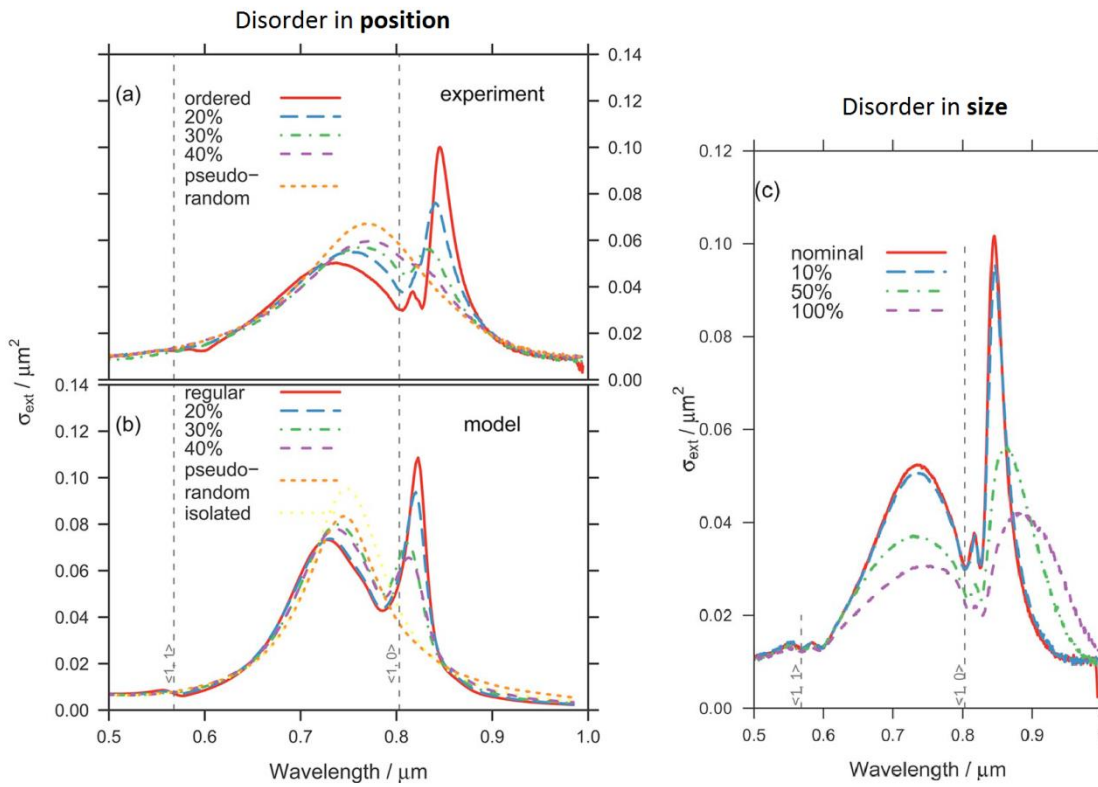


Figure 2.15: a) Extinction spectra from five different arrays of Au nanoparticles of varying positional disorder but with constant average occupancy. The deviation from the ordered array is indicated in the legend as a percentage of the nominal regular particle separation 550 nm. The vertical dashed curves indicate the $\langle 1,0 \rangle$ and $\langle 1,1 \rangle$ diffraction edges for the periodic array in a homogeneous environment (refractive index 1.46). The nominal particle sizes were 120 nm, 80 nm, 35 nm. b) Calculated extinction spectra using a coupled dipole model with the same parameters as (a). c) Extinction spectra from arrays of nanoparticles with regular positions but a variation in particle sizes. The legend indicates the level of disorder introduced in the length of the long-axis of the nanorods. [54]

While the ordered arrays show narrow and asymmetric peaks, the random ones are characterized by broad and roughly symmetric peaks. This change is mainly due to the suppression and enhancement of scattering at different wavelengths due to diffractive orders in the periodic array [94].

The comparison and the different features are even better demonstrated by Auguie *et al.* [54]. They investigated the effect of varying the degree of disorder in the geometrical arrangement from a periodic to a disordered lattice (keeping the surface coverage constant) and they explained well the suppression of the narrow peak, which, in ordered patterns, originates from the coherent superposition of partial waves scattered from all the particles in the array [21]. This narrow feature is actually present on the low-energy wing of the broad LSP resonance, which is not very clear in Figure 2.14, but is well visible in Figure 2.15.

We can also notice a dip in the extinction close to the diffraction edge (partial suppression by the coherent scattering). When the regular periodicity is broken, the sharp peak begins to decrease in intensity, gets broader and, with increasing the disorder, blue-shifts till disappearing into the broad LSP excitation peak, which gets instead stronger (Figure 2.15a-b).

In this study, Auguie *et al.* investigated the effect of not only the disorder in position but also the disorder in size: they considered an inhomogeneous distribution of particles, arranged in ordered arrays. From Figure 2.15c, it is seen that in this case the dip at the diffraction edge never disappears and increasing the dispersion in particles sizes all the spectral features broaden and red-shift. This trend is mainly due to the wide distribution of aspect ratios and volumes of the different particle in the array (in fact varying the particle size we also vary the correspondent LSPR frequencies). If we then also consider the dipolar coupling, what is happening is that, with different size distribution, some particles will have LSPRs that no longer match well with the period; they thus contribute less effectively to the coherent coupling and that is the reason for the constant presence of the dip.

Nishijima *et al.* [95] showed an electric field enhancement up to $(1-2) \times 10^2$ times as the disorder is gradually introduced within the particles pattern (Figure 2.16) and this could be used in favor of the applications of LSPs to photovoltaics (and not only).

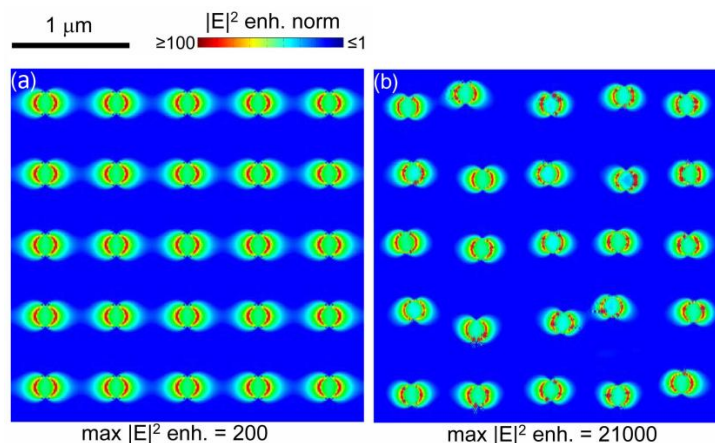


Figure 2.16: 3D-FDTD calculations: log-plots of normalized E-field enhancement on top of the nano-disks for **a)** periodic array and **b)** random-walk with $N = 2$ (N is the number of random walk step iterations off the central position, where the step is of 150nm), with incident wavelength of $\lambda=850$ nm. [95]

Furthermore, the introduction of the disorder was experimentally demonstrated to improve light trapping and thus the external quantum efficiency in thin film solar cells [96], leading to the conclusion that a spectrally broader but less strong (due to the disorder effect) coupling to individual waveguide modes for a specific wavelength is a clear advantage.

3. Schottky junction solar cells

In a photovoltaic device a built-in asymmetry is necessary to extract the generated carriers out of the device, before they can relax to the ground state, and to feed them into an external circuit. The extra-energy of the excited electrons generates a potential difference that drives them through a load in the external circuit. Typical solar cells consist of a p-n junction, here we consider instead a Schottky junction: the asymmetry is provided by the barrier between a thin transparent conductive layer (TCO), electrically acting as a metal, and an n-doped semiconductor thin film. In order to obtain a photovoltaic effect, the relationship between the n-type semiconductor work function (ϕ_{n-sc}) and TCO one (ϕ_{TCO}) is:

$$\phi_{TCO} > \phi_{n-sc} \quad (3.1)$$

Otherwise, an ohmic contact would be created. The working principle of a Schottky diode is very similar to that of a p-n junction.

In Figure 3.1a-b the band diagram of the two materials is shown before (a) and after (b) they have been put in contact. When the junction is created, the pinning of the two Fermi levels is achieved through the exchange of charge carriers across the junction: electrons flow from the semiconductor to the TCO, leaving a layer of positive fixed charge behind and a negative image charge on the “metal” until the charge gradient will be sufficient to prevent further (thermal equilibrium). This explains the bending of the energy bands and the generation of an electrostatic field at the interface, within the space charge, w , where there are no mobile carriers: the electric field drives electrons to one side and holes to the other, causing charge separation and creation of a depletion region (Figure 3.1c-d).

When the diode is irradiated, the incident photons can either be lost (through reflection and transmission) or, if they have energy higher than the bandgap of the semiconductor ($E_{ph} \geq E_{gap}$), be absorbed. The absorbed photons will promote electrons from the valence band of the semiconductor to the conduction band. Thus generated (Figure 3.1e-f) the electron-hole pairs are separated by the space charge layer and the electrons are now accumulating in the semiconductor while the holes go to the TCO layer. A new electric field opposite to the previous one and much bigger, the Fermi level is raised and the photovoltage occurs.

The Schottky diode geometry fits well the conditions required to achieve the goal of this thesis. In Chapter 2 it was explained how the electric field enhancement is localized within tens of nanometers in the surroundings of the plasmonic nanostructures; therefore, to better exploit the effect, a geometry which allows the metallic nanostructures to be in close contact with the active thin absorber, where we want the photoemission to occur, is chosen.

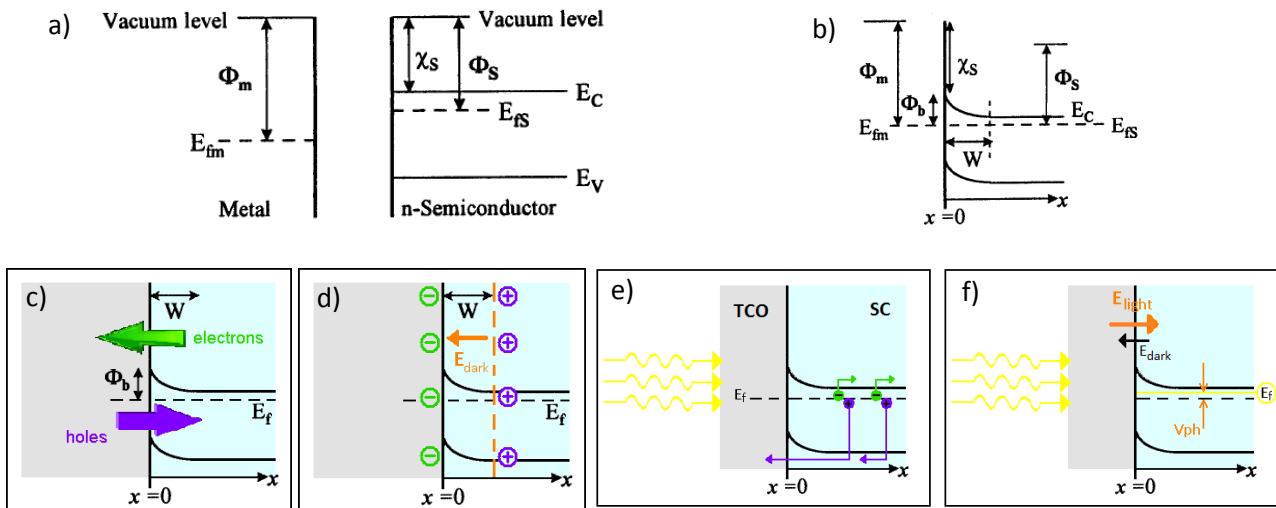


Figure 3.1: Band diagram of a metal (or TCO) and a semiconductor, before (a) and after (b) contact. Illustrations of the generation of the internal electric field at the interface, in dark (c-d) and under illumination (e-f).

3.1 GaAs solar cells

Gallium Arsenide is one of the most popular semiconductors that have intrinsic optoelectric properties superior to silicon as: direct energy gap (1.42 eV), higher electron mobility and lower power dissipation. These advantages make GaAs a very attractive material for optoelectronic devices and thus our choice as active material for the central device structure of this thesis (Figure 3.2). The absorber consists of an n-doped thin film grown by epitaxy on top of a bulk heavily doped layer, which creates an ohmic contact with the back metallic electrode. On top of GaAs, indium tin oxide (ITO) is deposited to complete the junction and a transparent top electrode; ITO combines light transparency with high electronic conductivity. Finally, at the interface of the Schottky junction metallic (Au or Ag) nanoparticles are incorporated.

This structure is not optimized to be working at the high efficiencies that can be achieved nowadays [97], in fact does not include any typical standardized expedients (like anti-reflection coating or back surface passivation and so on). It is instead designed to highlight only the pure effect of the LSP resonance originating from the nanoparticles.

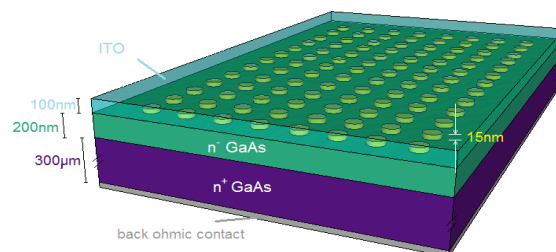


Figure 3.2: Sketch of GaAs Schottky diode studied in this work.

The photocurrent from the nanoparticle to the surrounding medium is proportional to the squared component of the electric field normal to the particle surface $|E_n|^2$ and the whole flow of electrons can be estimated by the average squared normal field, E_n , as [24]:

$$J = \frac{1}{S} \oint |E_n|^2 dS \quad (3.2)$$

where S is the area of the interface in the current flow direction. If the LSP excitation results from absorption of photon of energy below the bandgap of the semiconductor it will extend the spectral range of the solar cell.

3.1.1 Model and simulations

3.1.1.1 Order arrays of nanoparticles

The starting point of the design for the device was a result of the simulations based on the model shown in Figure 3.3a. The first structure is composed of a square grid of cylindrical silver nanoparticles of height h and elliptical cross section with the semi-axes R_l (long) and R_s (short) deposited on a GaAs substrate. The grid has period L and the nanoparticles layer is covered with ITO. The structure is illuminated with light of wavelength λ and intensity S , incident normal to the structure surface.

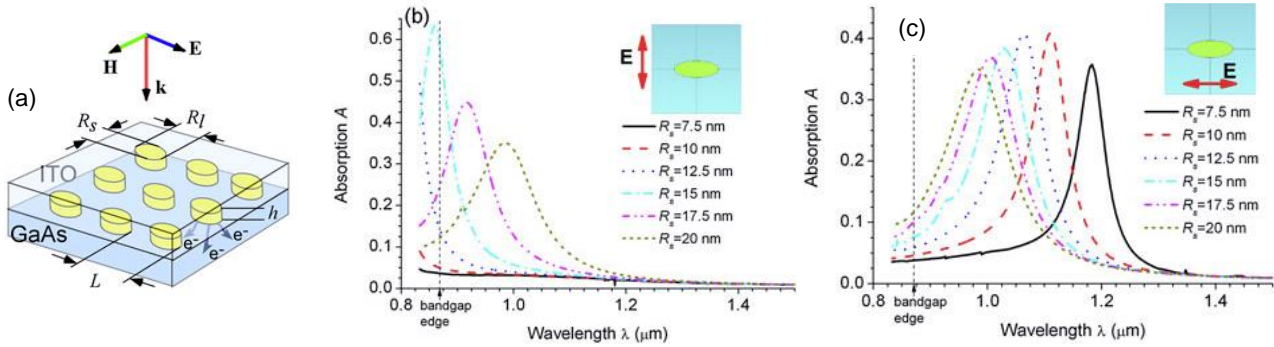


Figure 3.3: (a) Schematic diagram of the structure considered in the present study. Incident light induces the photoemission of electrons from the Ag nanoparticles into the GaAs. Light absorption spectra in the system of elliptical cylinders, for incident light polarized along (b) the long axes and (c) the short axes of the nanoparticles. In the calculations, $R_l = 20$ nm, $h = 10$ nm, and $L = 80$ nm. [24]

If the energy of a hot electron generated after the absorption of a photon is higher than 0.83 eV (i.e. wavelength shorter than 1494 nm), which is the Schottky barrier height of Ag on n-GaAs, then the electron can be transferred into the semiconductor. Thus, the photoemitted electron contributes to the photocurrent in the structure.

The current continuity is maintained by recharging the nanoparticles from the ITO layer through an external circuit.

The simulations were performed using the CST Microwave Studio modelling software and we refer to our published work (A. Novitsky *et al.*) [24] for more details.

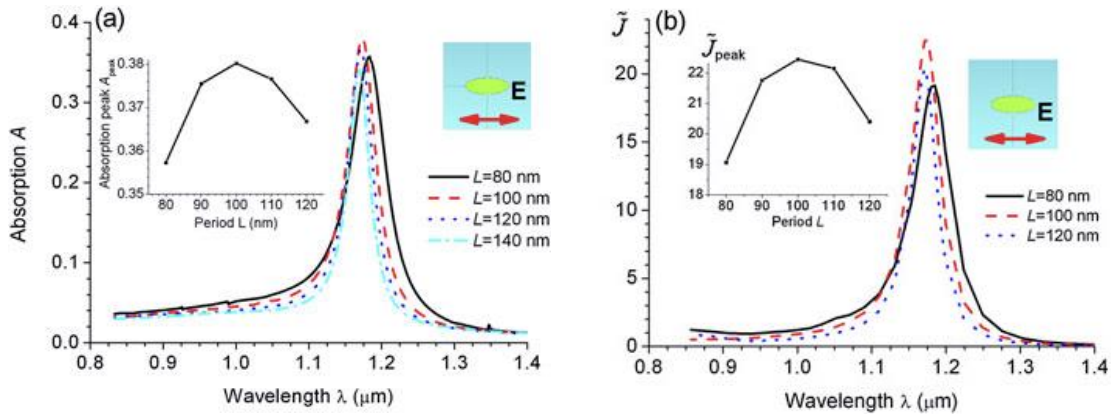


Figure 3.4: (a) Light absorption spectra and (b) spectra of the dimensionless photocurrent parameter J for several nanoparticle densities, that is, several values of L . The insets show the dependence of the resonance maxima A_{peak} and J_{peak} on L . In the calculations, $R_f=20\text{nm}$, $R_s=7.5\text{nm}$, and $h=10\text{nm}$. [24]

We show here the dependence of the absorption on the light polarization and on the size of the Ag nanoparticles (Figure 3.3b-c): an elliptical cylinder with $R_f \neq R_s$ has polarization-dependent plasmonic resonances that are strongly shifted from each other; increasing R_s the LSP peak blueshifts for polarization along the short axis and redshifts for the other one. In the context of the solar cell design, elliptical nanoparticles can be used to tune the plasmon resonance to a lower frequency, while maintaining the small volume of the nanoparticle, which is necessary for the efficient absorption and photoemission.

Plasmonic resonances for light polarized along the long semi-axes of all nanoparticles considered here lie at wavelengths longer than $\lambda_g = 0.88 \mu\text{m}$, which corresponds to the GaAs bandgap $E_g = 1.43 \text{ eV}$ and shorter than $1.49 \mu\text{m}$, which corresponds to the Schottky barrier at the Ag/GaAs interface. Therefore, the spectral responsivity of the device would be extended to longer wavelengths in comparison with GaAs. A signature of the presence of localized surface plasmons can be recognized in both the absorption, A , and the photocurrent, J , spectra, as shown in Figure 3 for different nanoparticle densities. The positions of the photocurrent maxima (Figure 3.4b) coincide with the positions of the absorption resonances plotted in Figure 3.4a. Both resonances are only slightly red-shifted and broadened with increasing the nanoparticle density (decreasing L) due to an increase in interactions between nanoparticles [53]; nevertheless, this effect is not comparable with the LSP frequency tuning deriving from the variation in size⁶. It should be stressed again that the resonance peaks are at wavelengths between 1.1 and 1.3 μm , thus corresponding to energies below the semiconductor bandgap. It is important to highlight how the resonance peak (in both A and J spectra) decreases in intensity and gets broader for smaller periodicity L ⁷: The contribution of the plasmonic nanoparticles to the absorption and photoemission must tend to zero for very low nanoparticle densities (large L), but, on the other hand, localized plasmon effects must vanish for a dense enough set of nanoparticles (small L), that is, when they start bridging with each other to form a homogeneous film. [24]

The second set of simulations focused on a model, whose geometry is shown in Figure 3.5a: In this model the nanoparticles are ideal gold cylinders with radius R and height h ; light impinges the device perpendicular to the semiconductor surface. The results of the CST simulations are shown in Figure 3.5b:

⁶ This is the reason why our first optimization of the EBL arrays nanoparticles focused more on getting small size particles keeping the periodicity constant to 100 nm.

⁷ In the next model for gold NPs this effect (deriving from the density variation) is shown better.

the black line is obtained from a model with parameters close to those of experimentally measured samples and the red dashed line indicates the red shifted resonance due to the presence of the ITO layer in the solar cell design.

The transmission dip occurs around 1 μ m wavelength for both periodical arrays (with periodicity L) and an individual nanoparticle indicating that it is caused by the excitation of localized surface plasmons within a nanoparticle and not the collective effects in arrays of coupled particles. This is important in order to get field enhancement which can yield the electron excitation with high probability.

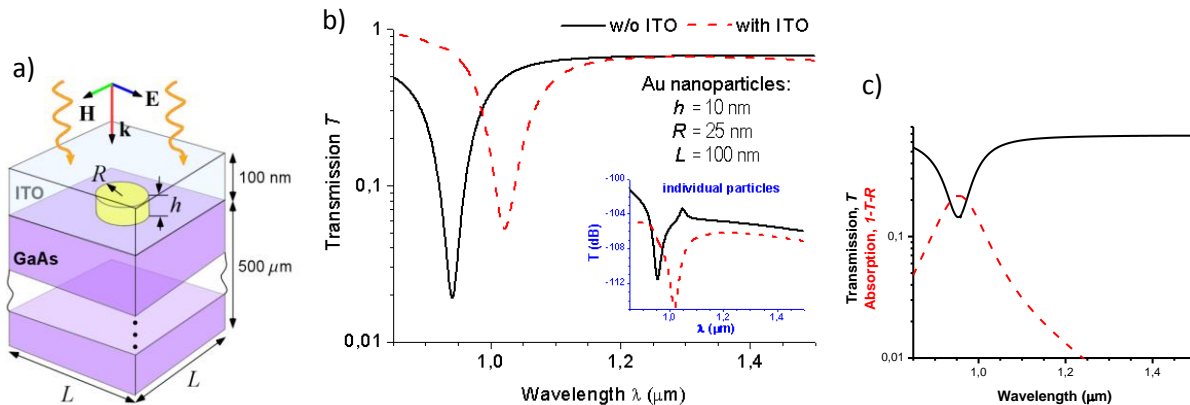


Figure 3.5: a) A unit-cell model (for Au cylindrical disks NPs) used in the CST simulations. b) Simulated transmission based on the model shown in Fig. a (red dashed line) and for the same structure but without ITO layer (black line); here h is the thickness of the nanoparticle, R the radius and L the periodicity of the array. Periodic boundary conditions are applied. The inset shows simulations for a single nanoparticle performed with open boundary conditions. c) Comparison of the simulated absorption and transmission curves. [98]

Therefore, at the beginning of this work, transmission resonance rather than absorption was chosen for optical studies (Section 4.3.1), due to its sharp definition and easier interpretation of optical experiments. It has to be stressed, however, that the simulations, giving both transmission (T) and reflection (R) curves, show that both T and R resonances occur at the same wavelength, see Figure 3.5c.

Simulations of transmission spectra for the varying density of the pattern are shown in Figure 3.6a: the dip redshifts for decreasing L (like for Ag elliptic disks). Even though the shift stops being noticeable for very dense NPs arrays (i.e. for $L < 80$ nm); the corresponding derived absorption (Figure 3.6b) visualizes the broadening of the LSP resonance which can be a good reason for using denser arrays within our solar cells, in order to achieve a better response to broader spectral range of light.

In conclusion, the modelling was used to determine parameters of NPs arrays to fabricate with electron beam lithography. It was found that LSP resonances for both Ag and Au NPs fall in the range of light wavelength, which is useful for photoemission. The resonance width broadens significantly for arrays with small period and so the densely packed NPs absorb light in a broad range of wavelengths that can contribute to photoemission. In Section 4.2.1 it will be described the optimization process which was performed in order to achieve small size NPs (diameter of 30-40 nm) with mainly three values of array periodicity (80-100-120 nm). The fabrication limits drove us to start with gold, or better with Ti/Au NPs (since a titanium layer is necessary to promote adhesion to the substrate): nanorods (to get elliptic disks as previously modelled for Ag) and circular disks were both aimed from the beginning but EBL rubs moved our focus on the circular shape.

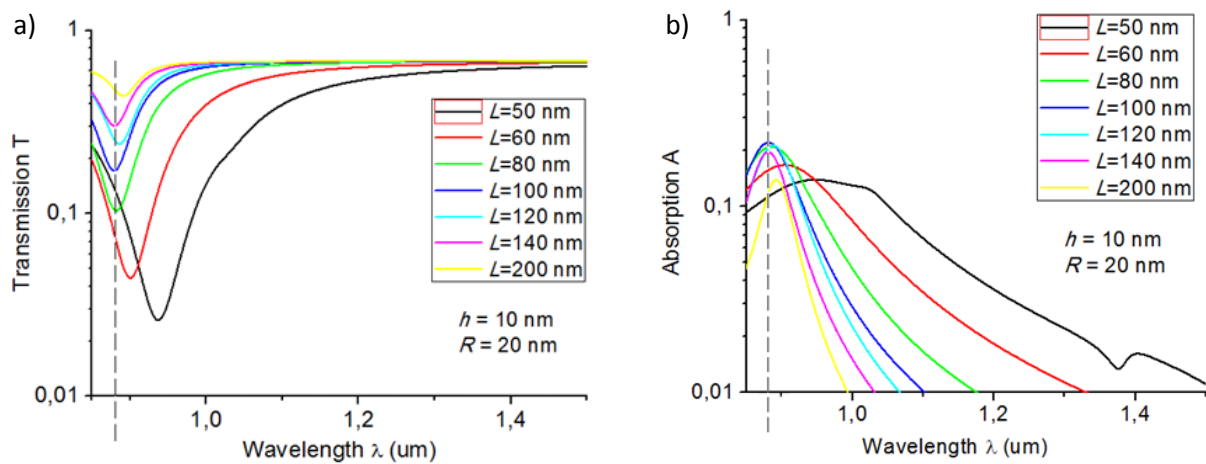


Figure 3.6: **a)** FDTD simulations of the transmittance of the diode shown in Figure 3.2. **b)** Calculated absorption by 1-T-R (also simulated but not shown here). The dashed line indicates the edge of the GaAs gap.

The actual fabricated arrays of gold NPs by EBL showed an interesting feature in shape, which convinced us we are in reality dealing with truncated cones (Figure 3.7a); therefore an investigation of how this shape could affect the LSP resonance was conducted.

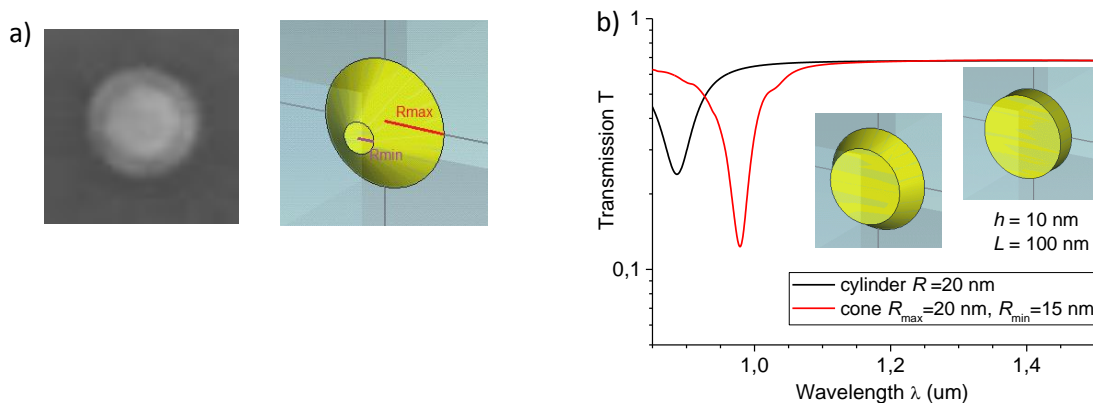


Figure 3.7: **a)** SEM image and relative model used of the FTDT simulations **(b)** of the golden NPs with truncated cone shape.

Simulations of the T spectra for cylindrical and conical shape (Figure 3.7b) show a difference in frequency, intensity and width of the LSP peak.

Moreover, both SEM images (Figure 3.8) and an AFM analysis (Figure 3.10) of the nanoparticles reveal a variation in the shape of the top and bottom radius within the same array; new simulations follow the input (Figure 3.10) showing how the shape can affect both position and magnitude of the T dip.

Figure 3.3b-c already showed that the resonance is highly shifted with size of perfect ellipsoidal cylinders indicating that size imperfections can broaden the spectra a lot; the last analysis, about the shape of gold NPs, is a confirmation of this.

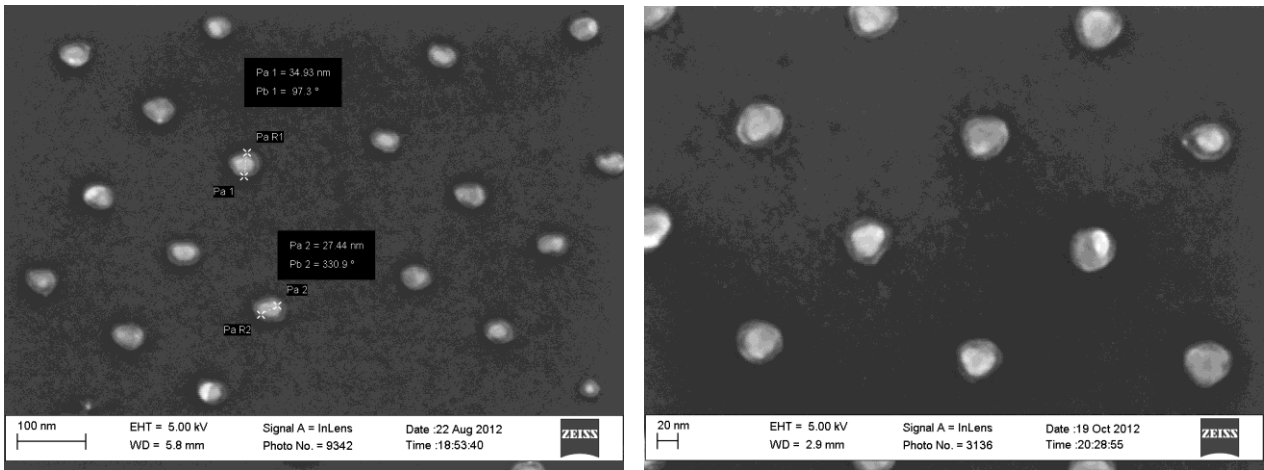


Figure 3.8: SEM images of Ti/Au NPs on GaAs substrate, showing conical shape of different size.

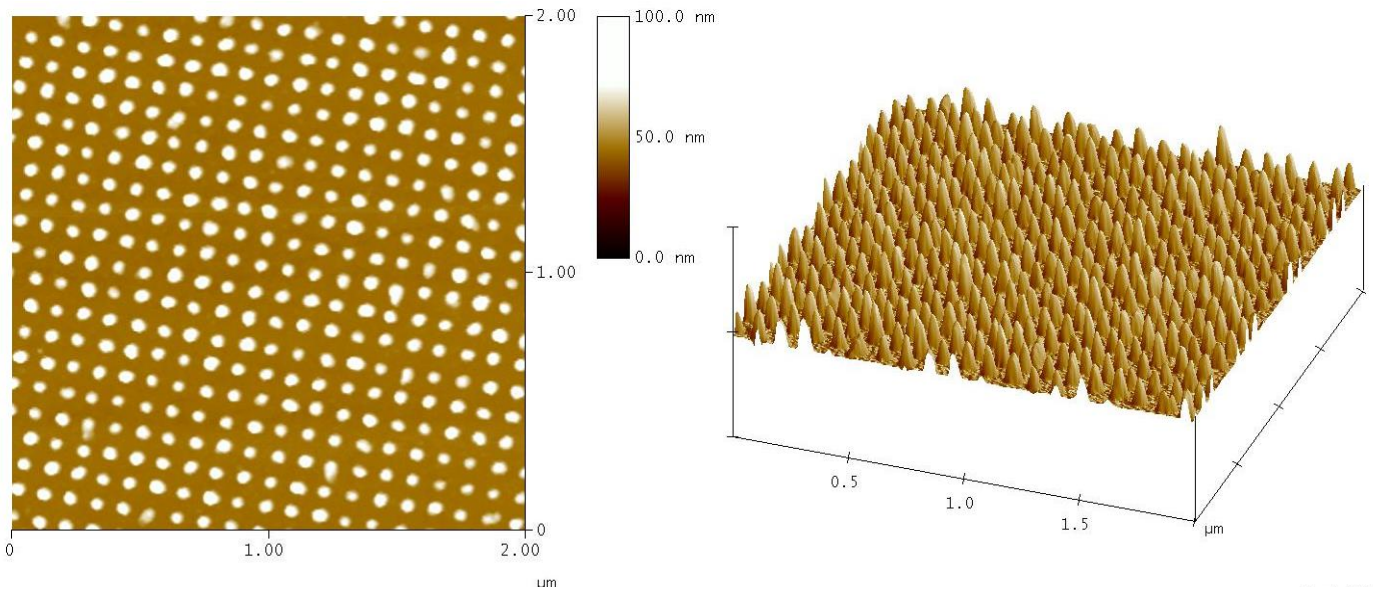


Figure 3.9: AFM scanning on the surface of the Ti/Au NPs of sample A4 (defined in Table?). left) top view; right) 3D view.

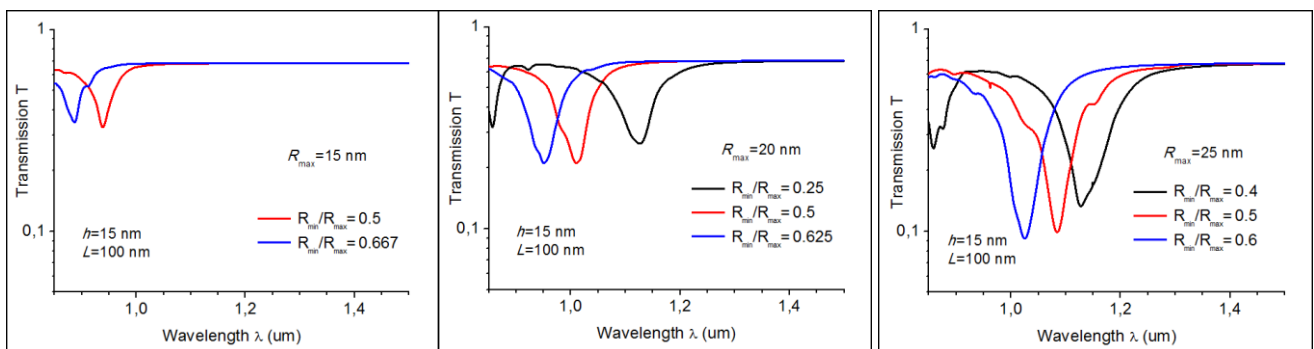


Figure 3.10: Simulations of T spectra for conical Au NPs with varying R_{min}/R_{max} .

3.1.1.2 Random distribution of nanoparticles

Next sections will introduce the two techniques used for the incorporation of the nanoparticles within the PV device, namely: electron beam lithography, which gives periodical arrangements of nanoparticles in square lattice; and electroless plating, giving random distribution of nanoparticles.

A new script to give random distribution design of the nanoparticles as input to CST simulations was developed: it allows the simulation of R and T on real patterns obtained by electroless deposition, whose design is extracted from the actual SEM image (Figure 3.11a), which is converted through Matlab code into black/white image (Figure 3.11c) with the possibility to choose the threshold for the contrast (Figure 3.11b); as an example of wrong contrast choice see Figure 3.11d.

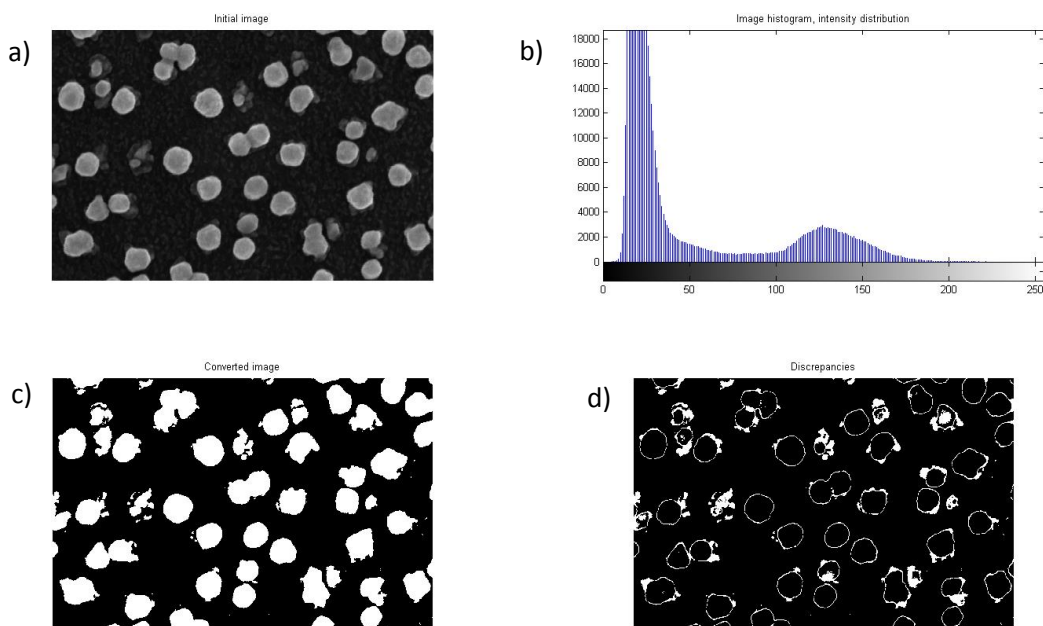


Figure 3.11: a) SEM image of random Ag nanoparticles deposited by electroless plating. b) Threshold graph used in the Matlab program in order to maximize the black/white contrast, which gives a correct representation in c) and a bad one in d).

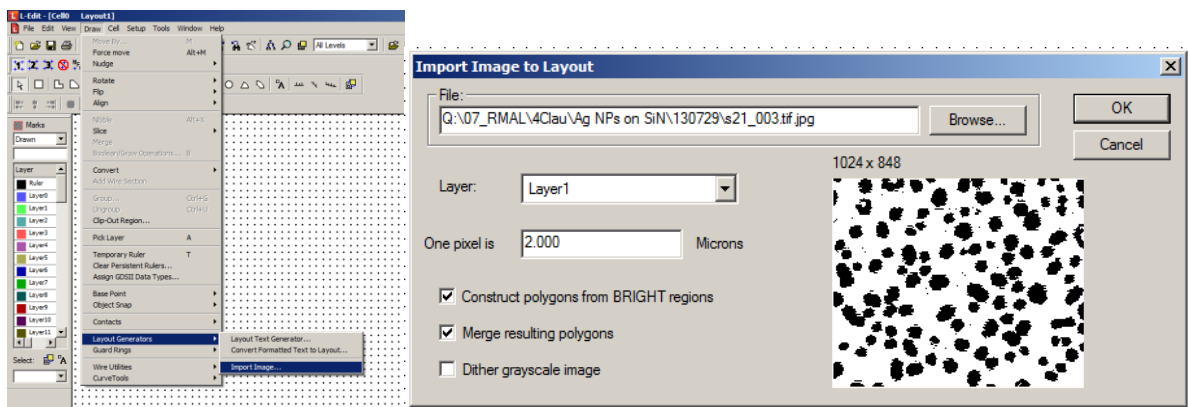


Figure 3.12a: Visualization (like a mask) of how to import a jpeg image (after being correctly converted in black/white) with L-edit program.

CST Microwaves software can import GDSII format and use the design as a layer of the structure (Figure 3.13a-b). The commutation of the SEM image (TIF file) in a GDSII file is done through a Matlab script (to first maximize the black/white contrast) and then L-Edit, which is a CAD software used to draw lithography masks (Figure 3.12a-b).

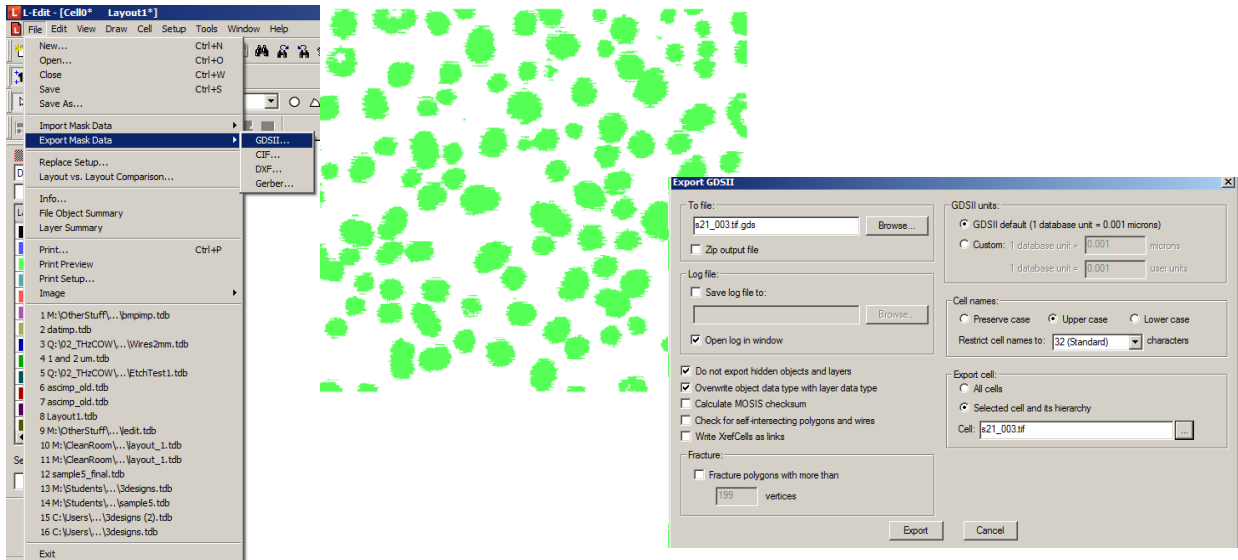


Figure 3.12b: Visualization of how to export (in L-edit) the mask, created starting from a SEM image, in GDSII format.

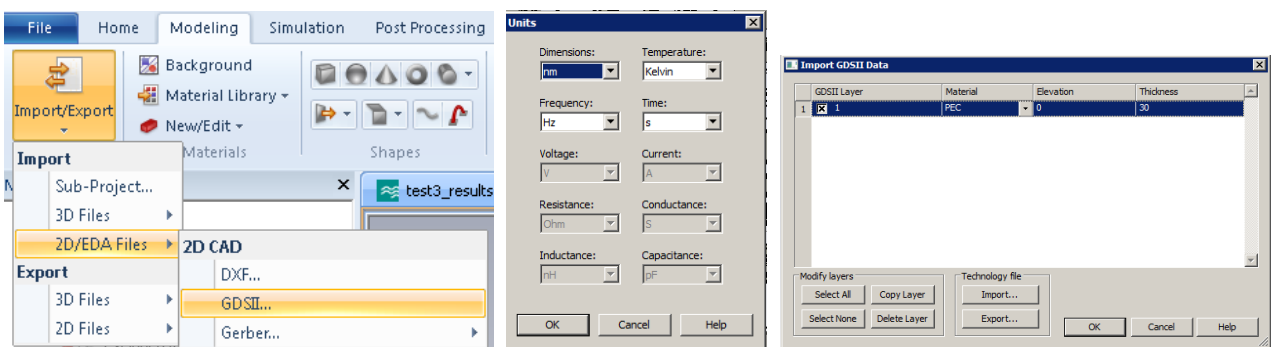


Figure 3.13a: Visualization of how to import a GDSII mask (created by L-edit), as a structure layer, in CST Microwaves.

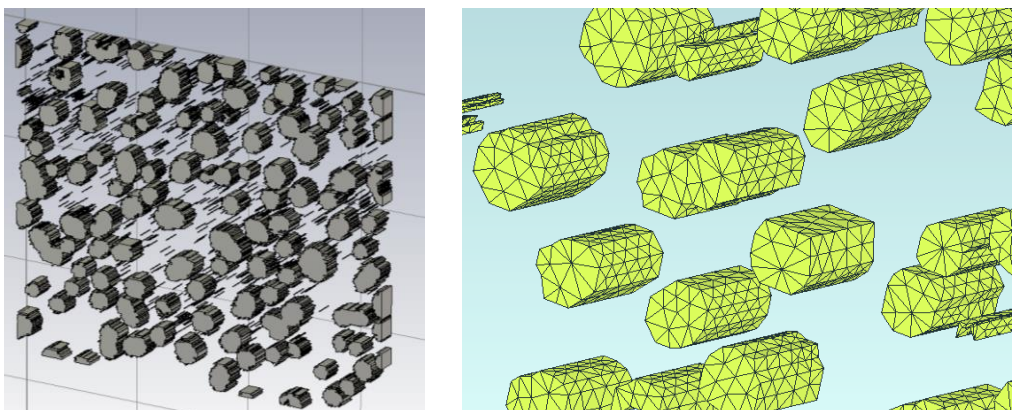


Figure 3.13b: Once the mask is imported in CST microwaves the main parameter to be set is the thickness of the NPs layer (see result on the left) and the kind of mesh that will be used for the simulations (right).

Simulations were run for random distribution of Ag nanoparticles (by electroless) on top of silicon and GaAs with and without ITO on top. For time-domain simulations: perfect electric field (x) and perfect magnetic field (y) were chosen as boundary conditions, with hexahedral mesh and small mesh steps (3-5 nm), in order to smooth out the imported shapes. For frequency domain simulations: unit cell boundary conditions and tetrahedral mesh were chosen.

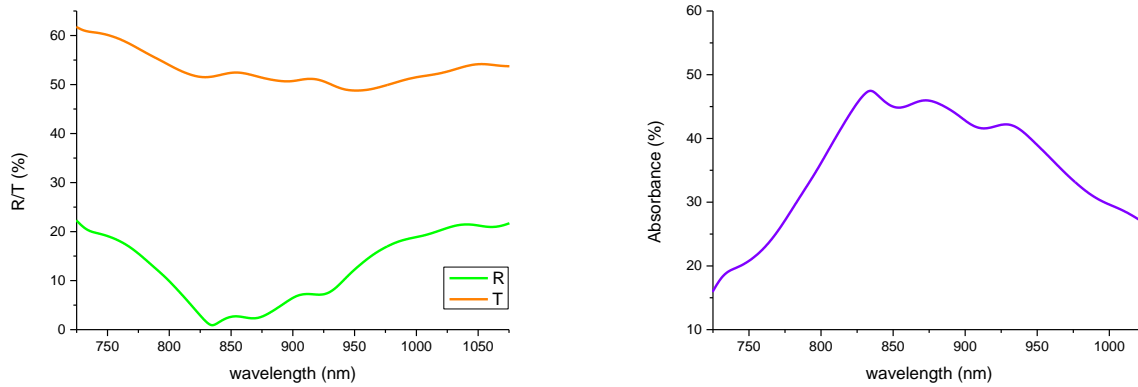


Figure 3.14: R/T simulations and derived absorbance spectrum of random Ag NPs on top of GaAs/Si₃N₄ and covered by ITO.

Nevertheless, even playing with the different parameters, we were not able to get simulations in agreement with our optical measurements (see a preliminary result in Figure 3.14). One of the reason could be the fact that in the model the height of the nanoparticles has to be fixed to a constant value for the whole array layer, whereas in the real electroless structures the NPs height is quite variable (Figure 4.41).

Further studies and development need to be done on this side.

3.1.2 Fabrication of the device

The devices used in this thesis are designed to study the plasmonic effects. They are kept as simple as possible, even though they do not perform with highest possible efficiency. GaAs devices are simply Schottky diodes and the processing includes at least defining the diode area by etching, providing an ohmic contact to the back of the device and formation of light transparent Schottky contact. Metallic nanoparticles, the subject of this study, are incorporated into the Schottky contact in close proximity of the GaAs surface.

The initial device structure is shown in Figure 3.2 and the process flow for its fabrication is described in the following sections.

1) Substrate

The thin absorbing GaAs layer is grown by epitaxy with MOCVD machine in the Nanophotonic Devices

group at DTU Fotonik; the nominal thickness and n-doping value are respectively 200 nm and 10^{16} cm^{-3} . The light doping is used as a compromise between carrier recombination and series resistance. Only a fraction of low energy photons is absorbed in 200nm thick layer, so any plasmonic effects should be visible.

The active absorber layer is grown on top of a heavily doped (10^{18} cm^{-3}) 350 um thick, 2" GaAs wafer. Such wafer is cut into 7-8 chips: the single chip is chosen with an area of at least 14 mm by 14 mm, in order to contain the whole mask (12 mm by 12 mm)⁸. Each chip is processed into 288 solar cells in several photolithography steps (Figure 3.15 and Figure 3.16).

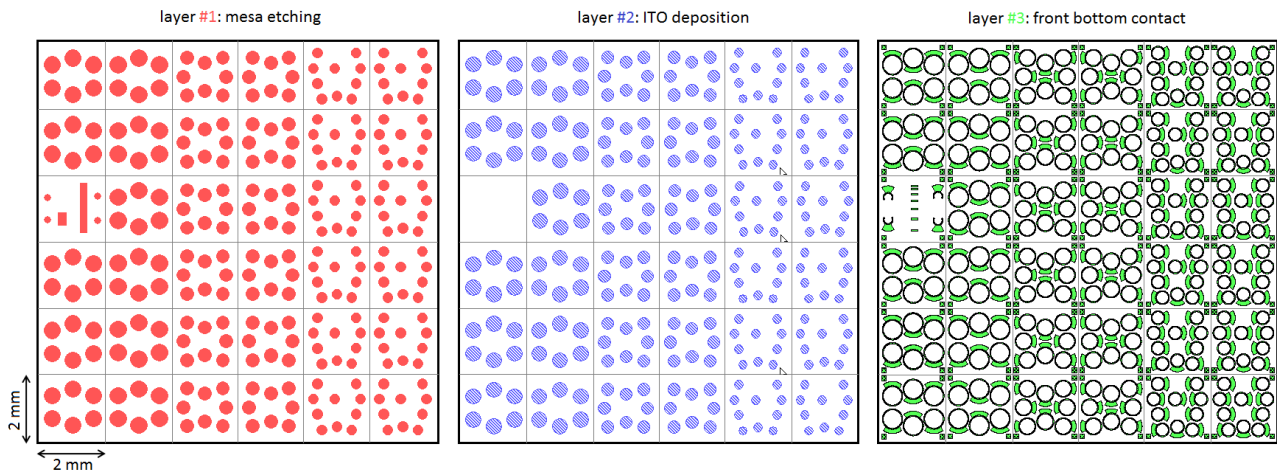


Figure 3.15: Masks used for the photolithography steps during the fabrication process of the GaAs devices. Note that layer #2 and #3 correspond to the reverse of the actual used masks, which are bright structures on dark field (since a positive resist is used); but for better visualization they are shown in the complementary way.

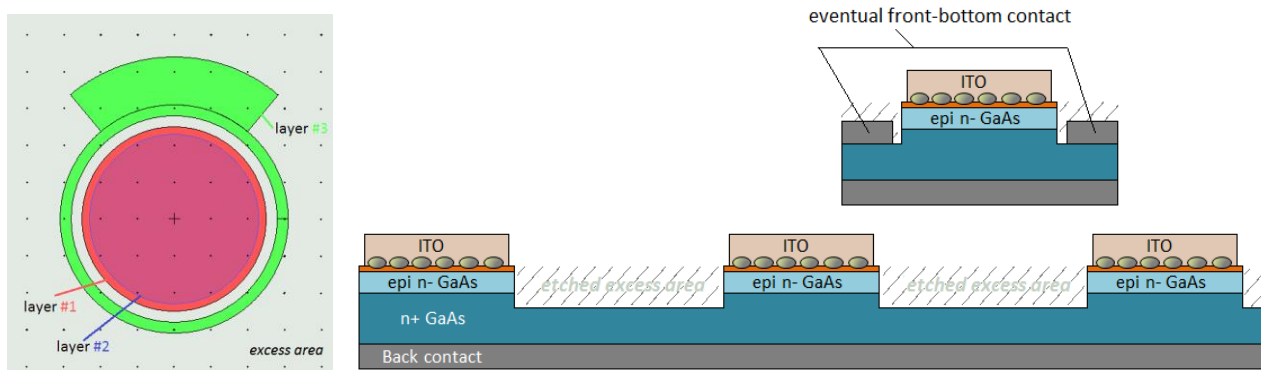


Figure 3.16: **left)** Top view of the photolithography layers mask (overlapped) of a single diode; **right)** cross section of the resulting devices on top of the same substrate.

2) Deposition of back electrode

As first step, an ohmic contact of the diode is formed through the back of the wafer while the front of the wafer is protected with a layer of photoresist. The ohmic consists of a metallic alloy deposited by electron beam evaporation.

⁸ Gallium arsenide is a very expensive material and the use of the wafers was parsimonious.

When metal is put in contact with a semiconductor, to create the electrode, their conduction and valence bands bend, creating a barrier at the interface for the mobile carriers. A photovoltaic device works collecting electrons from one electrode (here the bottom contact), then fed into a circuit which is closed with the other electrode (on top, here the ITO layer): in order to make ohmic contacts these barriers need to be designed as low enough that the current can cross the interface by thermionic emission, or narrow enough that the current can cross the interface by field emission [99].

Before the metal evaporation, the native oxide layer needs to be removed from the semiconductor surface in order to allow a better contact between the two materials. The removal of oxides from GaAs surface is done by wet etching in $\text{NH}_4\text{OH}:\text{H}_2\text{O}_2=1:1$ for 2 minutes, followed by rinse in running water for other 2 minutes. Straight after this step the chip is mounted inside the vacuum chamber of the e-beam evaporator and the following stack is deposited: 40 nm of germanium, 60 nm of gold, 27 nm of nickel, 250 nm of gold. The three elements, Ge, Au and Ni, have specific roles in the formation of the contact during subsequent step of rapid thermal annealing (RTA).

Nickel serves to react with the native oxide for a complete and uniform removal all over the processed area; moreover, it creates intermediate complexes with GaAs that will disturb the crystal lattice to make way for the diffusion of Ge into GaAs. The diffusion is facilitated also by gold, that reacts with Ga atoms. The driving forces of the Ni-GaAs and AuGa formation, reduce the thermal energy needed for the diffusion process, which would otherwise occur at temperature higher than 600°C. Instead, the temperature used for this alloy is 420°C.

Before the annealing, the front cover (resist layer) is removed with soaking in acetone for 15-20 minutes and few minutes of plasma ashing if the surface still looks dirty. Once it is confirmed with optical microscope check, that the resist layer is completely removed the n-alloy formation can be completed.

The RTA treatment following the alloy evaporation starts with a slow ramp to reach 150°C while purging and pumping the chamber 3 times; then N_2 gas is introduced in the chamber and a very rapid ramp of temperature to 400°C starts, which usually takes 30-35 seconds. From this temperature, in 5 seconds 420°C is reached and it stays at this level for 10 seconds. Finally the process concludes with fast cooling down. The temperature of the chamber is controlled by a thermocouple system.

A simple way to judge if the alloying is accomplished is through the color of the metal, which is usually golden, shining and mirror-like before the annealing, and gets silvery and satin, afterwards. For some batches of diodes, after RTA, the surface looked opaque and satin but not silvery, the alloy did not completely diffuse and performance of the completed solar cells was unreliable. The current-voltage (IV) characteristics of the diodes, shown in Figure 3.17, were unstable. Dark IV curves before (blue line) and after (green line) being illuminated were not reproducible, or showing unexpected behavior under illumination (orange line).

In order to recover the diodes, the chip was submitted a second time to RTA, this time increasing the annealing temperature to 430°C. The problem could have been that 420°C was not enough to properly and uniformly activate the diffusion of the metal into GaAs; or that the temperature in the chamber was not such uniform that the thermocouple was measuring a different temperature than the one lived by the wafer. In few cases, with this second higher-RTA, the back surface change to silver color but for one batch

of diodes it did not. Subsequently, this was anyway chosen to be the new RTA temperature for all future devices.

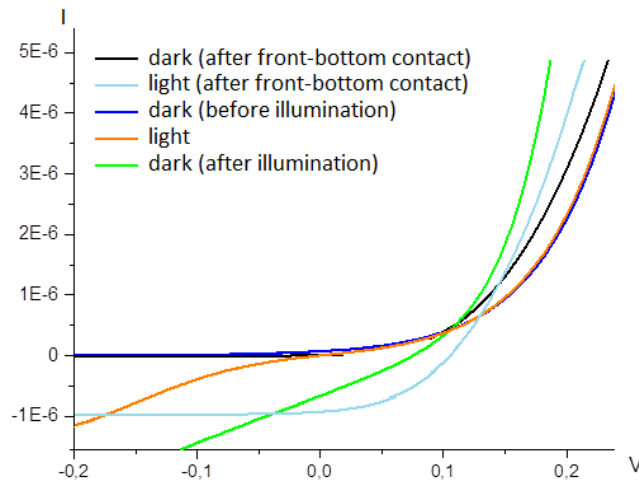


Figure 3.17: IV curves of GaAs Schottky diodes with odd behaviour due to bad alloy for back ohmic contact (blue, orange and green light), and normal behaviour after been recovered adding front-bottom contact (black and light-blue lines).

The final solution to the problem was the design of an alternative bottom electrode described in point 7) and giving normal Schottky behavior in the IV (line black and light blue in Figure 3.17).

3) Deposition of the insulating layer

The first batches of diodes were fabricated without including this step. However, surface of semiconductors is known to form fast non-radiative carriers recombination [100], which would counteract the photoemission from the incorporated nanoparticles, thus a thin layer (7-10 nm)⁹ of silicon dioxide has been introduced within the structure. The deposition is done, on the front side, with plasma enhanced chemical vapor deposition (PECVD) following this optimized recipe: 392 sccm N₂ flow, 1420 sccm N₂O flow, 12 sccm SiH₄ flow, 100 W of RF power at 550 mTorr, with an average deposition rate (calibrated for each batch of devices right before this step) of 1 nm/sec. The uniformity of the layer was evaluated on test samples, by measuring the distribution of the refractive index and thickness on the entire surface, with ellipsometry.

SiO₂ layer was chosen as insulating layer for solar cells with gold nanoparticles made by EBL, but for the incorporation of electroless NPs, it was substituted by a silicon nitride layer, for which we refer to Section 4.2.2.

4) Metallic nanoparticles incorporation

Two techniques have been used for this step (e-beam lithography for order arrays of Ti/Au NPs or electroless plating for random Ag NPs) and optimizations of both processes are described in Section 4.2.1-4.2.2.

⁹ A uniform thinner layer could not be achieved for limits in the equipment.

EBL particles are deposited only on the active areas of the diodes (aligned on layer #1 of Figure 3.15 and Figure 3.16 and here shown in Figure 3.18), while the electroless plating covers the whole surface of the chip, thus Ag will need to be etched in the excess area.

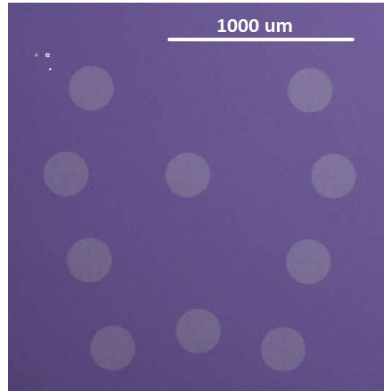


Figure 3.18: Optical microscope photo of 10 diodes defined by EBL nanoparticles. The circles show the resist (PMMA) pattern after development and before metal deposition.

5) Mesa definition by etching

In the next step of processing, independent devices within the same chip begins are defined through photolithography and etching.

A positive photosensitive resist (AZ5206E) layer of about 550 nm thickness is deposited by spin coating on the chip surface . Resist spinning is done after cleaning and dehydration of the surface: soaking in acetone for 3 minutes, then IPA (2 minutes) and rinse in water; pre-bake on hot plate at 180°C for 3 minutes.

This pre-treatment is very important in order to promote adhesion of the resist on the oxide layer. Working with small chips makes the uniformity of the resist difficult to obtain and often many attempts are needed before the coating is sufficiently flat. The spinning mode chosen for such small size substrate is dynamic, i.e. the resist is released on top of the substrate during pre-spinning rotation (and not statically).

After the spin coating, the resist layer is hardened by baking on a hotplate at 90°C for 90 seconds (standard bake for this kind of resist). Then alignment of the mask (layer #1 in Figure 3.15), with dark pattern on bright field, with the chip edges follows and subsequently UV exposure (5 seconds at 5 mW) of the bright areas. Development of the pattern is done in AZ351B:H₂O=1:5 for 1 minute. After development, the chip with the resist pattern is inspected under the optical microscope to avoid underdevelopment and, as last step, a short and gentle plasma ashing is useful to remove any resist traces from the developed areas.

Before starting with the etching sequence another bake of the resist pattern used as mask is recommended: 120 seconds at 120°C.

In order to define individual diodes, all the excess area, represented in Figure 3.16, needs to be etched away in 2-3 steps.

- I. For Schottky diodes with electroless nanoparticles, we first need to etch silver: 15 seconds in $\text{NH}_4\text{OH}:\text{H}_2\text{O}_2=1:1$, rinse in water for 2 minutes.
- II. The etching of the insulating layer is done with BHF for 8 seconds and then rinse in water for 2 minutes.
- III. Last etching step is what will isolate one diode from another, by etching through the epilayer and reaching the thick n+ layer. Since the epi-layer is 200 nm thick the etching through GaAs is calibrated for a safety depth of 250-300 nm using phosphoric acid:
from 60 to 75 seconds in $\text{H}_3\text{PO}_4(85\%):\text{H}_2\text{O}_2:\text{H}_2\text{O}=1:4:45$ and then rinse in water for 2 minutes.

Each etch step is controlled by measuring the profile step of the resist pattern, before and after the etching, with a profilometer. Afterwards, the resist mask is removed by Remover 1165 (10 minutes), then acetone (3 minutes), IPA (1 minute) and water rinsing; a few minutes of plasma ashing are added in the end if the surface of the chip is not totally clean.

6) ITO deposition

Indium tin oxide (ITO) is used to create the Schottky junction with the semiconductor and, at the same time, as top electrode of the solar cell. For the latter reason, it should exhibit a high transparency for the working spectral range of the device, which is expected to be between 400 nm and 880 nm due to GaAs absorption, and even longer wavelength if the photoemission in the NIR range will be generated by the NPs; but at the same time it needs to have high conductivity to avoid ohmic losses.

Sample	Pressure (mbar)	Power (W)	Sputtering Time (s)
#5	6	100	3600
#6	3	100	
#7	9	75	
#8	6	75	
#9	3	75	

Table 3.1: Specifics of the 5 of the ITO layers deposited by sputtering during optimization process.

The layer is deposited through magnetron sputtering (which is commonly applied for the preparation of TCO coatings). In the sputter process, argon ions (Ar^+) are created by a low pressure glow discharge and are accelerated towards a ITO target by means of an electric field (in our case DC) induced by two electrodes. By mechanical impact, the target material (ITO, created by the combination of indium oxide and tin oxide) is sputtered off and re-deposited on a substrate. Temperature, pressure and applied electric power at the electrodes can be varied independently to obtain different properties of the ITO coating. The optimization of the right combination of parameters in order to get a high transparent and high conductive layer was then conducted.

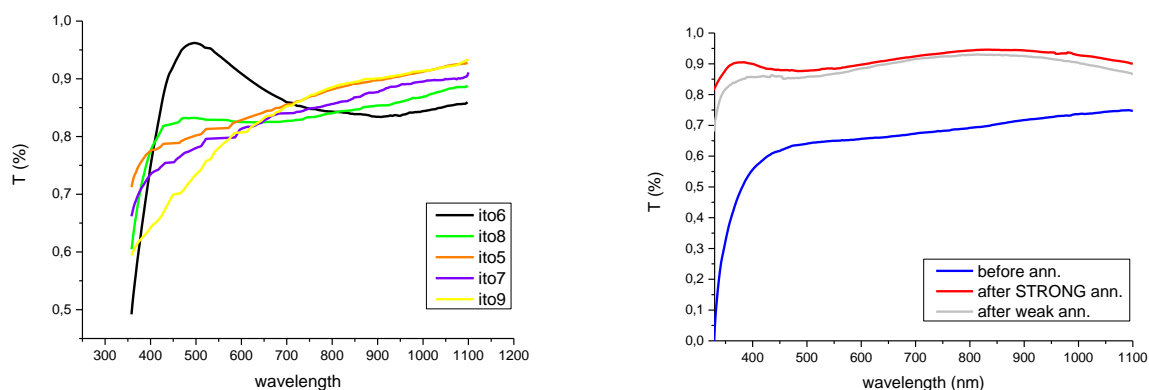


Figure 3.19: Transmission measurements of **(left)** different ITO layers (see details in Table 3.1) and **(right)** ITO layer after weak and strong annealing treatment.

Sputtering at high temperature was soon excluded due to bad quality of the obtained layer. With temperature fixed at room temperature, the pressure was varied between 3 mbar and 9 mbar, electric power from 75 W to 100 W and sputtering time between 1500 and 3600 seconds (Table 3.1). Different trends of transparencies are associated with different depositions (in Figure 3.19-left 5 layers with the same thickness are compared) and so different sheet resistance (R_{sh}) values, ranging between 0.6 and 1.9 kOhm/sq, indicating a very poor quality as electrode.

Due to the quite frequent exchange of targets in the sputtering tool (including ITO)¹⁰, the stability of the material was compromised and the ITO layers, deposited according to the same recipe, were impossible to reproduce.

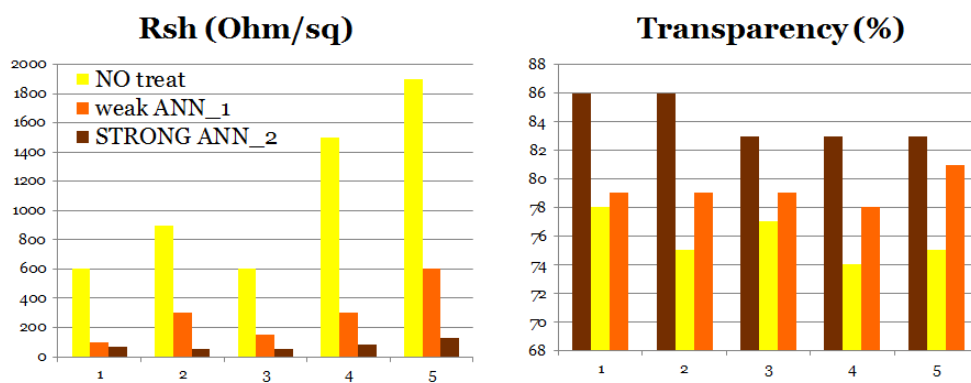


Figure 3.20: Effect of the weak and strong annealing on sheet resistance and transparency of different ITO layers.

In order to improve the quality of the layer and, at the same time, to find a method which could guarantee more reproducibility, a post-annealing treatment was introduced [101]. The investigation involved mostly¹¹ two kinds of annealing: one referred to as *weak*, consisting in 1h at 200°C, and the other one, *strong*, consisting of 1h at 350°C. All the layers submitted to the strong post-annealing were showing similar

¹⁰ There are only 6 crucibles in this sputtering machine and the target materials are changed weakly, depending on the users requests.

¹¹ Longer annealing at low and high temperature were also tested but did not improve the ITO quality.

properties, even if the starting layers were very different from each other: constant transparency along the whole spectrum (in Figure 3.19-right shown only till 1.1 μm for a representative sample; but, in Figure 4.40 and Figure 4.50, the effect of the ITO covering on the bare substrates reveals to even increase its transmission in the NIR range) of at least 80% and an average value of R_{sh} of about 30 Ω/sq (Figure 3.20).

Thus one recipe for the sputtering was selected (3 mbar, 100 W, 3000-3600 seconds¹²), on the basis of a certain number of depositions, as nominally the best and this was used for all the batches of diodes, relying on the effectiveness of the post-annealing treatment (strong) introduced as last step in the process flow (point 8)). The optimum thickness is 110 nm (see section 4.3).

The ITO sputtering was thus performed on the chip, after the patterning (Figure 3.22-left) with a double layer of resist (a Lift off Resist is added as bottom layer underneath AZ resist). The double layer can guarantee the undercut necessary for lift off photolithography (Figure 3.21). The steps are described as follows:

- Bake at 180°C for 3 minutes
- Spinning of LOR resist (750 nm)
- Bake at 180°C for 5 minutes
- Spinning of AZ5206E resist (750 nm)
- Bake at 90°C for 90 seconds
- UV exposure for 10 seconds at 5 mW (bright structures on bright field)
- Development in AZ351B:H₂O= 1:5 for 2.5 minutes
- Microscope inspection
- 1 minute of gentle plasma ashing

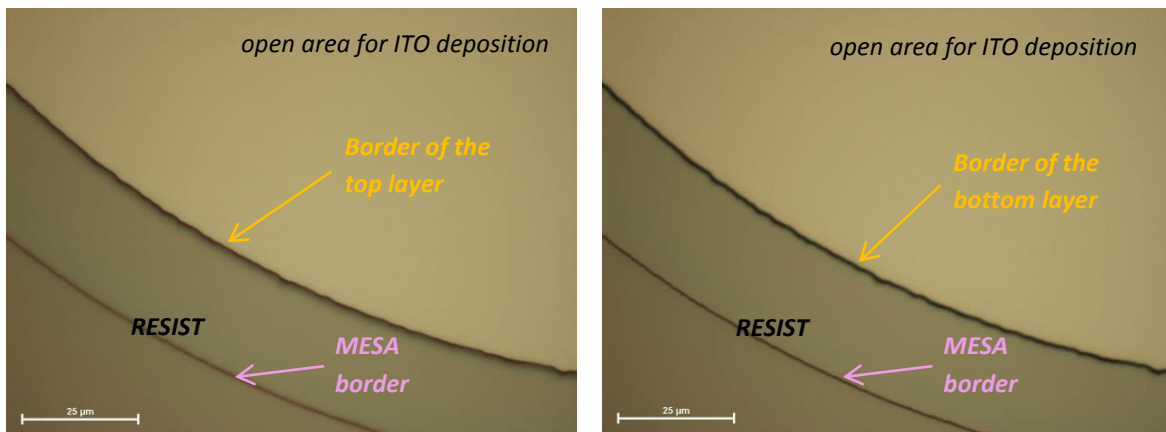


Figure 3.21: The two optical microscope pictures show the undercut which consists in a double border at the walls of the resist pattern. When the bottom layer is less visible (shadow in the left photo with focus on the top layer) but changing the focus of the microscope it can be visualized (right photo), where in fact also the border defining the mesa of the diodes (covered by the resist) are defined.

After the sputtering, lift-off is done. This is the most critical and difficult step of the whole fabrication process and the final optimization consists of: dipping in Remover 1165, at 70°C for 45-60 minutes in vertical position, while squirting and change of beaker (with clean 1165 at the same high temperature);

¹² The sputtering time was calibrated each time aiming to 110 nm of thickness.

another 40 minutes or more if necessary, squirting, 1 minute in ultrasonic bath at low power if needed and then acetone for 10 minutes, squirting, 2 minutes in IPA, water rinsing and blow drying. As an example, resulting final devices with good and bad lift off are shown in Figure 3.22-right; the latter ones are indicated by a narrow and can mean a risk of short-cut diodes.

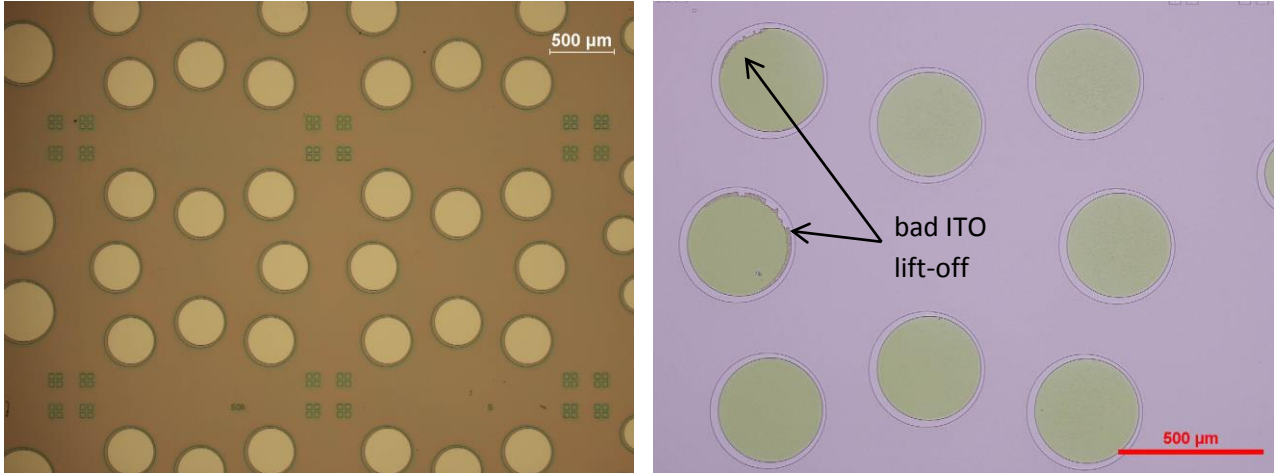


Figure 3.22: **left)** Microscope pictures of the resist pattern used for ITO sputtering in the photolithography by lift-off. **right)** Microscope pictures of the diodes after ITO lift off, showing good and bad examples.

After lift-off, the strong annealing follows.

The thickness of the ITO layer has been selected as a compromise between the two parameters: the thicker the ITO layer, the higher its conductivity but, on the other hand, increasing the thickness also leads to enhanced absorption losses. The thickness of the ITO layer ranges between 90 and 130 nm, opting for thicker layer (100-130 nm) with the solar cells incorporating electroless nanoparticles (see Figure 4.54).

7) Deposition of front-bottom ohmic contact

Whenever the back contact did not succeed in making a good alloy (judged only afterwards by the IV curves of the diodes), another ohmic contact is formed by deposition of n-alloy on the top of the (repeating steps of point 1)). The deposition of this contact is preceded by patterning with photolithography (same parameters described in point 6)), using as mask the layer #3 (Figure 3.15Figure 3.16); the result is a contact closer to the active layer.

All the batches of GaAs diode with Au NPs (by EBL) were fabricated following the described process flow. Processing of GaAs diode with random Ag NPs was modified: ohmic contact was formed as a last step of the process, the ITO annealing was substituted by the RTA annealing, simultaneously needed for the n-alloy. The last modification has been introduced only after having verified that the effect of the RTA on the ITO was still reasonably effective in terms of transparency and conductivity, without affecting the absorbance enhancement generated by the nanoparticles (Figure 4.54).

These devices, showed in microscope pictures from the top in Figure 3.23, were characterized both optically and electrically.

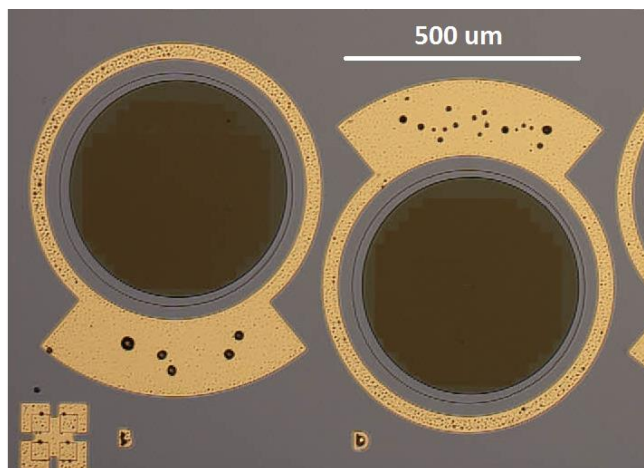


Figure 3.23: Microscope photo of two GaAs diodes with incorporated gold NPs (the EBL pattern is visible as a shadow under the ITO layer) and front bottom contacts.

3.2 A-Si:H solar cells

Hydrogenated amorphous silicon Schottky diodes were fabricated and characterized in collaboration with Ulrich Paetzold from FZ-Julich, in order to investigate the plasmonic effect within a thin film solar cell.

Since in a-Si:H the conservation of the momentum k in the electronic transitions is no longer granted [102], the material acts as a ‘quasi’-direct semiconductor with a much higher absorption probability of photons in the visible spectral region (photon energies above 1.8 eV), compared to c-Si. Therefore, for a-Si:H, film thicknesses of about 500 nm are sufficient to absorb light with wavelengths $\lambda \leq 600$ nm. Below 1.8 eV, the absorption in a-Si:H is determined by the density of tail states (shallow states) and dangling bonds (deep defects).

The fabrication of these devices (represented in Figure 3.24) follows a process optimized by the PV group in FZ-Julich, as briefly described below.

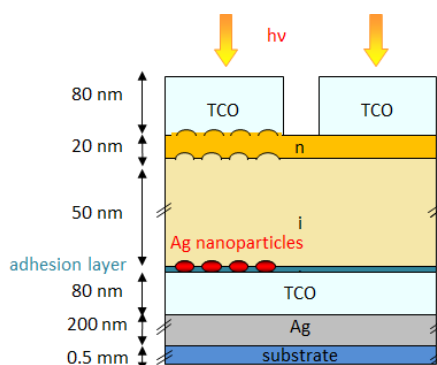


Figure 3.24: Cross section of the a-Si:H thin film solar cells studied in this thesis. The adhesion layer is Cr for EBL NPs; Si₃N₄ for electroless NPs.

1) *Back reflector deposition*

Processing starts from a back reflector, deposited on silicon substrate (to achieve high efficiencies) and consisting of:

- a thick silver mirror of 200 nm, deposited by e-beam evaporation
- a thin TCO layer, in this case aluminum zinc oxide (AZO) of 80 nm thickness, deposited by magnetron sputtering (see ITO sputtering of previous section), at room temperature, from the ZnO:Al target, characterized by Al concentration of 0.5 % to 1 %.

The thin TCO layer is commonly integrated between silicon and the Ag back contact to improve the reflection of the back reflector and thus the light absorption in solar cells [103], [104], [105].

2) *Nanoparticles deposition*

An adhesion layer is deposited at DTU depending on the type of nanoparticles. For EBL Ag nanoparticles a thin layer of chromium (3 nm) was deposited by e-beam evaporation, to promote adhesion of the PMMA e-beam resist; for electroless plating a silicon nitride layer was deposited by PECVD, in order to find good surface conditions for the optimization of an appropriate electroless plating recipe. We refer to Section 4.2.2 for details about this step.

3) *a-Si:H deposition*

Plasma enhanced chemical vapor deposition (PECVD) is one of the most commonly used methods of a-Si:H deposition. The moderate temperatures commonly used in PECVD process offer the possibility to use a large variety of substrate materials (also glass, stainless steel and plastic). Moreover, PECVD provides low energy consumption in industrial-scale process compared to e.g. crystalline technology, which requires temperatures larger than 1000 °C. The relatively lower electronic performance of a-Si:H solar cells is thus compensated by a cheaper production and high-volume production.

Deposition of a-Si:H films is done by decomposition of silane gas (SiH_4) and an excitation frequency of 13.56 MHz (RF-PECVD).

The properties of the resulting films and especially whether its structure is microcrystalline or amorphous depend on the deposition parameters such as silane to hydrogen ratio in the gas phase, plasma excitation frequency, substrate temperature, discharge power density and total gas pressure. To obtain n-type doped silicon material, phosphorus-containing source gases are introduced into the reactor.

The electron-hole pairs generated in the doped layers do (almost) not contribute to the photocurrent, as they are lost by recombination processes. Hence, the n-layer should be as thin as possible and realized using a wide band gap in order to reduce absorption losses. On the other hand, it should be thick enough to build up an efficient electric field across the intrinsic layer. A thickness of about 50 nm is suitable for our n-

layer. The i-layer has two main functions, namely to provide maximum absorption of the incident light and also enable a good electrical transport of the photo-generated charged carriers. Since defects in the i-layer lead to recombination of the charged carriers, it should exhibit a low defect density in order to reach an effective carrier collection. With increasing the thickness of the absorber layer, the absorption increases but at the same time the collection efficiency decreases due to reduced electric field and enhanced defect density. Typical thickness values are between 150 nm and 350 nm. In this work, cells containing metal nanoparticles/nanostructures with standard absorber thickness as well as very thin solar cells with i-layer thickness reduced to up to 20 nm are prepared, since the investigated electromagnetic field enhancement originating from plasmon effect is located in the surrounding of the nanoparticles.

4) Top electrode (AZO) deposition

Sputtering of a layer of AZO completes the device fabrication (see point 1)).

Optical and electrical characterization was conducted only on the diodes with ordered Ag NPs made by EBL.

4. Nanoparticles incorporation and optical characterization

4.1 Metal choice

Since metals tend to have large plasma frequencies and high electrical conductivity, they have traditionally been the materials of choice for plasmonics.

As previously mentioned, the choice of metal has a strong influence on the optical properties of the nanoparticles. For instance, the results presented in [47] demonstrate that gold and aluminum nanoparticles with identical geometries can behave in very different ways. Nanoparticles made from either metal are capable of supporting LSPs in the visible and NIR (which is of interest in this thesis), with the range extended into the UV for Al nanoparticles. In this study, the comparison enlarges further, including also Ag and Cu. The extinction peaks differ in LSP resonance frequency but also intensity and width.

Among the noble metals, we have reduced our options to gold and silver, which are the most common plasmonic metals (because of their low losses due to Ohmic heating).

Figure 4.1 shows values of C_{abs} and C_{sca} , normalized to the particle cross-sectional area πr^2 , computed as a function of particle radius r for Au and Ag nanoparticles using Equations (2.4a-b) [18] combined with values for the dielectric function, ϵ , obtained from the published literature [106]. All values are computed at the Fröhlich frequency (Equation (2.2)), in vacuum.

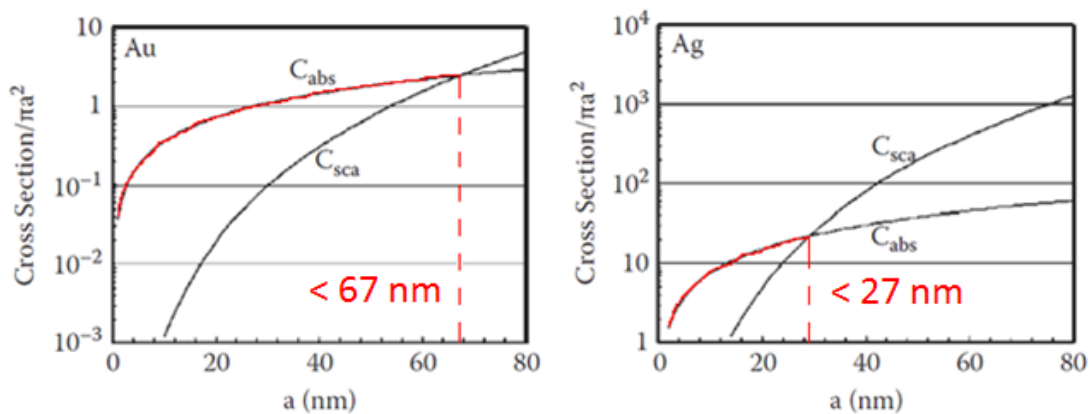


Figure 4.1: Calculated absorption and scattering cross sections for gold (left) and silver (right) nanoparticles in vacuum. [18]

As explained in Section 2.1, we are interested in the regime of dominant absorption, by means smaller nanoparticles sizes. From the figure one can see that, for Au NPs, C_{abs} is larger than C_{sca} for NPs much bigger (up to 67 nm) than in the case of Ag NPs (up to 27 nm). Thus, considering the technological difficulties in fabricating small nanoparticles in a controlled way, gold was chosen for the first experiments. Following optimization of the processing, Ag nanoparticles were also explored since C_{abs} for Ag, in the dominant

range, is 10 times bigger than C_{abs} for Au, in the dominant range. Furthermore, the interband transitions of Au has a strong negative effect on the extinction efficiency [47] and it is well known that Ag is a much better plasmonic metal than gold, having a bigger quality factor [83].

4.2 Fabrication techniques

4.2.1 Electron-beam lithography

E-beam lithography (EBL) is a lithography technique which is used when high resolution patterning with a lot of freedom in the design is needed. As mentioned in Section 2.7, this technology is not meant to be used for photovoltaics as it would highly increase the costs; nevertheless, it is in this research because it allows us to fabricate ordered arrays of nanoparticles, with varying pitches and sizes. The goal is to understand the general plasmonic behavior of gold and silver nanoparticles depending on their geometry and interactions: FDTD simulations can be easily compared with optical measurements on such precisely fabricated structures, simple for modeling. Once we understand the NPs properties, cheaper technologies, which can reproduce optimum geometry of the nanoparticles, can be developed with no need for any further simulations which would be more complex.

In this work the fabrication of the nanoparticles uses lift-off technique, which is preferred to etching metal to form patterns. The processing involves the following steps:

- 1) Preparation of the mask corresponding to the desired pattern and choice of exposure parameters: the mask is drawn with a CAD-software (in our case L-Edit) with dark objects on bright field (Figure 4.3), since we use a positive resist. Together with the mask another series of files needs to be prepared in order to give the machine the exposure parameters as input: the coordinates of the pattern and eventual alignment; the current (nA) and the aperture of the beam; the dose ($\mu\text{C}/\text{cm}^2$); the beam step between subsequent shots (nm); instructions about the movement of the beam on the whole pattern. These files will then give a script which can be compiled by the instrument.

The set of parameters, just described, needs to be chosen considering different aspects.

The dose D ($\mu\text{C}/\text{cm}^2$) can be considered as the quantity of charge reaching the sample on a defined area (A) for a certain time (T) and it is linked to the beam current (I) through the following relationship: $D \cdot A = T \cdot I$. For very small structures, and high resolution, one prefers to use small currents (in order to reduce the beam size) and, considering that you cannot expose a sample for days, this means limiting the highest possible dose value quite a lot. Furthermore, there is another limit to consider, given by the machine itself: the e-beam writer speed. This, in particular, affects the choice of the beam step (s , nm) in relation to all the other parameters. The electron beam writes the pattern at points on square grid with separation between the points of s , to cover the whole desired area (Figure 4.2).

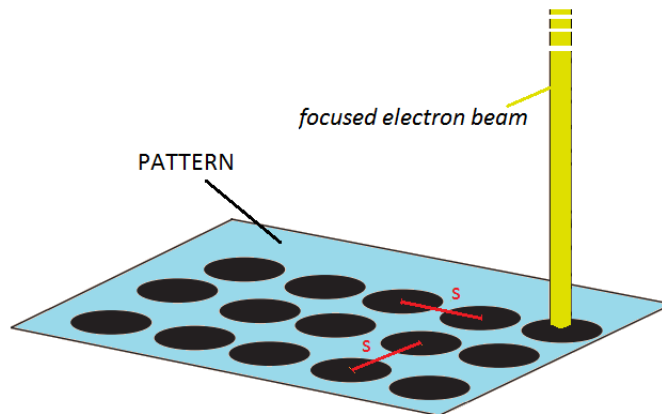


Figure 4.2: Sketch of e-beam exposure. The electron beam hits repetitively the area which is requested to be exposed (light blue): it shoots on one spot staying for the required time (by the dose) and then it moves to the next spot moving by s (beam step).

- 2) Substrate wafer cleaning: soaking in acetone for 3-5 minutes, IPA for 2 minutes and water rinsing.
- 3) E-beam sensitive resist deposition on the substrate: pre-bake of the substrate, spinning and post-bake. Pre-bake is necessary for the substrate dehydration to allow a good adhesion of the resist; the spinning rate is calibrated to get a certain thickness with uniformity; post-bake is needed to remove solvent from the resist layer and increase the subsequent writing resolution.
- 4) Electron beam exposure: Pattern is drawn in the resist by sending a focused beam of electrons, which break the polymer chains and change the solubility of the resist. The beam writes following the desired pattern, as described in point 1.
- 5) Development of the pattern: the electron beam exposure of the resist enables a selective removal of the exposed positive resist by immersing the sample, for a calibrated time, in a solvent (*developer*) specific for the chosen type of resist and followed by appropriate rinsing.
- 6) Metal (Au or Ag) deposition using e-beam evaporator.
- 7) Lift off: soaking in an appropriate solvent (*stripper*) which can remove the resist away together with the un-wanted metal, defining the final pattern.

4.2.1.1 ZEP resist

Fabrication of arrays of rods and circles, small enough to absorb light more strongly than scattering it (Figure 4.3), requires careful consideration. For examples, a pitch of the array must be at least 75 -100nm in order to avoid too strong proximity effect. Electron beam current must be kept small to keep the beam size small as well.

Finally the choice of e-beam resist is very important. The first e-beam resist that was used in this work was ZEP520(@5.5%), as it was commonly used in the clean room facilities of DTU. Although this resist is

preferably used for etching mask, its high contrast quality makes it appropriate also for lift off processes. Furthermore, its saturation regime is quite wide, this means that it offers a wide range of doses where small fluctuations (of 5-10 $\mu\text{C}/\text{cm}^2$) will not affect much the pattern and it makes ZEP a safe resist.



Figure 4.3: Draw of the structures that are initially aimed through EBL.

ZEP520 gets developed in ZEDN50 for 2 minutes and its stripper is Remover-1165, usually giving an efficient lift off with an overnight soak. Prior to exposure of real samples, a dose test is necessary, in order to find the right dose of exposure which, combined with a certain current (to control beam size), can give the desired dimensions.

With this in mind, we prepared a set of samples by spinning 130 nm ZEP resist on top of GaAs substrates to test a wide range of doses (using 0.7-0.8 nA electron beam current and 4 nm as beam step). Table 4.1 summarizes the first 5 test runs with arrays of nanorods and circles, with varying size and periodicity.

Sample	Mask	I (nA)	Dose range ($\mu\text{C}/\text{cm}^2$)	Metal (nm)
Test 1	Rectangle: 50nm X 15nm (pitch x-y: 100nm,30nm)	0.8	[150,280]	Au(10)
Test 2	Rectangle: 50nm X 1/4/8/12nm (pitch x-y: 100nm, 30/40/50/75/100nm)	0.8	[230,310]	Au(10)
Test 3	Rectangle: 50nm X 1/4/8/12nm (pitch x-y: 100nm, 30/50/75/100nm) Rectangle: 100nm X 30nm (pitch x-y: 200nm, 60/100nm)	0.8	[140,350]	Au(10)
Test 4	Rectangle: 50nm X 1/4/8/12nm (pitch x-y: 100nm, 30/50/75/100nm) Rectangle: 100nm X 30nm (pitch x-y: 200nm, 100nm) Rectangle: 70nm X 25 nm (pitch x-y: 140nm, 75nm) Rectangle: 60nm X 20nm (pitch x-y: 120nm, 60nm)	0.8	[200,540]	Ti(5) Au(10)
Test 5	Rectangle: 50nm X 8nm (pitch x-y: 75nm, 100nm) Rectangle: 50nm X 12nm (pitch x-y: 75nm, 100nm) Rectangle: 60nm X 20nm (pitch x-y: 100nm, 100nm) Rectangle: 30nm X 16nm (pitch x-y: 100nm, 80nm) Circle: radius 15/20nm (pitch x-y: 100nm, 100nm)	0.7	[200,660]	Al(20)

Table 4.1: Summary of the first 5 EBL tests on GaAs substrate, run with arrays of nanorods and circles, designed varying size and periodicity (indicated in the column “mask”). For each design/test, the current I , the dose range and the metal, deposited after development (in ZEDN50 for 2 minutes), are shown. All these exposures were done on ZEP520 (@5.5%) resist, with beam step s of 4nm.

Test 1, 2 and 3 were used to verify the correct development time. In Test 1, the sample was developed with a standard time of 2 minutes and lift off in remover-1165 overnight, while the development time for test 2 was reduced to 1 minute. These tests were needed as the pattern of closely spaced holes is very demanding due to reduced exposure contrast while there was no previous experience with such situation

in the clean room. In order to verify the exposure both samples were coated with Au and the patterns were inspected after lift-off using SEM. Comparing the results of the two exposures it became clear that 1 minute development time is too short, there was no metal left on the sample after lift-off. The results on sample 1 were not satisfactory either: most of the patterns were missing and the only structures (corresponding to doses ranging from 190 to 270 $\mu\text{C}/\text{cm}^2$) present, were some nanorods, 45nm in width, but merging in one direction (Figure 4.4).

Test 3 was repetition of test 1 with added new bigger structures to test the minimum periodicity needed to avoid merging of the patterns. Those were the only ones found after lift-off (Figure 4.4).

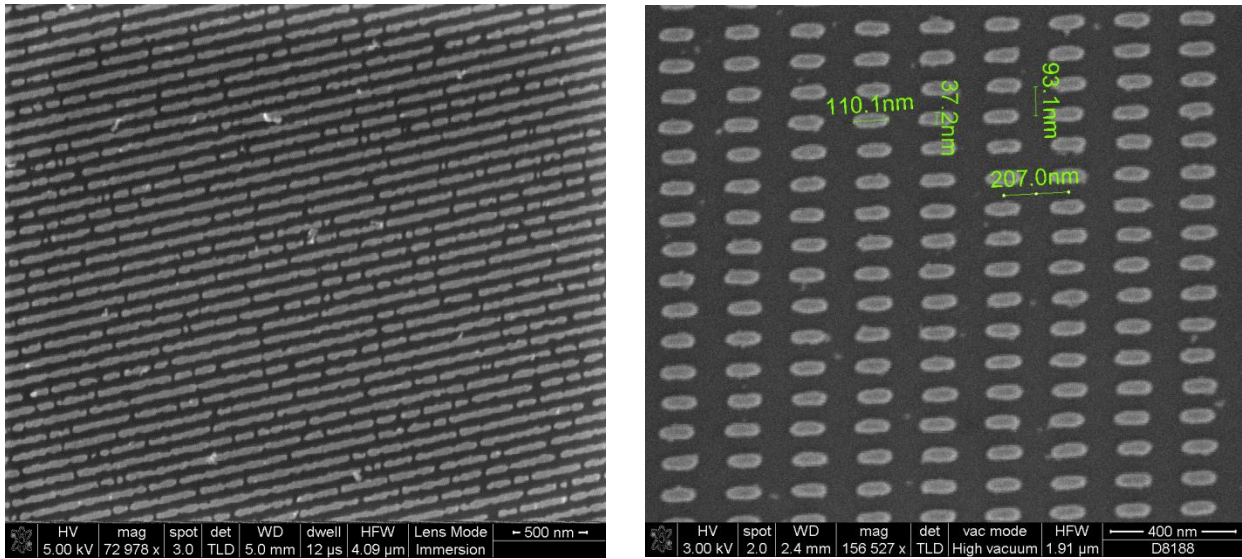


Figure 4.4: SEM image of some of the merged structures found in test 1 (left) and big nanorods obtained in test 3 (right).

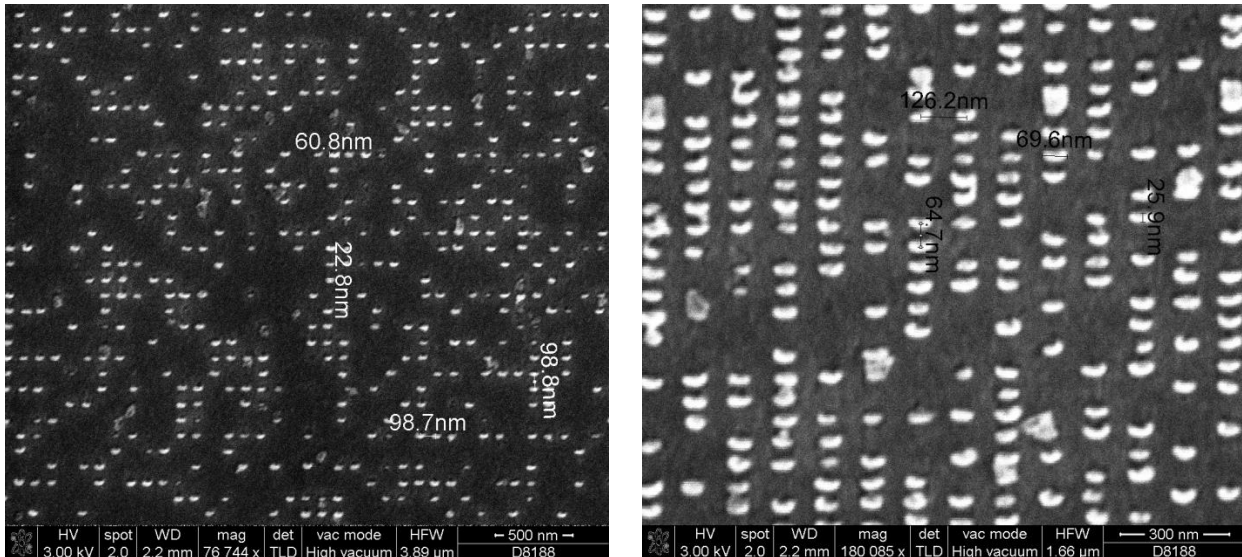


Figure 4.5: SEM images of the smallest structures obtained in test 4 (Ti/Au nanorods) but showing poor adhesion and not always regular shape.

While it is desirable for plasmonic effects to work with pure Au as metal, it is well known that adhesion of Au to the surface of semiconductors is poor. To test the possibility that the problems experienced in tests

1-3 were caused by metal adhesion, in test 4 metal deposition was changed to 5 nm of Titanium (as an adhesion layer) followed by 10 nm Au layer: small structures (60 nm X 25 nm) were finally obtained, but still the adhesion was sometimes very poor giving areas of $(100\mu\text{m})^2$ covered randomly by nanorods, which were also characterized by not very regular shape (Figure 4.5).

The following test (test 5) was designed to investigate the problems of test 4: higher doses were added, metal deposition was changed to Al and the circular patterns were introduced. Aluminium may not be a metal of choice for the project, but there was a suspicion that deposition of Au is performed in an evaporator which damages the resist. Quite nice patterns were obtained in test 5 (Figure 4.6).

Nevertheless, the reproducibility on larger areas, even using Al, was almost impossible and the main problem was again the lift off (Figure 4.7): the reason was the resist which did not allow us to work in such critical range of size defining a good undercut during the development.

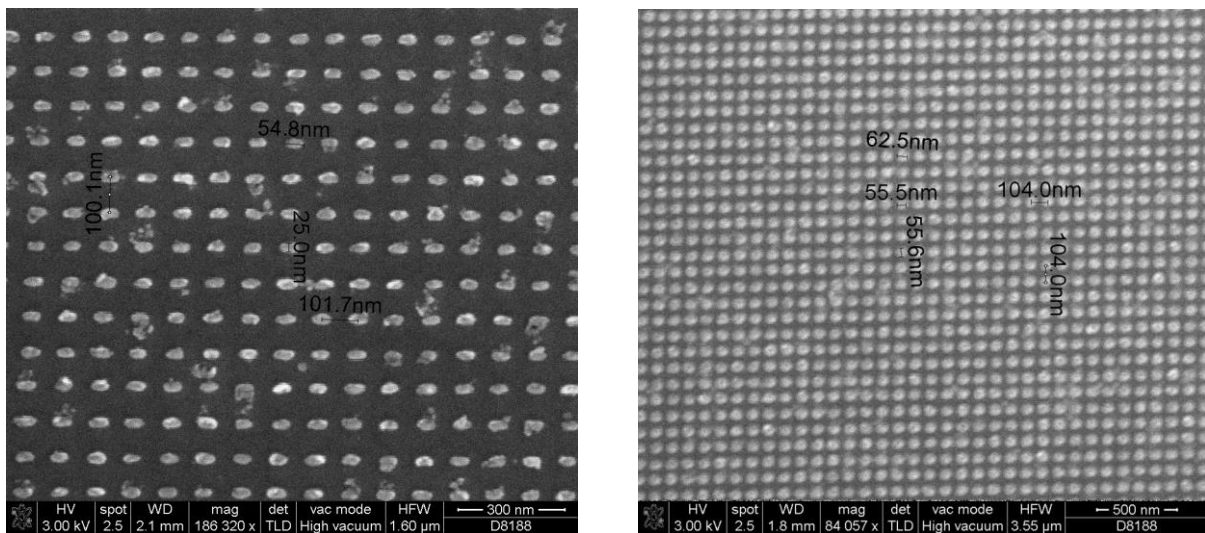


Figure 4.6: SEM images of Al small nanorods (55nm X 25nm) and circles (radius of 30nm) obtained in test 5.

L-Edit mask	Dose ($\mu\text{C}/\text{cm}^2$)	Actual structure
rect 50nm X 8nm ($p_x=100\text{nm}, p_y=75\text{nm}$)	500	nanorod 50nm X 30nm
rect 50nm X 8nm ($p_x=100\text{nm}, p_y=100\text{nm}$)	660	nanorod 50nm X 30nm
rect 50nm X 12nm ($p_x=100\text{nm}, p_y=75\text{nm}$)	460	nanorod 50nm X 30nm
rect 60nm X 20nm ($p_x=120\text{nm}, p_y=80\text{nm}$)	280	nanorod 80nm X 30nm
rect 60nm X 20nm ($p_x=120\text{nm}, p_y=80\text{nm}$)	360	nanorod 80nm X 40nm
"circle" R=15nm ($p=100\text{nm}$)	400	circle R=30nm

Table 4.2: Summary of the results from tests with ZEP resist.

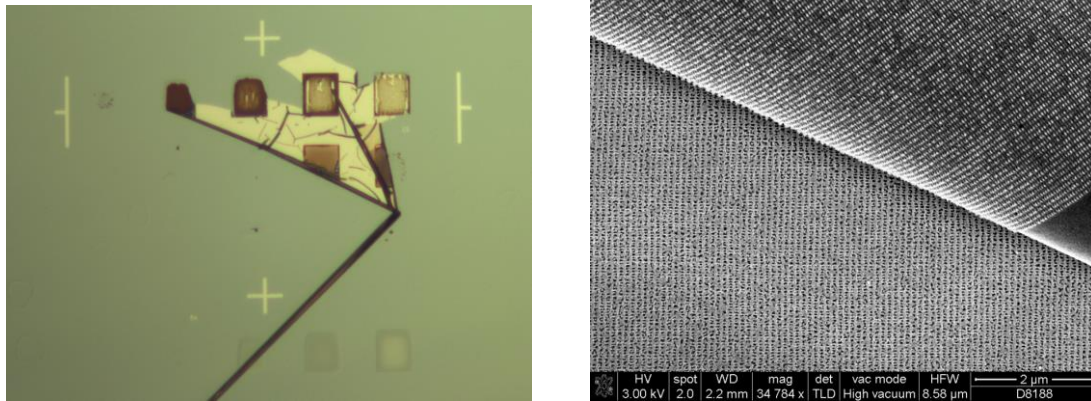


Figure 4.7: Optical microscope (**left**) and SEM image (**right**) of patterns with failed lift off. The metallic foil which is supposed to be ripped away together with the resist got stuck to the substrate.

A good lift off resist should give a profile that will avoid the deposition of a layer which coats the sample with a continuous film, preventing the remover from penetrating into the resist. The undercut is necessary to create a shadow (green in Figure 4.8) preventing the connection between the metallic parts in the exposed areas and the film deposited on top of the resist. In order to ensure the presence of an undercut, a double layer of resist is the best option for lift-off lithography. At this point it was decided to replace ZEP520 with a double PMMA e-beam resist (Figure 4.8).



Figure 4.8: Illustration of a good lift-off monolayer resist profile (**left**) because of the presence of an undercut; bad resist without undercut, thus preventing lift-off (**centre**); double PMMA resist (**right**), developing at different rate because of different molecular weight (the bottom one has a lower molecular weight).

4.2.1.2 Double PMMA resist

Based on prior work on PMMA for lift off, it was decided to use the following stack:

1. The bottom layer: A6 PMMA 100k diluted in anisole (1:1) and
2. The top layer: A4 PMMA 495k diluted in MIBK (1:1).

The total thickness of the double layer is about 80 nm. Note, that size of the pattern is defined by the top layer, due to its higher molecular weight. Lower molecular weight of the bottom layer makes the layer more sensitive to electron beam and upon development, larger diameter areas are removed.

We started over with a new dose test, using these parameters:

- ✚ Pre-bake at 120C for 5 min; mid-bake (between the 2 layers spinning) at 150C for 10min and post-bake at 160C for 15min
- ✚ beam current: 0.7 nA
- ✚ beam step: 4 nm
- ✚ wide range of doses: from 200 $\mu\text{C}/\text{cm}^2$ to 1500 $\mu\text{C}/\text{cm}^2$
- ✚ development: 10 sec in MIBK:IPA=1:3 (standard developer for PMMA)
- ✚ deposited metal: 5 nm of Ti, 10 nm of Au
- ✚ lift off: overnight soaking in acetone (good stripper for PMMA)

While there was a strong improvement in the pattern formation compared with ZEP, as can be seen from nicely defined arrays of nanorods in Figure 4.9, reproducibility and regularity in shape were still an issue.

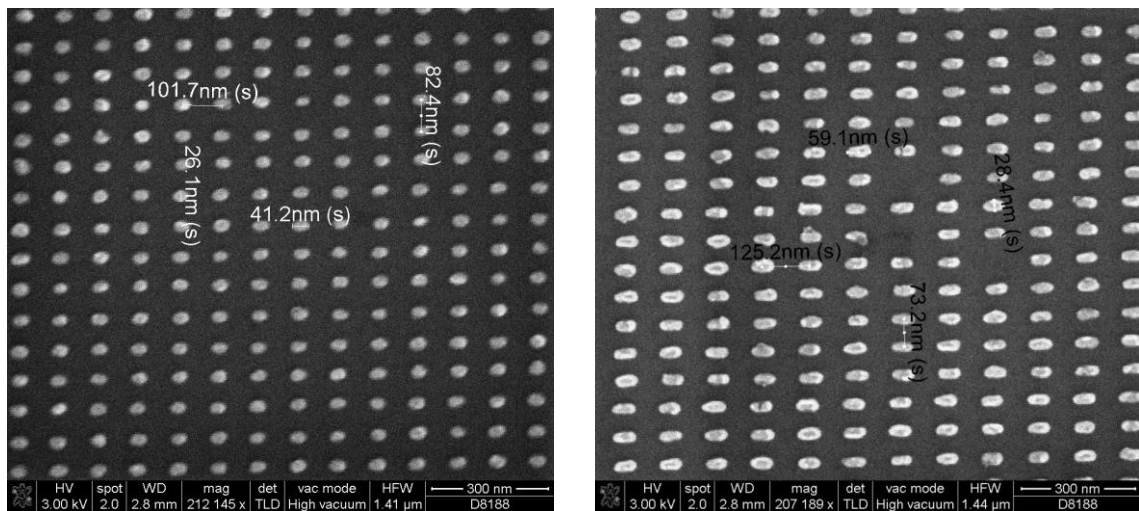


Figure 4.9: SEM images of first nanostructures (Ti/Au) obtained with double PMMA resist (80 nm). The parameters used for the exposure are: beam current 0.7 nA, beam step 4nm and: **left**) dose 1500 $\mu\text{C}/\text{cm}^2$ (from designed 30nmX16nm); **right**) 1250 $\mu\text{C}/\text{cm}^2$ (from designed 80nmX45nm).

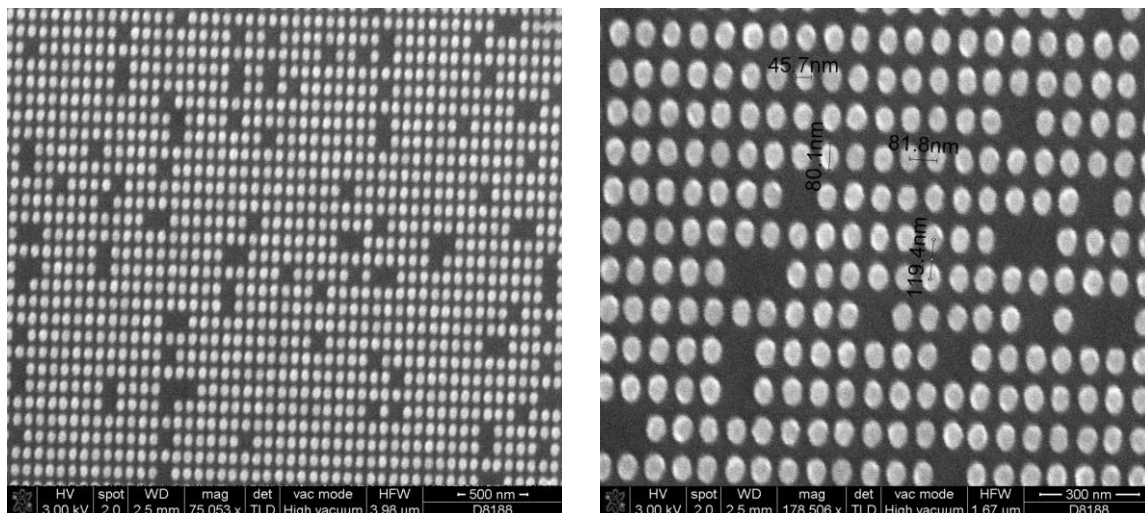


Figure 4.10: SEM images of nice Ti/Au nanorods obtained with double PMMA. The right picture is a zoom of the left one.

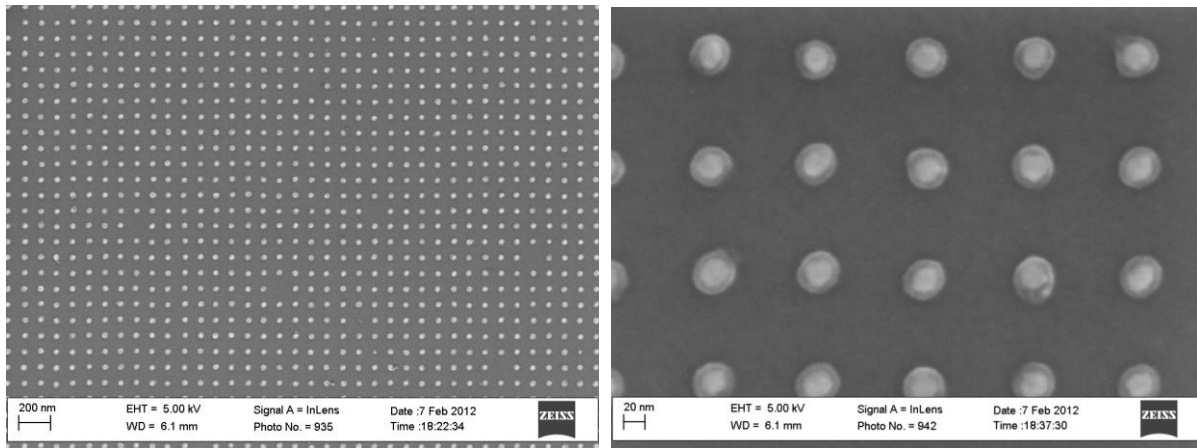


Figure 4.11: SEM image of Ti/Au circular nanoparticles obtained with double PMMA after a long optimization of the EBL process. The right picture is a zoom of the left one.

Several tests, performed over six months were needed to optimize the lift off EBL fabrication of gold nanoparticle arrays on large fields. Solving the problems, one by one, leads finally to nice and reproducible patterns on large areas (Figure 4.10 and Figure 4.11).

The optimisation of the process involved the following:

- 1) *Designed pattern has to incorporate the real exposure information.*

The first feature to be considered is the way the software, commanding the e-beam writing, works. When you ask to cover a designed structure from the mask, this software will decide the “most efficient” way to write depending on the exposed area, shape structure and beam step, combined with the pitch of the array. So for instance, the problem occurs easily in the circular shape defined as polygon, which can be filled in different ways (Figure 4.12).

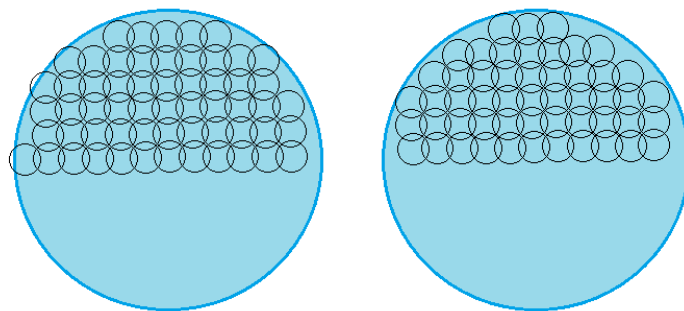


Figure 4.12: Illustration of two possible ways for the electron beam to write the same structure.

Since we are working with very low current, the way each structure is written becomes crucial because it can affect the total amount of electrons hitting the single structure varying the open area size after the development and thus, the particle size.

Having said that, it was decided to draw squares instead of “infinite” polygons (in order to get circles) and to choose rectangular size and array pitch as integer multiple of the beam step.

2) Optimization of the development procedure.

After dipping the sample in the developer (MIBK:IPA=1:3) for 1 minute¹³, the rinse needs to be done in IPA and not water.

3) High temperature baking of the resist to avoid its softening during metal deposition.

In order to improve reproducibility and uniformity of the structures after lift-off (Figure 4.13), many things were tried: for instance, the introduction of a de-scumming¹⁴ step after development and before metal deposition using very short and gentle plasma ashing; or gentle ultrasounds and manual squirting during/ after dipping in the remover.

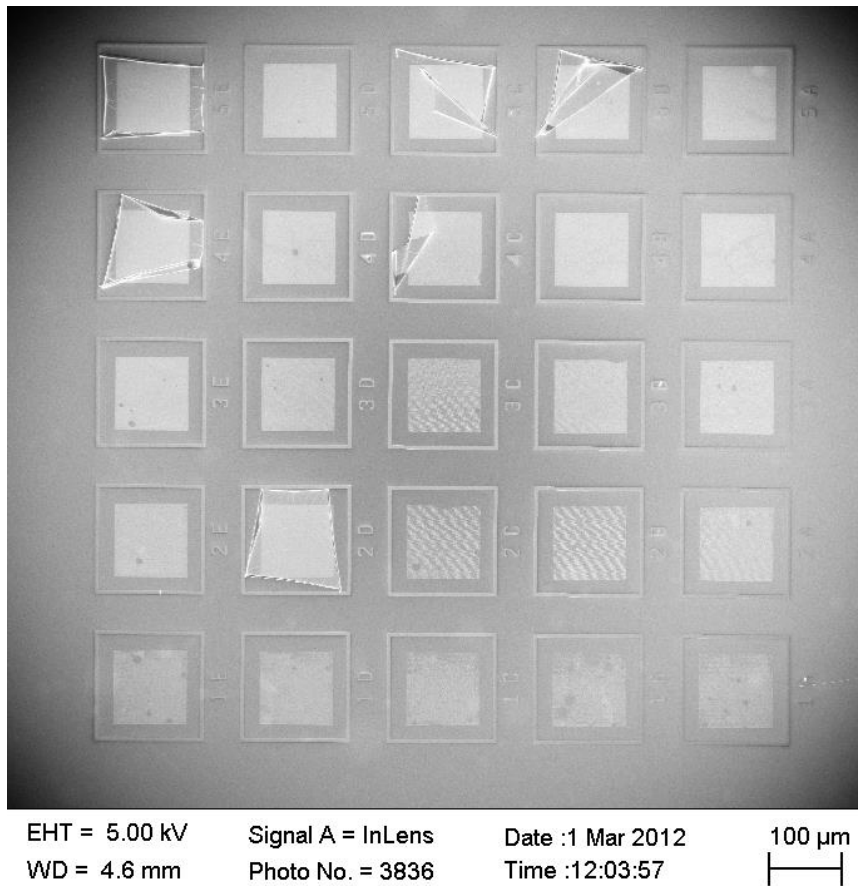


Figure 4.13: SEM image of one of the dose tests for Ti/Au structures; each square has been exposed with a different dose (increasing in number and letter) but 6 of them did not get the metal foil completely lifted off. A picture of the foil on the pattern, with higher magnification can be seen in Figure 4.14.

In order to better understand the situation it was decided to zoom on the un-lifted foils of metal getting stuck on the pattern (Figure 4.14): the profile of the foil is complementary to the resist profile and it indicates a situation similar to the one shown in Figure 4.8 when there is no undercut. In fact some particles

¹³ The initial development time was too short (10 seconds), thus the resulted pattern was not uniform; after being increased to 1 minute, a new dose test was carried out.

¹⁴ De-scumming is a gentle etching used to completely remove the resist from the open (exposed) areas and clean the pattern before the deposition. It can be done via plasma ashing or reactive ion etching (RIE).

kept stuck to the continuous Ti/Au film, because during the evaporation the metal has been deposited also onto the resist walls.

The lift off process and the reproducibility of the pattern were then significantly improved changing the bake parameters. After a review of the literature it was decided to increase the temperature for both mid- and post- bakes at 190C and we then decided to investigate at SEM the profile of the resist to verify the presence of the undercut.

The real problem was the bake, not long enough to make the resist structure solid, or at least not everywhere on the substrate, with a uniform distribution. The cross section of the double PMMA structure (after exposure and development with the correct dose and time of a solid resist pattern) is shown in Figure 4.15 and Figure 4.16: the double layer and the undercut are visible and highlighted in the SEM images.

The visualization at SEM of the cross section of such polymeric structure is very tricky because the e-beam sensitive resist gets charged very quickly and thus its shape and conformation modifies during the SEM investigation.

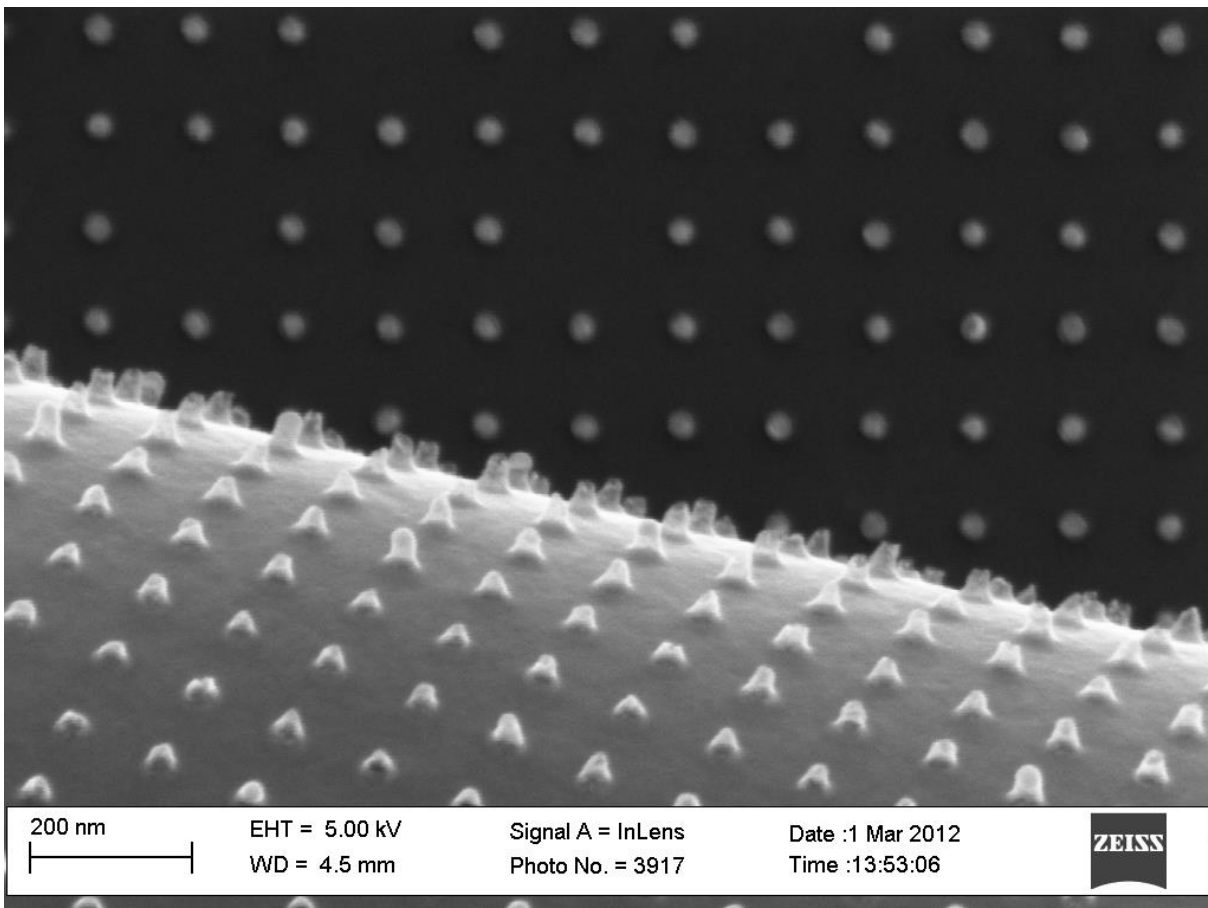


Figure 4.14: SEM image of the un-lifted foils of metal getting stuck on the pattern.

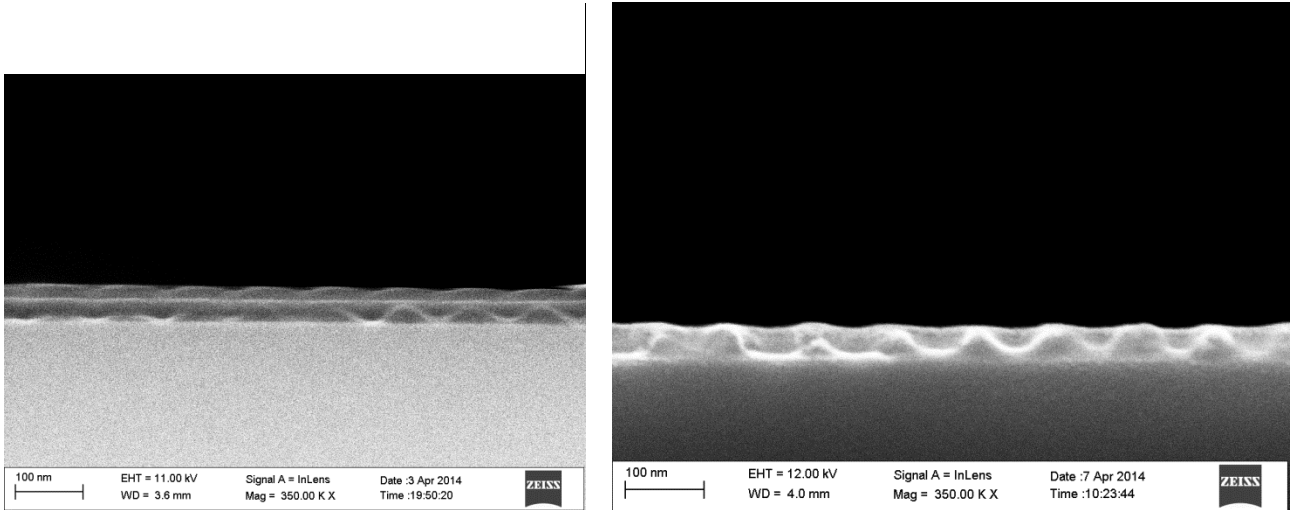


Figure 4.15: SEM images of the double PMMA resist profile. A cross section of the pattern (after correct resist bake, exposure and development of squares) is shown.

It has been tried low vacuum environment but then the resolution of the corresponding detector decreases a lot and for such small size it is impossible to distinguish the two layers.

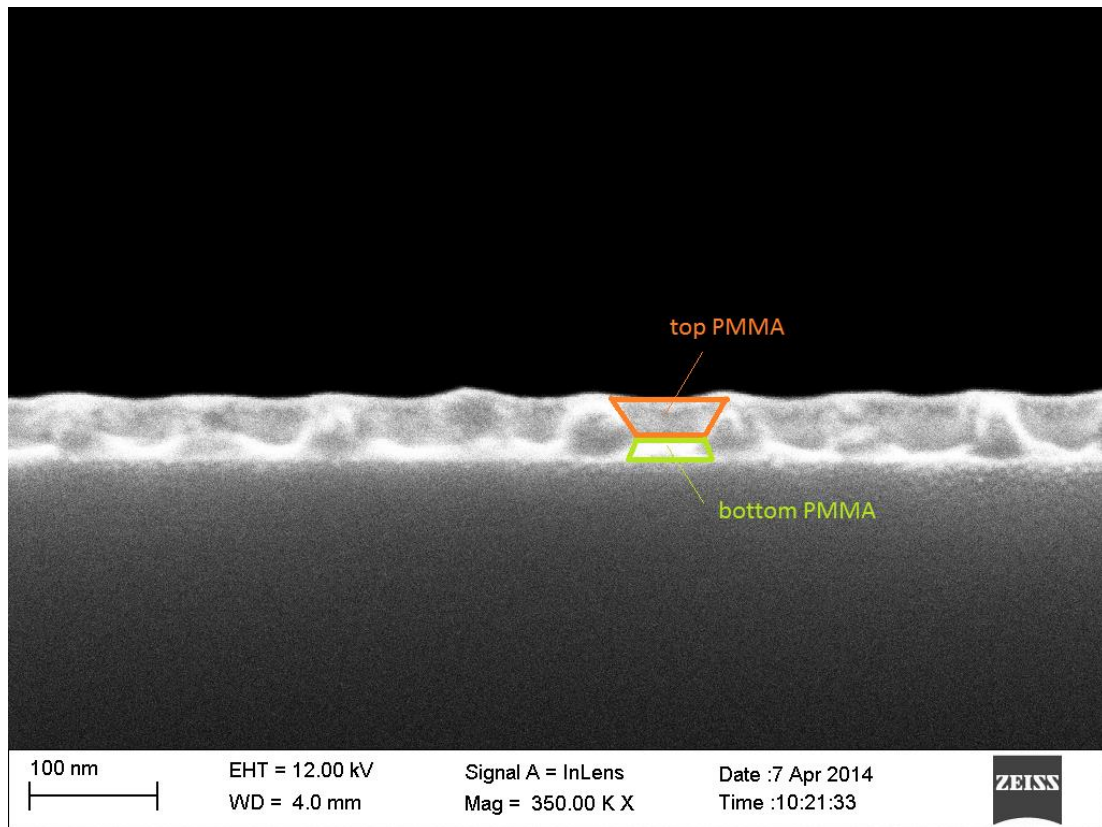


Figure 4.16: Another SEM image of the double PMMA resist profile with the two layers highlighted to show the presence of the undercut.

Finally, reasonable pictures, shown in Figure 4.15 and Figure 4.16, were taken in high vacuum, with 4 mm working distance, high voltage (12 kV) and fixing focus and astigmatism of the beam on spot 1 but moving straight after on spot 2 (at 1-2 μm of distance from spot 1) to take the photo.

4) *Eliminate electron beam blanking to reduce the total lithography time.*

The e-beam writer can work in two different ways for the kind of pattern we need: in the standard way described so far (see Figure 4.2 and Figure 4.12), which we will call *multi-shot exposure*, and in the so called *single-shot exposure*. The latter one is much faster, in fact it can reduce the exposure time of about 50%-80% (depending on the e-beam writer speed and the time optimization made by its software); moreover, it requires simpler mask design and it avoids the problem 1, guaranteeing that each particle is written in exactly the same way around the whole pattern.

The single-shot exposure works using a bigger beam current (usually from 5 nA up to 20 nA) that will directly define the particles size. In this mode the step size of the electron beam is set to be equal to the desired separation between the particles. Each exposure point defines one particle. The mask design will then be just a big square corresponding to the whole area to be exposed. A schematic illustration of the single-shot exposure, compared to the old one is shown in Figure 4.17.

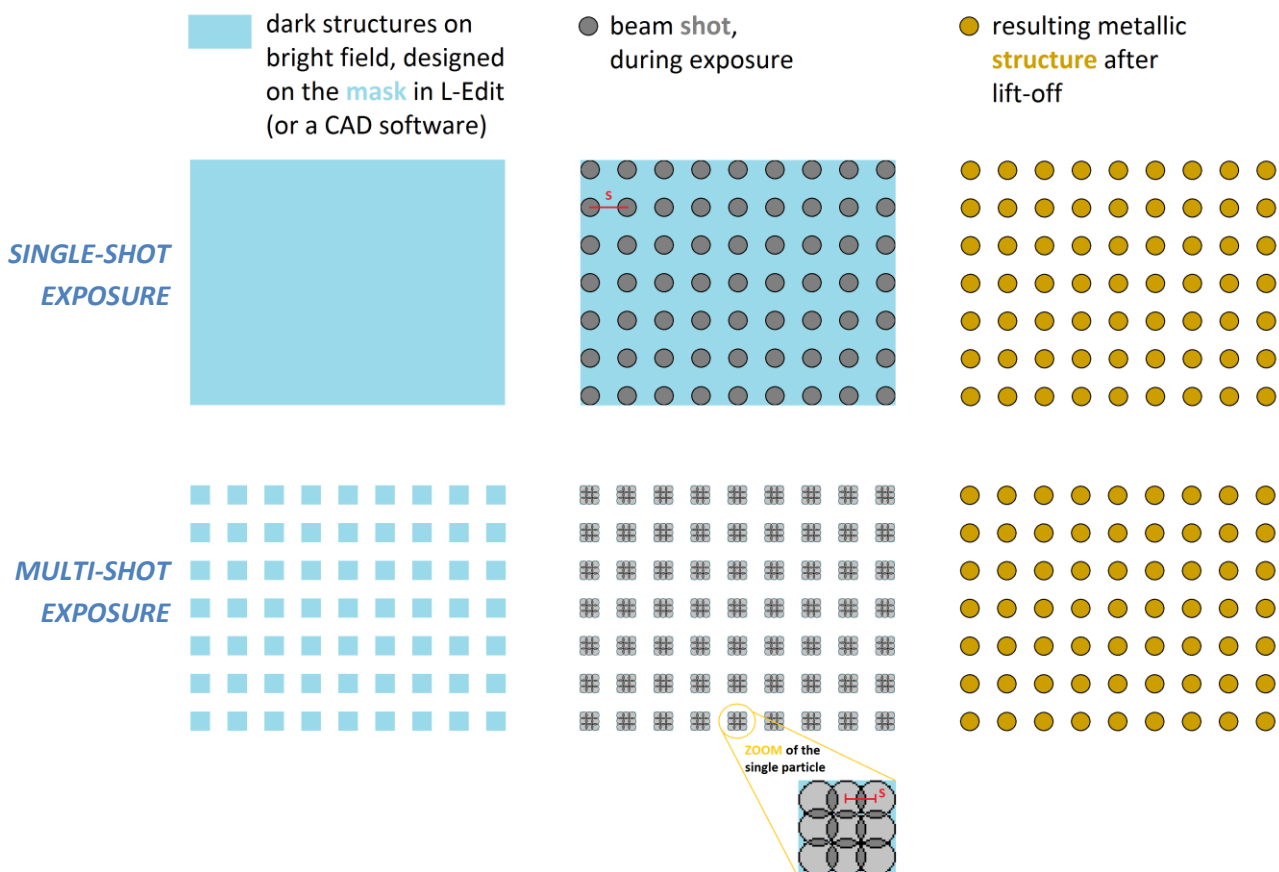


Figure 4.17: Schematic illustration of the two different ways to expose with an e-beam writer: single-shot (top line) needs higher current but much lower dose; here the beam step s (red) is equal to the desired array pitch. Multi-shot (bottom line) uses smaller current with very high doses and very shot beam step, that is why the exposure takes much longer.

The multi-shot exposure makes use of very small currents (down to 0.5 2nA) to exploit the smallest beam size for high resolution; but at the same time, very high doses are needed (up to 100 times higher than the doses used in a single-shot exposure) and this makes the exposure longer. The single-shot exposure is shorter mainly because the beam is not blanked between particles and beam blanking is a huge waste of time.

Nevertheless, with the used e-beam writers, there are two important limits for the apparently very advantageous single-shot exposure:

- ✚ only circles can be obtained
- ✚ the design must follow either square lattice or hexagonal one; for different periodicity in the two axes particular scripts would need to be coded for the e-beam software.

Several tests were performed to compare the quality of the obtained pattern with the two exposure modes and no differences were found, unless in terms of precision in the reproducibility: for the single-shot exposure the particle size is strictly dependent on the beam size (the current); working in such critical range of structures size means that a variation in the beam current of the 10% can be equivalent to a variation in the particle size of about 20%. In the multi-shot exposure the variation of the beam size would have a much less significant effect. But this drawback can be easily overcome running a more precise calibration script right before the exposure and changing the necessary parameters to fix the current value.

5) Occasional “smearing”.

Even after the optimization of the whole process, sometimes strange features were still visible in certain patterns, regardless the exposure mode, size or pitch: from Figure 4.18, it is visible this odd smearing of the metal outside the defined borders of the NPs (a sort of “aureole”, whose presence can be notice in Figure 4.11 as well).

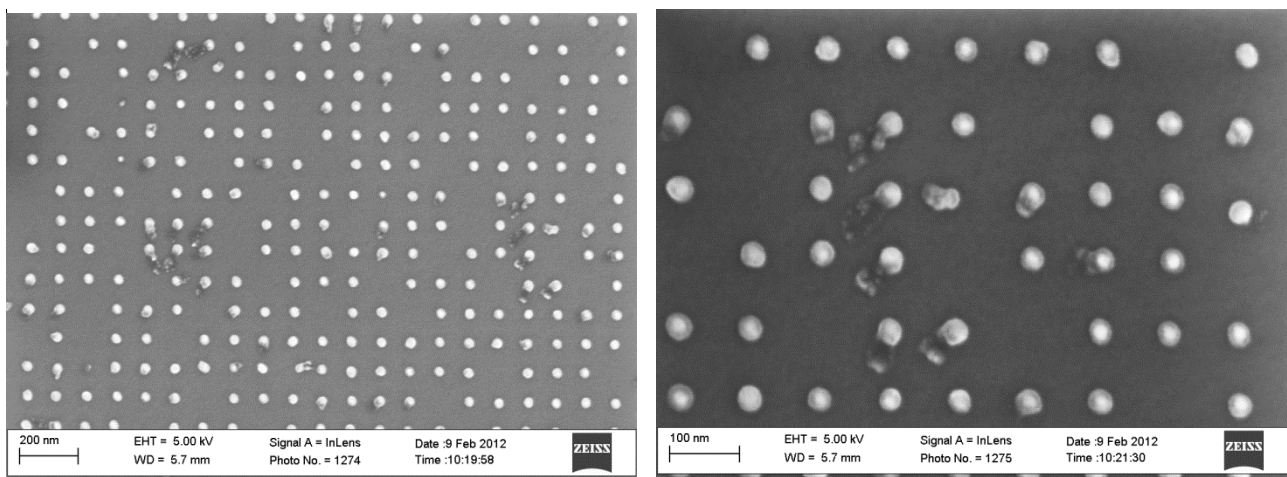


Figure 4.18: SEM images of Ti/Au nanoparticles showing a “double-circle” shape and the eventual splashing of the external “aureole”. The right image is a zoom of the left one.

As mentioned in Section 3.1.1 (Figure 3.7 and Figure 3.9), the shape of these particles can be thought to be like a truncated cone, instead of a disk (this would explain the double circle we see in Figure 4.11, creating the aureole illusion). The assumption is explained thinking to the sticking process occurring during the

metal evaporation of Au on resist walls: while gold is evaporating, it also sticks to the upper corners of the resist walls, creating a shadow that reduces the pattern area exposed to the evaporation (Figure 4.19a).

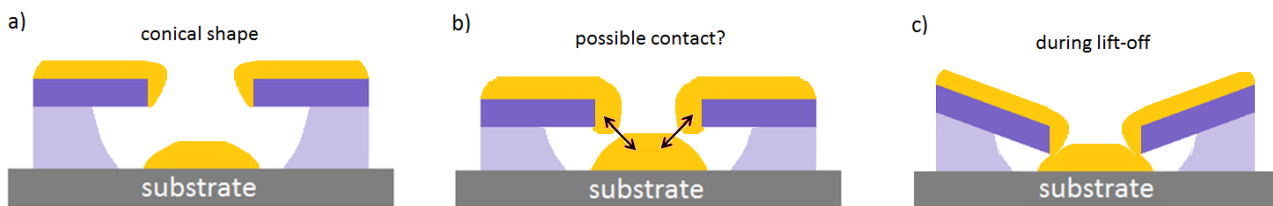


Figure 4.19: Illustration of the sticking process of the metal to the resist walls during the evaporation: **a)** this figure shows the actual process leading to a truncated conical shape of the NPs; **b)** this figure intends to show a possible unwanted effect where the contact between the NPs and the upper film occurs and would cause unsuccessful lift-off, but in order to happen a very thick layer of metal would be necessary (which is not our case); **c)** this figure shows what could possibly happen during the stripping of the resist (lift off) as potential explanation of the “smearing” effect.

Secondly, if the bottom PMMA layer is not thick enough and a lot of gold is sticking to the walls, the particle and the top film would end up touching and sticking each other (Figure 4.19b); but here we are depositing 5 nm of titanium and 10 nm of gold and we are sure that the bottom PMMA layer thickness is at least 40 nm, thus this option is excluded.

Another possible explanation could be that during the lift off, while the resist is dissolving in acetone, the upper film gets in touch with the deposited particles, enough for them to slightly stick to each other (Figure 4.19c). At this point, when the upper foil is lifted off, the edges of the holes drag the top of the conical particles aside, causing the “smearing” effect.

In order to better investigate what causes occasional smearing, another factor thought to play a role was the titanium layer (under Au); thus, different EBL samples were fabricated varying the Ti/Au thicknesses (nominally: 5nm/10nm, 1nm/10nm, 1nm/14nm) but there was no difference among them.

We finally blamed the occasional instability with the electron beam, since this effect began to occur more rarely, after the stabilization of some mechanical parts of the tool, and without significantly affecting the entire pattern.

In conclusion, it is important to point out that the first goal to create gold nanostructures of 25-60 nm of size (with different size (with different thickness), in arrays with pitch of 100 nm (the shortest possible in order to get well defined structures), 120 nm and 150 nm, has been successfully achieved (as an example see Figure 4.20 and

Figure 4.39): the patterns were then measured in reflectance and transmittance (Section 4.3) and many of them (Table 4.3), after being incorporated into the GaAs solar cells previously described, were electrically characterized (Section 6.2).

The final optimized process used to fabricate gold nanoparticles by EBL is described as follows:

- ✚ Pre-bake at 120C for 5 min; mid-bake (between the 2 layers spinning) at 180C for 10min and post-bake at 180C for 15min
- ✚ Exposure: see Table 4.3
- ✚ Development: 1 minute in MIBK:IPA=1:3 and then rinsing in IPA (2 minutes)
- ✚ Deposited metal: 5 nm of Ti, 10 nm of Au

- ✚ Lift off: overnight soaking in acetone, gentle squirtling and soft ultrasounds for 10-30 seconds (if needed), dipping in IPA (2 minutes) and rinsing in water

The set of parameters used to deposit Ti/Au particles by EBL within the PV devices measured in this work is:

exposure	beam step (nm)	Current	Dose ($\mu\text{C}/\text{cm}^2$)	obtained NP size (nm)	array pitch (nm)
single shot	100	1 nA	34, 47, 60	30, 38, 45	100
multiple shot	4		3200, 4000, 5000		100
single shot	120		30, 35, 43	32, 37, 43	120
multiple shot	4		3600, 4300, 5400		120
single shot	150		26, 31	30, 35	150
multiple shot	4		4700, 5900		150

Table 4.3: Parameters used for e-beam exposure in order to get Ti/Au NPs of a certain size, which were then incorporated into GaAs diodes.

The optimized process was then used to fabricate arrays of silver nanoparticles, focusing on circles (still in square lattice) in order to facilitate a comparison with randomly distributed circular particles which were meantime fabricated with electroless deposition.

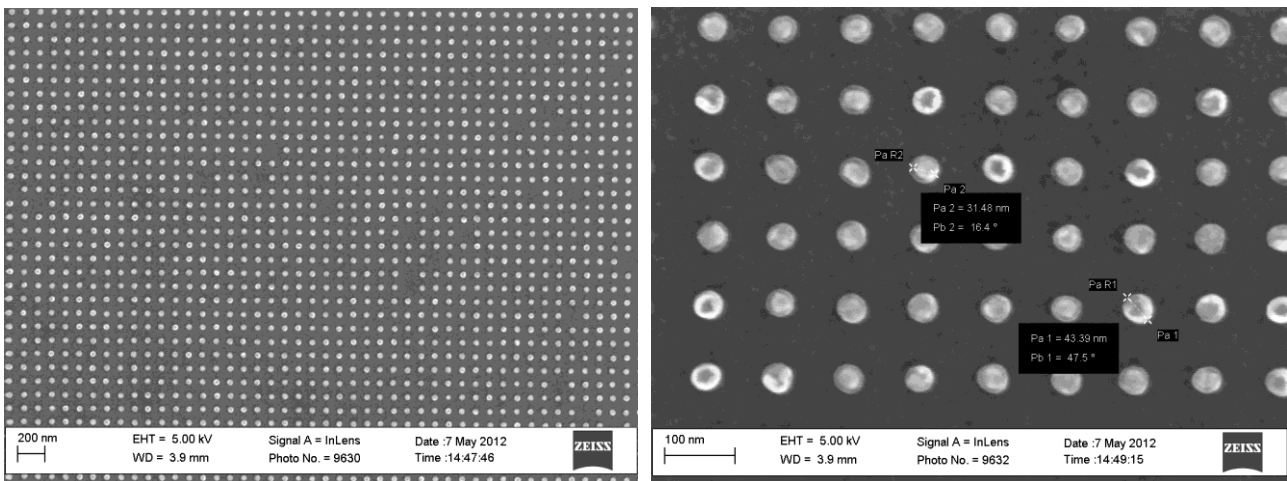


Figure 4.20: SEM images of the Ti/Au (5 nm + 10 nm) NPs deposited by EBL on GaAs/SiO₂ substrate, incorporated within characterized Schottky diodes. The right photo is a zoom of the left one.

The first thing we noticed was that with Ag the conical shape did not appear (Figure 4.21) and this is probably due to the fact that Ag has a lower sticking coefficient than Au [107]; moreover, the shape could be affected by the fact that when Au is evaporated as a film, it tends to form 30 nm sized grains.

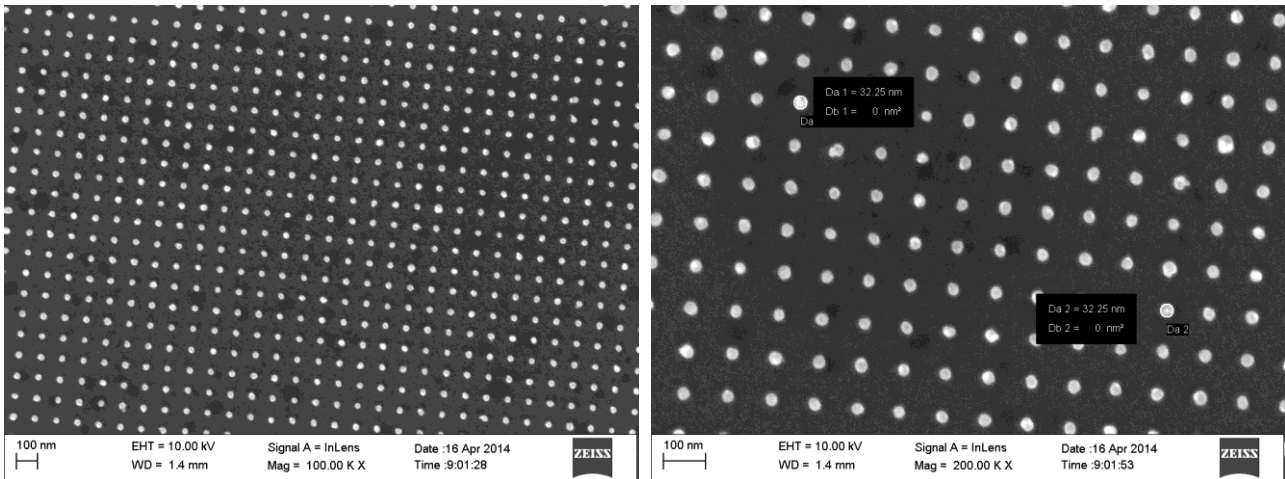


Figure 4.21: SEM images of Ag nanoparticles array (with 100 nm periodicity) deposited by EBL on GaAs. In the right photo (at higher magnification) one can notice the absence of the double circles (i.e. truncated cone shape) that was instead visible with gold NPs.

For this thesis, different arrays of Ag NPs were fabricated for optical characterization (Section 4.3.2) and eventually also electrical measurements (Section 6.3), following this variety of parameters:

- ✚ Substrate: 1) GaAs 2) Si/Ag/AZO coated with Cr. This is the structure used for a-Si:H solar cells and a thin (3 nm) chromium layer was added on top of it, in order to promote the adhesion of the PMMA resist, which does not otherwise adhere at all to AZO¹⁵.
- ✚ PMMA structure preparation:
 - Pre-baking of substrate at 120°C for 5 minutes
 - Spinning of bottom layer: A6 PMMA 100k diluted in anisole (1:1)
 - Mid-baking at 180°C for 10 minutes
 - Spinning of the top layer: A4 PMMA 495k diluted in MIBK (1:1)
 - Final baking at 180°C for 15 minutes
- ✚ Parameters used for single-shot exposure: beam current from 1 nA to 20 nA, with doses varying in the range of [30-330] $\mu\text{C}/\text{cm}^2$ and beam step of [60, 80, 100, 120, 140, 200] nm.
- ✚ Development: 1 minute in MIBK:IPA=1:3 and then rinsing in IPA (2 minutes)
- ✚ Ag layer e-beam evaporation: from 10 nm to 27 nm (the maximum allowed with such PMMA structure).
- ✚ Lift off: 30 minutes in acetone, squirting and soft ultrasounds (10 seconds) if necessary
- ✚ Obtained size of particles: 20 to 120 nm.

Silver requires a shorter lift off (30 minutes) but at the same time it is more difficult. A combination of short intervals (20-30 seconds) of ultrasounds at the minimum power and constant agitation can produce satisfactory results but sometimes few traces of metal were found on the pattern. Occasionally, too aggressive agitation would result in too many vacancies in the array.

Some representative images of the silver structures are shown in Figure 4.22.

¹⁵ The adhesion of PMMA and other resists on top of Transparent Conductive Oxide layers is quite arduous. Before taking the decision to deposit Cr many attempts to promote adhesion were tried: HMDS treatment, two different adhesion promoter (AP3000 and SURPASS3000), a combination of temperature ramps before spinning in order to dehydrate the surface, static and dynamic spinning at different speed with different dilution of the PMMA resist.

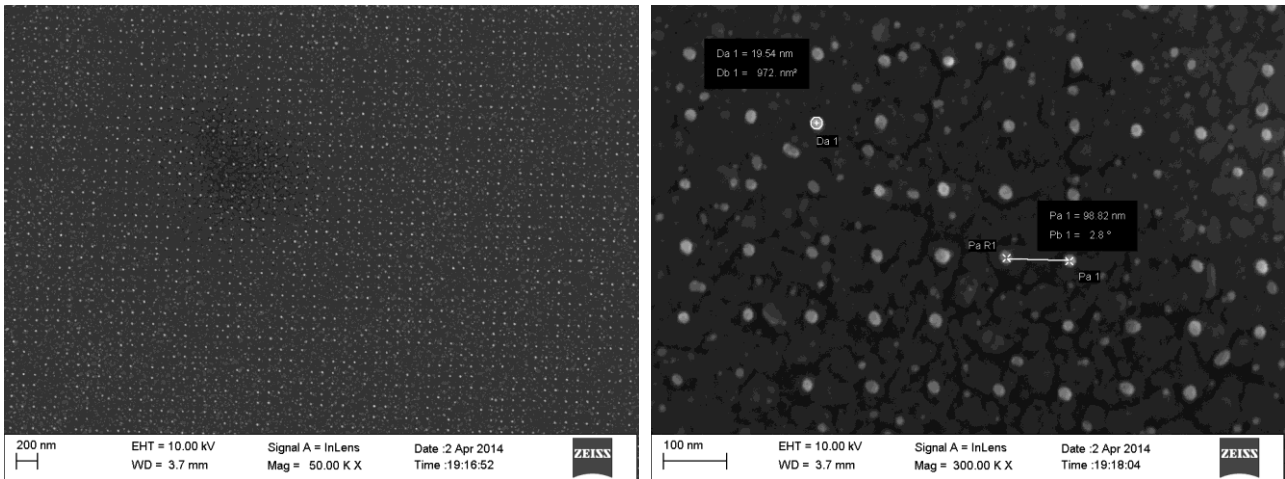


Figure 4.22: SEM images of Ag NPs deposited by EBL on top of Si/Ag/AZO/Cr, relative to solar cell E1.

Figure 4.23 shows, as an example, two graphs giving the point-doses¹⁶ necessary to match a certain range of Ag particle size in single-shot mode. In particular, from the first graph (left) it is visible the difference in NP diameter obtained for the same point-dose (and beam current, 2 nA) with different array periodicity (with 80 nm pitch the NP size is larger than that with 100 nm), due to the proximity effect. While the second graph (right) shows, for given periodicity (100 nm), the increase in NP size for the same point-dose, due to higher beam currents (and thus beam sizes).

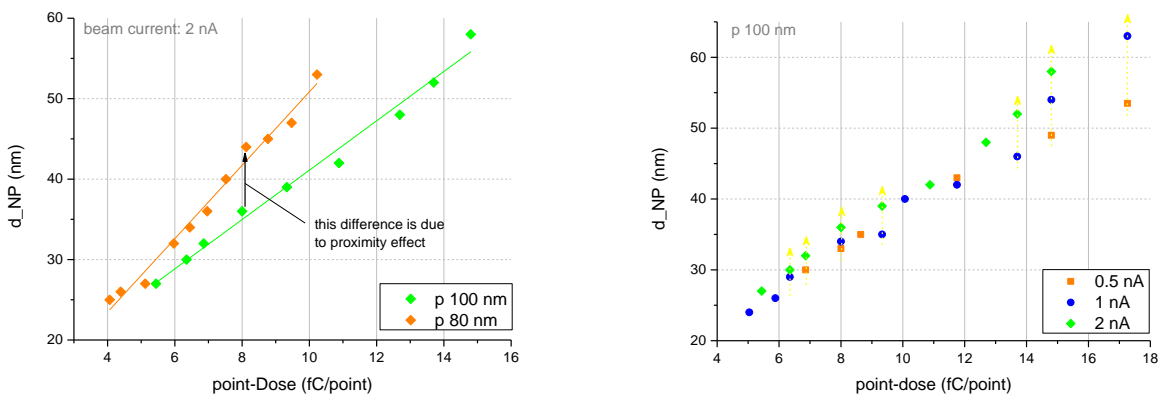


Figure 4.23: left) Graph showing the dependence of the NP diameter on the point-dose for two different array periodicities. The black arrow indicates the difference caused by the proximity effect. **right)** Graph showing again NP size (diameter) obtained for different point-doses used with different beam current values: increasing the current leads to larger beam size and thus NP diameter (highlighted by the yellow arrow).

4.2.2 Electroless plating

Electroless plating was first discovered by accident from Wurtz in 1844 while working with nickel [108]. This

¹⁶ Exposing only one point per p (pitch, nm), it makes sense to consider the dependence of NP size on the point-dose, defined as: $D^*(p)^2/cm^2$.

technique exploits a reduction reaction without using electric current. There are three different kind of electroless deposition based on the following processes [109]:

- i. Autocatalytic [110]. The reducing agent reacts with the noble metal ions, forming a deposit and a sort of action chain begins: the reduced metal serves as the catalyst for further reduction of the metal salt. Thick layers are possible.
- ii. Substrate catalyzed [111], [112]. We still have a reducing agent and a metal salt but the catalyst in this case is the substrate surface; this means that, once the film is deposited covering the whole substrate, the reduction stops.
- iii. Galvanic displacement [113]. There is no external reducing agent, since this role is played by the surface through its bonding electrons; the deposition can continue as long as the oxidized substrate ions can permeate and electrons can transfer through the metal film (i.e. when the substrate finishes to oxidize growing the entire dielectric film on top, the reaction stops). Any metal with a sufficiently positive redox potential can be a good candidate for this kind of electroless.

Electroless plating has attracted great interest due to simplicity of operation, cost effectiveness, high throughput, and lack of elaborate equipment [110], [109]. Its first application is the fabrication of uniform metal coatings on any kind of substrate, such as glass, ceramic, plastic, or metal [114]; in fact, metal films prepared in this manner exhibit excellent adhesion to the underlying semiconductor. Secondly, it has attracted considerable attention for depositing metal coatings on a variety of nanostructures, showing promising prospect in fabricating metal composite nanoparticles (metal-ceramic or metal-dielectric) [115], [116], [117], [109]. Over the last few years, in contrast to complex and expensive vacuum methods of metallization, electroless deposition has also been used as a cheap method for the fabrication of metallic nanoparticles [118], [119] as an alternative to colloidal solutions and self-assembly techniques.

The third process (iii) is the one implemented in this work for the growth of Ag NPs to be incorporated into GaAs Schottky diodes, and then also into a-Si:H solar cells; the electroless recipe involves silver nitrate powder diluted in water and hydrofluoric acid.

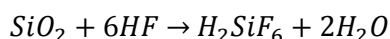
This recipe was chosen as starting point for this thesis due to the experience of the group colleagues which used it for silver plating on silicon substrates.

The reactions involved can be divided in two main phases [120]; the first phase is divided into two steps:

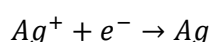
- a. the silicon substrate gets oxidized



- b. then it gets dissolved



The second phase implies silver reduction:



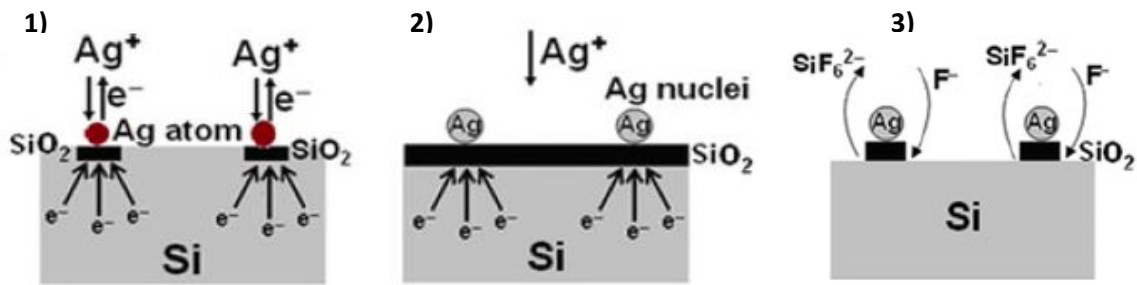


Figure 4.24: Scheme of Ag NPs growth mechanism through electroless plating (galvanic displacement) rearranged from [121].

For a better understanding, the process is illustrated in Figure 4.24. The Ag^+ ions attract electrons from the Si substrate (step 1) and Ag atoms are produced. Thus, they start to grow and agglomerate into nanoscale Ag nuclei to form nanoclusters (step 2). Then, H^+ and NO_3^- , contained in the solution, consume most of the deposited Ag atoms, preventing Ag cluster coalescence (step 3). Therefore, Ag nanoclusters do not grow as a continuous membrane, instead they approach nanoparticles shape. Simultaneously SiO_2 is produced and the released electrons are then used to reduce Ag^+ . SiO_2 is etched by HF but the speed of the process is faster than the etching of the SiO_2 layer underneath the Ag particles.

4.2.2.1 Silver NPs on silicon and gallium arsenide substrates

While nanoparticle arrays defined using electron beam lithography were used to develop design rules for the optimum nanoparticle coating of semiconductors, electroless deposition was studied in this thesis as a practical, inexpensive method for nanoparticles incorporation in real devices.

The silver plating solution is composed by $AgNO_3$ (silver nitrate) diluted in water at 2% and HF (hydrofluoric acid, 5% of concentration).

The process is done in 2 steps: a pre-dipping of the sample in HF[5%] for time t_1 , and a subsequent transfer of the sample into the beaker containing what we call active solution for time t_2 .

Initial experiments aimed at developing a process that would yield a homogenous size distribution of nanoparticles to be compared with ordered patterns fabricated by EBL. The starting point was based on results of Ag deposition on Si substrates, developed within our group. However, a recipe that resulted in small NPs of about 20-30 nm on Si, repeated on undoped GaAs samples, resulted in very inhomogeneous distribution of big and small Ag crystals. Following a systematic study of the deposition parameters, one most promising recipe (here labeled as #0 and defined in Table 4.4), with a narrower distribution of size has been selected.

t_1	Active Solution			t_2
Pre-dip in HF[5%]	H_2O	$AgNO_3$ [2%]	HF[5%]	Dip in active solution
2'	24 ml	0.5 ml	1 ml	20''

Table 4.4: Electroless sample/recipe #0.

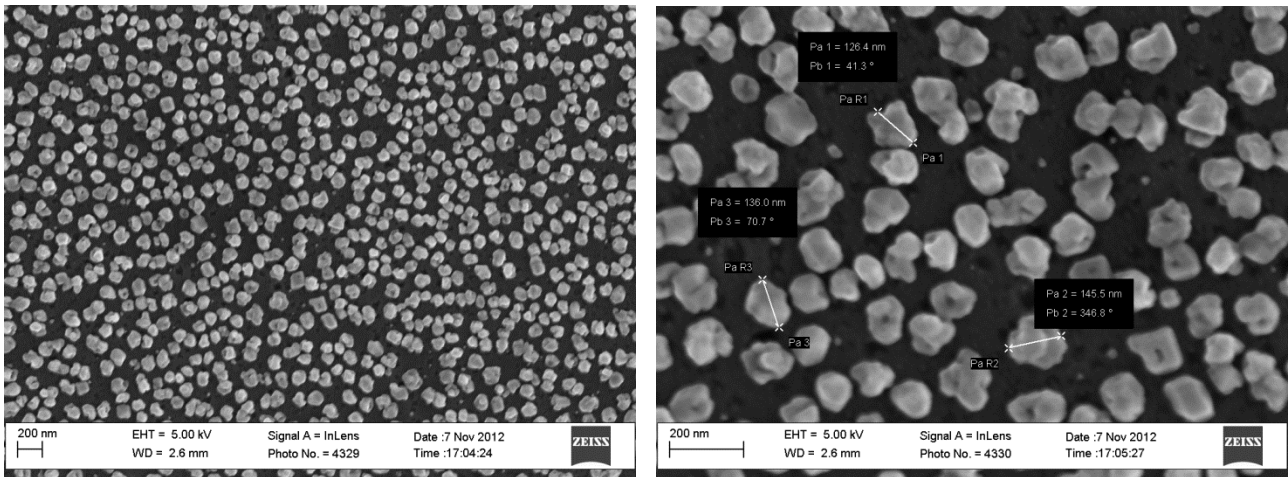


Figure 4.25: SEM images of sample #0; the right image is a zoomed photo of the left one.

From SEM images of the results of the first satisfactory deposition (Figure 4.25) we can see a very dense and not very uniform distribution of particles which are not very rounded (crystals) of average size about 130 nm. This was our starting point for the optimization of the Ag electroless plating on GaAs and subsequent experiments concentrated on reducing the size of the NPs to ensure strong absorbance of light (Figure 4.1). As a rule of thumb, the concentration of the silver nitrate is responsible for the density of the pattern, the crystal size is proportional to t_2 ; but the relation between [silver nitrate] and [HF] is also playing an important role, preventing to draw a linear dependence between the involved parameters and leading to more or less homogeneous size distributions.

As an example, in Figure 4.26, images of other two samples with longer (#1) and shorter (#2) t_2 than for sample #0 are shown (recipes in Table 4.5). The average size of NPs from longer reaction time is 250 nm ($t_2=80$ seconds) and 80 nm for shorter time ($t_2=10$ seconds).

The modus operandi used in this thesis for the optimization of an electroless recipe that can match some desired parameters is based on systematic variation of t_2 and the elements of the active solution one at the time (using the same type of substrate). The role played by the pre-dipping in HF is not clear¹⁷: many tests were run varying t_1 and the picture was difficult to interpret; it was then chosen to keep t_1 as constant parameter (equal to 2 minutes).

<i>sample</i>	t_1	<i>Active Solution</i>			t_2	<i>NPs size</i> (average value)
	Pre-dip in HF[5%]	H₂O	AgNO₃ [2%]	HF[5%]	Dip in active solution	
#0	2'	24 ml	0.5 ml	1 ml	20''	130 nm
#1	2'	24 ml	0.5 ml	1 ml	80''	250 nm
#2	2'	24 ml	0.5 ml	1 ml	10''	80 nm

Table 4.5: Electroless recipes of sample #1 and #2; obtained from a variation in t_1 from recipe #0 and relative averaged size calculated from several SEM images.

¹⁷ HF on Si surface crests H-Si bonds and prevents oxidation; on GaAs it removes Ga atoms and F binds with remaining Ga atoms. The two surfaces and the relative chemistry are very different.

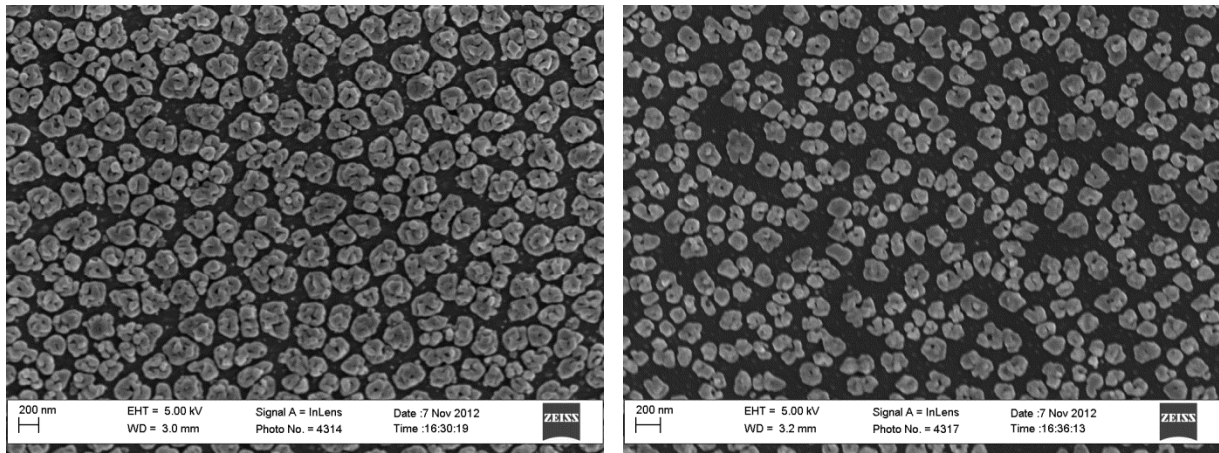


Figure 4.26: SEM images of electroless samples #1 (left) and #2 (right).

Since we are aiming for small nanoparticles, $t_2 = 10$ seconds (#2) has been used in the following experiments which were designed to optimise the concentration of the active solution components, by means dilution of silver nitrate powder combined with varying HF[5%] concentration. Moreover, the tests were run on 3 different substrates.

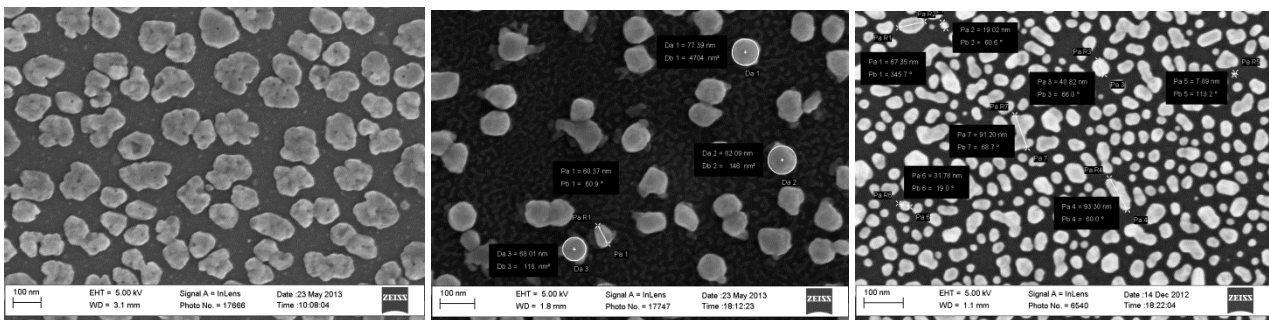


Figure 4.27: SEM images of recipe #2 performed on undoped GaAs (left), Si-doped GaAs (centre) and p-silicon (right).

The type of surface of the substrate (material and doping level) is fundamental for electroless plating and a clear difference between undoped GaAs, n-doped GaAs and p-doped Silicon substrates can be seen for the same deposition, see Figure 4.27. In fact even the doping level of the surface is important and this represents the main limit of this technology: the same result is not easily reproducible on nominally equal substrates or transferable to different material substrates.

In Table 4.6a-c, results of this analysis, conducted to better understand the mechanism behind the electroless technique, are shown. The investigation was conducted on the three different substrates that we consider for solar cells with NPs. Some samples showed an interesting feature: together with standard Ag crystals, very tiny dots around the surface (see Figure 4.28-left) appear.

sample	Active Solution (ml)			Ratio1	Ratio2	FF	D_{av} (nm)	Size range (nm) (average value)
	H ₂ O	AgNO ₃ [2%]	HF[5%]					
on silicon substrate				AgNO ₃ [2%]/H ₂ O	HF[5%]/Ratio1			
A	36	0.5	1	1.4E-02	72	40%	24	(20,70)
B	24	0.4	1	1.7E-02	60	30-32%	29	(15,44)

#2	24	0.5	1	2.1E-02	48	49%	35	(15,85)
C	24	1	1	4.2E-02	24	60%	60	(23,155)
D	24	2	1	8.3E-02	12.0	65-70%	Highly elongated, wire-like	
E	24	0.5	1.5	2.1E-02	72	46%	36	(<20,>50)
F	24	0.5	0.5	2.1E-02	24	44%	28	(18,140)
G	24	1	2	4.2E-02	48	55%	65	(55,130)
H	24	1	3	4.2E-02	72	52%	50	(15,100)
I	24	0.25	0.5	1.0E-02	48	32%	18	(10,40)
J	24	0.25	0.25	1.0E-02	24	32%	14	(10,20)

Table 4.6a: List of recipes and consequent results of Ag electroless plating on (p-doped) silicon. Parameters: $t_1 = 2$ min and $t_2 = 10$ seconds. FF is the filling fraction of silver.

sample	Active Solution (ml)			Ratio1	Ratio2	FF	FF*	D_{av} (nm)	Size range (nm)
undoped GaAs	H ₂ O	AgNO ₃ [2%]	HF[5%]	AgNO ₃ [2%]/H ₂ O	HF[5%]/Ratio1		(excluding dots)		(average value)
A	36	0.5	1	1.4E-02	72	43%	41%	78	(50,185)
#2	24	0.5	1	2.1E-02	48	53%	49%	80	(85,185)
G	24	1	2	4.2E-02	48	56%	(56%)	88	(75,225)

Table 4.5b: List of recipes and consequent results of Ag electroless plating on undoped GaAs. Parameters: $t_1 = 2$ min and $t_2 = 10$ seconds. FF is the filling fraction of silver and FF* is calculated excluding the tiny dots (if present).

sample	Active Solution (ml)			Ratio1	Ratio2	FF	FF*	D_{av} (nm)	Size range (nm)
n-doped GaAs	H ₂ O	AgNO ₃ [2%]	HF[5%]	AgNO ₃ [2%]/H ₂ O	HF[5%]/Ratio1		(excluding dots)		(average value)
A	36	0.5	1	1.4E-02	72	30%	16%	70	(70,150)
#2	24	0.5	1	2.1E-02	48	32%	19-20%	71	(60,80)
G	24	1	2	4.2E-02	48	45-47%	38%	78	(65,120)

Table 4.5c: List of recipes and consequent results of Ag electroless plating on n-doped GaAs. Parameters: $t_1 = 2$ min and $t_2 = 10$ seconds. FF is the filling fraction of silver and FF* is calculated excluding the tiny dots (if present).

Based on the depositions described in the tables above we can draw some general conclusions which serve as guidelines for the optimization of a recipe responding to particular size or density requirements for a certain substrate:

- ✚ The size distribution is always quite broad (as example see Figure 4.28-centre): this could mean an advantage for us, since the increase of the disorder in size can redshift the resonance [54] (which is usually in the visible, for Ag NPs, and we are interested to absorb in the NIR).
- ✚ The size of the nanoparticles is usually larger (using the same recipe) on GaAs than silicon. This might be also related to the fact that HF interacts with the two semiconductor surface very differently: this acid is a very common and uniform silicon etchant; while for GaAs (100), HF, completely remove gallium oxides but only decreases the amount of arsenic oxides. This affects the

reduction reaction and explains the big variation in results on different GaAs substrates¹⁸.

- ✚ If we increase silver nitrate concentration in water (*Ratio1*), keeping constant the amount of HF, by means of decreasing *Ratio2*: with silicon, filling fraction, average size and distribution width increase (see samples A-#2-C and F-I); for GaAs, filling fraction and average size again increase, but less rapidly and instead the width distribution gets narrower (see A-#2 for both GaAs).
- ✚ Increasing silver nitrate concentration in water (*Ratio1*) but keeping constant *Ratio2*: FF, average size and width distribution increase (see C-F-J, #2-G-I and A-E-H ; see also #2-G for both GaAs).
- ✚ Increasing HF amount in respect to constant AgNO₃ solution (*Ratio2*) has 2 effects: the filling fraction slightly decreases and the size distribution gets narrower (see #2-E-F for silicon).
- ✚ For very high level of silver nitrate concentration (sample D), a clustering of the crystals begins creating elongated wires (Figure 4.28-right); on GaAs substrate this effect starts at more diluted solutions.

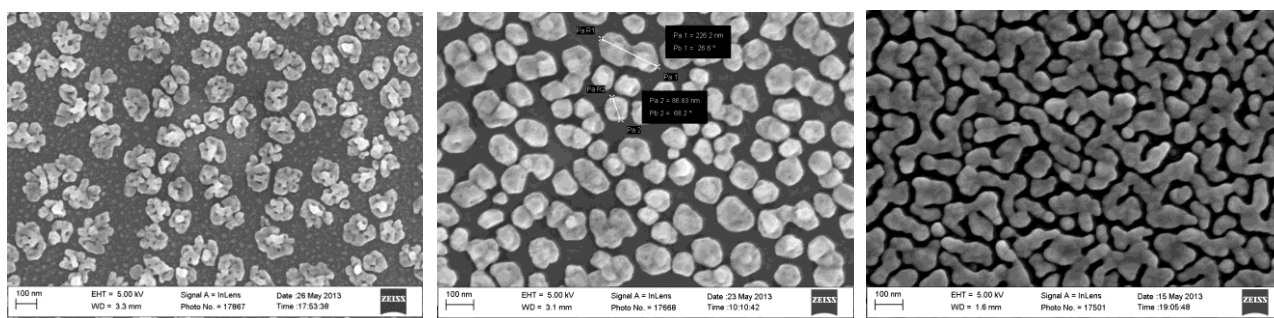


Figure 4.28: SEM images of: **left**) results of electroless recipe #2 performed on a different n-GaAs substrate (undoped-GaAs/n⁺GaAs/n⁻GaAs); **centre**) results of recipe G on undoped GaAs substrate; **right**) results of recipe D on silicon substrate.

A big variety of Ag NPs both in size and shape (from rounded to big crystals similar to flakes) can be obtained with this technique and some examples are shown in Figure 4.28.

Sometimes the samples were not showing very uniform patterns all over the treated surface; in order to improve the adhesion of Ag crystals to the substrate (and thus the uniformity of the pattern) a surface pre-treatment with tin chloride (SnCl₂) [122] diluted in water 1:50 was tried, but without success.

Many of these samples were then measured in reflectance and transmittance, using an integrating sphere (Section 4.3): the samples giving absorbance enhancement in the NIR range were those with a filling fraction of at least 16% and they would have been good candidates for the incorporation in photovoltaic devices (as shown in Chapter 3). These samples were then compared to ordered patterns with the same average size and filling fraction, taking into account another parameter: the nanoparticles thickness, which we tried to measure by SEM. The cross section of two representative samples with Ag NPs grown on top by electroless plating is shown in Figure 4.29 and the thickness ranges between 20 and 30 nm.

¹⁸ Another n-doped GaAs substrate (nominally similar to the one just described) was used to test the same recipes and the results (not reported in this thesis) were quite different.

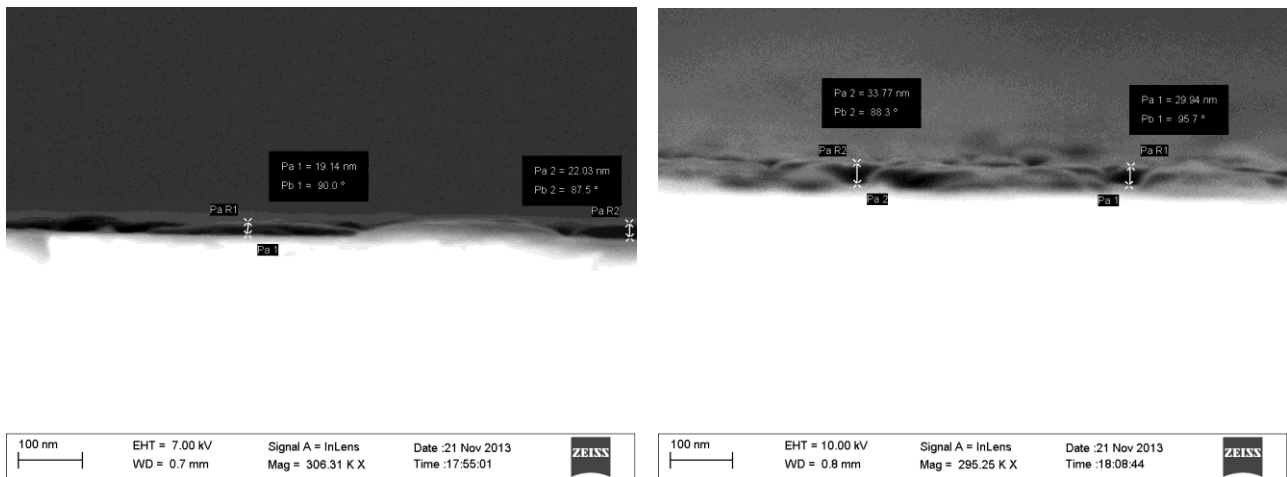


Figure 4.29: SEM images of the cross section of two samples with Ag NPs grown on top by electroless plating.

After several tests, following the guidelines previously described, the recipe chosen for electroless deposition on n-doped GaAs, of NPs to be incorporated within photodiodes, was #2 due to its optical effectiveness and SEM images of the results are shown in Figure 4.52-left. This recipe is the optimum process for the structure GaAs/Ag NPs/ITO, which gives significant absorbance enhancement in the NIR range (of about 20%, see Section 4.3).

4.2.2.2 Silver NPs on silicon nitride for GaAs solar cells

Subsequently, another surface was tested with electroless plating: silicon nitride (Si_3N_4) layer deposited by PECVD on top of different substrates. This layer was introduced in the second generation of our device structure (Figure 3.16-right), as insulating layer on top of the GaAs active absorber, in order to reduce surface recombination and eventually preventing the lost of the plasmonic effect. In addition it was preventing GaAs from etching with HF.

The electroless process in this case was performed quite differently: first, the pre-dipping in HF was eliminated, since this acid etches silicon nitride quite rapidly. Recipe #2 was used as starting point on two different substrates consisting of a PECVD Si_3N_4 layer of two thicknesses (10 nm and 60 nm) on top of silicon substrate and the results were similar (particle size ranging between 15 and 30 nm and filling fraction of about 10%). This means that the thickness of the silicon nitride layer is not affecting the reaction (as we also expected). Moreover, in order to double check the etching effect of HF, one sample with thin (10 nm) Si_3N_4 layer was dipped into a solution of 24 ml of H_2O and 1 ml of HF[5%], exactly corresponding to the components of the active solution #2 (AgNO_3 [2%] excluded) and the layer thickness has been measured before and after the dipping via ellipsometry: there was no sign of etching; at this dilution (in total 0.2%) the etch rate of HF on Si_3N_4 must be very slow.

For these tests the silicon nitride layer was deposited only on silicon, expecting to be able to reproduce similar results (using the optimized recipe) on the other substrates (for the PV devices), covered by the same Si_3N_4 layer (the back of the sample is always covered with a proper tape). This was proved with a single test by running the same recipe (C*, Table 4.7) on the 3 different substrates (p-Si, undoped GaAs, n-

GaAs) coated with the same silicon nitride layer (12 nm) on top: the obtained Ag NPs were almost identical (represented in Figure 4.30a).

<i>sample</i>	t_1	<i>Active Solution</i>			t_2	<i>NPs size</i> (average value)	<i>FF</i>
	Pre-dip in HF[5%]	H₂O	AgNO₃ [2%]	HF[5%]	Dip in active solution		
C*	/	24 ml	1 ml	1 ml	10''	22 nm	10%

Table 4.7: Electroless recipe C* tested on different substrates covered with the same Si₃N₄ layer and giving the same results.

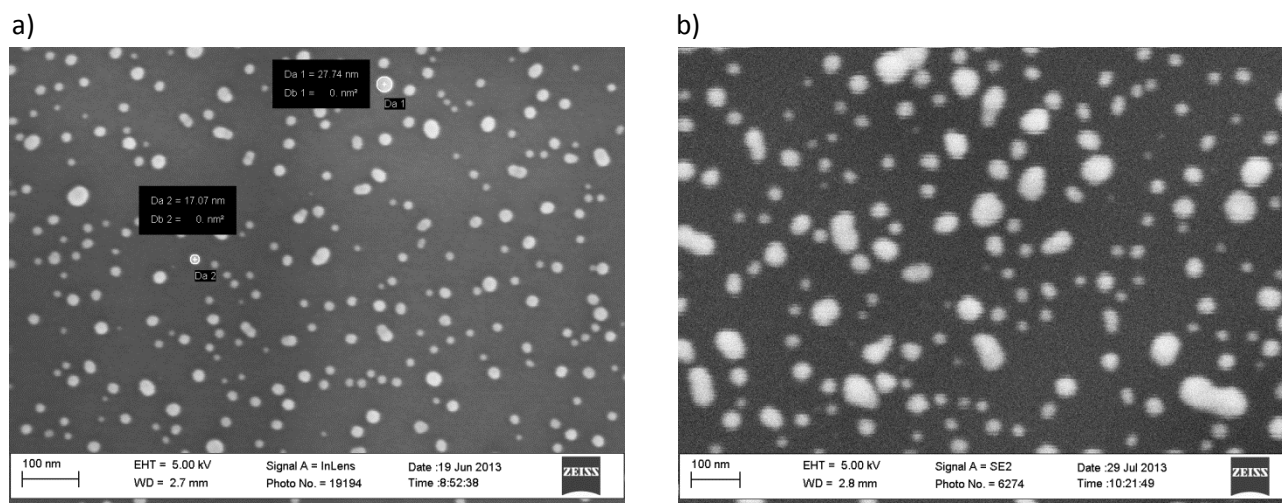


Figure 4.30: **a)** SEM image of sample C* (Ag NPs by electroless on n-GaAs/Si₃N₄; recipe of Table 4.7). **b)** SEM image of sample #14 (Ag NPs by electroless on Si/ Si₃N₄; 2-steps recipe of Table 4.8).

This paved the way to the optimization of a new recipe for silicon nitride, aiming to denser patterns (from at least 16% of filling fraction). The filling fraction, regardless the NPs size, was the parameter deciding for absorbance enhancement in the NIR range (see Section 4.3) and therefore the probability of plasmonic photoemission.

After systematic tests, in which the dipping time together with different active solutions was varied, following the general guidelines derived from our previous experience with Si and GaAs substrates, we realized that the process on a dielectric surface, which is simultaneously etched (even if slowly) during the electroless process, is working differently. The results were not sufficient (too low density of NPs), thus, another *2-steps** recipe was introduced:

1. AgNO₃ diluted in water without any HF was prepared, then the sample was dipped for a time t_1^* (note that it does not have anything to do with previous t_1);
2. HF[5%]¹⁹ was subsequently added to the solution and the samples left for time t_2^* .

About 30 recipes were tested on 12-15 nm of Si₃N₄ deposited on top of silicon. In all, the silver nitrate concentration was fixed (0.5 ml AgNO₃[2%] in 24 ml H₂O), and following variations were introduced: the HF[5%] amount (from 0.25 ml to 4 ml) to be added in the second step; t_1^* (1-4 minutes) and t_2^* (1-7.5 minutes).

¹⁹ Usually the HF was gently added, in a spot quite far away the position of the sample inside the beaker, at -3 seconds of t_1^* countdown; in this way t_2^* could start exactly when the total amount of HF was included.

During these tests also silver nitride layers deposited with a different PECVD machine, following a slightly different recipe, were used and the results were, as expected, different than the other substrate. The composition of the surface exposed to the reaction plays an important role in this technique and we then decided to use only one PECVD tool, the same recipe for all our Si₃N₄ depositions; the silicon nitride layer was deposited with these parameters: 1470 sccm for N₂ gas flow, 30 sccm for ammonia (NH₃) gas flow and 30 sccm for silane (SiH₄); pressure at 650 mTorr and RF power of 20 W alternating low frequency (2 seconds) with high frequency (6 seconds) to ensure low stress within the deposited layer.

An example of Ag NPs grown following the new process is shown in Figure 4.30b, as result of sample #14, corresponding to the recipe described in Table 4.8.

<i>sample</i>	<i>t</i> ₁ [*]	<i>Active solution</i>			<i>t</i> ₂ [*]	<i>NP size</i>	<i>FF</i>
		<i>Pre-solution</i>		<i>Added HF</i>			
Si₃N₄ on top of silicon	Dip in pre-solution	H₂O	AgNO₃ [2%]	HF[5%]	Dip in active solution	Average value	
#14	2.5'	24 ml	0.5 ml	0.5 ml	3'	60 nm	14%

Table 4.8: Electroless recipe #14.

At this point, the average size of NPs is about 60 nm and size distribution is very broad; the filling fraction is bigger (about 14%) than our starting point (10%), but still not enough. The experimental results shown in Chapter 5, drove us to look for higher density distribution and a narrower range of size, in order to increase the probability to create dimers (formed by smaller nanoparticles touching each other, with comparable resonating lengths), or merging of small particles to form elongated ones. These are the elements giving plasmon excitations in our range of interest (see Section 5.4).

The first recipes, which resulted in clear optical response from the NPs, were #29 and #30 (indicated in Table 4.9). They were measured in reflectance and transmittance with the integrating sphere showing absorbance enhancement in the NIR region (Section 4.3). Before depositing the NPs on top of GaAs/Si₃N₄ substrates, the etching rate of HF on silicon nitride was tested, to make sure that after such high concentration of HF during the electroless process, the insulating layer (necessary for the solar cell) is not removed. The etch rate of 4 ml HF[5%] in 24 ml H₂O was about 10nm/min, thus the new silicon nitride thickness chosen for the GaAs and a-Si:H solar cell fabrication was 25-28 nm.

<i>sample</i>	<i>t</i> ₁ [*]	<i>Active solution</i>			<i>t</i> ₂ [*]
		<i>Pre-solution</i>		<i>Added HF</i>	
Si₃N₄ on top of Si and GaAs	Dip in pre-solution	H₂O	AgNO₃ [2%]	HF[5%]	Dip in active solution
#29	1'	24 ml	0.5 ml	4 ml	60''
#30	1'	24 ml	0.5 ml	4 ml	90''
#34	1'	24 ml	0.5 ml	4 ml	75''
#35	1'	24 ml	1 ml	3 ml	90''
#36	1'	24 ml	1 ml	3 ml	60''

Table 4.9: Electroless recipes #29-30-34-35-36. See some correspondent SEM images in Figure 4.31 and Figure 4.32. Recipe #34 was chosen to be the optimum for solar cell fabrication.

The two recipes were then repeated on undoped GaAs/Si₃N₄ and n-GaAs/Si₃N₄ and the results were quite similar (Figure 4.31); they were also measured in reflectance and transmittance (see Section 4.3) and they showed absorbance enhancement in the NIR region: #29 of about 19% (at 1.1 μm of wavelength, see diode #4 in Figure 4.53) and #30 of even 25%.

The latter sample has a very high concentration of particles, which are touching and clustering (Figure 4.32-left), thus probably scattering a lot in the visible²⁰, therefore: suitable within the solar cell for light trapping (considering that the nanoparticles are covered by ITO), or instead just preventing a lot of photons to be absorbed by the thin GaAs layer. Recipe #30 was thus excluded and 3 more recipes (Table 4.9) were tried; but again the recipe which best fulfills our requirements was #29. Recipe #34 was also giving absorbance enhancement of about 20%, but showing some particles aggregations (Figure 4.32-right), it was again excluded for the same reason of #30 and also because recipe #29 gives results comparable with the NPs obtained directly on top of GaAs substrate (without insulating layer), thus the relative electrical measurements can be reasonably compared as well (Section 6.2).

In summary, recipe #29 was the optimum chosen for the incorporation of electroless nanoparticles in the GaAs/Si₃N₄/Ag NPs/ITO solar cell structure.

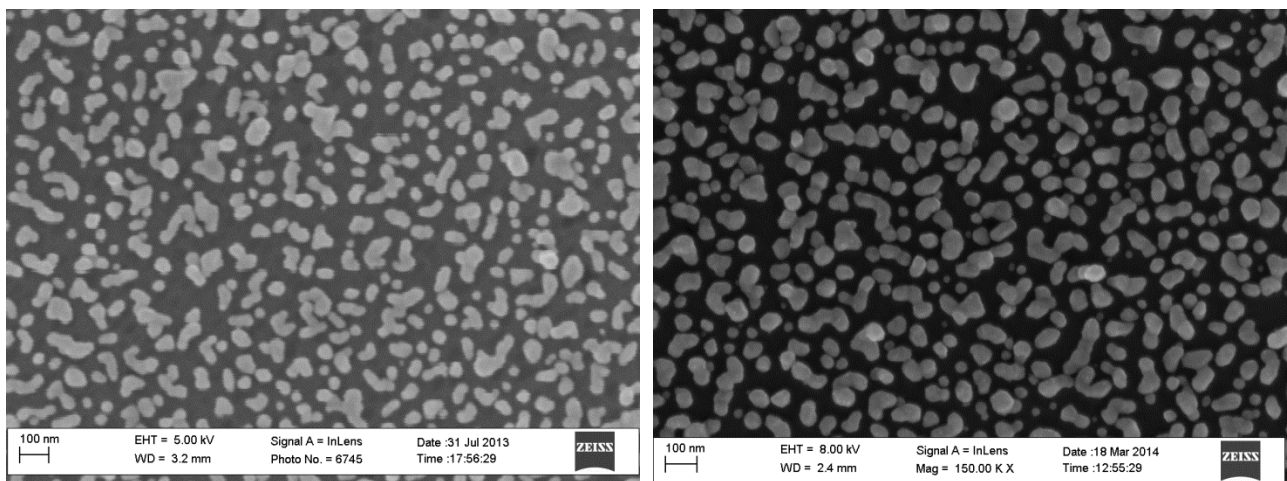


Figure 4.31: SEM image of Ag NPs deposited by electroless recipe #29 on top of **(left)** undoped GaAs covered with thin Si₃N₄ layer and **(right)** n-GaAs covered with the same Si₃N₄ layer.

²⁰At this point of the process no visible spectrometer for R/T measurements with the integrating sphere was available.

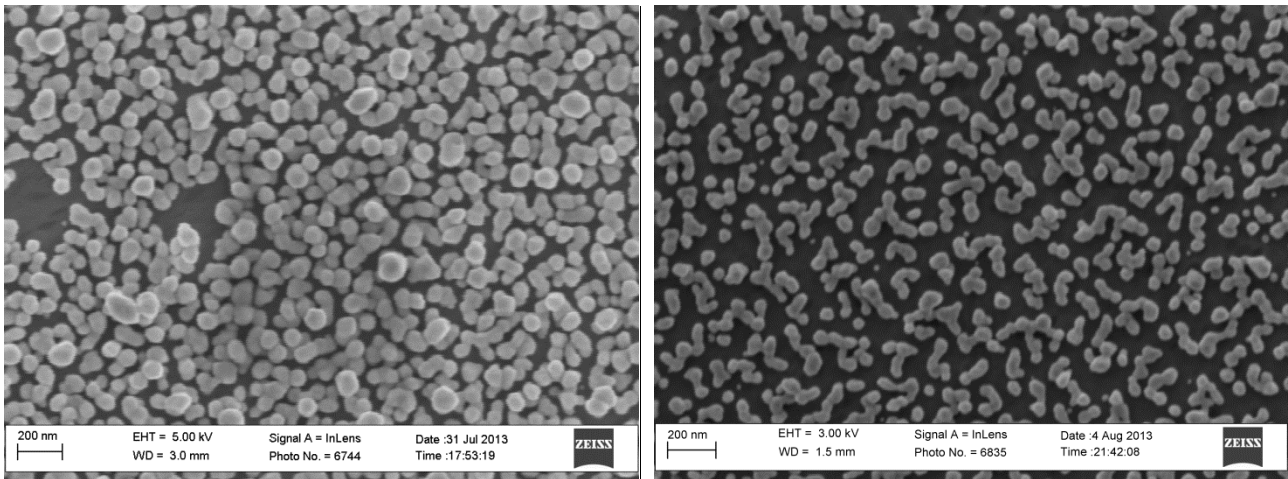


Figure 4.32: SEM image of Ag NPs deposited by electroless (**left**) recipe #30 on top of undoped GaAs covered with thin Si_3N_4 layer; and (**right**) recipe #34 on top of n-GaAs covered with thin Si_3N_4 layer.

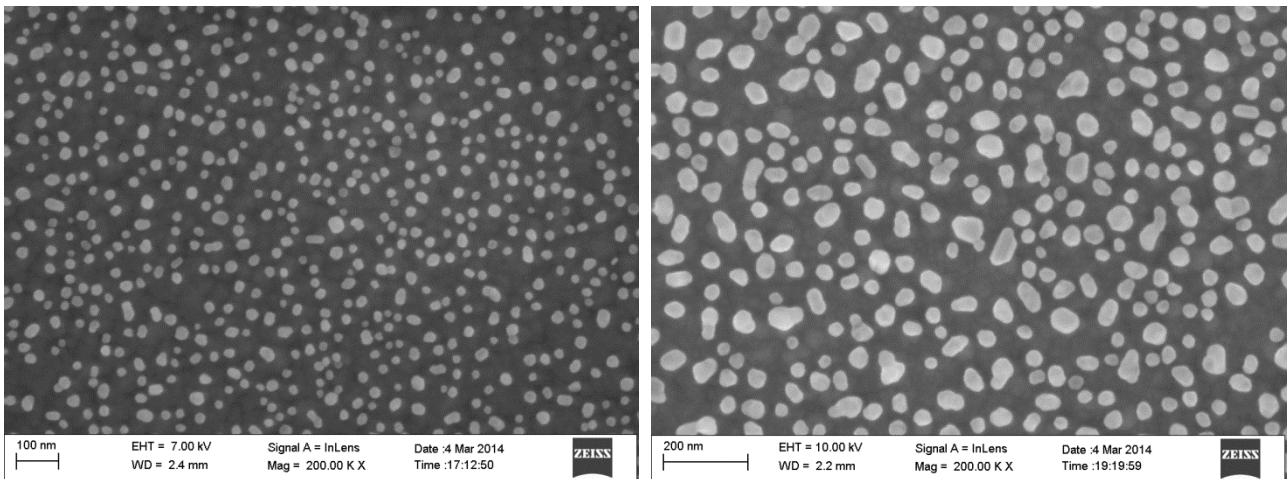


Figure 4.33: **left**) Results of electroless recipe #55 on Si/Ag/AZO/ Si_3N_4 substrate. **right**) Results of electroless recipe #56 (optimum) on Si/Ag/AZO/ Si_3N_4 substrate.

4.2.2.3 Silver NPs on silicon nitride for a-Si:H solar cells

The incorporation of electroless nanoparticles within amorphous silicon solar cells required another optimization of a new 2-steps recipe. In first place, the electroless plating was experimented directly on top of AZO (having as substrate the stack Si/Ag/AZO), but HF reveals to be too aggressive on the TCO. Following experiments with different protection layers, a silicon nitride layer (40 nm) on top of the substrate stack Si/Ag/AZO was chosen in order to take advantage of the experience gained on the GaAs solar cells.

Following this development, we found that the recipes working well for GaAs (#29 or #34) were giving a non-homogeneous distribution of the pattern. The reason was found to be much larger area (at least 5 cm by 5 cm) of Si:H devices compared to typical GaAs devices of maximum dimension of (1 cm)². Moreover, the results indicated that the exposed sides of the structure also play a role in the chemical reaction.

In order to fulfill the usual requirements for the deposition (high density, no high particles aggregations, many close dimers and elongated particles) a new recipe was developed.

sample	t_1^*	Active solution			t_2^*	NP size (average) nm	FF (%)
		Pre-solution		Added HF			
		H ₂ O	AgNO ₃ [2%]	HF[5%]			
Si ₃ N ₄ on top of Si/Ag/AZO	Dip in pre-solution				Dip in active solution		
#50	60''	24 ml	1 ml	4 ml	30''	37	27
#51	60''	24 ml	1 ml	4 ml	45''	62	32.5
#52	90''	24 ml	1 ml	4 ml	30''	56	22
#53	60''	24 ml	1.5 ml	4 ml	30''	74	26
#54	90''	24 ml	1 ml	4 ml	45''	23	24
#55	90''	24 ml	1 ml	4 ml	60''	43	22
#56	90''	24 ml	1.5 ml	4 ml	75''	78	31
#57	60''	24 ml	2.5 ml	4 ml	90''	60	16

Table 4.10: Brief summary of the best recipes for particles deposition on top of Si/Ag/AZO/Si₃N₄.

In Table 4.10, a brief summary of the best recipes for particles deposition on top of Si/Ag/AZO/Si₃N₄ is shown and in Figure 4.33 two of them are shown after SEM inspection. Finally, recipe #56 (Figure 4.33-right) was chosen as optimum deposition for Si/Ag/AZO/ Si₃N₄ substrate.

4.2.2.4 Silver NPs on silicon nitride for TEM membranes

Since it was decided to investigate the plasmonic properties of the Ag NPs grown by electroless plating through EELS analysis (Chapter 5), the deposition technique needed to be applied to the typical TEM substrates. These substrates, specifically made for TEM, are windows of very thin silicon nitride membranes on a frame of very small (3mm by 3mm) silicon chips of 100 um thickness (Figure 4.34).

The maximum thickness of support layer that allows observation of NPs with reasonable high resolution and sensitivity with TEM is about 20-25 nm, thus the starting point were Si₃N₄ membranes of 10 nm and 50 nm thickness. The first attempts were made on thicker membranes, considering that during the electroless

process, part of this layer is etched: recipes #29 and #56 were then used and in both cases the membrane resulted completely etched away.

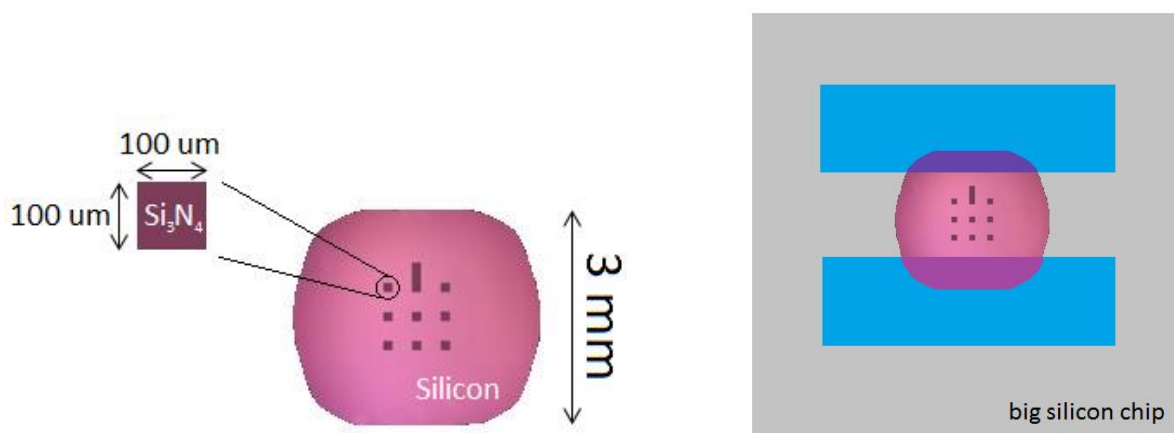


Figure 4.34: Sketch (from top) of the 9 Si_3N_4 membrane windows used as substrate for STEM measurements. On the right the chip is attached with blue tape onto a thick larger silicon chip to facilitate handling during electroless process.

Silicon nitride layer on these substrates had a different composition compared with the one we used on GaAs and a-Si:H (we actually experienced different results using different PECVD machine or silicon nitride recipes), thus, another approach was followed. We deposited our standard Si_3N_4 layer of 30 nm thickness and further precautions were taken during the electroless process: the small chip was attached to a bigger thick silicon substrate on its back using some blue tape at the edges of the chip (Figure 4.34). In this way the back of the membranes was covered in a better way (than just using the tape) and the handling of the sample was easier. Following these developments, in order to get a result as similar as possible to the Ag NPs showing absorbance enhancement²¹ and estimating the silicon nitride thickness reduction during the electroless deposition, recipe #41 was selected as the optimum for TEM samples starting from a Si_3N_4 membrane of 10 nm with a further deposited layer of 20 nm (which would have become 10 nm thick after electroless process).

<i>sample</i>	t_1^*	<i>Active solution</i>			t_2^*
Si_3N_4 on top of TEM membrane	Dip in pre-solution	<i>Pre-solution</i>		<i>Added HF</i>	Dip in active solution
		H_2O	AgNO_3 [2%]	HF[5%]	
#41	70''	24 ml	1 ml	4 ml	90''

Table 4.11: Optimum electroless recipe (#41) used for TEM samples; results are shown in Figure 4.35.

In Figure 4.35 a representative SEM picture of the deposited silver nanoparticles, later analyzed with STEM (see Chapter 5), is shown. The nanoparticle size is on average smaller than what we usually get on Si_3N_4 layers but similar layers but similar particles (in size and FF) deposited on silicon substrates were measured in R and T and they showed the desired absorption enhancement in the NIR region (see the relative transmittance measurement represented by the measurement represented by the pink curve in

Figure 4.51).

²¹ These TEM samples could not be measured in reflectance and transmittance (because too small for our light source) in order to verify the absorbance enhancement.

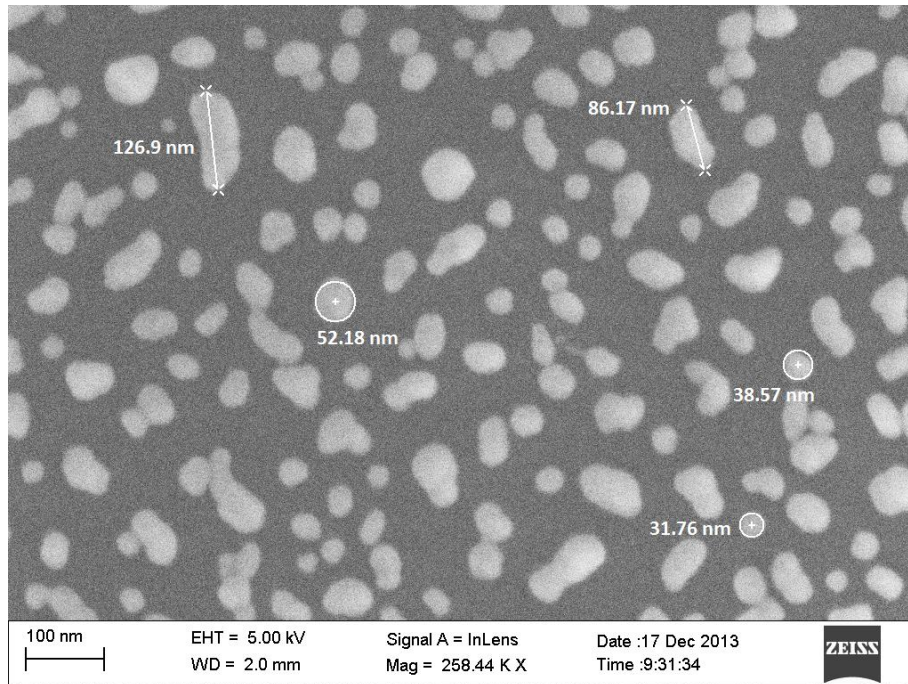


Figure 4.35: SEM images of Ag NPs deposited by electroless (using recipe #41) on Si_3N_4 membrane.

4.3 Indirect absorbance measurements

4.3.1 First optical characterization setup and first gold order samples

The initial modeling used for this thesis (Section 3.1.1), showed that the absorption peak, caused by the excitation of a localized plasmon in the nanoparticle, corresponds to a dip in transmission (T); on this basis it was decided to measure transmission in order to study the position of the surface plasmon resonance.

The first measured samples were NPs arrays of titanium/gold with a total thickness of 15 nm, deposited by patterning with EBL and metal evaporation followed by lift off on the surface of undoped GaAs substrate. The samples were characterized using an optic fiber-based setup. A broadband supercontinuum light source (500-2400) nm from the NKT Photonics was coupled, through a polarizer controller, into a polarization maintaining (PM) photonic crystal optical fiber. The light from the PM fiber was then used as excitation for the structure while the transmitted light was collected with a single-mode fiber and measured using an Optical Spectrum Analyser (OSA), see Figure 4.36. The maximum spectral range measurable with the OSA stretches from 500 nm to 1700 nm, but since GaAs is absorbing for wavelengths shorter than 880 nm, here T spectra are shown only from 900 nm.

The measurements (Figure 4.37) showed the presence of the LSP resonance at around 1250 nm wavelength, and did not change with the nanoparticles size and periodicity of the array (see Fig. 5). The measurements were done on 70 different GaAs samples, with Ti/Au nanoparticle size ranging between 25 nm and 50 nm and periods of 100 nm and 120 nm; 76% of them exhibit the dip in transmission spectra at wavelengths within the [1200, 1300] nm range.

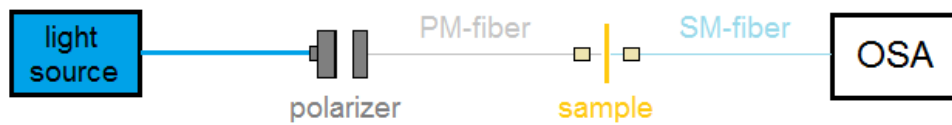


Figure 4.36: Scheme of first transmission measurements fiber setup.

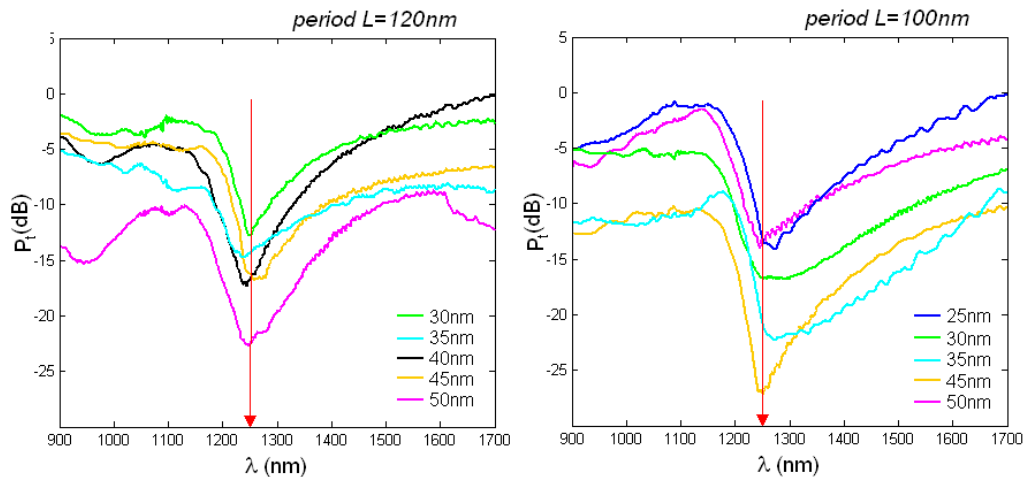


Figure 4.37: Transmission spectra representative of several measurements taken on different samples of Ti/Au NPs arrays with two periodicities: 100nm and 120nm; the nanoparticles size range is (25, 50) nm. [98]

Spectra in Figure 4.37 show similar behavior with small deviations in position of the resonance and its magnitude, which, averaging the whole set of measurements not shown here, can be estimated to be about -10dB. The levels of transmitted power need to be calibrated against the references signal. Different areas without nanoparticles on the GaAs wafer substrates close to the nanoparticles were chosen as references. Since the substrate used for these samples has unpolished back surface, transmitted intensity depends on the back scattering, thus affecting the amount of detected light from the SM-fiber. The irrelevance of the pitch size on the resonance position is clearly seen comparing spectra of the right and left panels in Figure 4.37. While this is not surprising that the position of the localized surface plasmon should not strongly depend on the period of NPs arrays (Figure 3.6) [24], the insensitivity of the resonance to the size rose several doubts. Nevertheless, a correlation between measurements and simulations from the first model existed and therefore, this part of the work was published in the Proceeding of SPIE 2012 [98]. As explained in Section 3.1.1, further studies brought light on these doubts showing that the size of the NPs seemed to be overtaken by the effect of shape (conical instead of cylindrical) which can tune the LSP resonance (Figure 3.10).

The investigation on the position of LSP resonance continued on more GaAs samples with order Ti/Au NPs but the measurements shown in Figure 4.37 were not reproducible.

The setup used for this previous experiment was collected signal corresponding to the normal T but with both the nanoparticles on the front and the not polished surface on the back, the scattered light intensity may be significant causing large errors. The solution was the introduction of an integrating sphere.

4.3.2 Integrating sphere for reflectance and transmittance measurements

With an integrating sphere all the specular as well as scattered light transmitted and reflected by the sample is measured: the instrument consists of a hollow spherical cavity with its interior covered by a diffuse white reflective coating; all the photons entering the sphere are diffused and collected by an optical fiber connected to the spectrometer. Thus the absorbance calculated as a difference ($100-R-T$) is realistic. Since the sphere at the disposal of this project was 2 inches of size, it was not equipped with an internal sample holder²², thus the sample is always placed outside the sphere, attached to the entrance port (Figure 4.38). Two integrating spheres were used for this work: one of them, in collaboration with the FZ-Julich research institute, was connected to a spectrometer covering a very wide range of wavelength (300-2200 nm). The other one, available at Optical Microsensors & Micromaterials group of DTU Fotonik, could be connected to either a visible range spectrometer (450-950 nm) or a NIR spectrometer (1000-2000 nm). Thus, measured and presented here spectra are covering different range of wavelengths depending on the availability of some of the instruments.

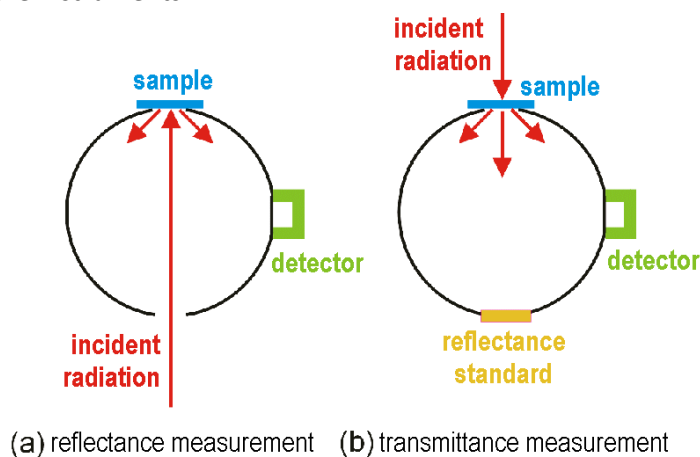


Figure 4.38: Illustration of the working principle of the integrating sphere, used for the next R/T measurements shown in this thesis.

We are here mostly interested in the NIR range up to the limit given by the Schottky barrier height between the metal of the particle (Ti/Au or Ag) and the semiconductor (GaAs or a-Si:H)²³, but we will sometimes show also the behavior in the visible range, if the case requires attention. All the measurements shown in this thesis comes from the average of measurements taken on 2-4 spots in different areas of the sample. The NIR spectrometer has a lower detectivity than the visible one, thus some smoothing of the signal has been performed to reduce the noise in the longer wavelength range. When these two spectrometers are combined a small gap between 950 nm and 1050 nm will be noticed.

4.3.2.1 Ordered gold nanoparticles

As first thing, ordered arrays of Ti/Au nanoparticles defined by EBL on GaAs were measured before and after ITO covering and since we were not sure of how titanium would affect the LSP resonance, 3 different samples (A1, A2, A3) were prepared following Table 4.12.

²² The internal sample holder is fabricated only with bigger size integrating sphere (at least 6").

²³ The Schottky barrier height between Ag and n-GaAs is 0.63 eV (i.e. 1968 nm of wavelength) [163].

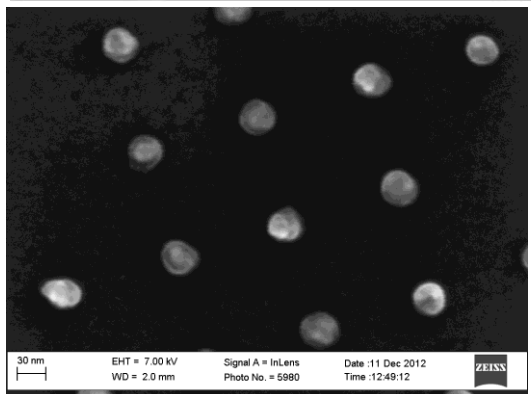
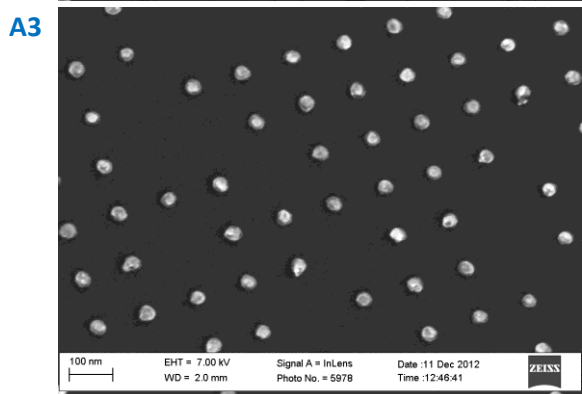
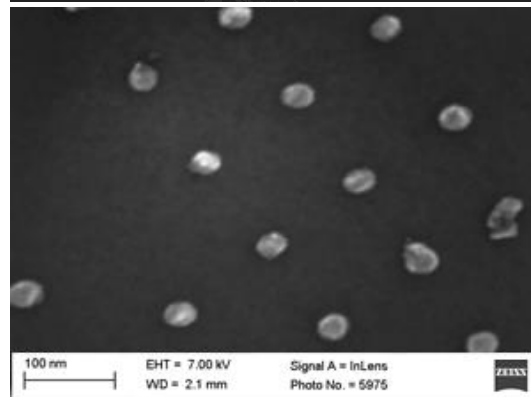
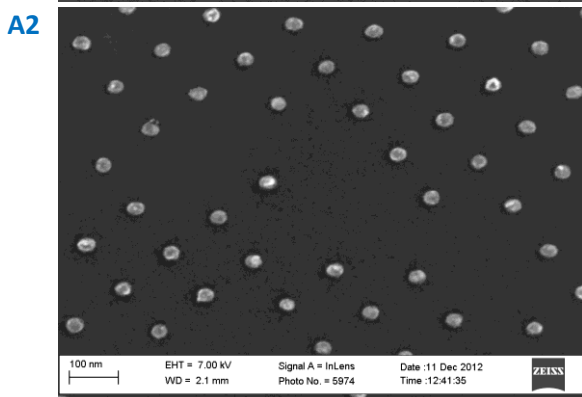
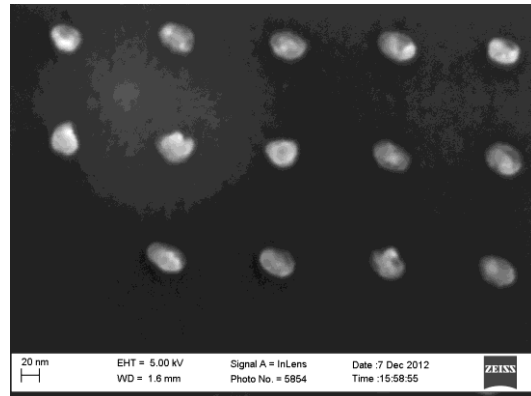
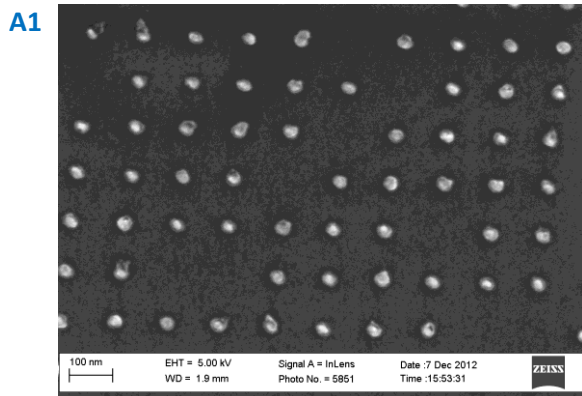
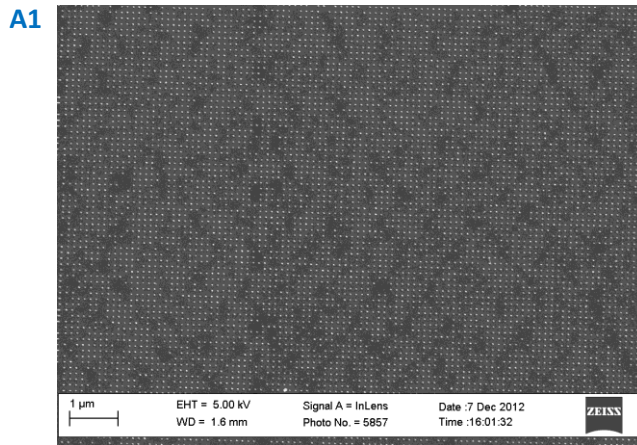


Figure 4.39: SEM images of samples A1, A2 and A3.

In Error! Reference source not found. SEM images of the samples were taken before ITO sputtering and in Figure 4.40 the measured R/T spectra and calculated absorbance are shown.

(on GaAs)	Single shot exposure			Evaporation		SEM
sample	Dose (uC/cm ²)	Beam current	Beam step (periodicity)	Ti (nm)	Au (nm)	Resulted average size
A1	43	1 nA	120 nm	5	10	30 nm ±2 nm
A2				1	10	
A3				1	14	

Table 4.12: Description of the parameters used to prepare samples A1, A2, A3.

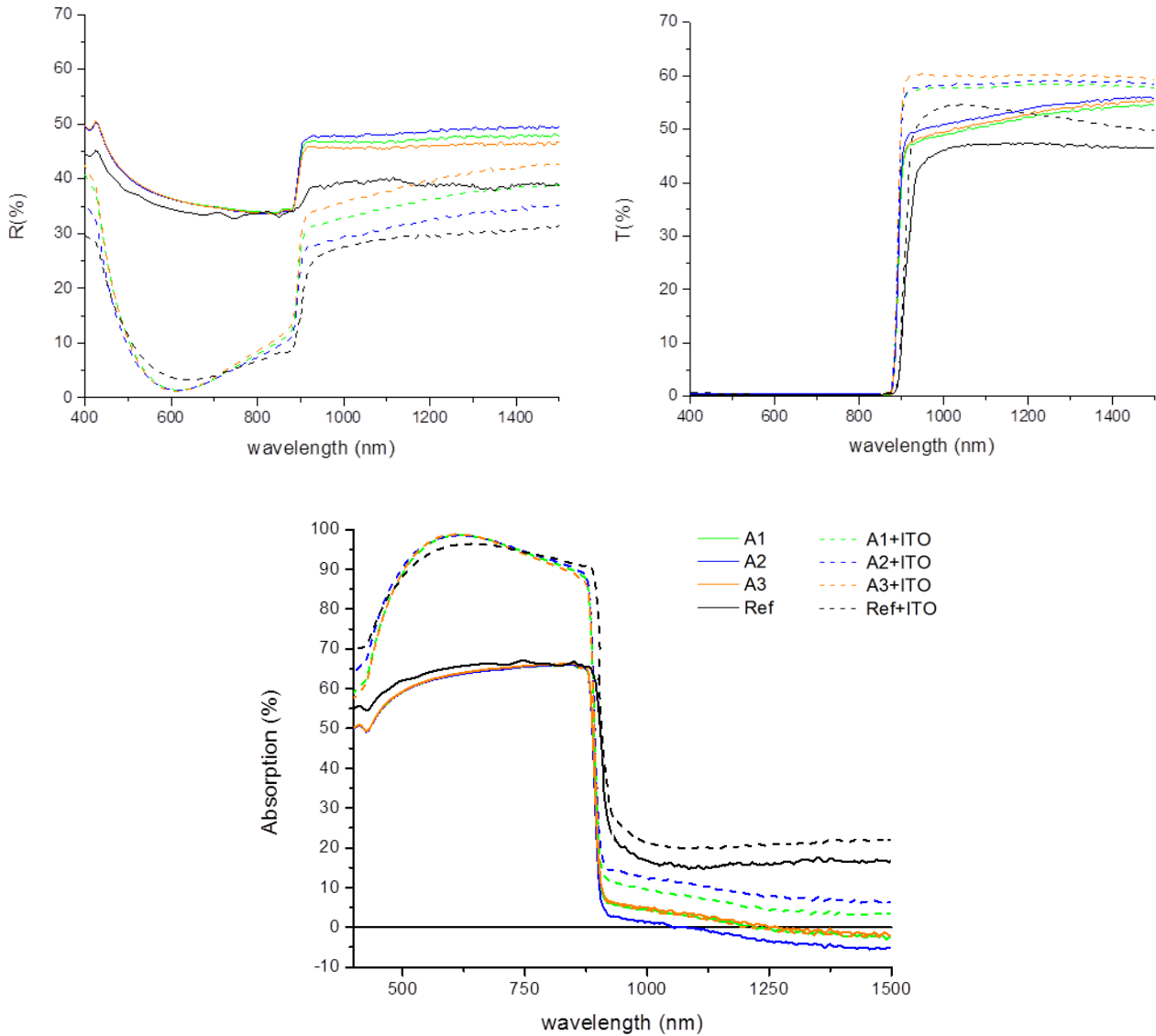


Figure 4.40: Measured R/T spectra and calculated absorbance for samples A1, A2, A3 (arrays in square lattice of Ti/Au NPs).

The calculated absorption spectra shows absorption below zero: these measurements were taken with the setup in Julich, for which in case of small size chips, there is a small uncertainty in sample positioning. This may cause errors in evaluating the actual absolute values of R and T, which seems to be the case here; thus, we can only rely on trends.

Looking at the relative trends, we can notice a very small dip in R around 600 nm for all the arrays covered with ITO, which results in a very small absorbance enhancement (3%); the ITO layer is acting as a very effective antireflection coating.

In order to increase the effect of NPs, sample with thicker Au layer (20 nm, on top of 5 nm Ti) was fabricated. This change was intended to alter the aspect ratio of the nanoparticles and other 3 different samples (Table 4.13) with varying pitch were measured in the NIR range (spectra not shown here), but no absorbance enhancement was noticeable coming from the NPs.

(on GaAs)	Single shot exposure			Evaporation		SEM
sample	Dose (uC/cm ²)	Beam current	Beam step (periodicity)	Ti (nm)	Au (nm)	Resulted average size
A4	60	1 nA	100 nm	5	20	40 nm ±2 nm
A5	43		120 nm			
A6	31		150 nm			

Table 4.13: Description of the parameters used to prepare samples A4, A5, A6.

SEM (Figure 3.7 and Figure 3.8) and AFM measurements (Figure 3.9 and Figure 4.41), showed that size, shape and height are very variable with Ti/Au nanoparticles fabricated by EBL and this might be one reason for the unmeasurable absorbance enhancement.

We can in fact notice, from Figure 3.9, that the profile of sample A4 shows a conical shape (as mentioned in Chapter 3) with a cone height varying from 33 to 44 nm (Figure 4.41). Something went probably wrong during the metal evaporation: the underlying layer of titanium was probably un-uniform as first.

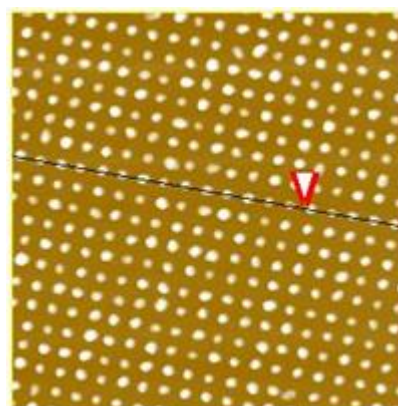
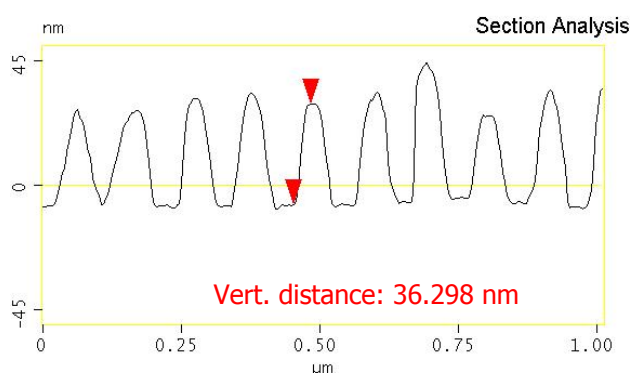


Figure 4.41: Scanned profile of sample A4 with AFM.

4.3.2.2 Silver nanoparticles

Ordered Ag nanoparticles patterns

While Au is an attractive metal due to relatively large absorption cross section compared to the scattering one, Ag is the most commonly studied plasmonic metal, with more promising properties for the purpose of this thesis (Figure 4.1).

We started from fabrication and characterisation of EBL samples with two different periodicities (Table 4.14): 120 nm and 80 nm.

(on GaAs)	Single shot exposure			Evaporation	SEM	Sputtering Of ITO
sample	Dose ($\mu\text{C}/\text{cm}^2$)	Beam current	Beam step (periodicity)	Ag	Resulted average size	
A4	43	1 nA	120 nm	10 nm	38-41 nm	110 nm
B4	82		80 nm		25-28 nm	

Table 4.14: Specifics of the fabricated samples A4 and B4 consisting in Ag NPs arrays on GaAs, then covered with ITO.

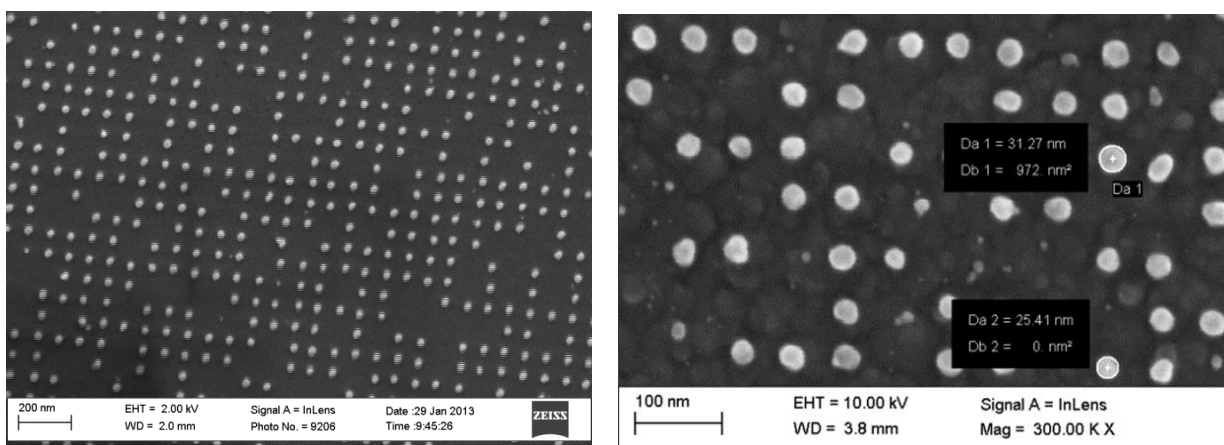


Figure 4.42: **left)** SEM image of sample B4 (see details in Table 4.14). **right)** SEM image of sample C2 (see details in Table 4.16).

The measurements (Figure 4.43) were taken after covering the NPs with ITO. There is a gap between the visible and the IR range due to the use of the different spectrometers, showing a relative constant offset in all the spectra.

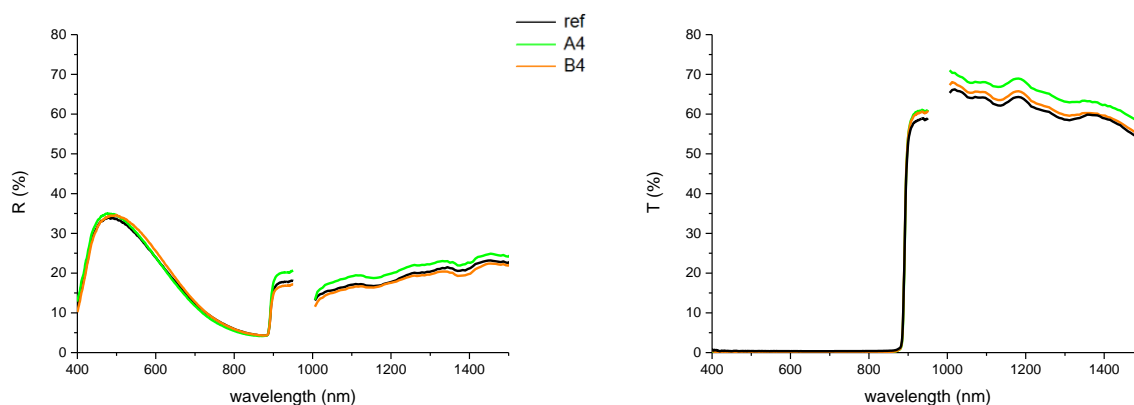


Figure 4.43: Reflectance and transmittance measurements with integrating sphere of samples A4 and B4 (Table 4.14).

The denser array of Ag NPs (sample B4) works better in terms of reflectance in the NIR range. The calculated absorbance spectra are shown in Figure 4.44: these nanoparticles do not seem to absorb anything in the NIR range but, subtracting the reference absorbance (dA) we can see a very weak enhancement (1%) in the visible range for sample A4 (with 120 nm of periodicity).

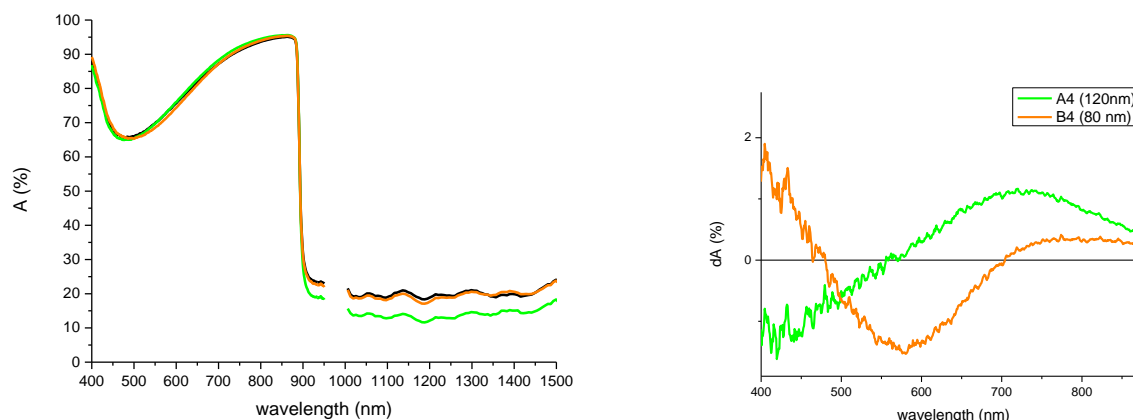


Figure 4.44: Absorbance spectra (**left**) and their difference relative to the reference (**right**) of samples A4 and B4 (Table 4.14).

The following step was again the increase of the thickness, up to 27 nm, (Table 4.15) with array pitch of 100 nm but two different range of NPs size, to be compared with samples characterized by same size and pitch but thickness of 15 nm.

(on GaAs)	Evaporation	SEM	Array pitch (nm)	ITO sputtering
sample	Ag thickness (nm)	Resulted average size		
s11h15	15	24-28 nm	100	NO coating
s11h27	27	24-28 nm		
s18h15	15	30-34 nm		
s18h27	27	30-34 nm		

Table 4.15: Specifics about samples with Ag NPs arrays to compare thickness.

This set of samples was measured only before ITO coating²⁴ and relative R/T/A spectra are shown in Figure 4.45. In the NIR spectral range none of the samples show absorption enhancement, but in the visible range it is noticeable a peak varying between 500 and 600 nm of wavelength due to suppression in reflectance. Moreover for both of the thicknesses one can see that the peak in the visible redshifts with increasing the NPs size. These two features would identify the peak as due to scattering. Comparing thickness no clear trend is found: for small NPs size the LSP resonance in the visible appears at the same frequency but higher intensity characterizes smaller NPs size; for larger NPs size, higher thickness shows a higher peak (slightly blueshifted) and broader absorbance enhancement covering the whole measured visible range.

It was thus decided to choose 27-30 nm as constant NPs thickness for future samples and devices.

²⁴ During the ITO sputtering of these samples something went wrong and the deposited layer was really un-uniform and opaque; a post-annealing treatment has been tried but the layer was still of really bad quality making the following characterization meaningless.

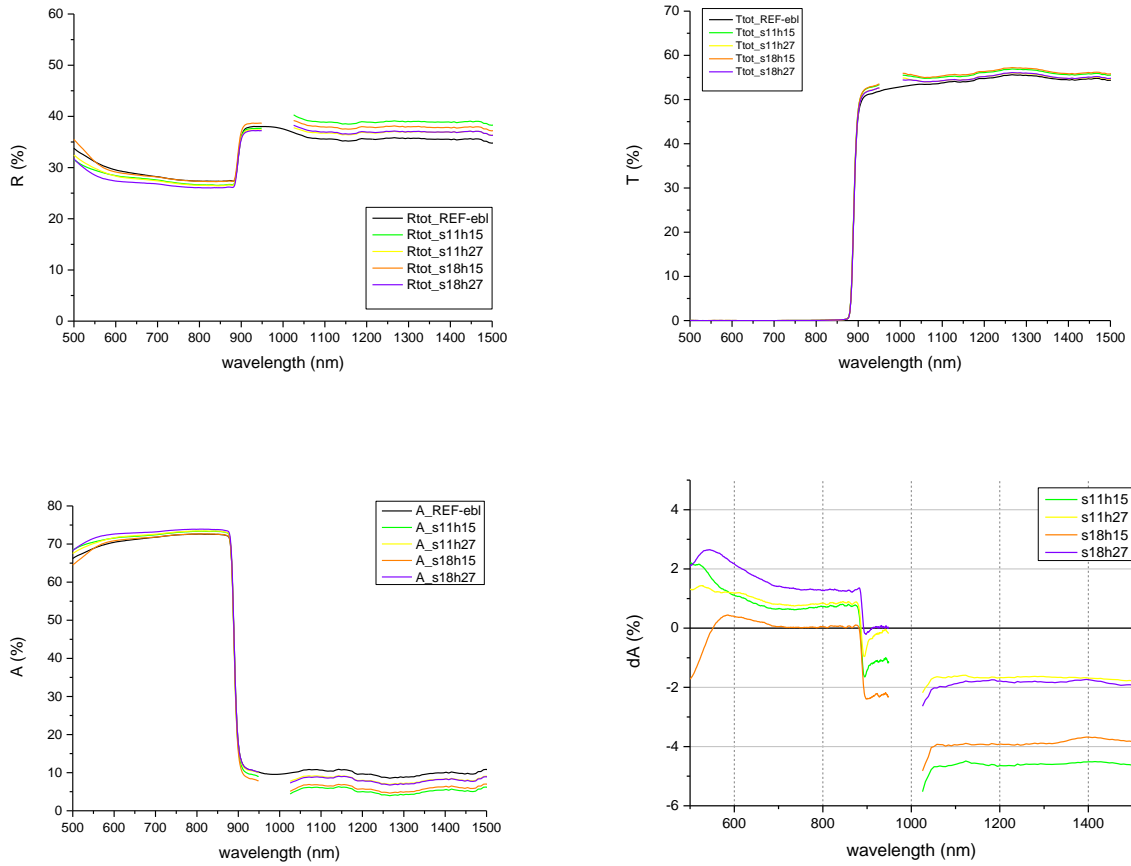


Figure 4.45: Measured R/T spectra of Ag NPs arrays defined in Table 4.15.

Next set of samples was fabricated on top of the entire substrate stack used for a-Si:H solar cells (Si/Ag/AZO/Cr), therefore the optical characterization is limited to “reflectance” measurements²⁵ (here labelled as R_{meas}). With this we mean that what we actually measured is given by:

$$R_{meas} = (1 - R)^2(1 - A)^2 + R \quad (4.1)$$

where it is assumed that the bottom contact, acting as a mirror, would be characterized by $R_{bottom}=1$ (see Figure 4.46).

These samples are described in Table 4.16 and, after SEM analysis (see sample C2 in Figure 4.42-right), the samples were fully processed into a-Si:H solar cells, whose electrical properties are shown in Section 6.3. This means that, before optical measurements, they have been covered with amorphous silicon thin absorber layer (i/n) and then again another layer of AZO on top to make the Schottky junction (Figure 3.24).

²⁵ The silver layer within the stack (part of the bottom contact together with AZO) is about 200 nm and it kills the whole transmitted signal, thus transmission could not be measured but, since we have a mirror, it can be assumed as 0.

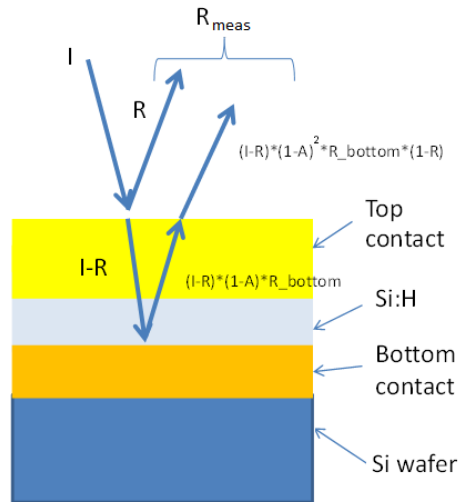


Figure 4.46: Schematic representation of the R measurements performed on a-Si:H cells.

For a-Si:H	Single shot exposure			Evaporation	SEM
sample	Dose (uC/cm ²)	Beam current (nA)	Beam step, nm (periodicity)	Ag thickness	Resulted average size (nm)
C2	172	0.5	60	30 nm	25-31
D1	79	1	80		20
D2	117	2	80		27
E1	58	1	100		20
E2	93	8	100		30
E3	117	8	100		34

Table 4.16: Specifics of the fabricated arrays of Ag NPs with varying size and pitch on Si/Ag/AZO/Cr substrate (then incorporated in a-Si:H solar cells).

From the spectra of R_{meas} in Figure 4.47, we can clearly see that in 4 out of the 6 cells the nanoparticles arrays act as scatterers re-directing light inside the active absorber (thin a-Si:H) and thus increasing light trapping, but this can be true only till the gap edge of the semiconductor (770 nm), while in this case we can notice a difference between the spectra (NPs patterned sample VS flat reference) also below the gap. For cell D1 and E1 the effect is not very evident but still the reflectance of the sample with the nanoparticles is smaller than the reference sample.

Subtracting the reference reflectance from the spectrum with the pattern we can highlight the absolute effect of the silver nanoparticles and in particular see the LSP resonance, identified by 3 dips in ΔR (Figure 4.48): (i) around 450 nm, ii) 560 nm and iii) 740 nm). The plasmonic effect begins to be significant for particle size of 27 nm and it increases with increasing the size.

From the panels in Figure 4.48, we can see that dip i) and iii) show similar features: the pitch affects the intensity and the width of the dip (the denser, the deeper and larger) but not the LSP frequency (panel A), and this follows the absorption model [24]. On the other hand, dip ii) maintains constant intensity and width, for different pitches, but varies its position (panel A). Moreover, dip ii) clearly shows a redshift of the

LSP resonance due to the increasing of the NPs size (panels B and C). These two features are typical of the scattering. We thus have both effects combined together working at different frequencies enhancing the absorption of the solar cell. This means that we do not have NPs characterized by a dominant regime (Figure 4.1).

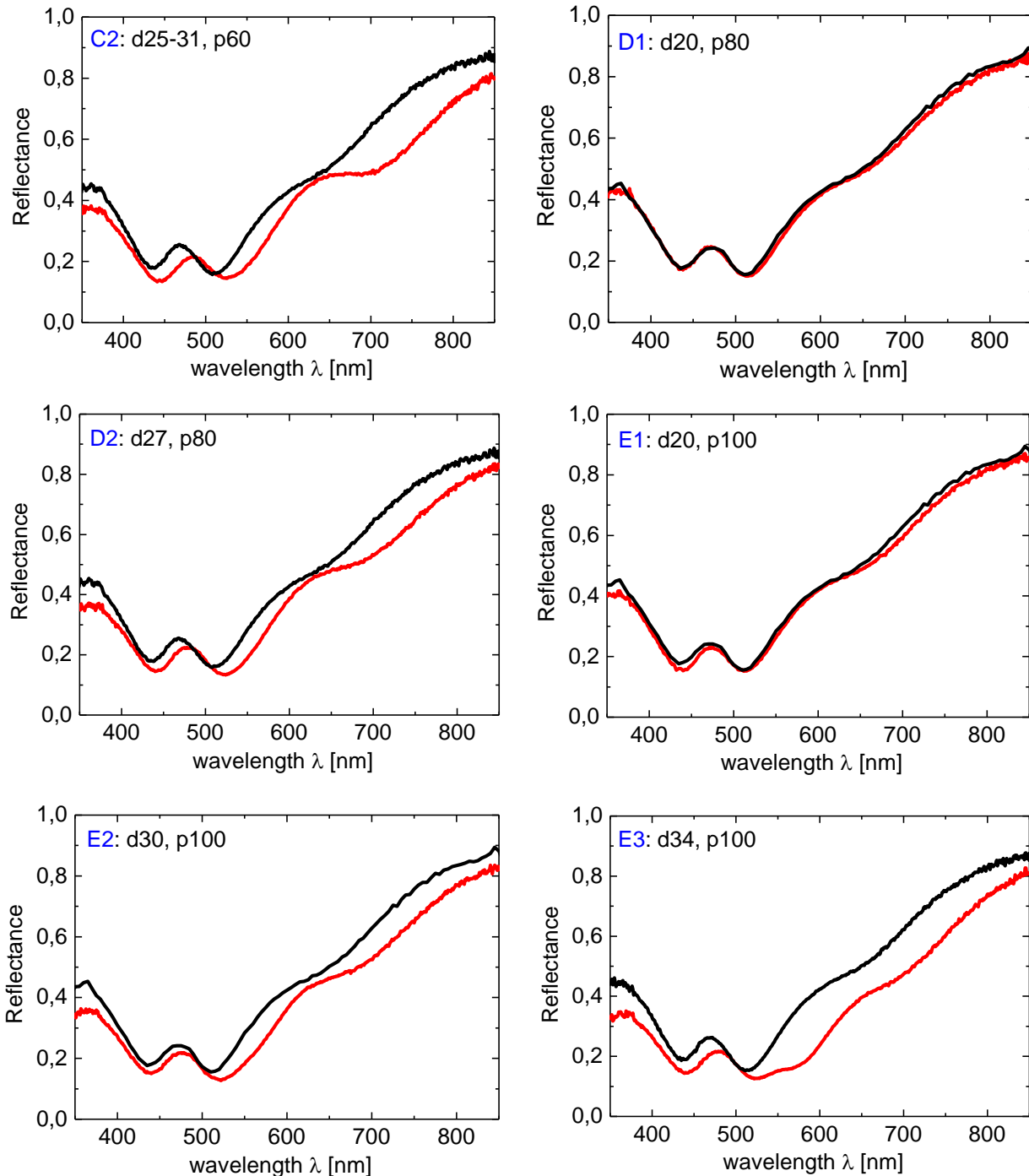


Figure 4.47: “Reflectance” measurements (R_{meas}) on a-Si:H solar cell substrates (with AZO coating on top). Red line indicates the substrate with the NPs and black line only flat substrate, as reference.

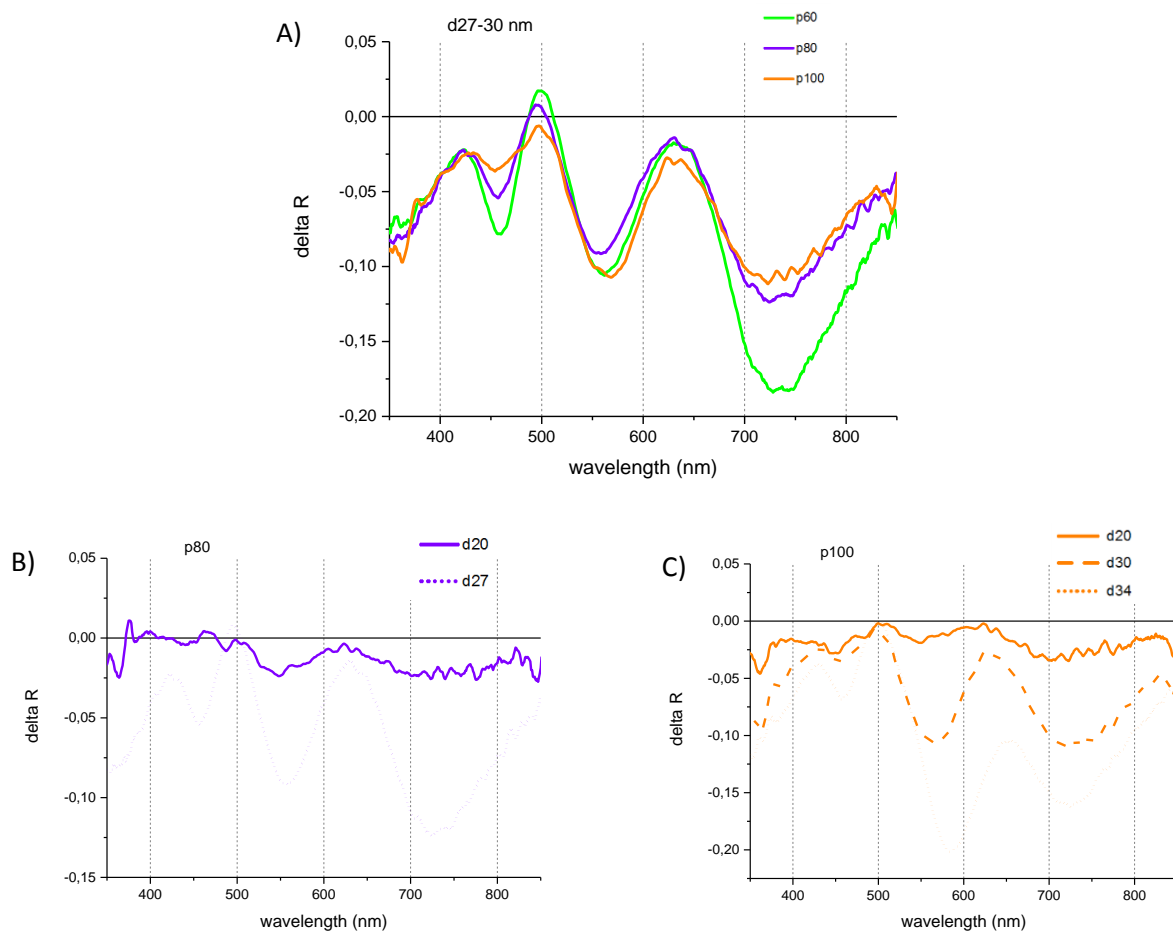


Figure 4.48: Delta-“reflectance” measurements (ΔR_{meas}) calculated by difference between measured spectra of samples with Ag NPs and without. These samples are fabricated on a-Si:H solar cell substrates and then covered with AZO. Panel **A** shows the LSPR dependence on pitch array for fixed NPs size; panel **B** and **C** show LSPR dependence on NPs size for fixed array pitch.

In this kind of measurements, there is no need of transmittance to judge the absorbance of the a-Si:H layer, since, assuming the bottom contact as a mirror, what we have measured here is in fact everything but absorbed (see Figure 4.46 and Equation 4.1). Thus, we can state that this dip in R_{meas} corresponds to peaks in absorbance.

In particular dip (iii) is very interesting for our purpose: the tail of the peak in absorbance, which might results from the tail of the dip shown here, is falling below the gap of the semiconductor and the energy of these photons can be used to excite the LSPs, resulting in consequent emission of hot electrons [71], [123]. We cannot see here for dip (iii) a dependence of the LSP frequency on the size of the particles (panel C in Figure 4.48) but both our model and the literature can confirm that there is a possibility to adjust the size to tune the corresponding LSP resonance in order to move it to even longer wavelengths.

Results of electrical characterisation, confirming our hypothesis, are discussed in Chapter 6.3.

Comparing these set of samples with previous one (Table 4.15), the common factor is the LSP resonance here indicated by (ii): from dA-spectra in Figure 4.45, one can see the same behaviour nicely represented

by panel C in Figure 4.48. In the previous set, LSP resonances (i) and (ii) were not found probably because of the missing TCO coating on top.

Random Ag nanoparticles patterns

As already mentioned, a second technology for the fabrication of silver NPs has been introduced after EBL: the electroless plating, which gives random distribution of particles, both in size and placement. The optically measured samples, have been fabricated following the optimum recipes developed as discussed in Section 4.3. Since it has been shown that the electroless plating can give different results for different surfaces (not only in terms of material), each sample under study is characterised with SEM and SEM images will accompany the optical measurements throughout this section.

One of the first attempts made by electroless plating and then assessed optically before and after ITO coating, is shown in Figure 4.49 (labelled as I for simplicity): it is characterized by quite big crystals (150 nm) in a very dense pattern (FF=48%).

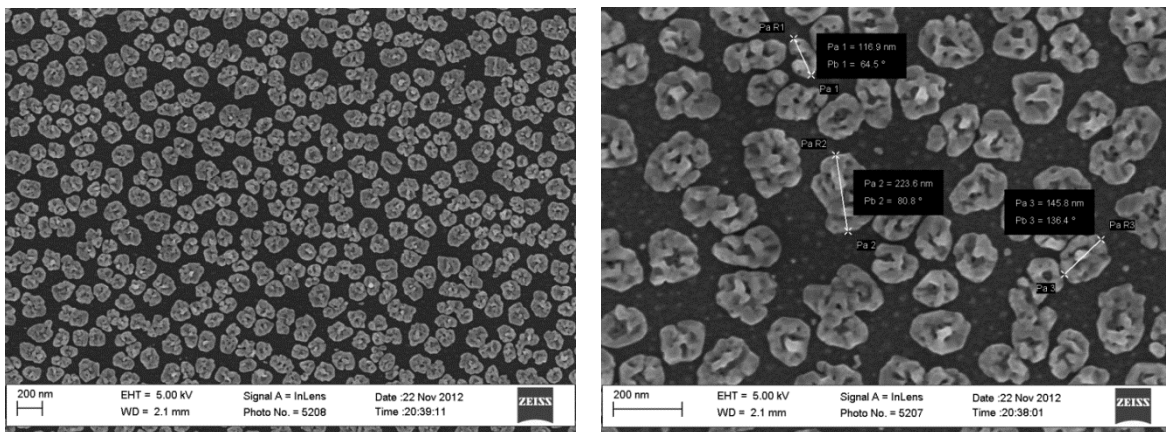


Figure 4.49: SEM images of sample I.

In Figure 4.50a-b we can see the relative R/T measurements. Introduction of NPs on the surface of GaAs leads to a broad increase of reflectance in the NIR range centred around 1350 nm. Following the ITO deposition on the surface, the reflection of both bare and NPs coated samples change. The ITO layer acts as antireflection coating reducing reflection in the whole range of wavelengths. The low energy photons (absorbed for a 20% by the substrate below the gap) are not re-directed and transmitted through the whole substrate being lost, in fact from the T spectra it is visible that only the NPs are playing to enhance absorbance, being responsible of the suppression in transmittance noticeable from the gap edge to really long wavelengths and centred around 1550 nm.

As result, in the absorbance spectra (Figure 4.50c) we see an enhancement only due to the NPs, starting from 1200 nm of wavelength, reaching about the 8% around 1700 nm. The change of the surrounding (by ITO coating) bluishifts the broad absorbance peak of about 400 nm, making it potentially useful for hot electrons photoemission in the NIR range (where the solar radiation is still significative). It must be noticed, though, that above the gap presence of the NPs causes reduction of photon absorption of -20% of the light

at 500 nm. Since it is most likely a combined effect of ITO and NPs it may be possible to reduce this effect by improvements of ITO coating.

Finally, in Figure 4.50d, “delta-absorbance” spectra are calculated as follows:

-  Abs(GaAs/NPs) - Abs(GaAs) (blue solid line)
-  Abs(GaAs/NPs/ITO) – Abs(GaAs/ITO) (blue dots line)

useful to visualize the net effect of the NPs presence, and:

-  Abs(GaAs/ITO) – Abs(GaAs) (violet solid line)
-  Abs(GaAs/NPs/ITO) – Abs(GaAs/NPs) (violet dash line)

in order to see the net effect of ITO coating.

It is clear that the combination of the nanoparticles together with ITO is giving the most intense effect, without losing any photons all over the entire range of wavelengths.

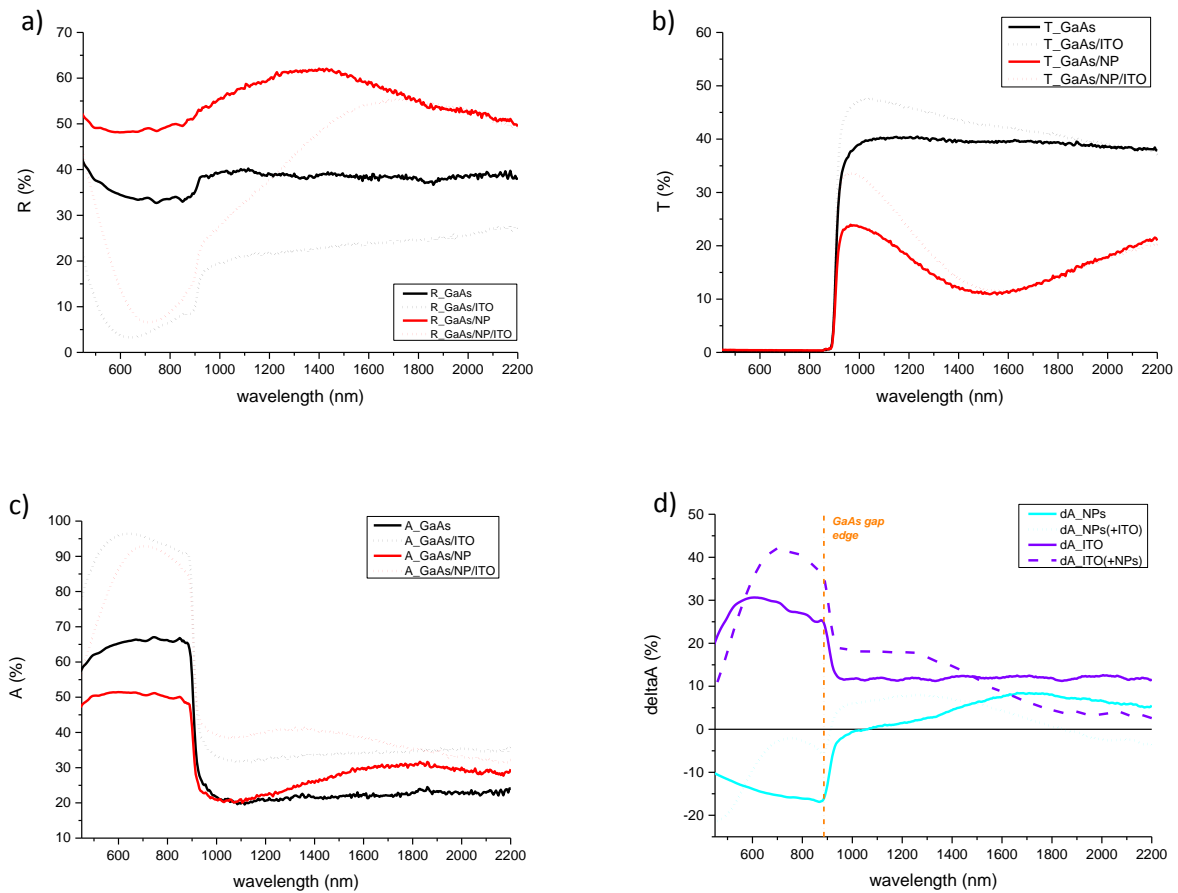


Figure 4.50: R/T measured spectra and relative calculated absorbance of sample I and its reference (substrate without NPs), before and after ITO covering.

Considering here the dip in transmission as the main sign of potential absorbance enhancement, during the optimization of a recipe the samples were investigated by SEM and measured in transmittance straight after the electroless process (thus without ITO cover).

In

Figure 4.51, a representation of the deposition development method (varying the recipe) is given through the transmission measurements taken on a sequence of samples with silicon nitride layer: sample #22 and sample-TEM show potential absorbance enhancement; thus, they would have been subsequently measured also in reflectance and the respective NPs would have eventually been incorporated into solar

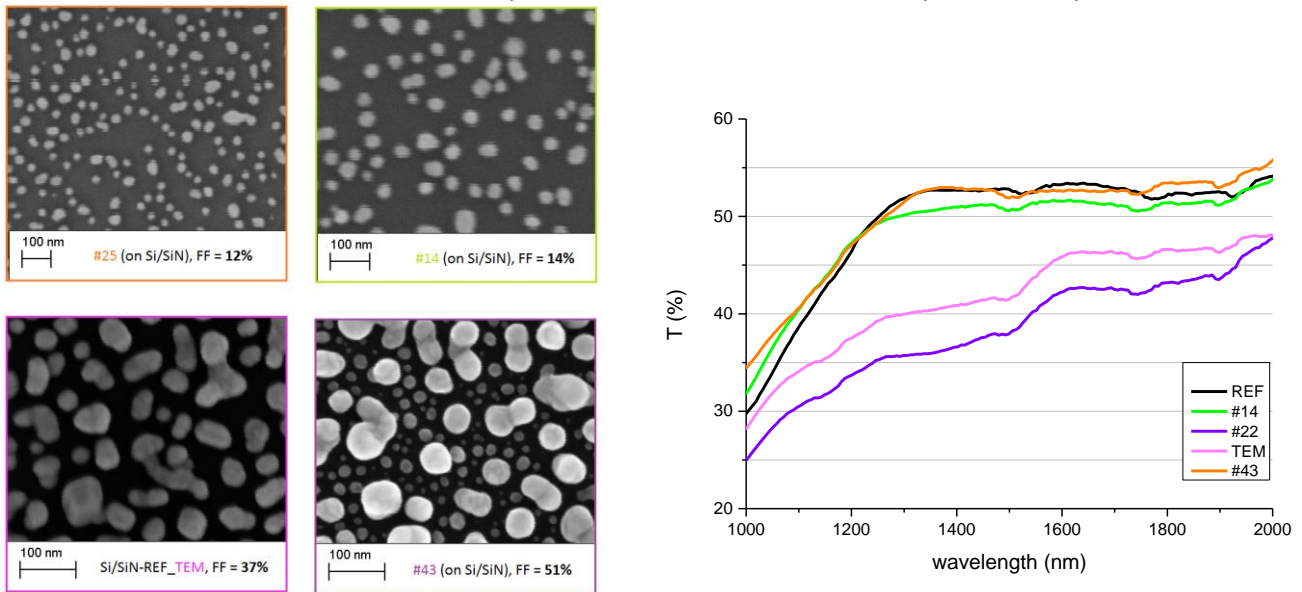


Figure 4.51: SEM images of different samples and relative measured T spectra. The samples were prepared by electroless on top of Silicon/Si₃N₄ substrates and they were measured without being covered with ITO.

In particular, it is here shown also the sample submitted, simultaneously, to the same electroless process during the preparation of the deposition on the TEM membranes (Table 4.11). This is a small silicon chip with the same silicon nitride layer deposited on top; the result is not exactly the same as what we found on the TEM membranes but similar and its T spectrum shows a nice suppression which can correspond to increase in absorbance (as previously explained).

The filling fraction has been chosen as the parameter to consider for defining a threshold between potentially working samples and not. From the experience, it has been deduced that FF bigger than 15% are expected to give absorbance enhancement in the NIR region of at least 5%. This is only an estimate, since with increasing the FF during electroless, also the size of the NPs tend to increase, thus a real dependence on the surface coverage independently from the size, was difficult to be drawn.

We show now in Figure 4.52 the NPs which have been incorporated into GaAs diodes #1 and #4.

²⁶ This is meant to give a description of the modus operandi.

The geometry of the diodes is indicated in the illustration of Figure 4.53, together with the relative optical characterization: again, the transmission suppression is causing absorption enhancement in the NIR range. It is also interesting to notice that in diode #4, reflectance is lower than in diode #1 due to the presence of Si_3N_4 layer and this results in higher absorption enhancement.

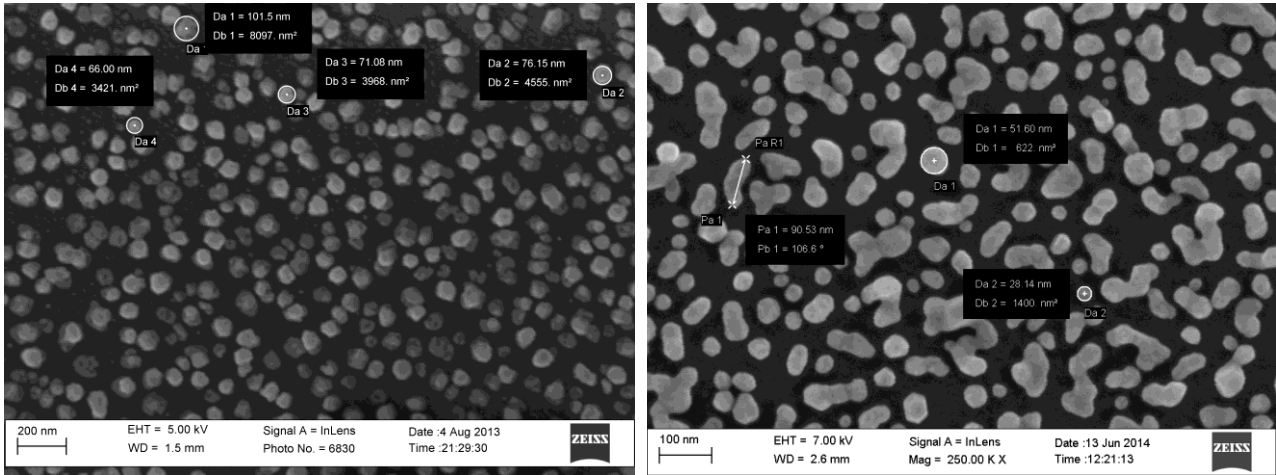


Figure 4.52: SEM images of Ag NPs deposited by electroless plating within fabricated and measured Schottky diodes: #1 on the left and #3 on the right.

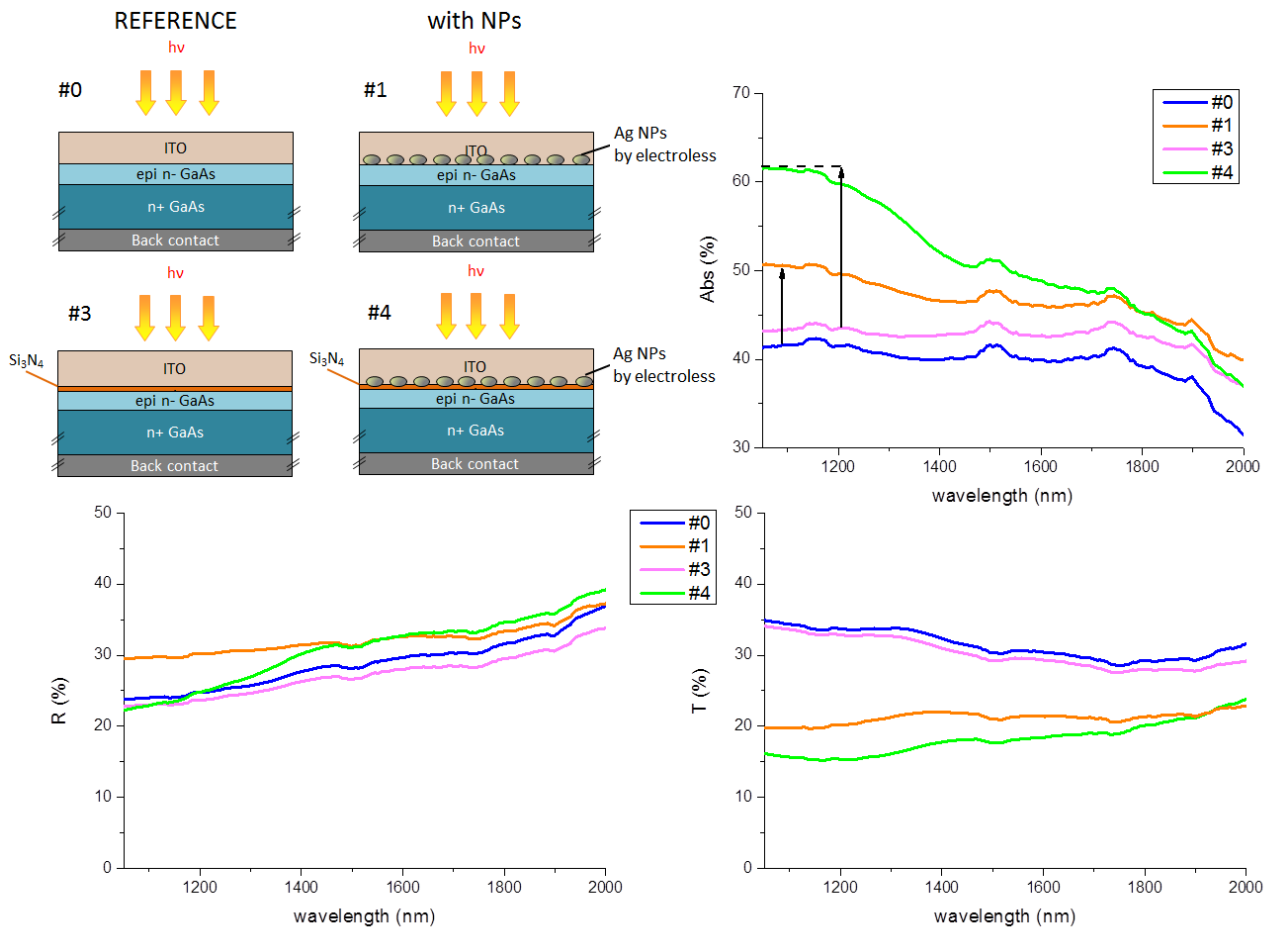


Figure 4.53: Illustration of the main electroless-diodes fabricated in this thesis and relative R/T measurements. Absorbance spectra are consequently calculated by difference.

Another aspect to be considered was the effect of the ITO covering. While we already showed that it works well in red-shifting the resonance, we should also consider that, within the fabrication process straight after the ITO sputtering and lift off, an annealing treatment is necessary in order to make the layer more transparent and conductive (see Section 3.1.2). Therefore, we investigated the effect of the annealing on the absorbance of the structure with incorporated NPs.

Three different thicknesses of the ITO layer were considered (here labelled with the corresponding sputtering time in seconds) and R and T values for the whole structure were measured before and after the annealing treatment for wavelength longer than 1000 nm. Resulting absorbance spectra are shown in Figure 4.54. Increasing the thickness reduces both transmittance and reflectance (not shown here) resulting in increased absorbance. This is true both before and after annealing treatment, with and without nanoparticles. It is important to notice, though, that the annealing can decrease the absorption effectiveness of the NPs at short wavelengths (within the NIR considered range). As optimum ITO layer thickness, 110 nm (corresponding to what is here labelled as 2700s) was chosen.

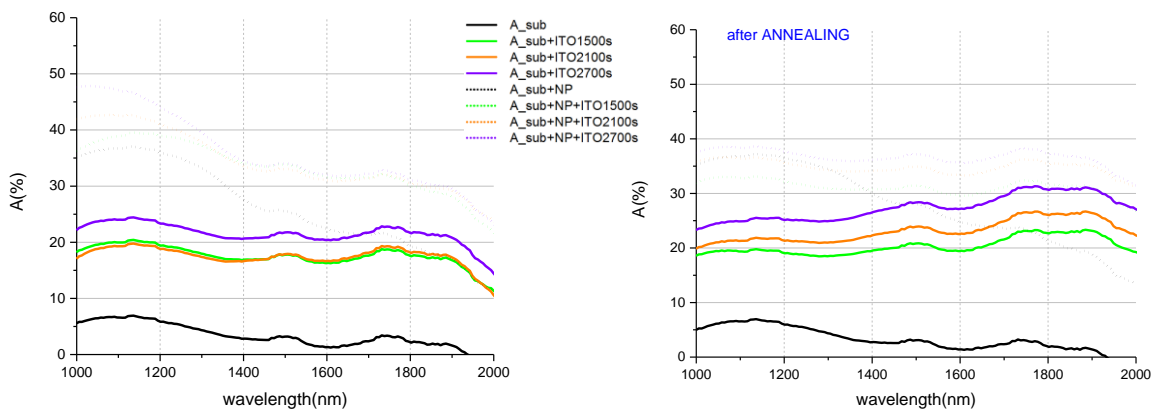


Figure 4.54: Absorbance spectra of GaAs/Ag NPs/ITO samples with varying ITO thickness before and after annealing treatment.

In order to better understand the nature of the absorbance enhancement, a variety of samples with electroless plating (on different substrates: undoped and doped GaAs) with different average size, shape of the NPs and FF has been optically characterized in the NIR, after being covered with ITO: their absorbance spectra show enhancement up to 40% and very similar trend for size ranging between 50 nm and 200 nm, with more or less broad distribution size and with or without small dots. Their trend is well represented by the few absorption spectra selected to be shown here in

Figure 4.55: we can see several curves deriving from measurements performed on electroless NPs deposited on top of both undoped and n-doped GaAs. The parameters of the samples are described in Table 4.6b-c: the different samples are characterized by nanoparticles with similar size range and no clear trend in dependence of the surface coverage of silver (the filling fraction FF) is defined, probably because of non-homogenous (in both size and filling fraction distribution) samples. Nevertheless, it is important to notice that about 60% of absorbance is reached regardless the substrate doping: this excludes the

possibility that the absorbance of the small IR photons is only due to the Rayleigh scattering of the photons absorbed by the bulk of the semiconductor (20% for undoped GaAs and 30% for doped GaAs).

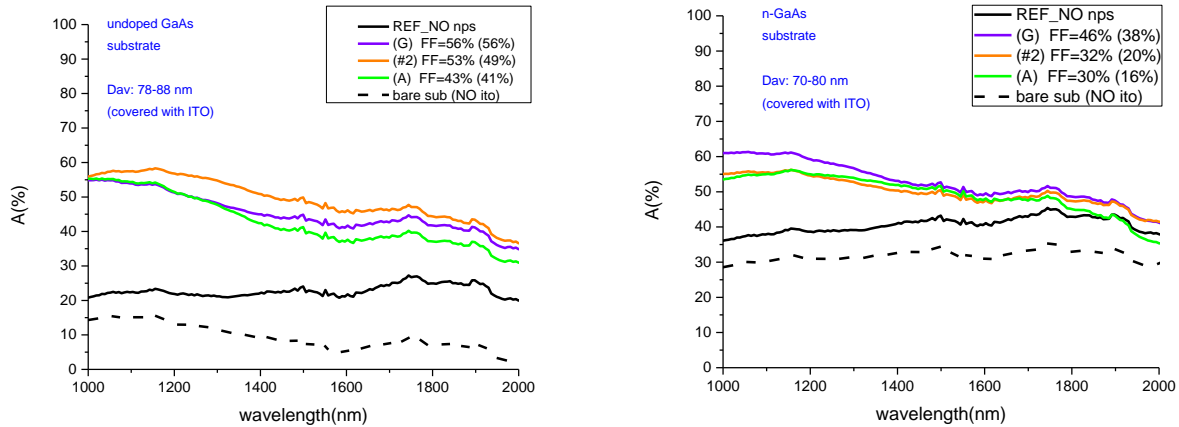


Figure 4.55: Absorbance spectra calculated by R/T measurements of different GaAs/Ag NPs/ITO samples.

Ordered VS Random

The investigation on the nature of the absorbance enhancement in the electroless-samples continued through a comparison between ordered and random Ag patterns. A representative electroless sample giving absorbance enhancement of 20% was chosen; it is characterized by nanoparticles size ranging between 60 nm and 110 nm with a filling fraction ranging between 19% and 24% (Figure 4.56-left).

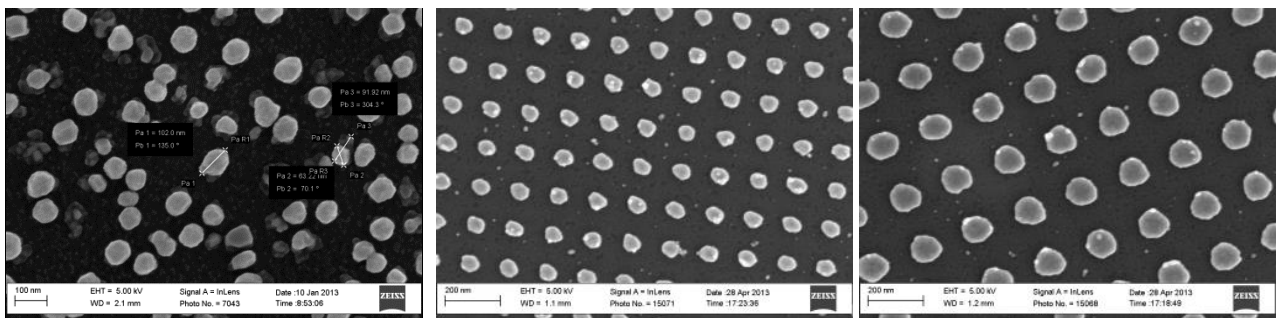


Figure 4.56: SEM images of: **left)** *random*-sample (with Ag NPs deposited by electroless plating); **centre)** ordered sample with array periodicity of 140 nm and NPs size of 65 nm (by EBL); **right)** ordered sample with array periodicity of 200 nm and NPs size of 105 nm (by EBL). These 3 samples were fabricated and optically measured for the comparison random/ordered.

Two samples were then prepared depositing ordered patterns of Ag NPs by EBL (Figure 4.56-centre/right): the first with periodicity of 140 nm and particle size of about 65 nm giving a filling fraction of 19%; the second with 200 nm as periodicity and NP average size of 105 nm. These parameters are considered quite equivalent to those of the electroless sample. The R/T measurements of the 3 samples (performed after being covered with ITO) are shown in Figure 4.57.

The main difference is noticeable in transmittance: the *random* pattern gives a huge suppression while, between the order ones, only sample *p200* shows a reasonable dip. Sample *p140* is behaving very similarly to the reference (flat substrate), beside an increase in reflectance in the short wavelengths. Analysing the

other two samples in reflectance we can notice that the *random* pattern reflects more than the reference for long wavelength, while the order *p200* pattern is reflecting more all over the spectrum range. Between 700 nm and 1000 nm, the *random* sample is actually reflecting less than the reference.

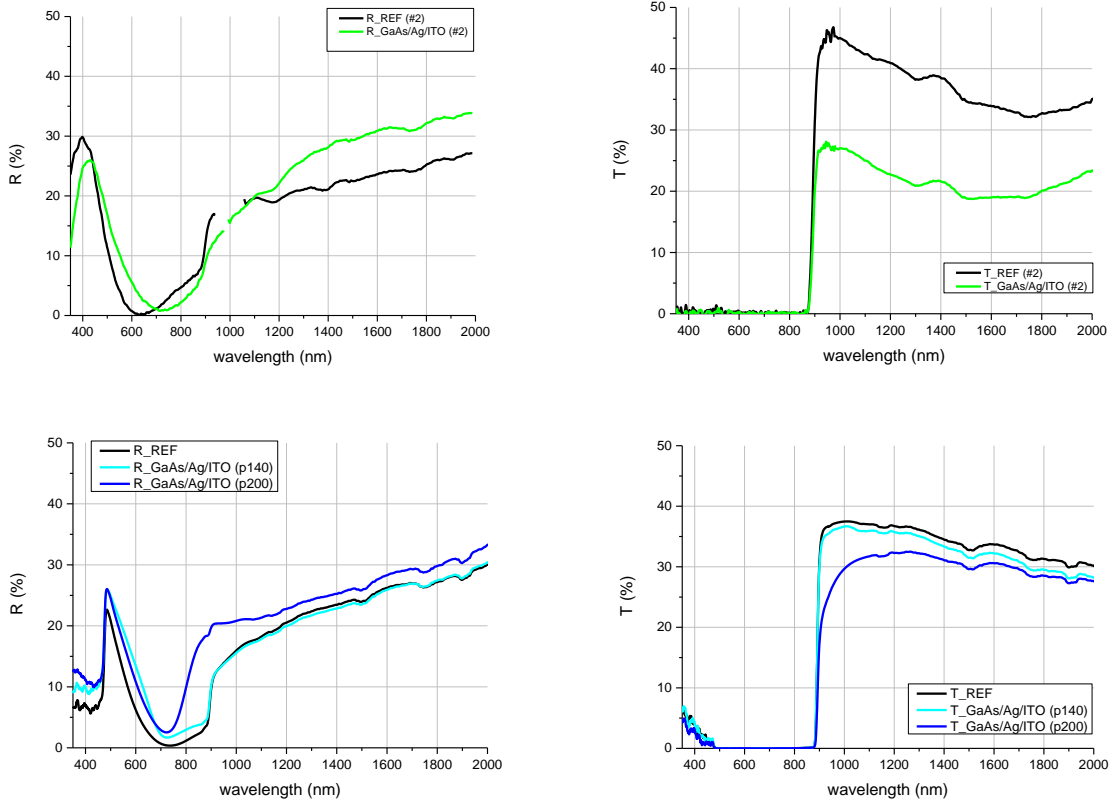


Figure 4.57: R/T measurements of random (green) and ordered (blue and light blue) Ag NPs distributions (on GaAs and covered by ITO) with similar average size and filling fraction.

Respective calculated spectra and the difference between absorption of the pattern with NPs and the one without (dA), are shown in **Error! Reference source not found.:** we can see a huge (up to 25%) enhancement in absorbance for the *random* sample in the whole IR range and also in some parts of the visible spectral range; we then notice a hint of absorbance enhancement in *p140* below the GaAs gap and a small peak reaching 5% of increase in *p200* around 900 nm of wavelength. Above the gap the 3 samples have in common a dip in dA close to 600 nm; on the other hand, around 800 nm ordered samples show another dip while the random one gives a broad small peak.

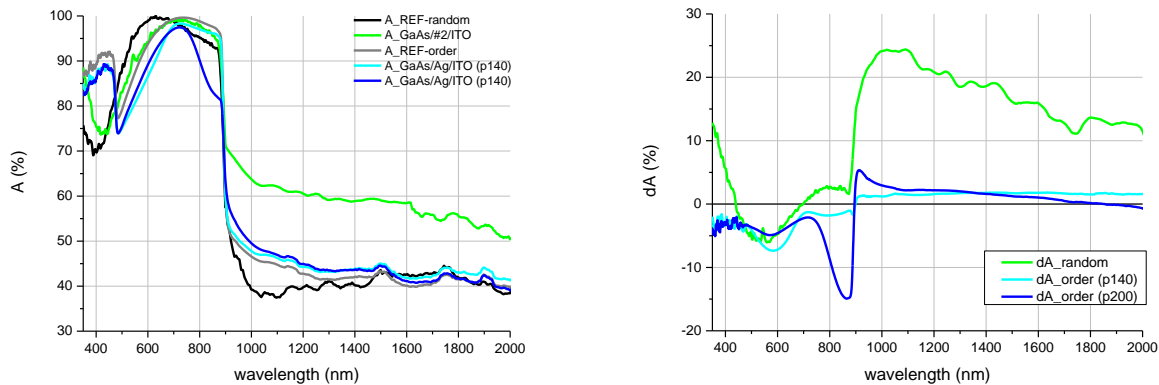


Figure 4.58: **left**) Absorbance spectra calculated from R/T measurements for random (green) and ordered (blue and light blue) Ag NPs distributions (on GaAs) and covered by ITO) with similar average size and filling fraction. **right**) Delta-absorbance spectra are calculated by difference between patterned sample and flat reference.

A variety of metal nanoparticles on GaAs and a-Si:H have been studied. It has been found that only Ag nanoparticles have measurable photon absorption while no effect was seen with Ti/Au nanoparticles. SEM and AFM measurements showed that size, shape and height are very variable with Ti/Au nanoparticles fabricated by EBL, within the pattern, and this combined with small density of patterns might be a reason for the unmeasurable absorbance enhancement.

The behavior of ordered Ag NPs fabricated by EBL depends on their size, in particular:

- ✚ Small Ag NPs on GaAs without TCO coating show absorbance enhancement in the visible range between 500 and 600 nm of wavelength, for thickness ≥ 15 nm (size range 24-34 nm and array pitch 100 nm), which increases at 27-30 nm of thickness.
- ✚ Small Ag NPs incorporated into a-Si:H solar cell structure (thus with TCO coating) (size range 20-34 nm, thickness 27-30 nm and array pitch 60/80/100 nm) show 3 dips in R_{meas} (which will corresponds to peaks in absorbance): around 450 nm, 560 nm and 740 nm). The plasmonic effect begins to be significant for particle size of 27 nm and it increases with increasing the size. Dip at 560nm originates from scattering, while dips at 450nm and 740nm, are due to NPs absorption. The tail of the peak at 740nm, falls below the gap of the semiconductor (a-Si:H) and the energy of the photons exciting the LSPs, can be translated in consequent emission of hot electrons.
- ✚ Big Ag NPs on GaAs covered with TCO, show a significant dip in transmittance, in the NIR range, only for higher filling fraction (24%) and average size (105 nm), which does not result in significant absorption enhancement due to increased reflectance.

Random Ag NPs arrays fabricated by electroless plating:

- ✚ on GaAs and Si, with filling fraction higher than 15%, show slightly increased reflectance for short wavelengths, but huge suppression in transmittance resulting in a significant absorption enhancement, in the NIR range. The enhancement is increased even more (up to 25%) if the nanostructures are covered by TCO and this effect can be exploit to promote photoemission in PV

devices.

- ✚ on silicon nitride deposited on top of GaAs and Si substrate show reduced reflection over the whole measured spectral range (visible and NIR), which results in a further contribution to absorption.

It is clear from the results that the system of NPs is rather complex. Small changes of NPs size of distribution can lead to marked differences in their behavior. Local dielectric environment (eg. presence of TCO) is equally important in the analysis of absorption by NPs. Processing related variability of these parameters made any quantitative, systematic analysis of the LSP impossible.

5. EELS for Ag nanoparticles

In principle Electron Energy Loss Spectroscopy (EELS) can probe bright and/or dark plasmon modes and higher order modes [124]; this means that, using this technique, we are able to excite with an electron beam at least all the dipolar resonances that we found to be optically active and, thus, we think are the cause of the absorbance enhancement.

Historically, electrons have been essentials to the discovery and investigation of plasmons in metals [125] bulk plasmons are remarkable in a metal, but also surface plasmons play an important role and are the source of interesting phenomena and applications that configure the plasmonics field.

5.1 STEM and Electron Energy Loss Spectroscopy

In order to perform spectroscopy at the smallest possible length scale, electron-based spectroscopies need to be involved.

Transmission electron microscopy (TEM) is an electron microscopy technique, i.e. the “illumination” is provided by an electron beam, driven and focused through electromagnetic lenses and metal apertures in order to be transmitted through a very thin specimen. The electron source consists in field emission guns. The system only allows electrons within a small energy range to pass through, so the electrons in the electron beam will have a well-defined energy. The sample holder is connected to a mechanical arm for holding the specimen and controlling its position. The image is then formed from the transmitted electrons and it is focused, with other lenses, onto an imaging device (fluorescent screen, CCD camera...). These components are assembled into a vertical microscope column (Figure 5.1), which is kept under vacuum.

In particular, a scanning transmission electron microscope (STEM) is a type of TEM that can focus the electron beam into a narrow spot which is scanned over the sample in a raster. This rastering makes the microscope suitable for different kind of analytical mapping, like electron energy loss spectroscopy.

In this thesis, we are interested in finding out about the excitations that small metallic objects (NPs) can sustain. TEMs are the best option for resolving both localized and extended excitations with subnanometer spatial detail and 0.15 eV energy resolution in any type of material [126], [127], [128]. The use of an electron beam instead of freely propagating light gives in fact the possibility to investigate localized excitations (involving wave-vector components of the electromagnetic field that lie outside the light cone), thanks to the evanescent field of the electron. The STEM is very powerful in terms of both the range of energy loss events attainable by it and the high spatial resolution these energy loss events can be mapped.

In EELS, after exposing the object under study to an electron beam with a defined range of energy, the transmitted electrons are collected. There will be a large number of electrons undergoing elastic scattering and forming the so called zero-loss peak and another fraction of electrons undergoing inelastic scattering

and giving us information about the material. The amount of energy lost by these electrons can be measured with a magnetic spectrometer and typical inelastic scattering events in EELS include plasmon excitations, intra and inter band transitions, inner shell ionizations (i.e. core excitations, fundamental to detect the elements composing the investigated object) and Cherenkov radiation²⁷. While losing energy, the scattered electrons also deflect their path and the scattering angle can also be measured to get information about the dispersion relation of different identified excitations [125].

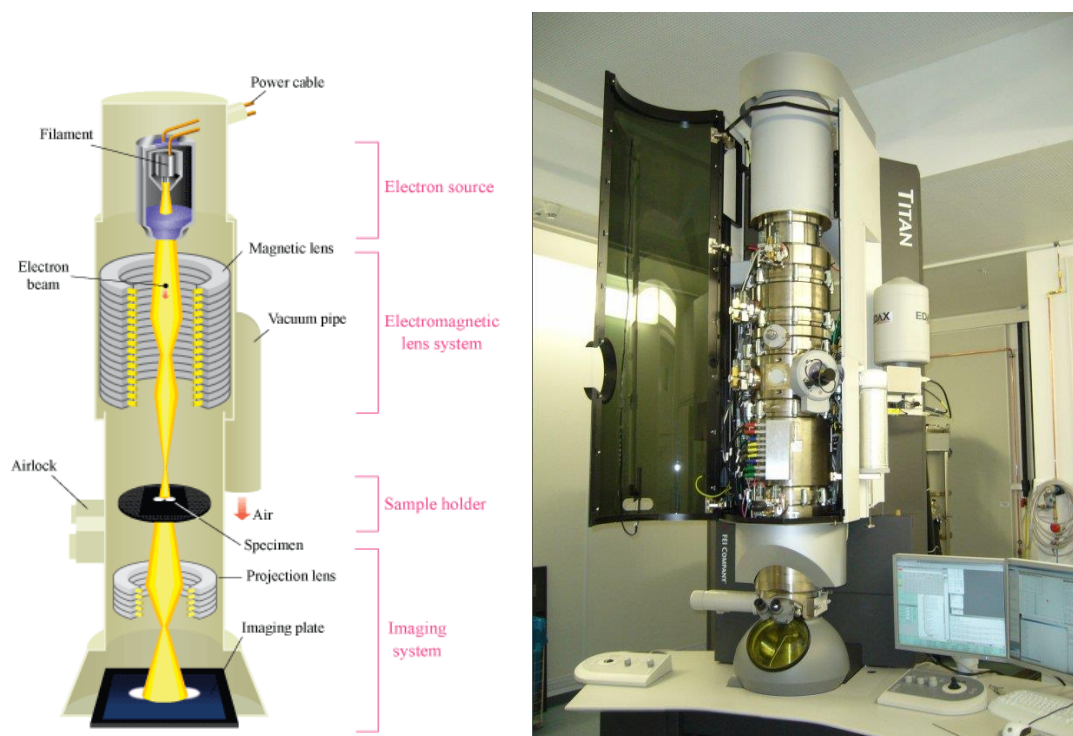


Figure 5.1: On the left, it is shown a schematic outline of a TEM, which contains four parts: electron source, electromagnetic lens system, sample holder, and imaging system. On the right, a real TEM/STEM.

An EELS spectrum (Figure 5.2) consists of different peaks corresponding to the excitations they are caused by: the intensity of the peak (y) is given by the number of electrons which were scattered with a certain energy loss value (x).

The most intense part of the loss spectrum is the one concerning low-energy (<50eV) excitations, by means excitations involving electron and holes in the valence and conduction bands but also collective modes (bulk and surface plasmons).

²⁷ The TEM available for this work could not give the energy resolution to resolve phonons excitations.

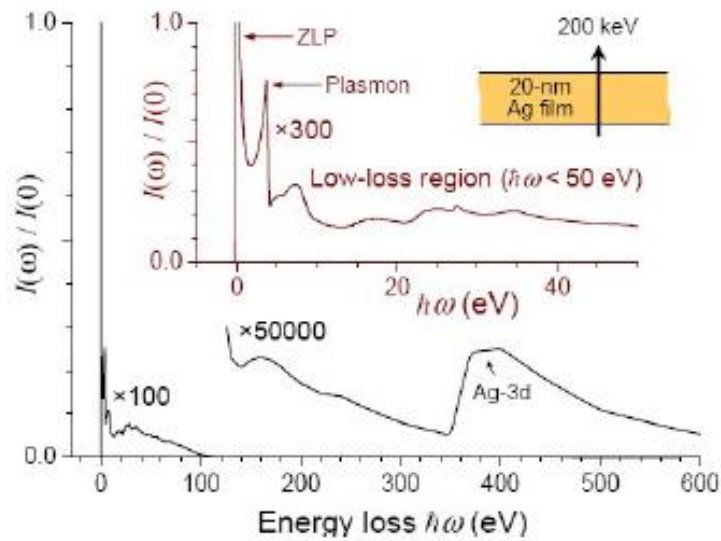


Figure 5.2: Typical electron energy-loss spectrum showing a narrow zero-loss peak (ZLP), collective modes in the valence loss region (e.g., the 3.7 eV plasmon of Ag in the inset), and much weaker core excitations at higher lost energies. The spectrum has been calculated for 200 keV electrons traversing a 20nm Ag film. [129]

5.2 EELS for metallic nanoparticles

In this thesis we are aiming to characterize metallic nanoparticles that are then incorporated into photovoltaic devices because of their plasmonic properties; EELS measurements focused on the role of plasmon dispersion in small spheres can be found in [130].

A small metallic sphere embedded in a dielectric host exhibits plasmon modes at frequencies dictated by the following condition [131]:

$$(l + 1)\varepsilon_1 + l\varepsilon_2 = 0 \quad (5.1)$$

where l indicates the multipolar order of the excitation, ε_1 and ε_2 are the permittivities of the host and the metal, respectively. This has been the “starting point” for different studies establishing the basis for the theoretical understanding of fast-electron interaction with spherical particles [132], leading to formulas which could explain EELS spectra of spheres made of different metals [130], [133], but also corrugated metal surfaces [134].

When the particle is not exactly a sphere we can expect that the EELS spectrum will change due to the variation of the plasmon resonance previously explained in Chapter 2 (depending on the shape, the aspect ratio and the eventual presence of tips).

Furthermore, it needs to be reminded that in noble metal nanoparticles non-local effects are noticeable up to a size of 10-20 nm (at optical frequencies) [130], [135], [136], leading to a blue-shift of the spectrum.

5.3 Dimers: from classic to subnanometer regime plasmon modes

In Section 4.3 we came to the conclusion that a very important role is played by the presence of dimers and elongated particles (appearing in patterns grown by electroless plating), which can make the difference in absorbance enhancement and thus, we suspect, in eventually increasing the photocurrent of the solar cells. In order to investigate more deeply this point it was decided to apply EELS on our random distributed Ag nanoparticles patterns, focusing on these two objects, since individual NPs with aspect ratio close to 1 showed (EBL samples) to be responsible of LSP resonances falling at shorter wavelengths than the range of interest of this thesis, regardless NPs size or array density tested during this project.

Elongated particles are characterized by plasmonic excitations of longer wavelengths than particle with aspect ratio close to 1 [47], [68]; thus, if the absorbance spectra of ordered circular Ag NPs showed LSP resonances in the visible range and in particular also between 700 and 800 nm of wavelength (LSPR (iii) in Figure 4.48), we expect a redshift which moves the resonance within the NIR range. As mentioned in Chapter 2, dimers are characterized by a redshift of the LSP resonance as well.

For a first introduction about the effect of the interaction between neighboring particles we refer to [133].

When it comes to dimers, it is important to know that the interaction between the nanoparticles will lead to a hybridization of the plasmons characteristic of the individual NP [137], [138], [139], [140]. The hybridization of the longitudinal dipole modes will, in particular, give rise to:

- ✚ a “bonding” mode (at lower energy), also called *bright*: the two dipoles of the two NPs are in phase and the resulting mode has a large dipole moment;
- ✚ an “antibonding” mode (at higher energy), also called *dark*: the two dipoles are in this case out of phase and the resulting mode has negligible dipole moment; therefore it cannot be excited by an incident plane wave.

For the hybridization of the transverse dipole modes, it is valid vice versa. [141]

The interaction between more than two non-aligned particles is difficult to explore by analytical techniques. A particularly suitable method that yields highly convergent results, including retardation, consists in expanding the electromagnetic field in terms of multipoles around the particles, and then allowing these multipoles to propagate among particles, thus generating a self-consistent field [142]. Cylinder pairs have been theoretically addressed as well in the non-retarded limit by [143]. This study was later extended to include retardation and to cope with more than two cylinders [144], [145].

What is most appealing for nanophotonics applications (like sensing [146] and SERS [146], [147]), as already mentioned in Section 2.6, is the strong local field confinement and enhancement (hot spots) occurring within the interparticle region at the plasmonic frequencies [146] and the possibility to tune these frequencies varying the distance between the two particles: in particular the bright dipolar mode redshifts with decreasing the gap, and this has been explained by classical electromagnetic models using the local response function [148]. On the other hand, for gaps below 2 nm, non-local theory has to be considered in order to describe the plasmonic response more accurately [129], [135], [149]; moreover, particular

attention needs to be paid for subnanometer gaps, because quantum effects²⁸ play here a very important role [150].

In particular, the theoretical investigation on the response during the transition from non-touching particle dimers to touching ones [128], [151], [152] has been faced but the experimental study of these structures is hard because of challenging fabrication methods necessary to create, manipulate [153] and probe [129], [154] such small (<1nm) dimer gaps.

At this regard, only recently came the experimental confirmation of the existence of the so called Charge Transfer Plasmon (CTP) modes, characteristic of the quantum regime. The nature of these modes, depending on the interparticle distance, is basically of two types: either originating from the quantum tunneling [155], [156] or deriving from the formation of conductive nanobridges [153], [156], [157], [158], between the two close particles.

In order to understand the interpretation of the EELS spectra characterizing our samples, we have, first, to describe in details the CTP modes and we are going to do it referring to the meticulous work conducted by Kadkhodazadeh *et al.* in 2013 [157]; Shima Kadkhodazadeh is also the scientist who performed the STEM measurements (necessary for the derivation of our EELS spectra showed in the **next section**) for this thesis.

In their research Kadkhodazadeh *et al.* have focused on silver dimers (with NP size of about 20nm) and, varying the interparticle distance d , they have studied and measured the correspondent surface plasmons showing the transition from the classical regime (with d ranging from 1 nm to 7 nm) to the subnanometer²⁹ one (starting from d around 0.3 nm), where the CTP can evolve from the tunneling mode to the nanobridge mode (for negative values of d).

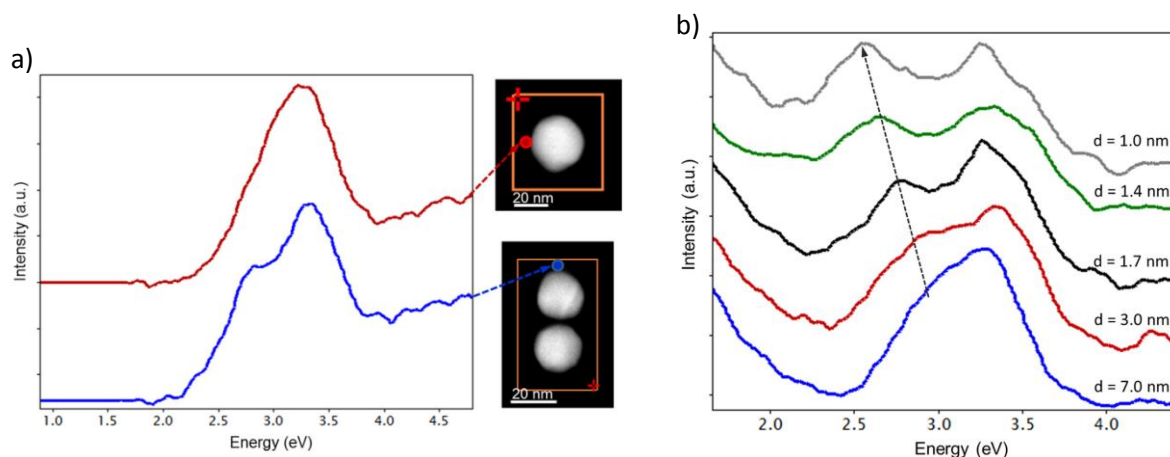


Figure 5.3: **a)** Plasmon resonances of an isolated sphere and a dimer due to plasmon hybridization. **b)** Plasmon resonances of a dimer with varying the interparticle distance d . [157]

²⁸ It must be mentioned that it is debated in the literature the nature of the effects occurring in subnanometer regime [164].

²⁹ It could be defined as quantum regime but Mortensen *et al.* ([164]) would argue that what has been identified as a tunnelling plasmon in [157] is in fact a higher order classical mode and it is not possible to understand the nature with EELS. Keeping this comment in mind, for simplicity we will refer, in this work, to this regime as *quantum*, assuming possible *tunnelling* between close dimers.

The variation of the dimer gap d was feasible thanks to the particle position manipulation made by the electron probe [156], [159].

First of all, it is worth showing the effect of the interparticle coupling [140] comparing the EELS spectrum of a single Ag sphere with the one of a dimer characterized by a few nanometers gap. In Figure 5.3a it is visible the hybridization of the dipolar surface plasmon resonance (single peak at 3.22eV for the individual particle) into a double peak representing the bright mode (bonding dipolar plasmon at 2.75eV) and the more intense [124], [139] dark mode (antibonding dipolar plasmon at 3.30eV). With decreasing d , the interparticle coupling effect gets stronger leading to a red-shift of the bright mode [151] which is shown in Figure 5.3b.

In Figure 5.4 we can see the EELS spectra for dimers with gap reduced from 1 nm to -0.6nm ($d < 0$ indicates an overlap between the particles) showing the dipolar bright (iii) and dark (i) modes (classic regime) but also the appearance of a CTP tunneling mode (ii) when $d = 0.3$ nm.

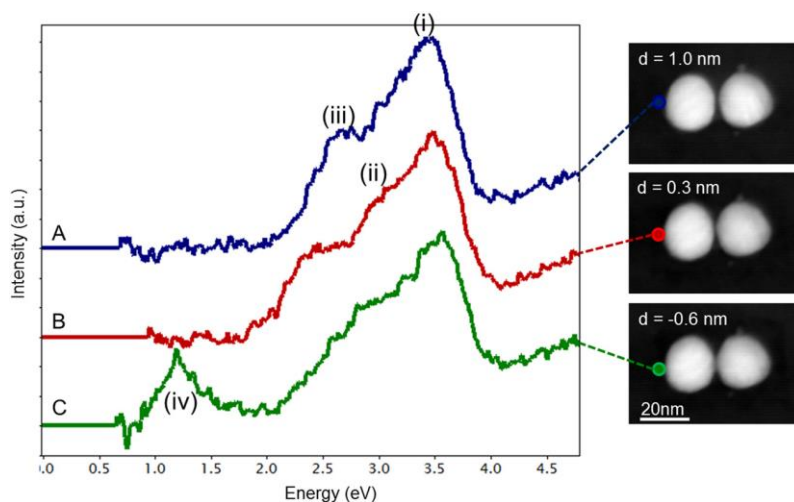


Figure 5.4: STEM images and EELS spectra from silver dimers in non-contact-, tunnel-, and contact-regimes collected from the same dimer but with decreasing gaps. Spectra A, B, and C represent the non-contact-, tunnel-, and contactregimes, respectively. The bright (iii), dark modes (i) and a charge transfer plasmon mode (ii) related to the tunnel current are marked in the spectra. The circle indicates the position of the electron beam. Spectrum B shows the coexistence of the classical and quantum related plasmons in the dimer. [157]

What we want to highlight is the situation shown by spectrum C, i.e. when the two particles start to overlap creating a *nanobridge*: here the classical dipolar modes break down, in fact the bright mode (iii) is not present anymore and the same happens to the dark one (i), which is “substituted” by another CTP mode at high energy [158]. The CTP-tunneling mode (ii) is still visible but a third interesting peak (iv) appear at low energy (1.21eV): this CTP mode is originating by the oscillating current flowing throught the nanobridge between the two particles now in contact.

Kadkhodazadeh *et al.* further analysed the CTP modes, measuring EELS spectra of dimers with d varying from 0.2 nm to -0.9 nm. In Figure 5.5 the evolution of the CTP-nanobridge mode (iv) is visible: it is increasing in intensity and blue-shifting, with increasing the overlap between the NPs (i.e. decreasing d); the limit comes when the contact is not forming a nanobridge anymore, but it is actually a merging between the spheres giving rise to a single classical elongated particle (Figure 5.6) and at this point the peak at low energy “becomes” again the dipolar mode.

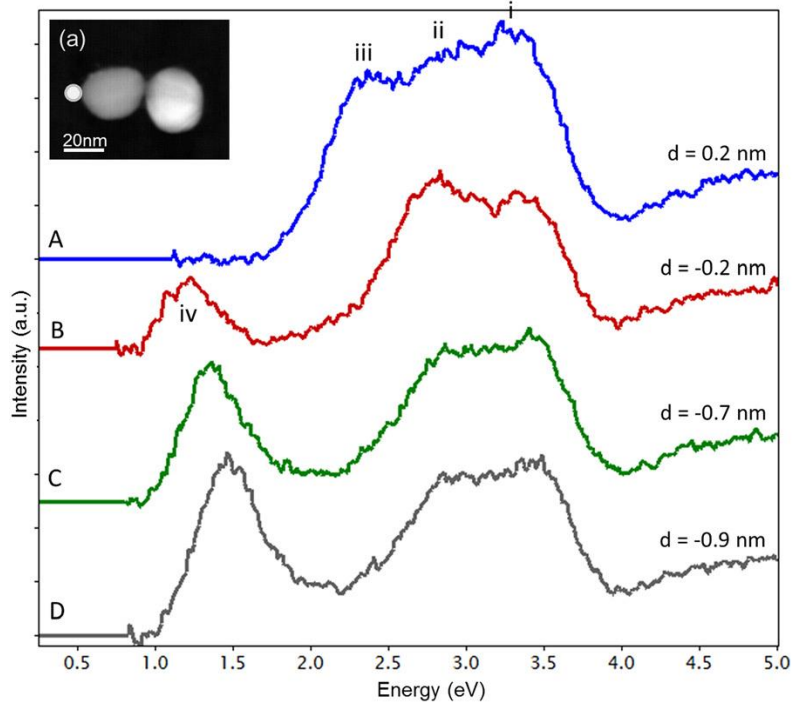


Figure 5.5: EELS spectra collected from a dimer during the transition from tunneling to a nanocontact regime. The circle in the STEM image indicates the position of the electron beam. Spectrum A represents the tunneling regime, where the classical dark (i) and bright (iii) modes coexist along with a tunneling related CTP mode (ii). After the particles make contact in spectra B-D, a second lower energy CTP mode (iv), related to current flow between the particles appears. Mode (i) is now likely to be a third CTP mode. [157]

The intensity of the CTP-nanobridge mode peak increases with decreasing d because as the bridge gets wider more current can flow in between; at the same time the tunnel probability and the correspondent CTP mode peak (ii) decreases till disappearing.

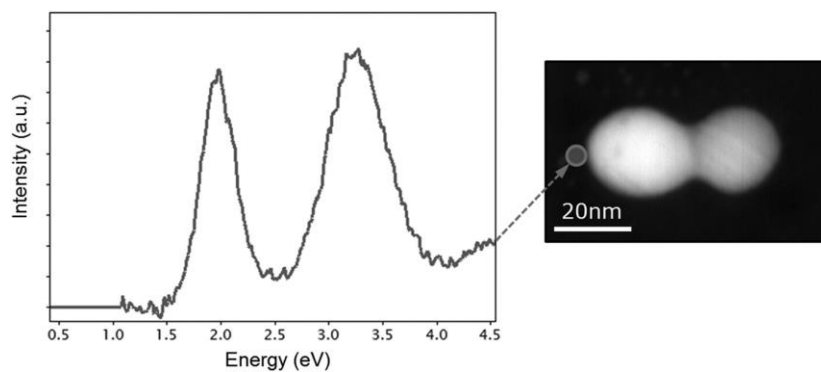


Figure 5.6: STEM image and EELS spectrum of two merged spheres, behaving as a classical elongated nanoparticle. The EELS spectrum displays only the dipole mode ($\sim 2\text{eV}$) and a higher order mode ($\sim 3.3\text{eV}$) of the plasmonic structure. The circle indicates the position of the electron beam [157]

This plasmonic excitation (CTP-nanobridge) is of our interest since, beside the classical mode typical of elongated particles, it is the only one occurring in the energy range (NIR) that we want to investigate

5.4 EELS measurements of Ag nanoparticles deposited by electroless

5.4.1 Sample preparation and data processing

As previously mentioned, with EELS analysis we are aiming to get more informations about the silver nanoparticles used in this work to incorporate into photovoltaic devices. Following the optical characterization in Section 4.3.2 we will compare the absorbance measurements with the EELS spectra in order to try to explain the enhancement we observed.

The samples were prepared using, as substrate, windows of 10 nm thick silicon nitride membranes on a frame of very small (3mm by 3mm) silicon chips of 100 μm thickness (Figure 4.34). Those substrates are specifically made for TEM measurements.

On top of the membrane, a further Si_3N_4 layer was deposited by PECVD, to compensate for HF etching during the subsequent electroless process; the total thickness of these samples was about 20 nm, which is good for TEM measurements. We refer to Section 4.2.2.4 for the full sample preparation.

From Figure 4.35, we can see a very wide distribution in size and shape: circular particles with diameter ranging from about 20 nm to 70 nm and elongated particles with different aspect ratios (even bigger than 2) and reaching length of about 130nm. It is important to highlight the position distribution, which is completely random but in particular gives rise to dimers or group of particles very close to each other (if not overlapping), with even subnanometer gaps (it will be shown better later on).

EELS measurements were then performed on different areas of these 9 windows, with the help of Shima Kadkhodazadeh from DTU CEN, using an FEI Titan TEM fitted with a monochromator and aberration corrector. After carrying out the measurements an analysis of the data is needed and is done using two softwares: “TEM Images & Analysis” and “Digital Micrograph”.

During the STEM session, within the sample surface, an area of a certain size is picked and it is scanned sending the electron beam pixel by pixel; the pixel size can be defined. These parameters (scan area size and pixel size) come from an arbitrary choice, which is a trade-off between the desired resolution of the measurements, the level of noise in the measurements and possible damage to the sample: the smaller the pixel area the longer time it will take to perform the measurements and higher is the probability that the sample will get damaged or move during the acquisition. For each pixel the transmitted electrons are sorted in terms of their energy loss; thus, each pixel corresponds to an EELS spectrum (similar to the one previously shown, for instance, in Figure 5.6 and exactly represented by the spectrum shown on the right of Figure 5.8) which is derived from the measured data after subtracting the zero-loss (elastic) peak (using “Digital Micrograph” software, see Figure 5.7). This “fitting and cleaning” was done for each pixel of all the maps that will be shown afterwards.

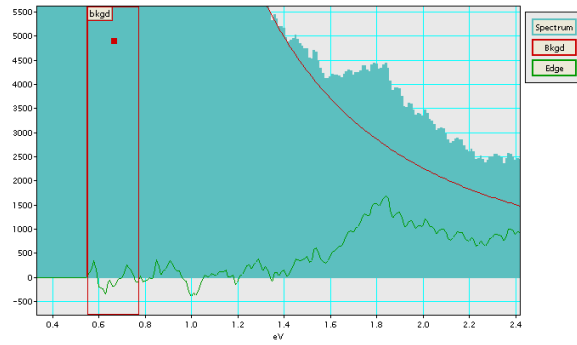


Figure 5.7: Part of the EELS spectrum measured by STEM in a pixel: it needs to be processed to filter out the background (red line) through a reasonable fitting on the slope of the zero-loss peak. The final obtained signal is represented by the green line.

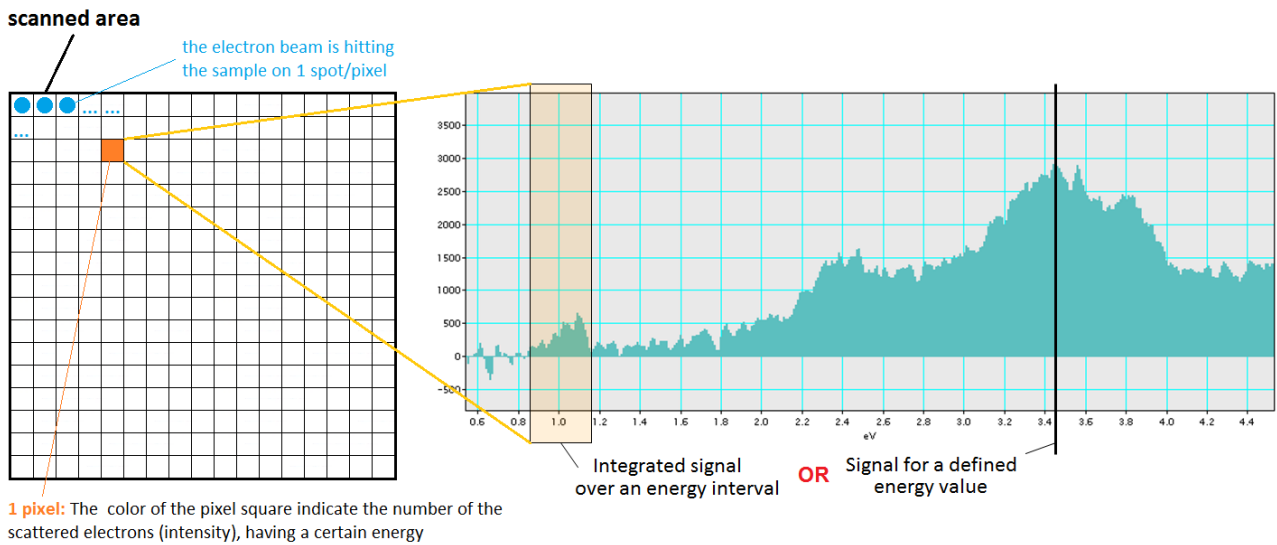


Figure 5.8: On the left: schematic representation of a single EELS map; you can draw a map for each electron-energy-loss value or range of values. On the right: EELS spectrum measured in each pixel.

Finally, all the spectra were assembled together to form different maps, each of them representing, in every pixel of the scanned area, the number of scattered electrons for given electron-energy-loss (Figure 5.8).

5.4.2 Results

We will now show the EELS maps keeping in mind that they give informations about the excitations distribution and therefore, not directly about the electric field enhancement distribution. The two distributions can be, instead, defined “complementary” (Figure 5.9).

It is important to remind that what is measured with EELS is very dependent on the position of the electron probe (e.g. Figure 5.3b is valid for the beam placed in the periphery of the dimer; in the gap of the dimer only the dark mode would be visible).

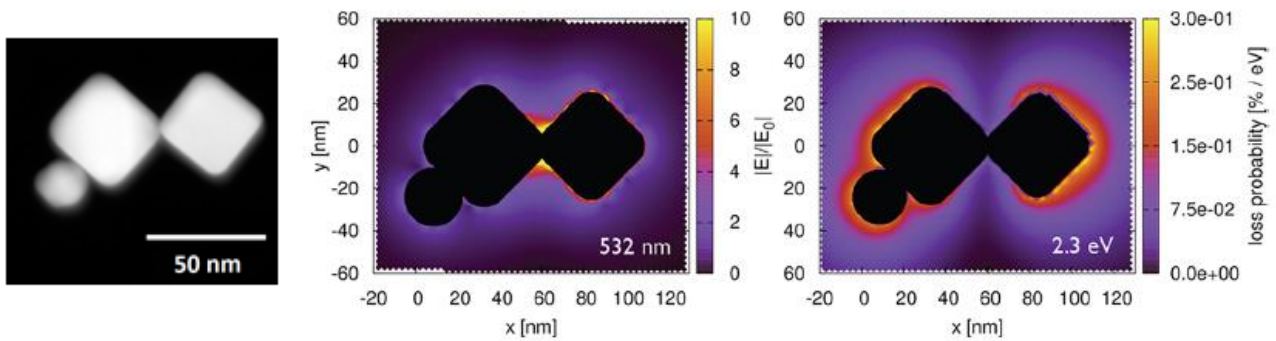


Figure 5.9: Comparison of the calculated electric near-field magnitude obtained from plane-wave excitation (graph on the left) with the EEL probability map for a 100 keV electron beam (graph on the right) for the trimer displayed in the TEM image on the very left of the figure. [160]

We investigated plasmonic excitations in the range of energy going from 0.9eV to 1.5eV corresponding to the wavelength range varying between 827nm and 1378nm. The low energy limit is given by EELS resolution limit³⁰; the high energy limit was chosen to reasonably narrow the study, considering that we are here more interested in plasmonic excitations occurring below the GaAs band gap edge ($E=1.4\text{eV} \rightarrow \lambda=880\text{nm}$).

From each of the following maps we could extract up to 1600 EELS spectra (1/pixel), but in this thesis we will show only some of them, corresponding to interesting *white spots*, i.e. spots of very intense plasmon excitation peaks³¹, around dimers showing CTP excitations.

The map is elaborated from the data measurements using “Digital Micrograph” and it has been overlapped with the outline of the particles obtained by the correspondent SEM image (in red); obviously, there is the possibility of a small misalignment between the two, due to the unavoidable drifting of the specimen during the measurements (and the SEM image was taken before the measurement starts).

The first scanned area here presented (*zone 1*) is about $(500\text{ nm})^2$ with a pixel size of 12 nm; it is identified by the orange square in Figure 5.10.

³⁰ For electron energy loss values smaller than 0.85eV, the tail of the zero loss peak becomes too intense and does not allow reliable extraction of information from the spectra.

³¹ We decided to call them “white spots” because of the white pixel color corresponding to maximum intensity (since the intensity scale here used is in temperature colors). We wanted to avoid the expression “hot spots” to not get confused with what its usual meaning: spot with very intense local electric field (see Figure 5.9).

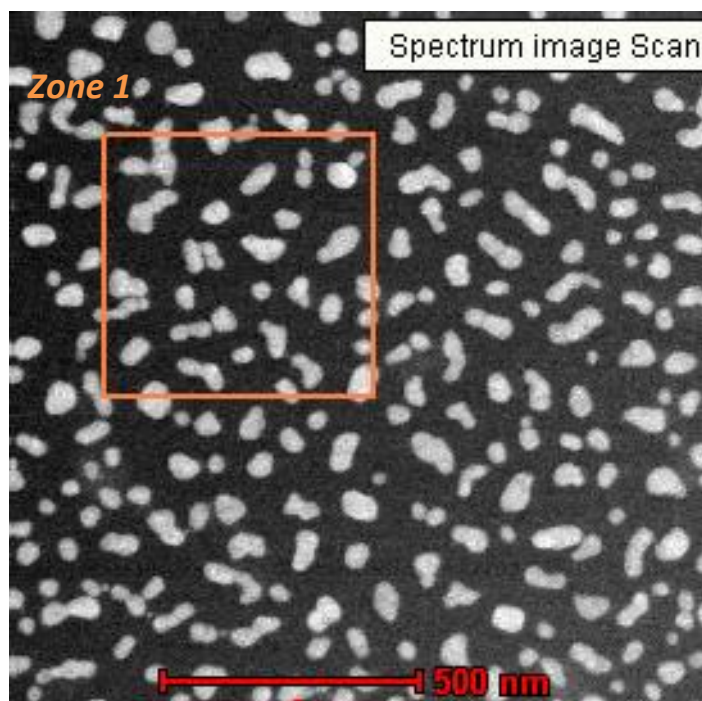


Figure 5.10: SEM image of the selected area for the scanning. The orange square part is then zoomed out (Figure 5.11) to better show the particles which will be submitted to EELS measurements.

In *zone 1* we see particles of different shapes and dimensions (with minimum size about 40nm) and, in particular, we can spot 6 dimers (A-F) and 7 elongated particles (1-7), highlighted in Figure 5.11. All these elements will be characterized by a big variation of plasmon modes, which can also fall in a range of energy outside the interval of our interest, (0.9-1.5) eV.

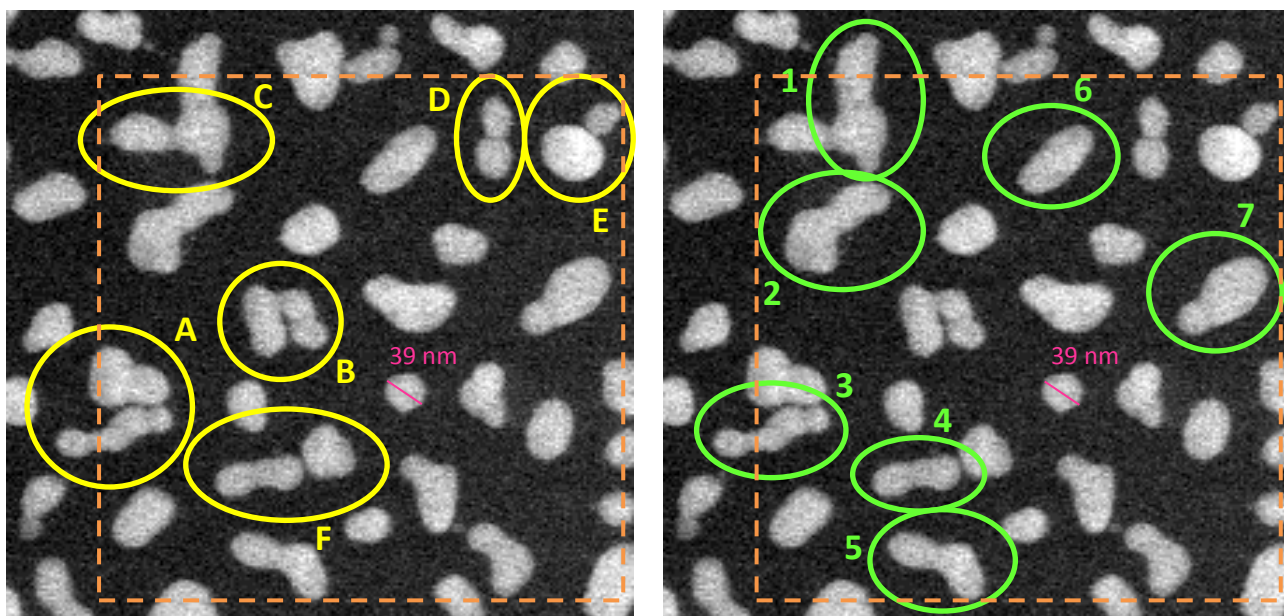


Figure 5.11: Zoom of *zone 1* (the real scanned area is indicated by the orange dashed square). Dimers (left) and elongated particles (right) are highlighted by yellow and green circles. The smallest size particle is also indicated (pink) as indications of the dimensions.

We will now show the EELS maps corresponding to *zone 1* for different energy values; the intensity scale ranges from 0 to 1500 counts for the 7 maps in Figure 5.12 and Figure 5.13 and from 0 to 3000 for the 4 maps in Figure 5.14.

During the analysis we have noticed that the specimen drifted slightly in the vertical direction, which means that the pattern (and thus the red outline) should be shifted a little up respect to the EELS distributon.

Analyzing the maps one by one we summarize the results in Table 5.1.

Electron Energy Loss	Resonating elements
0.9 eV	Dimer A and also B starts to show excitation
1.0 eV	Dimers A, B; dimer C starts to show excitation
1.1 eV	Dimer C
1.2 eV	Dimer C (now with more white spots); particle 2 starts to resonate
1.3 eV	Dimer C (intense); particle 2; particle 3 starts to resonate
1.4 eV	Dimers C (less intense); dimer D starts; particle 2 (intense); particle 3; particle 4 starts
1.5 eV	Dimers C (less intense) and D; particle 2 (more intense); particle 3 (intense); particle 4 (intense); particles 1 and 5 start to resonate.

Table 5.1: Summary of the plasmon excitations (within the range 0.9eV-1.5eV), characterizing *zone 1*.

In general, peaks corresponding to the excitations can be more or less broad, therefore giving signal at more than 1 energy value. It will be then interesting to show also maps corresponding to excitations integrated over a range of energy. This is done afterwards.

When the dimer is composed by elongated particles (f.i. C-1 and A-3) the excitations could lead to confusion but, within our range of energy, we can distinguish the plasmon mode relative to the single elongated particle considering the point of excitation, i.e. the spot where the electron beam is hitting in the vicinity of the particle (Figure 5.15).

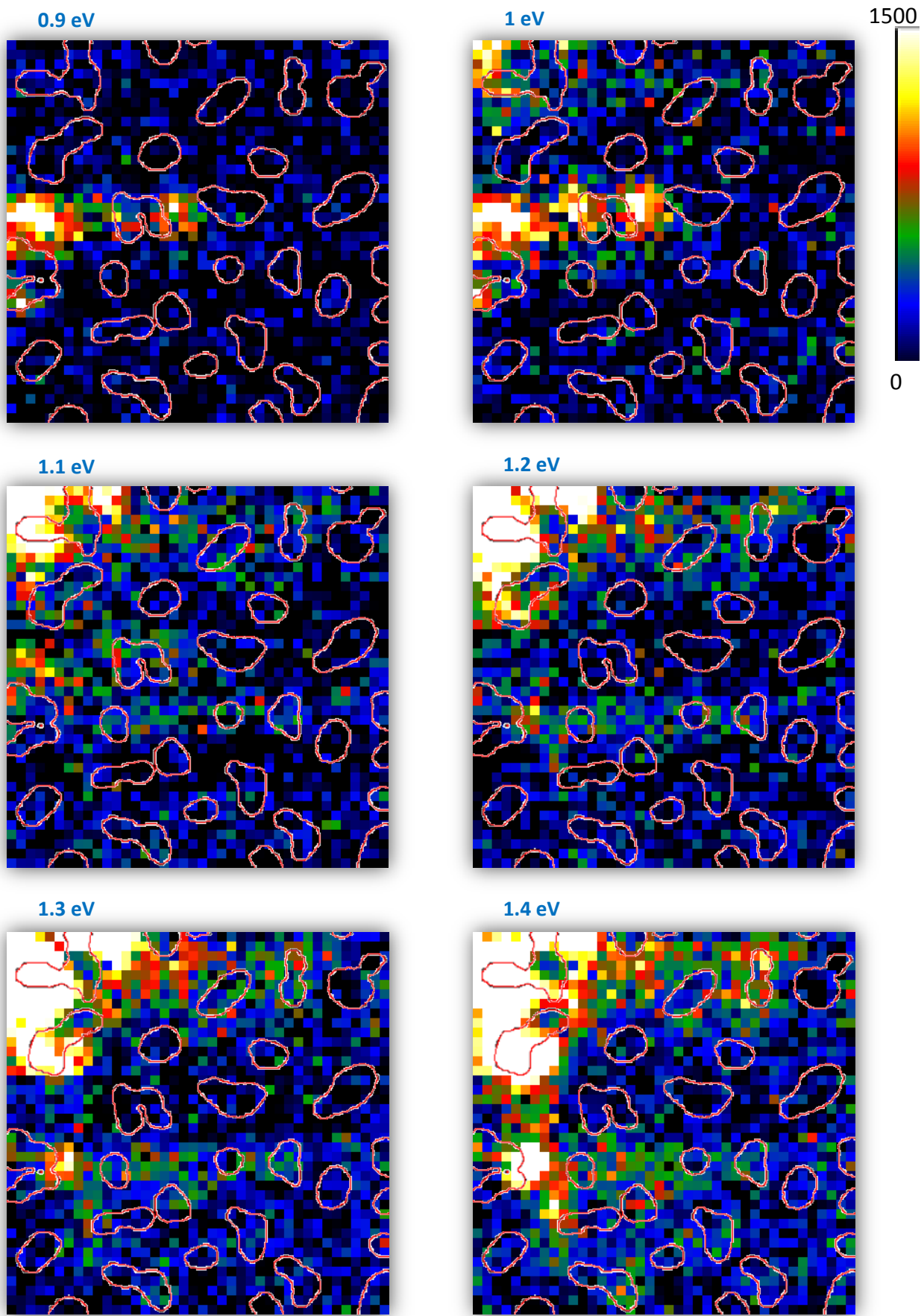


Figure 5.12: EELS maps of zone 1 for loss energy ranging from 0.9eV to 1.4eV, with intensity scale 0-1500.

1.5 eV

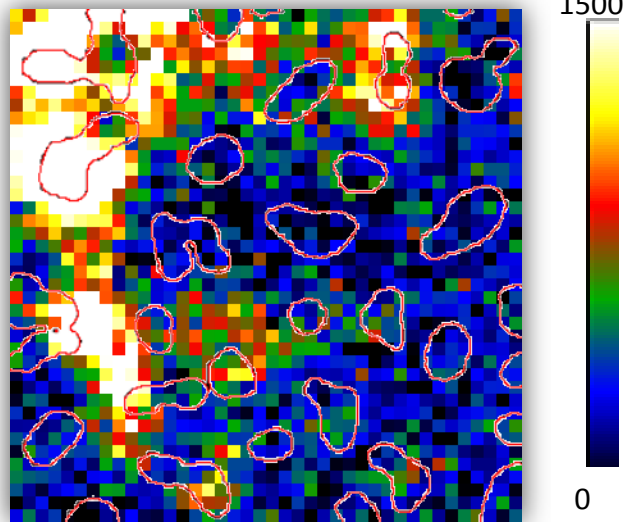
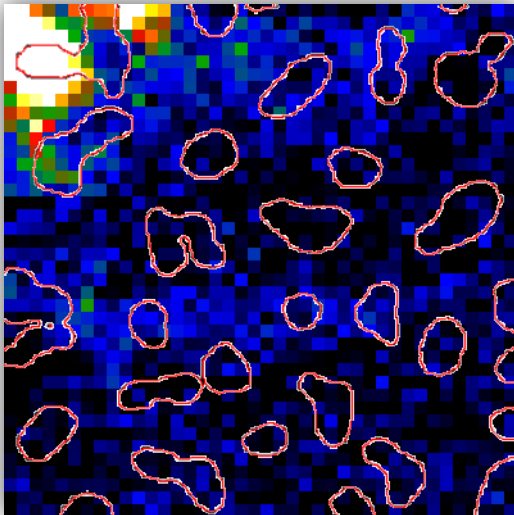


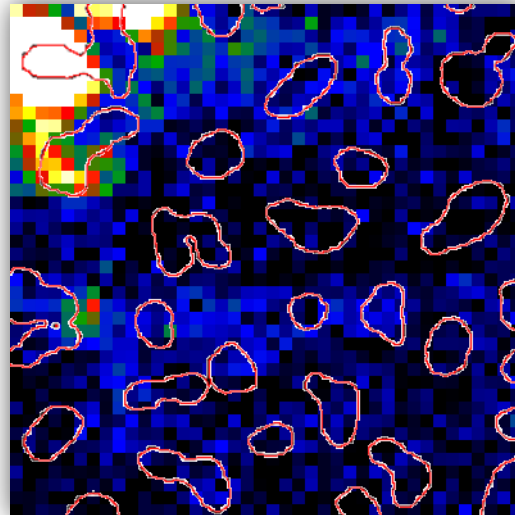
Figure 5.13: EELS maps of *zone 1* for loss energy equal to 1.5eV, with intensity scale 0-1500.

From 1.2eV to 1.5eV there are many white spots, in order to better visualize the excitations in this range we expand the intensity scale till 3000 (Figure 5.14).

1.2 eV



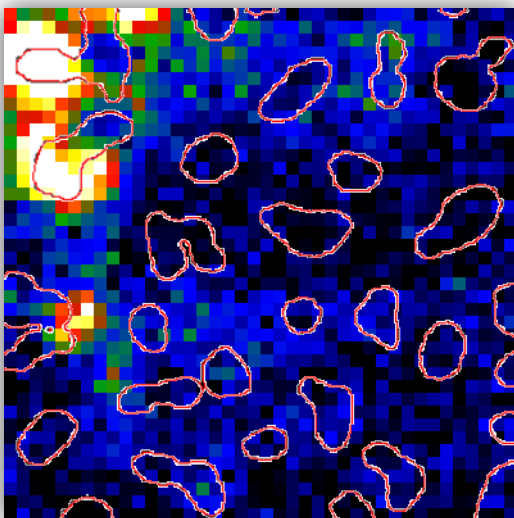
1.3 eV



3000

0

1.4 eV



1.5 eV

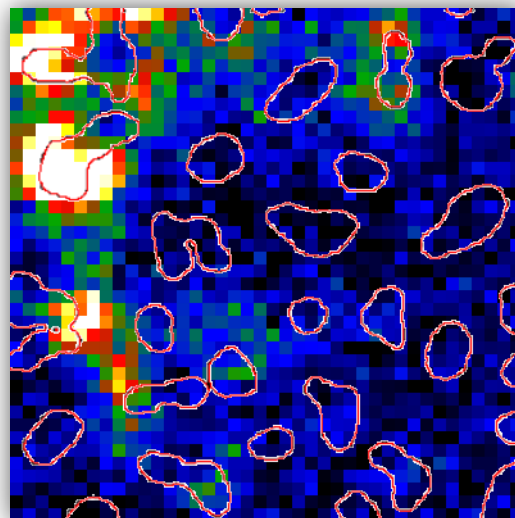


Figure 5.14: EELS maps of *zone 1* for loss energy ranging from 1.2eV to 1.5eV with intensity scale 0-3000.

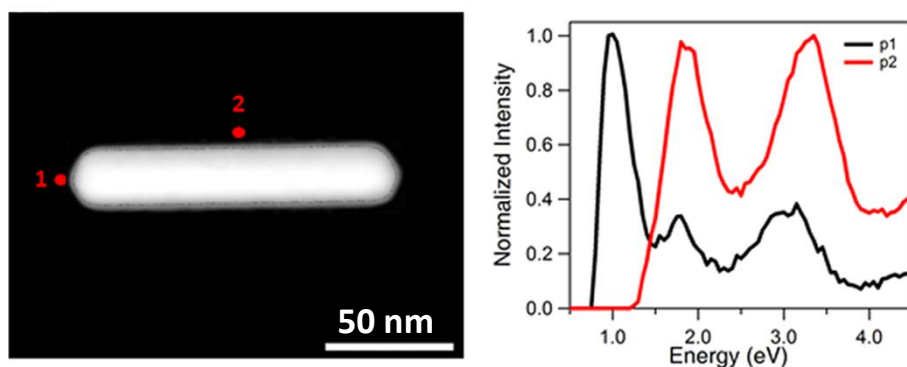


Figure 5.15: Image (left) and EEL spectra (right) for selected points around a nanorod [160]. In this thesis the investigated energy range allows only the individualization of the mode at 1 eV coming from the excitation in point 1.

We can then draw these first deductions:

- ✚ Single particles with aspect ratio close to 1 or in general with not-regular shape but not elongated: do not show excitations in the range of interest.
- ✚ Elongated particles: it is difficult to define the aspect ratio if the shape is not regular. Considering the resonating ones (1-5), we could say that they are characterized by an approximation of the aspect ratio of at least 2.8, but also by a not-rounded shape (visible for particles 6, 7).
- ✚ Dimers: from [157] we expected to find CTP-nanobridge modes for energy values ranging between 1.1 eV and 1.5 eV (Figure 5.5) and we actually did, for dimers C and D. Dimers A and B show modes resonating at lower energy and it is difficult to explain the reason; we could think that dealing with bigger particles than the ones measured in [157], the CTP mode might redshift. Dimers E and F do not show excitations in this range of energy and an explanation on this regards will follow.

Concerning the dimers, in our energy range, we cannot see dipolar bright/dark modes, or higher order modes, nor tunnelling modes, since all of these occur at higher energy. What we can see here are the CTP-nanobridge modes which occur when there is small contact between the two particles. Nevertheless, we also have to think within the limits of our images resolution, which is not as good as that of Figure 5.4; actually even in that figure is not so easy to distinguish a nanometer gap from contact. On the basis of this argument, we assume that from our available images we cannot distinguish between a (sub)nanometer gap and a nanobridge, due to an uncertainty of 2 nm. Moreover, another aspect must be considered: the relative size and shape of the two particles; from a classical point of view: the more they are different from each other, the more the dimer symmetry is broken and the more the hybridization of their plasmon modes is difficult to be predicted. From a quantum point of view (which is more of our interest here), we believe that what is making a dimer formed by relatively different particles is not defined by the absolute size and shape of the two particles, but by what we call their relative *resonating lengths* (L_1 and L_2), which are defined on the *line of contact* (of the nanobridge), C_L , between the two NPs, and whose sum is giving the *total resonating length* (L_{tot}) of the oscillating electrons within the dimer. The concept is shown in Figure 5.16 and when L_1 is “very different” from L_2 (i.e. if $L_1 > L_2$, $L_1/L_2 > 1.2^{32}$), like for E and F, we define the two particles as *not-comparable* and we refer to this kind of dimer with *NC*.

³² The threshold 1.2 was defined by the analysis of 17 potentially nanobridge-dimers.

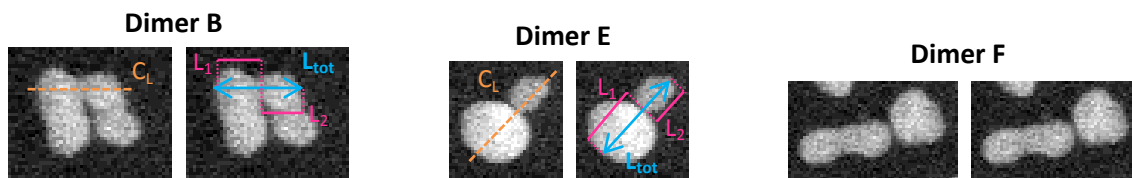


Figure 5.16: As an exemple, C_L (line of contact), L_1 , L_2 and L_{tot} (resonating lines) are shown for dimers B, E and F, taken from *zone 1*. Dimers E and F can be classified as NC, which do not show any CTP-nanobridge mode.

In order to compare the behaviour of NC-dimers with not-NC ones, but also aiming to get a better statistics of the plasmon excitations characterizing our electroless silver nanoparticles, we analysed other 5 zones. All the relative maps are shown in Appendix.

For *zone 2* the same job was repeated and during TEM measurements we decided to focus more on two dimers, increasing then the resolution (pixel size of 6 nm) for a smaller area (called *zone 2-zoom*), containing them (Figure 5.17).

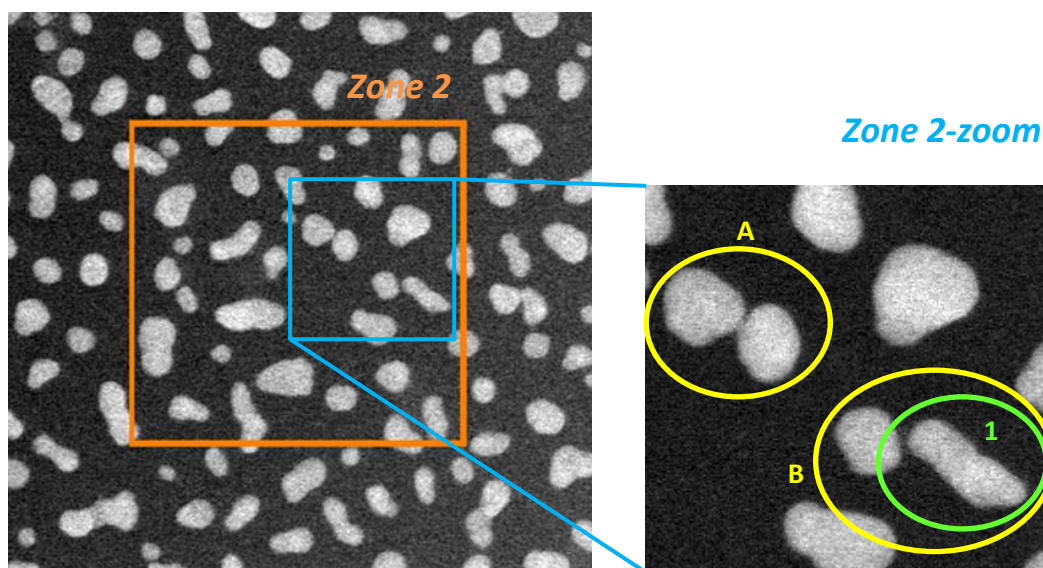


Figure 5.17: TEM images of the scanned area *zone 2* (and its *zoom* on the right).

We are showing now only the EELS maps for 1.0 eV, presenting CTP-nanobridge excitation for dimer A, and for 1.5 eV, correspondent to the dipolar mode of the elongated particle 1.

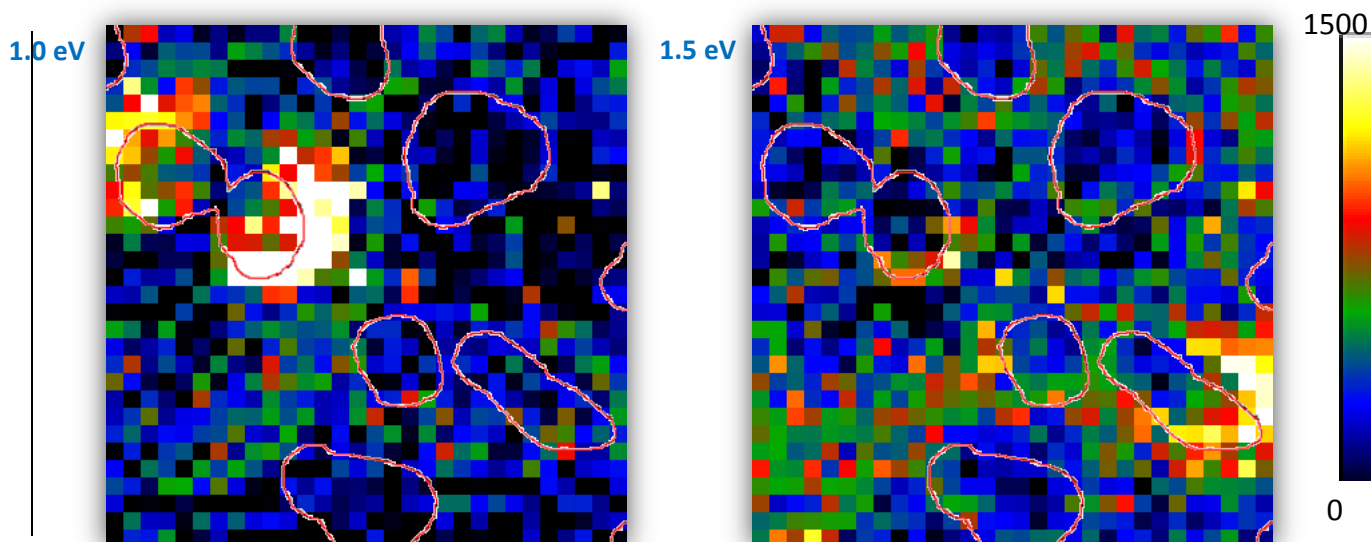


Figure 5.18: EELS maps of *zone 2-zoom* for electron energy loss of 1 eV (left) and 1.5 eV (right), with intensity scale 0-1500.

Dimer B is not showing the CTP-nanobridge mode because there is not contact between the particles and this is out of any doubt since the resolution of the picture is here higher.

Within all the 6 zones we have scanned a total of 17 dimers were spot: we counted only potentially nanobridging dimers, by means they were judged by the TEM images and considered only if there was visible contact (and not merging) or reasonably small gap (nominally 3-4 nm). Out of 17, 11 were showing a CTP-nanobridge mode belonging to the range [0.9-1.5] eV; the 6 non-resonating were all NC-dimers (and none of the resonating ones was NC).

We are going to show now, as an example, the EELS spectra relative to 2 representative dimers, excited by the electron beam in different spots and having their CTP-nanobridge excitation at 1 eV (Figure 5.19 and Figure 5.20)

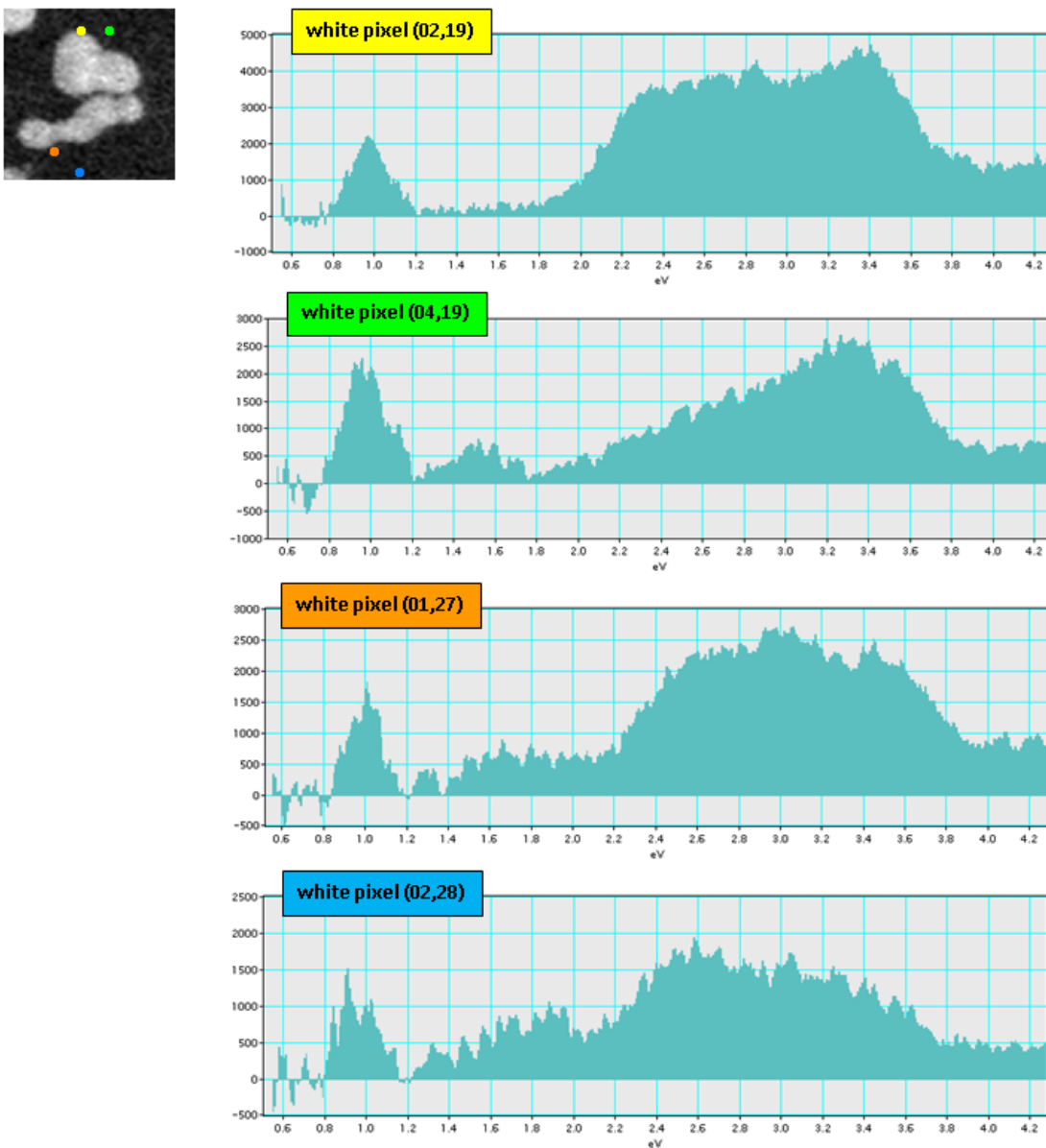


Figure 5.19: EELS spectra correspondent to dimer A of zone 1. The coloured circles indicate the position of the electron beam, which corresponds to the listed set of coordinates (x,y).

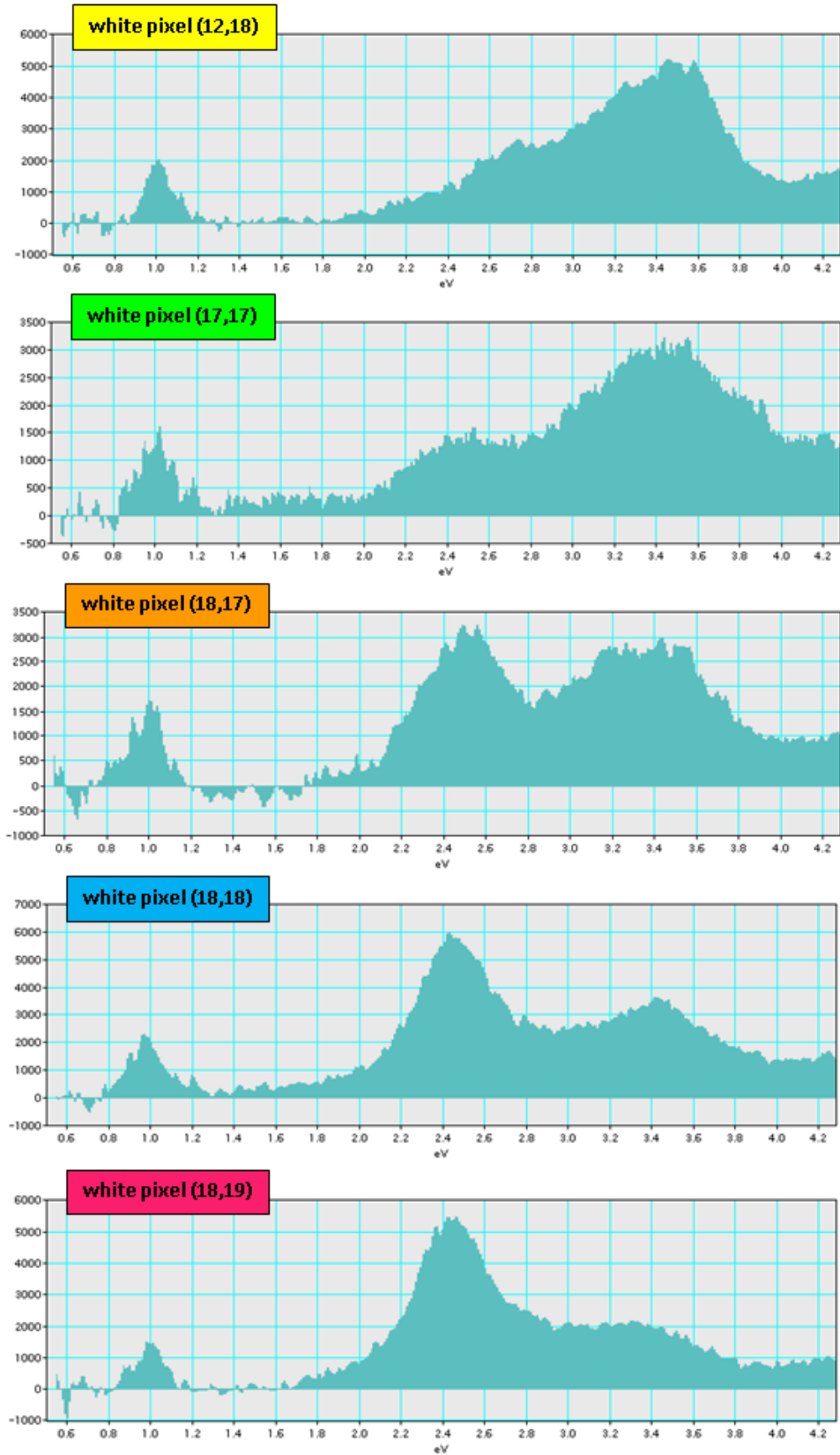
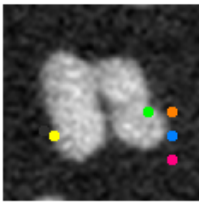


Figure 5.20: EELS spectra correspondent to dimer B of *zone 1*. The coloured circles indicate the position of the electron beam, which corresponds to the listed set of coordinates (x,y).

These spectra find good agreement with our reference work [157]. In particular, the orange spot in Figure 5.19 shows that the LSP excited there, corresponding to 1 μ m, originates from the dimer and not from the elongated particle (compare with Figure 5.15).

The other element that arouses interest in our range of energy is the elongated particle, which we saw (from Table 5.1, Figure 5.18 and the other *zones* mapped in Appendix) can resonate mainly between 1.2 eV and 1.5 eV. In particular, it is interesting to see the white spots for tapered/pointed elongated particles.

In zone 3 there are many of these particles and an EELS map (with pixel size of 24 nm), with the integrated signal over the whole range, is show just beside in Figure 5.21 (notice once again the drifting of the specimen).

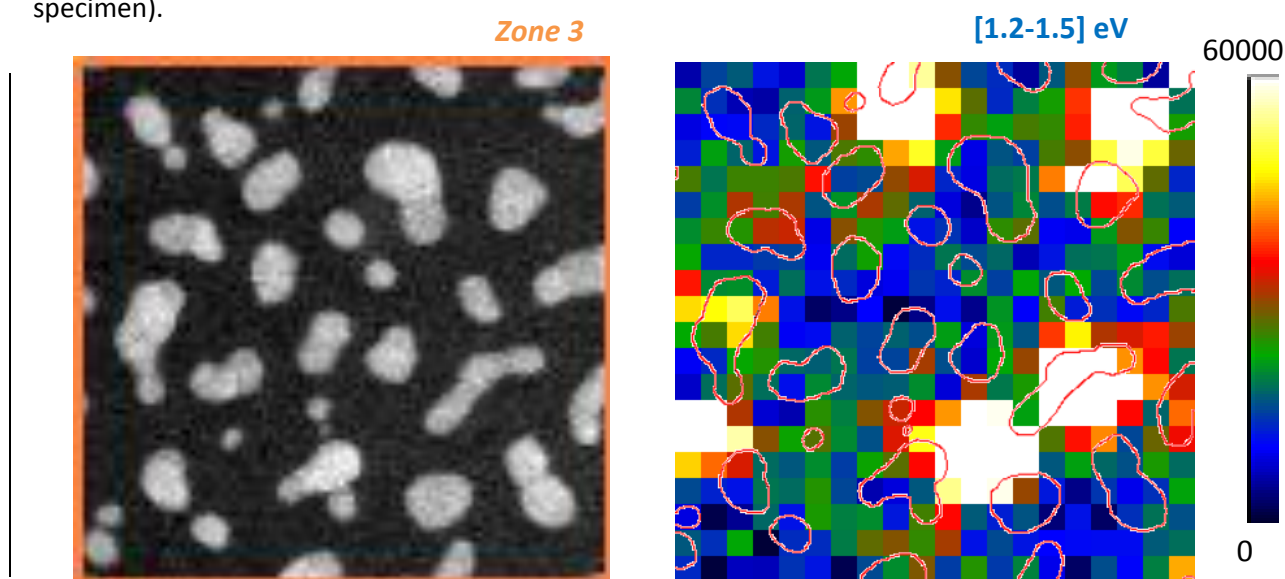


Figure 5.21: TEM image of the scanned zone 3 (left) and the correspondent EELS measurement with signal integrated over the interval [1.2-1.5] eV (right); the pixel size is 24nm and the intensity scale 0-60000.

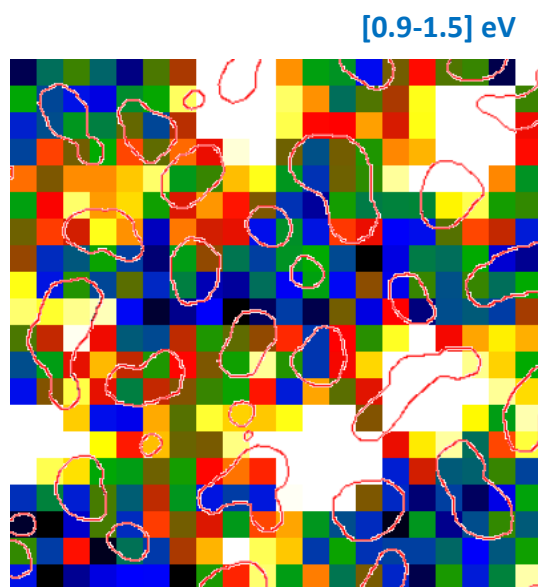


Figure 5.22: EELS maps of zone 3 with signal integrated over the interval [0.9-1.5] eV (right); the pixel size is 24nm and the intensity scale 0-60000.

From SEM images, it is difficult to distinguish between a subnanometer gap/just-touching dimer and a single elongated particle created by two NPs merging; nevertheless, in both cases we can expect plasmonic excitations in the energy range of [0.9-1.5] eV (see as an exemple **Error! Reference source not found.**), that we think are the mainly responsible for the absorbance enhancement measured on similar samples in Section 4.3.

5.4.3 Conclusions

After depositing silver nanoparticles by electroless plating on top of silicon nitride membranes, electron energy loss spectroscopy on several areas has been performed. The randomness deriving from the deposition technique results in different shape and size of particles. In particular: a reasonable density of elongated particles (with high aspect ratio, long dimension varying between 80 nm and 130 nm, and eventual pointed tips) and dimers of particles, creating nanobridges and with comparable L_i (with total resonating length L_{tot} ranging from about 55 nm to 110 nm) has been observed. These objects, if pertubated with an incident electric field, are characterized by plasmonic excitations in the NIR range, which would generate photoemission and thus photocurrent enhancement in PV devices incorporating those nanostructures. Fabrication of NPs to be incorporated into solar cells should then focus on such shapes.

Although the attempt to model the experimental data did not yield a good agreements, it is most likely a result of a different refractive index (n) of the sourrounding medium used in the calculations compared with the uncertain local n seen by the NPs on silicon nitride membrane, but it will be a future work.

6. Solar cells electrical characterization

6.1 Short circuit current and quantum efficiency

A semiconductor solar cell is basically a diode working in photovoltaic regime with voltage in forward direction, in the fourth quadrant of the I-V plane. The spectral response of a solar cell can be measured as photocurrent dependence on the wavelength, when solar cell works in short-circuit conditions (I_{sc}), i.e. by keeping the two electrodes of the solar cell at $\Delta V=0$.

From the measured I_{sc} data it is then possible to calculate the quantum efficiency $QE(\lambda)$ of the device as:

$$QE(\lambda) = \frac{I_{sc}(\lambda) hc}{P_{in} q\lambda} \quad (6.1)$$

The quantum efficiency can be interpreted as the probability that an incident photon with specific energy (at a specific wavelength) generates an electron-hole pair and that so generated carriers reach the contact. It is typical to refer to this value as “external” quantum efficiency³³.

The measurements of the short-circuit current density (J_{sc}) of the GaAs devices were performed at room temperature using a probe station to connect the top and back contact of the diode with Keithley Model 4200-SCS Characterization System. The solar cells were illuminated from the top using a Xenon lamp in combination with a monochromator working between 350 nm and 1750 nm. The whole system was controlled through a Labview program. With the lamp power of 150W and finite efficiency of the optics the light intensity was a fraction of 1 Sun value.

The QE measurements of a-Si:H solar cells were performed using a probe station with the light illuminating the device provided by a sun-simulator which creates a calibrated AM 1.5 spectrum and has large enough spot size for the device.

6.2 GaAs Schottky diodes

All the types of solar cells fabricated from GaAs are summarized in Figure 6.1. All the cells have back and front Schottky contacts, some have insulating layer under the Schottky metal while some do not; some are fabricated with and some without Au-order or Ag-random nanoparticles. A typical spectral response of these devices is shown in Figure 6.2 and it is typical of GaAs devices, with the cut-off at GaAs bandgap and low wavelength decrease of sensitivity due to the absorption in ITO layer.

³³ The “external” quantum efficiency of a solar cell includes the effect of optical losses such as transmission and reflection. However, it is often useful to look at the quantum efficiency of the light that entered the device (was not reflected) . This is so called "internal" quantum efficiency and it defines a probability that a photon which entered the device is absorbed and generated carries are extracted to the external circuit. .

From optical characterization of gold nanoparticles (Section 4.3), the absorbance enhancement in the NIR range could not be measured; but it may be possible to measure any LSP enhancement electrically in a Schottky diode because then the absorption in the substrate does not contribute anymore. For this reason and also aiming to see a correspondence with absorbance enhancement measured in the visible range, solar cells with Ti/Au NPs have been fabricated and characterized. On the other hand, diodes with random Ag NPs, which showed absorbance enhancement in the NIR range, were fabricated and characterized with the goal to prove photoemission by the NPs in that range (below the GaAs gap).

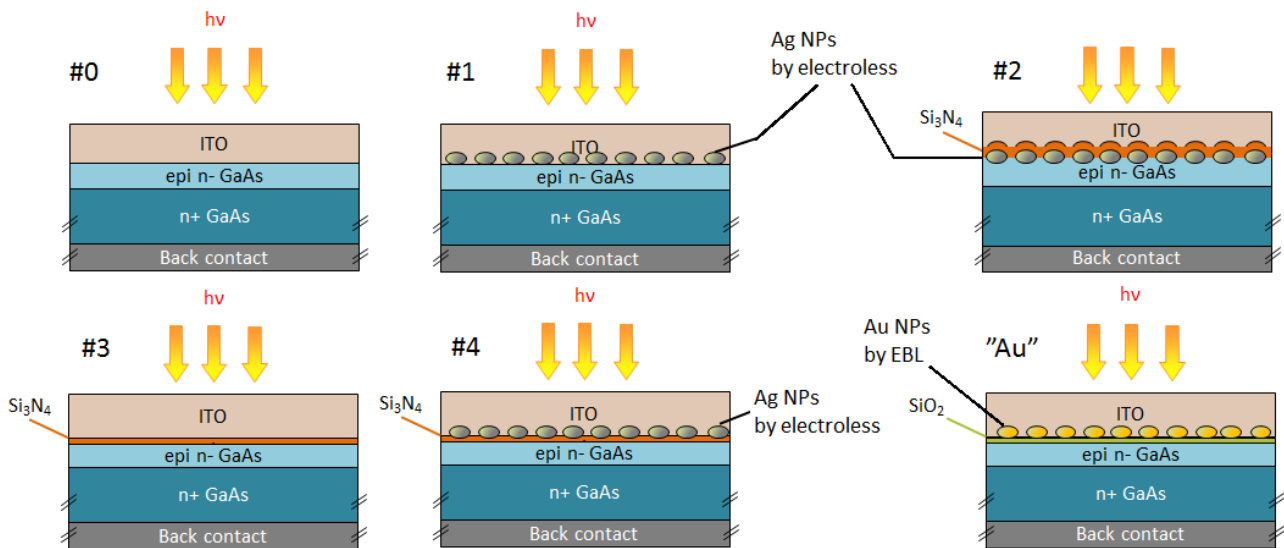


Figure 6.1: Schematic illustration in cross section of the GaAs solar cells fabricated and measured in this thesis.

The inset in Figure 6.2 shows a zoom into the NIR range, where we would expect an additional photocurrent from the absorption in the nanoparticles. However, there was no response in this range for any of the considered devices, the small increase seen between 1000 and 1250 nm originates from the device itself. The QE corresponding to the photocurrent in this range, shown in more detail in Figure 6.3 is not even 0.01%.

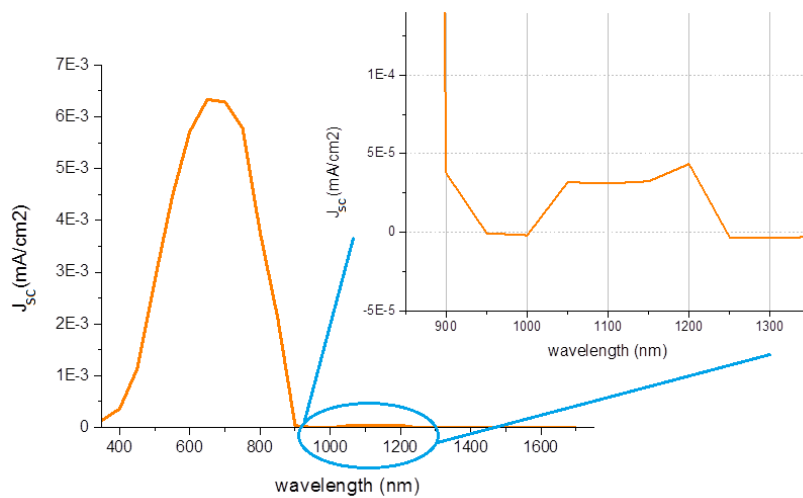


Figure 6.2: Short-circuit density current in dependence of wavelength, measured for GaAs diodes.

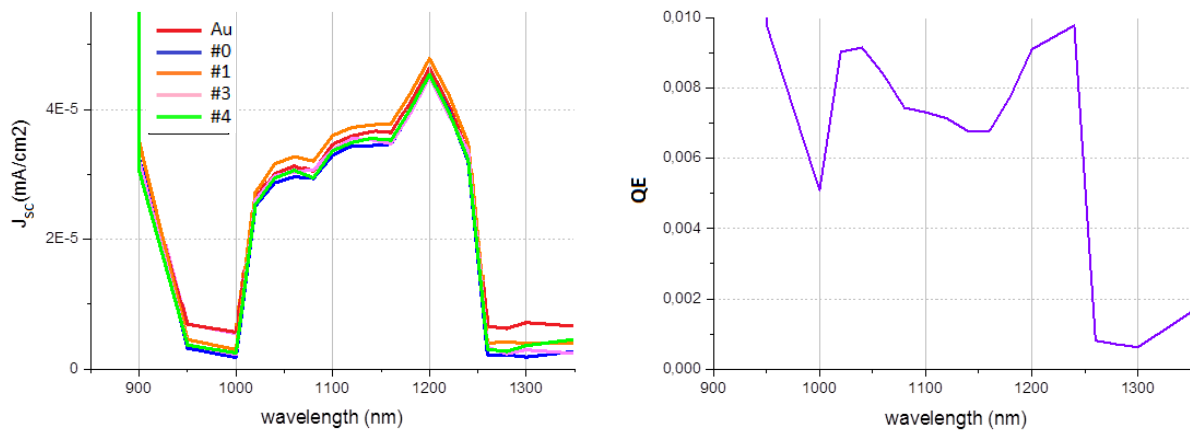


Figure 6.3: left) Zoom of Figure 6.2 in the NIR range. right) Correspondent calculated quantum efficiency.

Regarding the electroless-diodes, the absence of the expected plasmonic enhancement below the gap can be explained either because it is not measurable because of not enough sensitive setup, or because the effect gets dissipated through heat. The latter is very likely since GaAs is known to have very fast surface recombination which was not reduced well enough with Si_3N_4 layer, as it is noticeable from Figure 6.4: comparing diode #0 with diode #3 we see identical spectral response. Moreover, they overlap on blue edge and this could be for two reasons: i) the ITO layer absorbs the “blue photons”, or ii) ITO does not absorb the “blue photons” and the silicon nitride layer does not passivate the surface properly, otherwise diode #3 should have its peak response more towards the blue range than diode #0. We can exclude the first hypothesis (Figure 3.19).

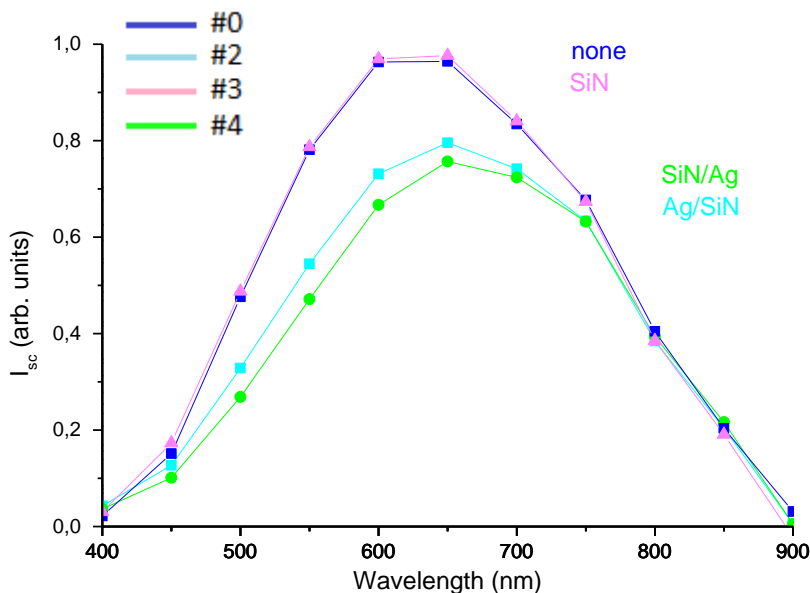


Figure 6.4: Short-circuit current measured in dependence of the wavelength for different GaAs diodes.

Furthermore, comparing diodes #2 and #4 (with NPs), with diodes #0 and #3 (without NPs), the peak sensitivity is shifted to longer wavelengths, which means that more “blue photons” are lost in these samples. Again there are two possible interpretations:

- i. NPs reflect the blue photons: from Figure 4.50, it is the case but still about 60% of photons are absorbed in GaAs.
- ii. Absorbed in GaAs blue photons recombine on NPs.

Most likely both effects are in operation. If we then compare the change of absorption from Figure 4.50 between 500 nm and 700 nm with change of photocurrent at these wavelengths, we find for all samples that: the absorption ratio is at most 1.5, while the photocurrent one is about 2-3. Clearly some blue photons are lost on recombination.

6.3 A-Si:H amorphous solar cells

6.3.1 QE spectra

The structure of the a-Si:H solar cell used for electrical characterisation is shown in Figure 6.5 and it is identical to the one used for optical characterisation (Section 4.2). In order to evaluate the effect of NPs, spectral responses were measured for two neighbouring cells, one with NPs and one without them (reference).

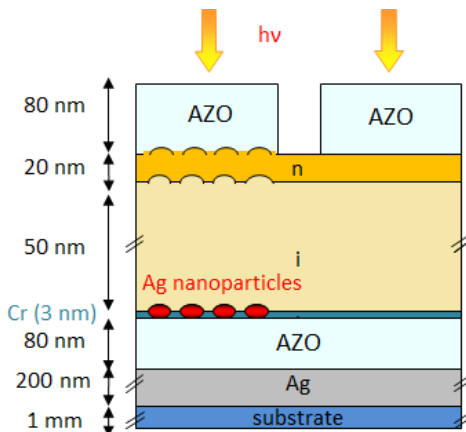


Figure 6.5: Illustration of the cross section of the a-Si:H solar cells.

The six solar cells differ with the parameters (size and pitch) chosen for the NPs array defined with EBL; details corresponding to each diode are included as labels in the graphs of the quantum efficiency spectra calculated from the measured spectral response at different voltage (Figure 6.6, Figure 6.7, Figure 6.8): a series of panels wants to show QE spectra for each cell and relative zooms around the wavelengths corresponding to the 3 LSP resonances found from optical characterization (Figure 4.48): (i) 450 nm, (ii) 560 nm, (iii) 740 nm; where (i) and (iii) are due to absorption by the NPs, whereas (ii) is caused by scattering.

LSPR (ii) is clearly responsible of QE enhancement, at all the measured voltage values, for 4 cells out of 6: in cell D2 (Figure 6.6e) it is barely visible at 0V and in cell E1 (Figure 6.7b) the diode response is instead worse

when Ag NPs are incorporated. It must be said that this cell did not show a clear resonance even in the optical measurements. The solar cells showing to be enhanced by the LSP scattering with the most significant intensity are C2 (Figure 6.6b) and E3 (Figure 6.8e), which are respectively characterized by: C2) very dense pattern (shortest array pitch, 60 nm) and disorder in NPs size (Figure 4.42-right), which are both elements enhancing scattering; or E3) quite big size of NPs (34 nm), which again increase the filling fraction of the sample producing similar consequences as dense arrays. Both these samples showed an intense resonance also in R_{meas} spectra.

The more intense plasmonic effect for the LSP resonance around 560 nm (ii) can be highlighted plotting the relative differences between the QEs (subtracting the reference QE to the one of the cell with NPs), which are shown in Figure 6.10; the same features found for the behaviour of the corresponding dip (ii) in R_{meas} , are found here. In fact, for denser patterns there is a clear increase in the QE (a-b-c), and also a redshift can be seen in two sequences of spectra (b-c). The same effect results from increasing the size of the nanoparticles maintaining constant the periodicity (c).

LSPR (iii) causes QE enhancement in all 6 cells: even if the effect is not intense, it is visible at all voltages and it generates enhancement over a more or less wide range of wavelengths (indicated by the grey arrows in the panels). Cell D2 (Figure 6.6f) is the one which is most positively affected by this resonance in absorption. In the long wavelength range the used setup is also quite noisy, thus a clearer analysis of the LSP absorption effect on photocurrent can be conducted with the analysis of resonance (i).

LSPR (i) is responsible of QE enhancement in all cells at zero voltage (Figure 6.9), but in particular it positively affects the diode behaviour at higher voltages of cell E1 (Figure 6.7b). This cell is characterized by small particles (20 nm in diameter, Figure 4.22), thus photon absorption cross section is larger than the scattering one. Moreover, from Figure 6.11, one can see that the effect, for response at zero voltage, is more intense for cell E3, both at LSPR (i) and (iii).

To conclude the analysis, absorption contribute by NPs is enhanced by LSP less effectively than scattering; furthermore, it is also less effective than absorption in semiconductor so really only worth it if the peak can be shifted below the bandgap. Finally, the variability of the enhancement of peaks (i) and (iii) from sample to sample is hard to understand, so possible surface recombination due to processing variations have to be considered.

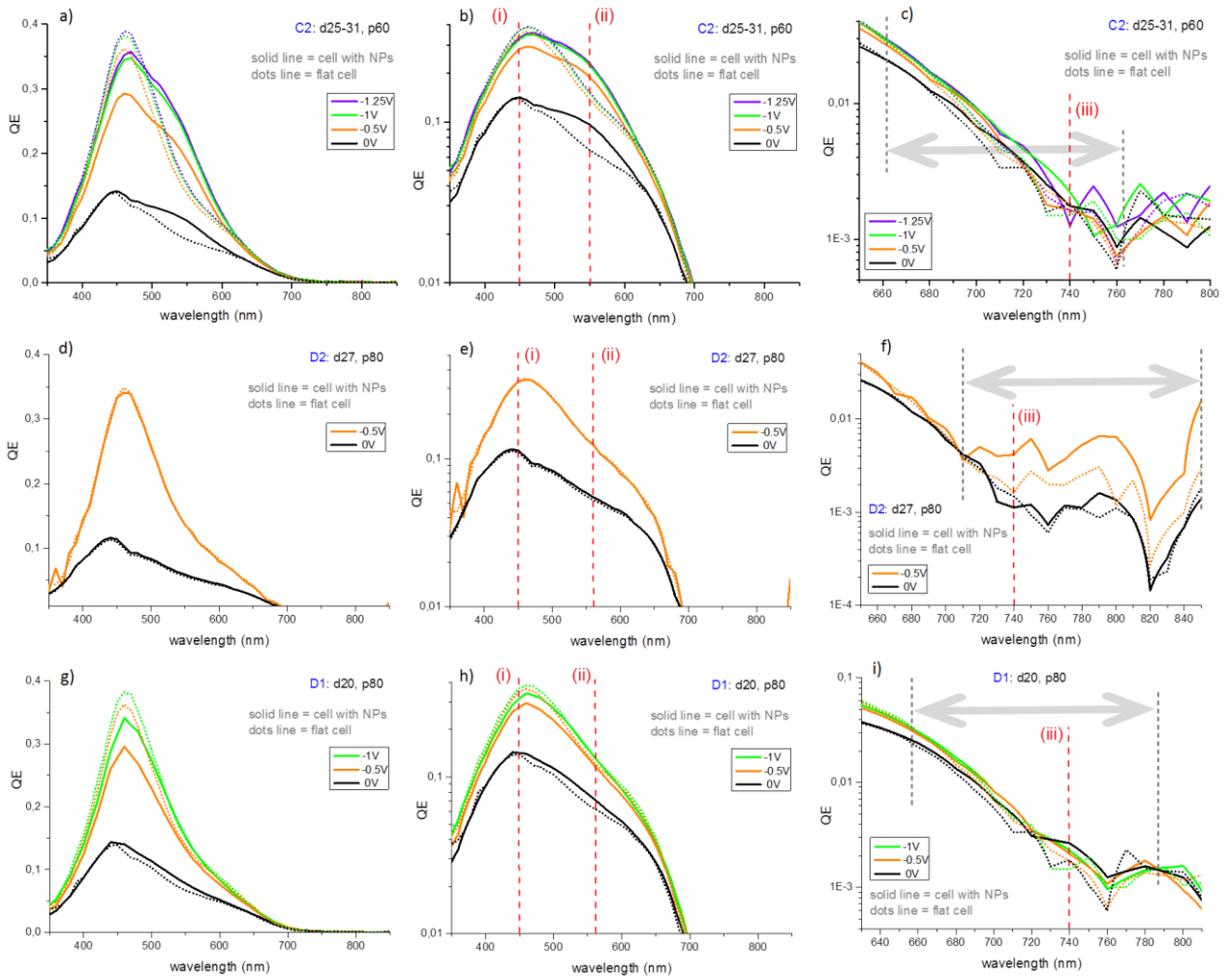


Figure 6.6: QE of cells C2, D2, D1.

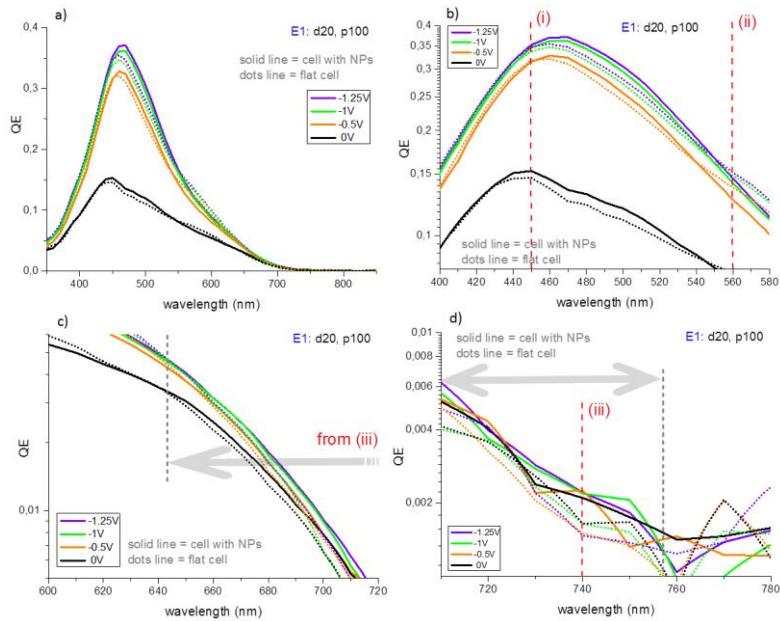


Figure 6.7: QE of cells E1.

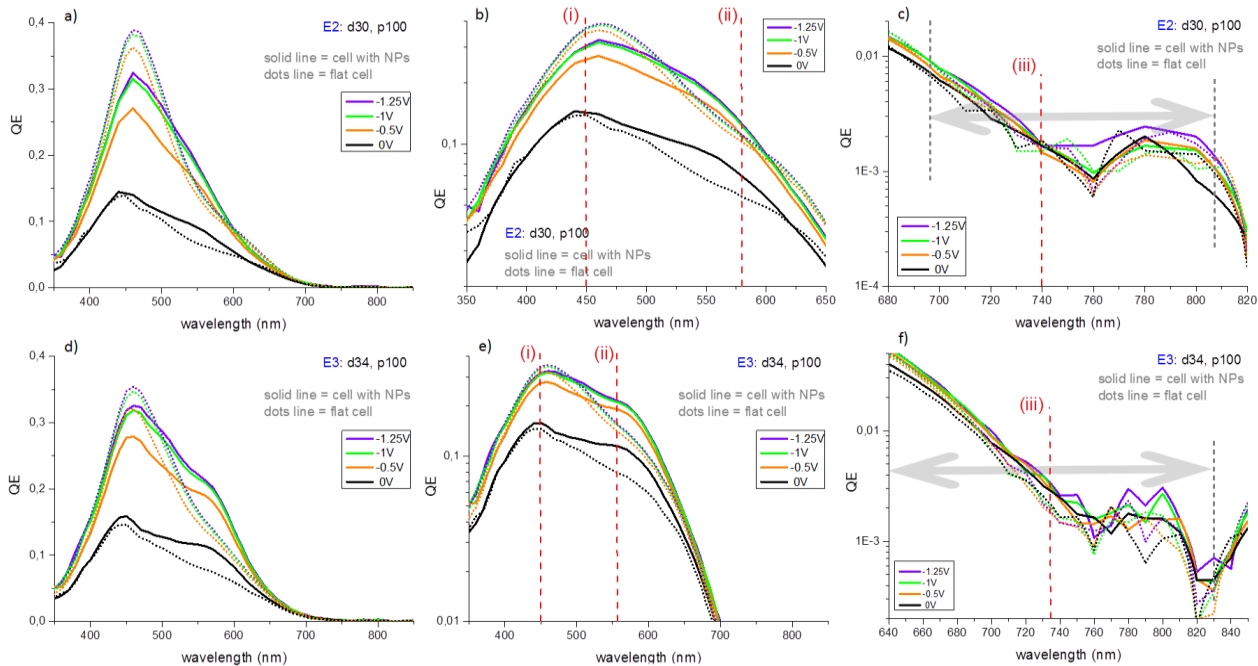


Figure 6.8: QE of cells E2, E3.

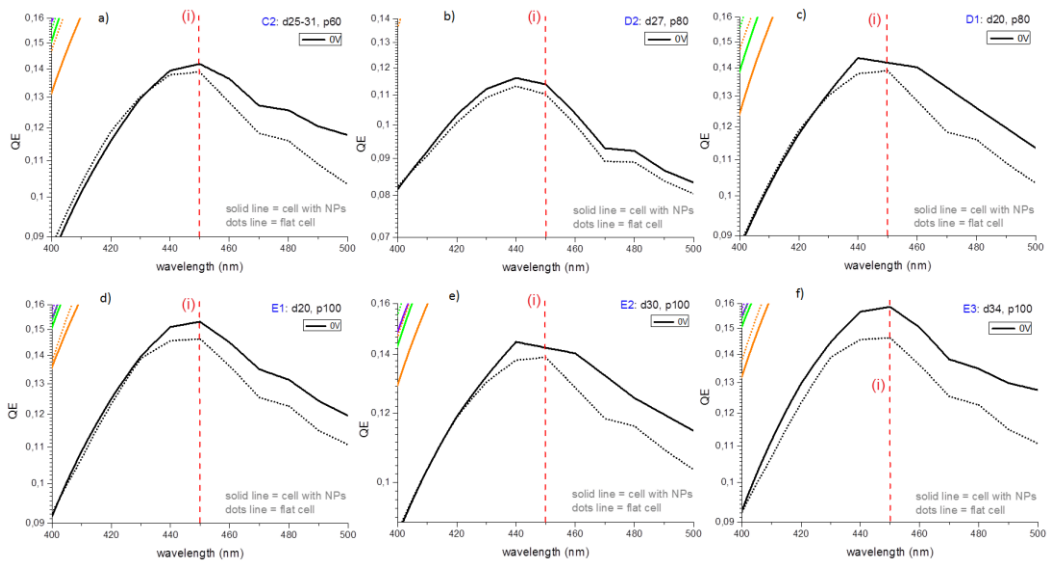


Figure 6.9: QE zoomed at 450 nm (LSPR (i)), at V=0.

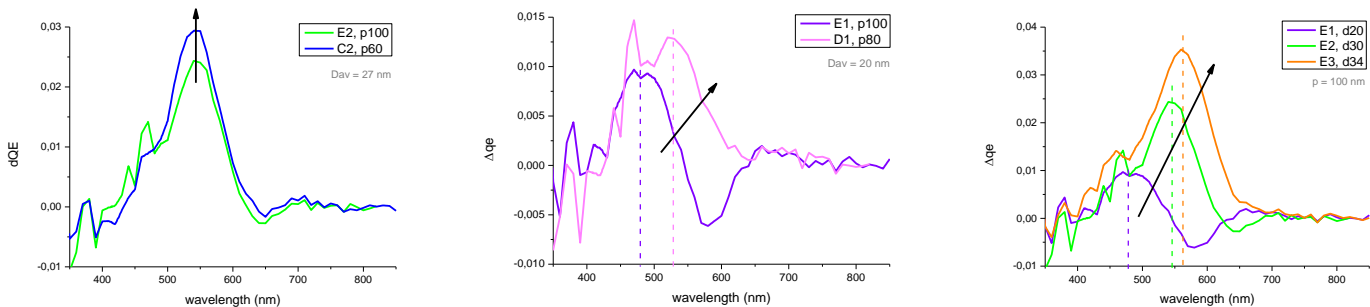


Figure 6.10: Delta-QE (at V=0), focused around LSPR (ii).

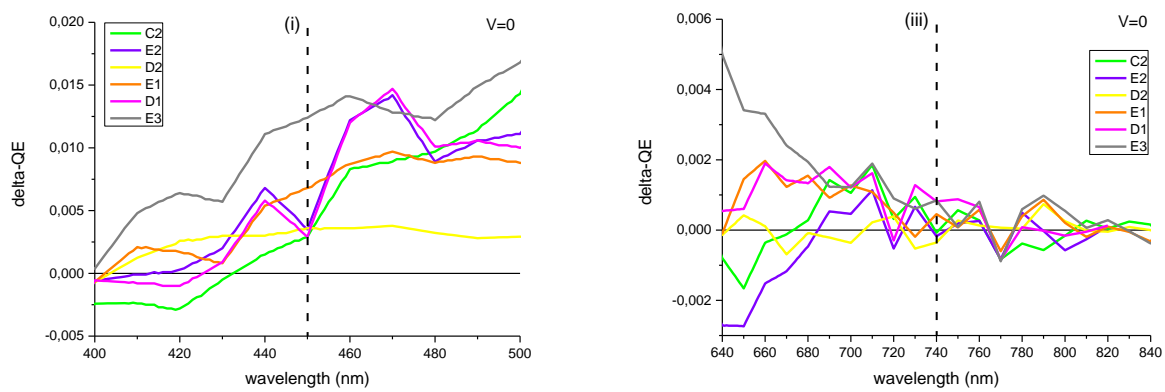


Figure 6.11: Delta-QE of all cells at $V=0$, zoomed around LSPR (i) and (iii).

7. Conclusions and outlooks

Two techniques for depositing metallic nanoparticles on semiconductor or oxides have been optimized: EBL and electroless plating.

A variety of metal nanoparticles on GaAs and a-Si:H has been studied. Only Ag nanoparticles have measurable photon absorption while no effect is seen with Ti/Au nanoparticles. SEM and AFM measurements show that size, shape and height are very variable with Ti/Au nanoparticles fabricated by EBL, within the pattern, and this combined with small density of patterns might be a reason for the unmeasurable absorbance enhancement.

The behavior of ordered Ag NPs fabricated by EBL depends on their size and thickness: 24-34 nm of diameter, array pitch of 100 nm and 15-30 nm of thickness give absorbance enhancement in the visible range between 500 and 600 nm of wavelength. Ag NPs of 20-34 nm size and 30 nm thick, incorporated into a-Si:H solar cell structure (thus covered by TCO) with varying array pitch (60/80/100 nm) show 3 localized surface plasmon resonances (LSPR): around 450 nm, 560 nm and 740 nm. LSPR at 560nm originates from scattering, while LSPRs at 450nm and 740nm, are due to NPs absorption. The tail of the peak at 740nm, falls below the gap of the semiconductor (a-Si:H) and the energy of the photons exciting the LSPs, can be translated in consequent emission of hot electrons.

Random Ag NPs patterns fabricated by electroless plating are characterized by larger size (larger than 60 nm) and, if, characterized by filling fraction higher than 15%, they give significant absorbance enhancement (20%) in the NIR range regardless the size or shape and already without TCO coating. This enhancement is caused by a huge suppression in transmission and can be exploited to promote photoemission in PV devices.

EELS measurements are conducted on Ag NPs deposited by electroless plating in order to investigate the nature of the absorption enhancement, which is not found on similar ordered patterns. Particular dimers (forming nano-bridges) and elongated particles are the responsible of the plasmonic excitations in the energy range of 0.9-1.5 eV, corresponding to part of the NIR range characterized by absorbance enhancement.

Spectral responses of Schottky diodes with the optically characterized NPs, are measured and in two types of GaAs solar cells (with Au and Ag nanoparticles) there was no clear efficiency enhancement in the NIR spectral range. In the case of Au nanoparticles it could be explained in similar way to the absorption data: the effect being broad is too weak. While, the absence of the expected plasmonic enhancement below the gap in devices with Ag NPs suggests that the energy of absorbed photons does not lead to photoemission but is dissipated through heat. GaAs is known to have very fast surface recombination and possibly it was not reduced well enough with the introduced Si_3N_4 layer.

On the other hand, quantum efficiency of a-Si:H solar cells show enhancement corresponding to the 3 LSPRs found in absorption spectra, but absorption contribute by NPs is enhanced by LSP less effectively

than scattering; furthermore, it is also less effective than absorption in semiconductor so the effect is worth to be used only if the peak can be shifted below the bandgap.

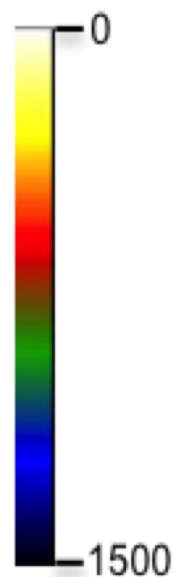
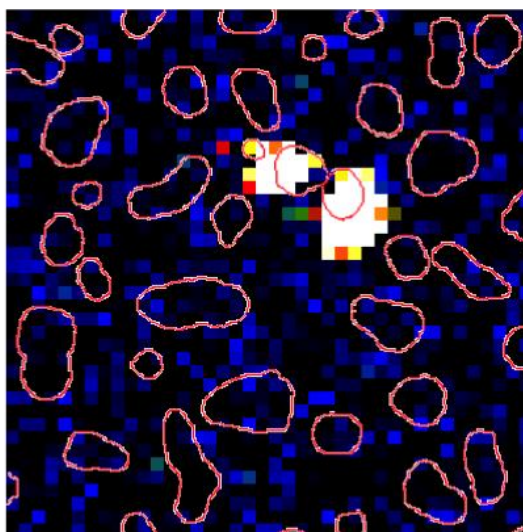
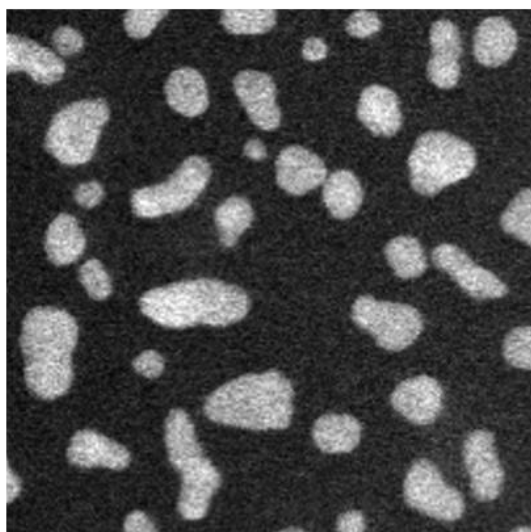
The main difference between GaAs diodes and A-Si:H diodes is the location of the NPs: apparently incorporating them at the back of the structure, even though still in direct contact with the absorber, seems to work better and a future work can be etched away the whole GaAs substrate, leaving only the thin film of GaAs. Another future development of the solar cell structure would be the incorporation of embedded NPs: if they are placed inside the semiconductor less energy would be lost to heat [65].

In conclusion, further developments are needed in the solar cell structure in order to reduce surface recombination and exploit the photoemission below the semiconductor energy gap; nevertheless, promising optical results showed here, confirmed the possibility to use nanostructures, in particular randomly distributed, to extend solar cells spectral response to longer wavelengths, through possibly cheap and simple technologies: EBL can be substituted by colloidal solutions implementation and electroless plating is not expensive and results to be effective within a broad set of parameters (size, shape, density). Another application of the studied NPs can be in NIR photodetectors.

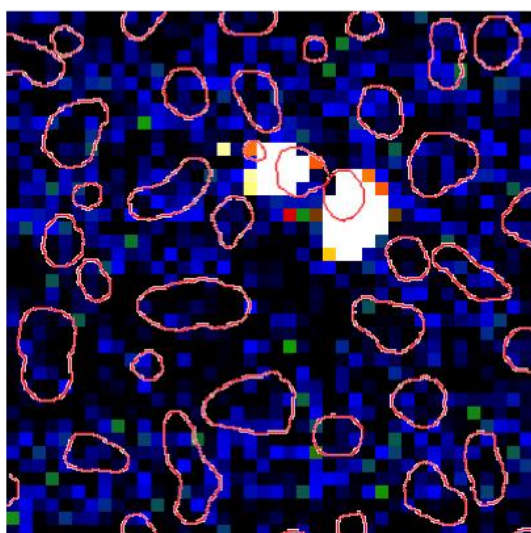
Appendix

Zone 2

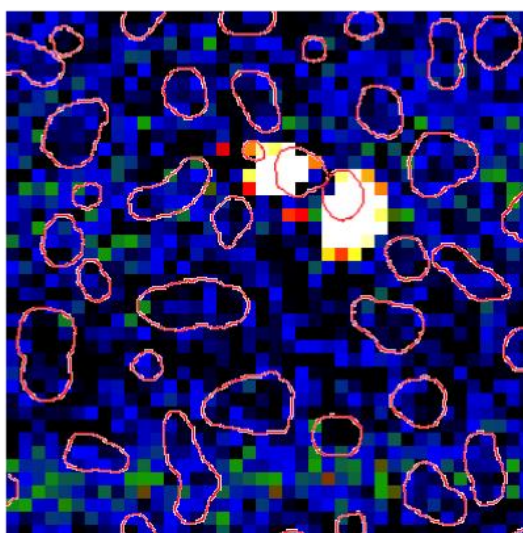
0.9 eV



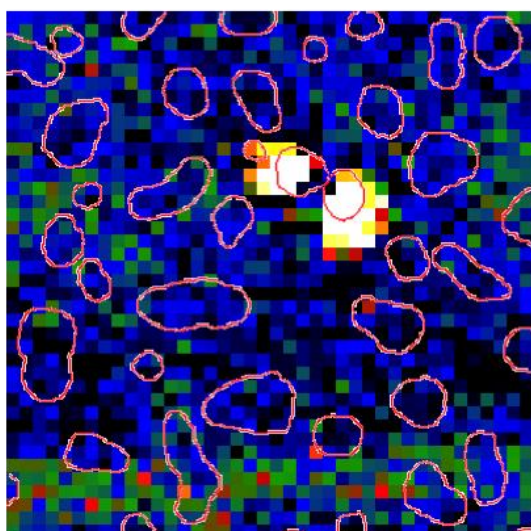
1.0 eV



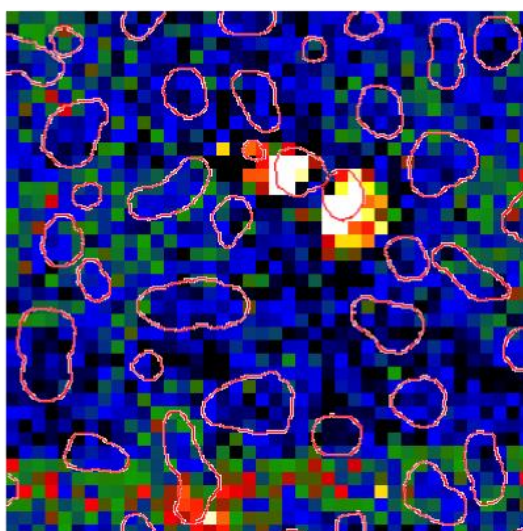
1.1 eV



1.2 eV

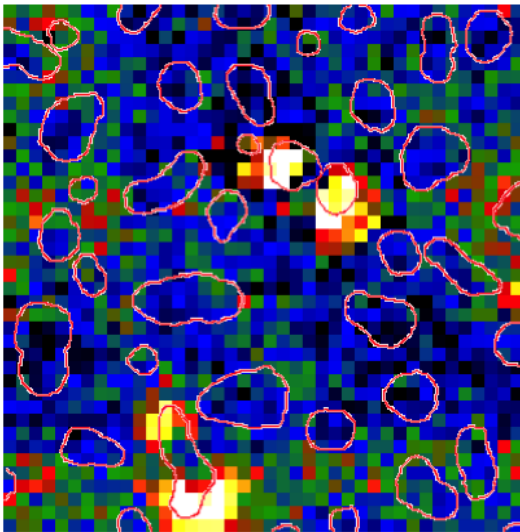


1.3 eV

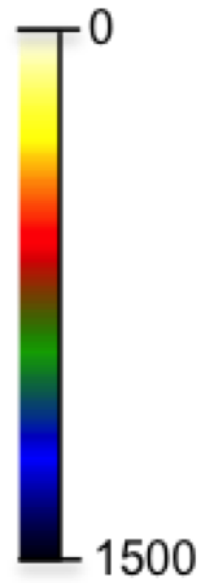
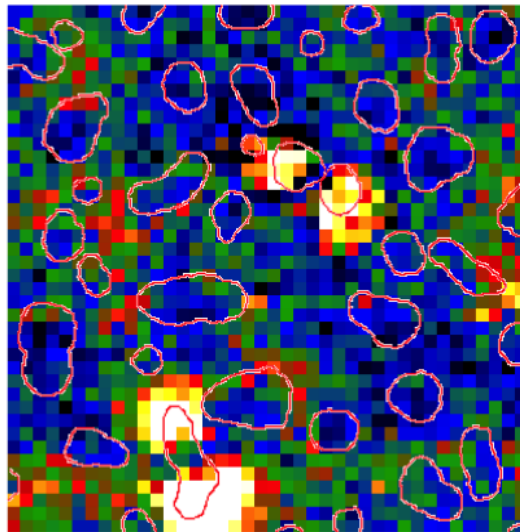


Zone 2

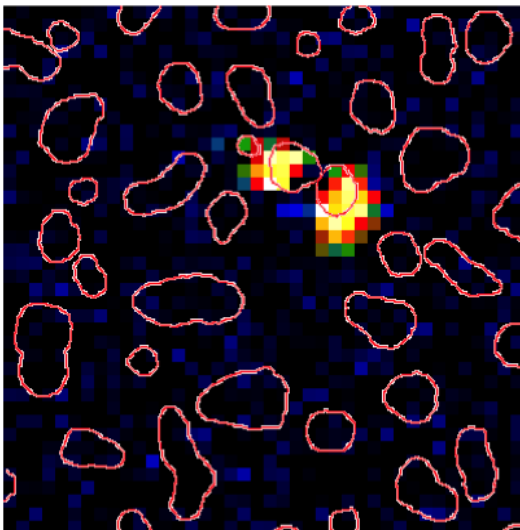
1.4 eV



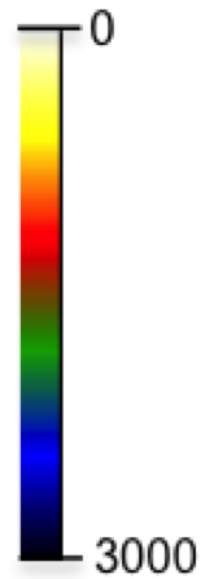
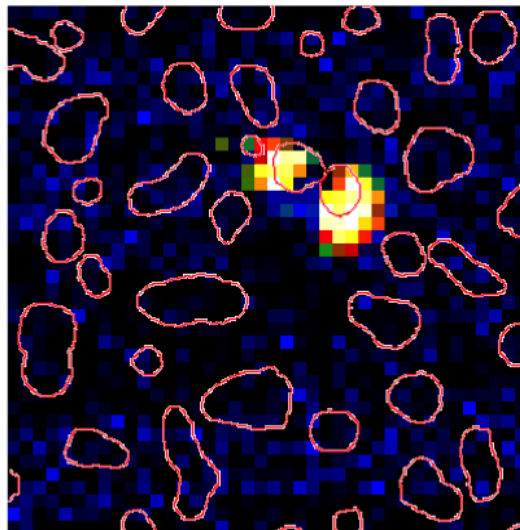
1.5 eV



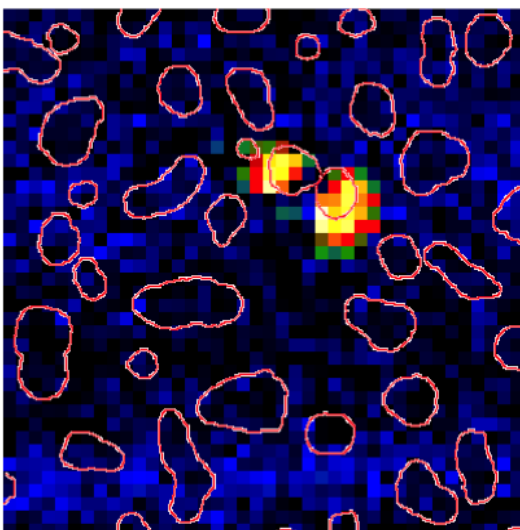
0.9 eV



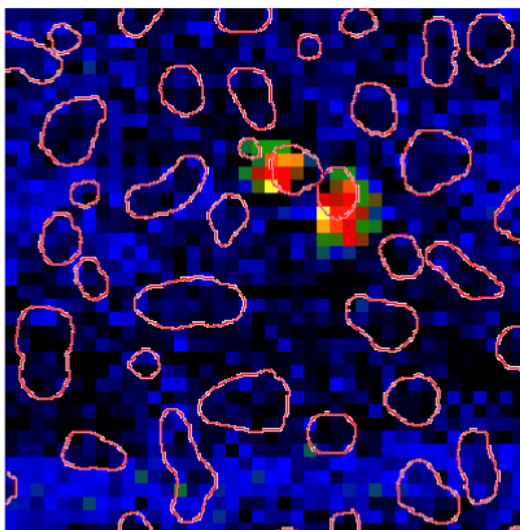
1.0 eV



1.1 eV

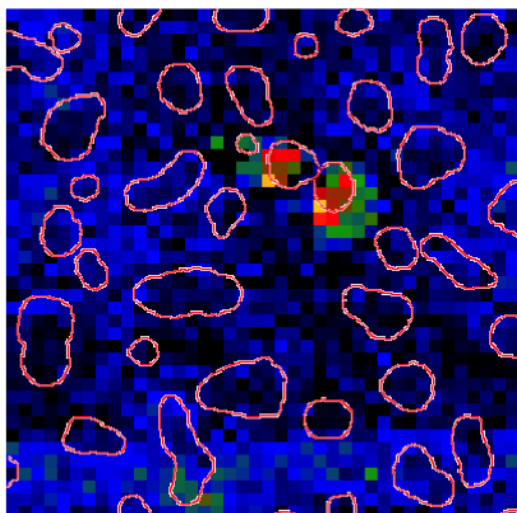


1.2 eV

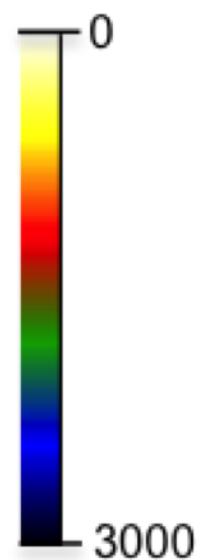
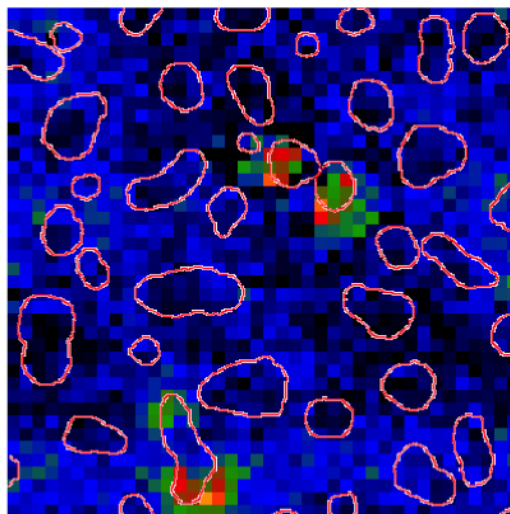


Zone 2

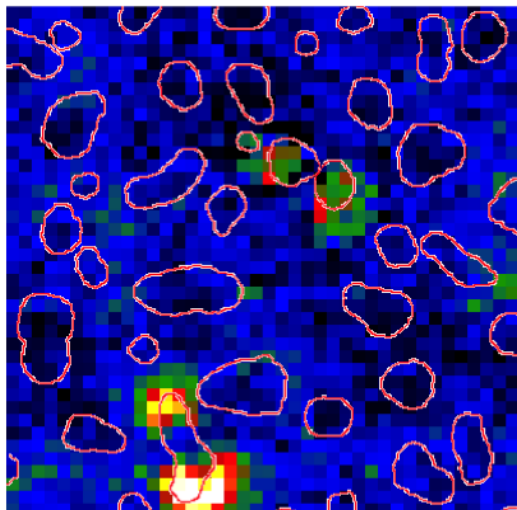
1.3 eV



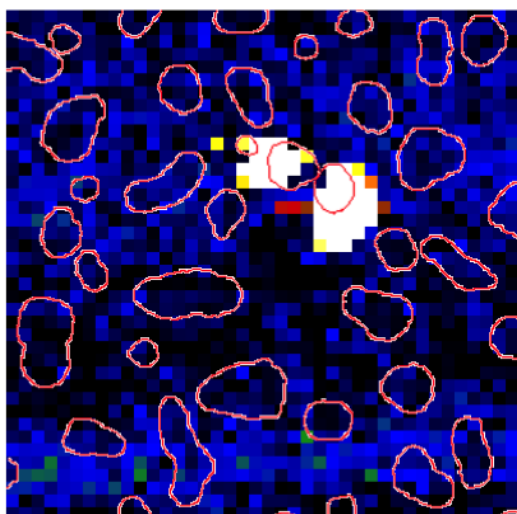
1.4 eV



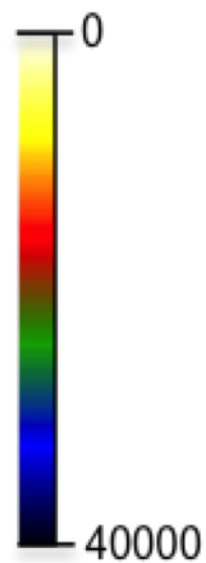
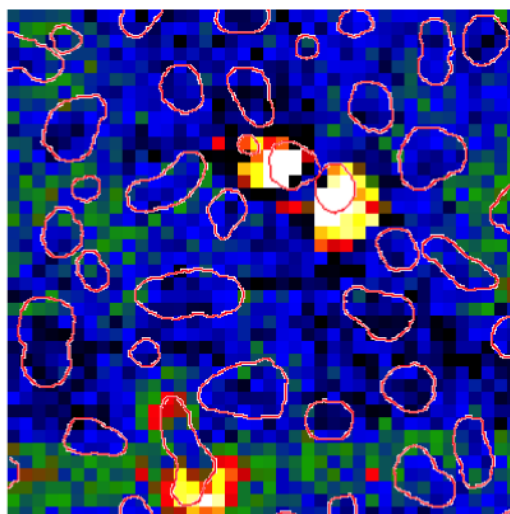
1.5 eV



0-9-1.2 eV

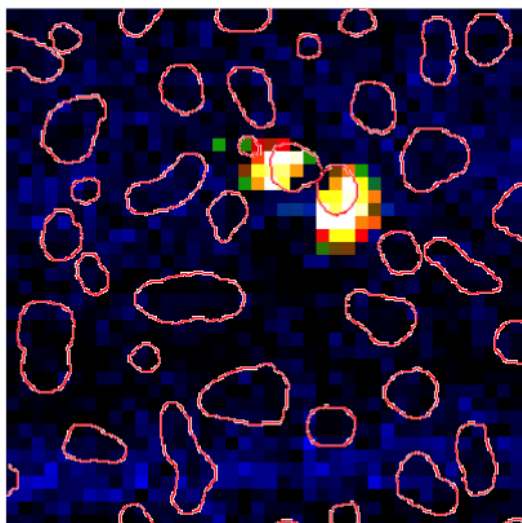


1.2-1.5 eV

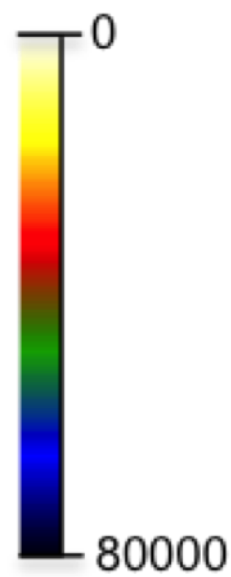
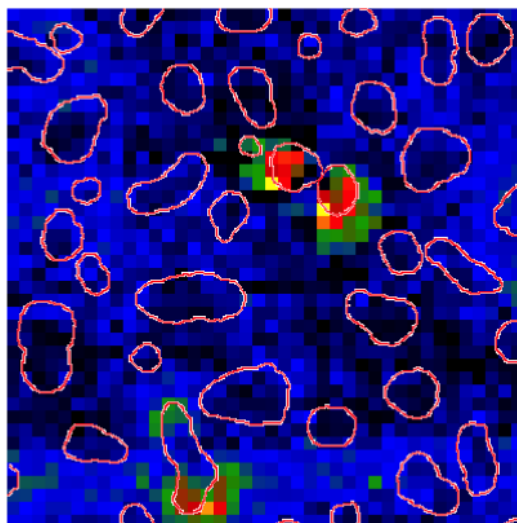


Zone 2

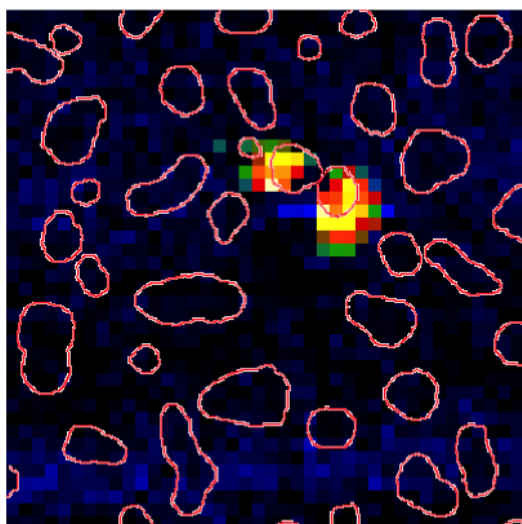
0-9-1.2 eV



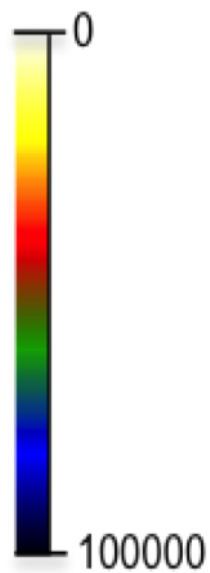
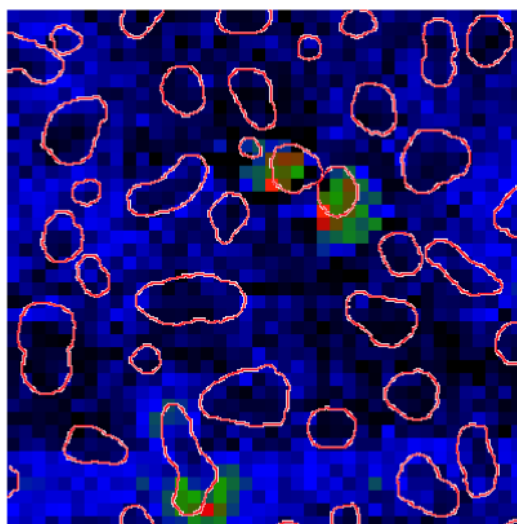
1.2-1.5 eV



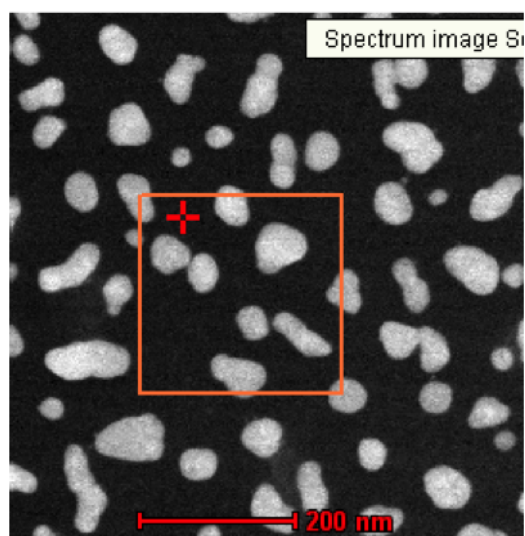
0-9-1.2 eV



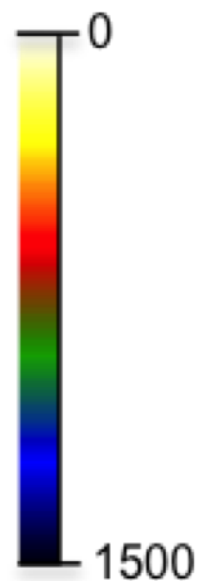
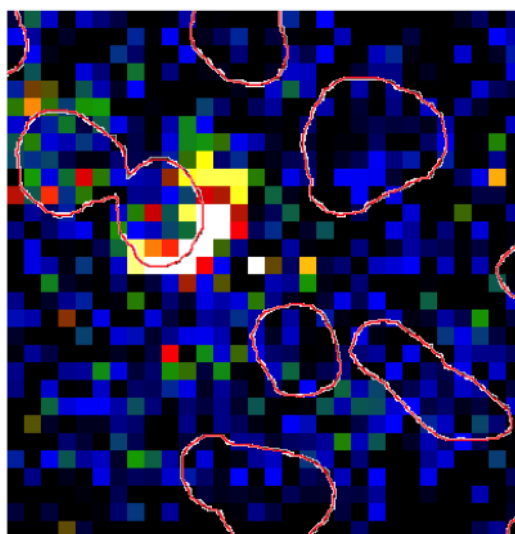
1.2-1.5 eV



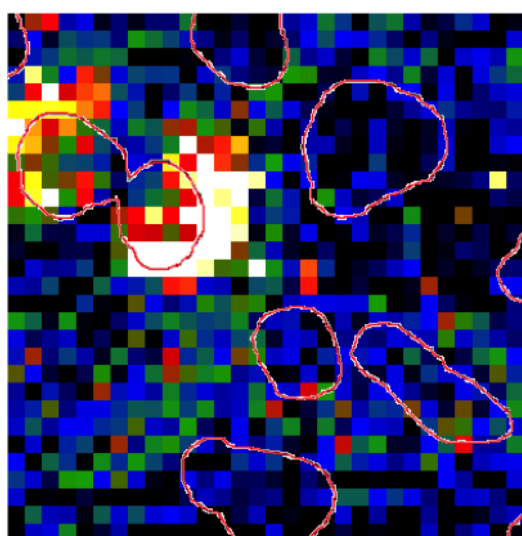
Zone 2-zoom



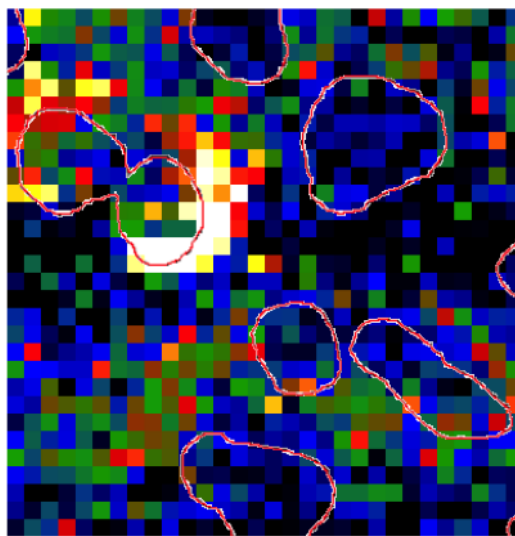
0.9 eV



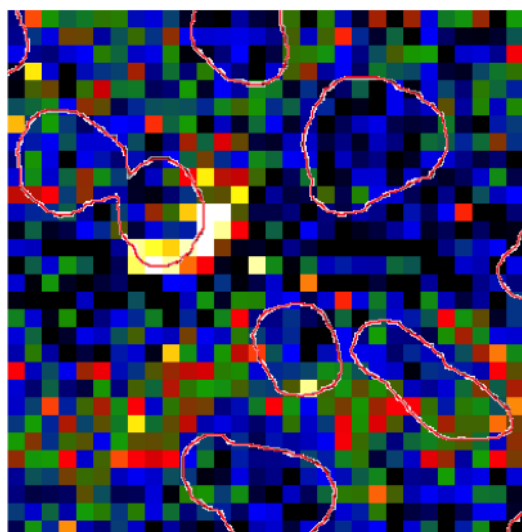
1.0 eV



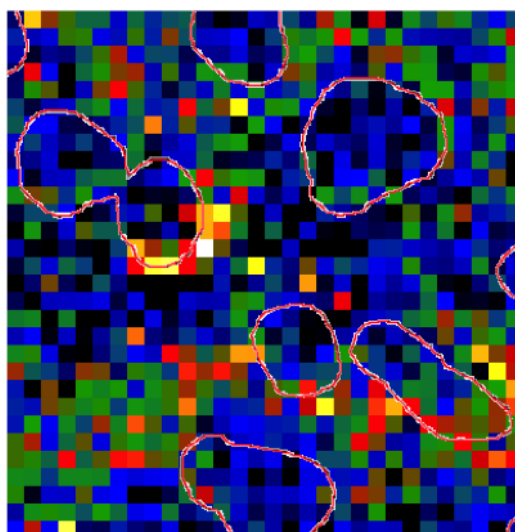
1.1 eV



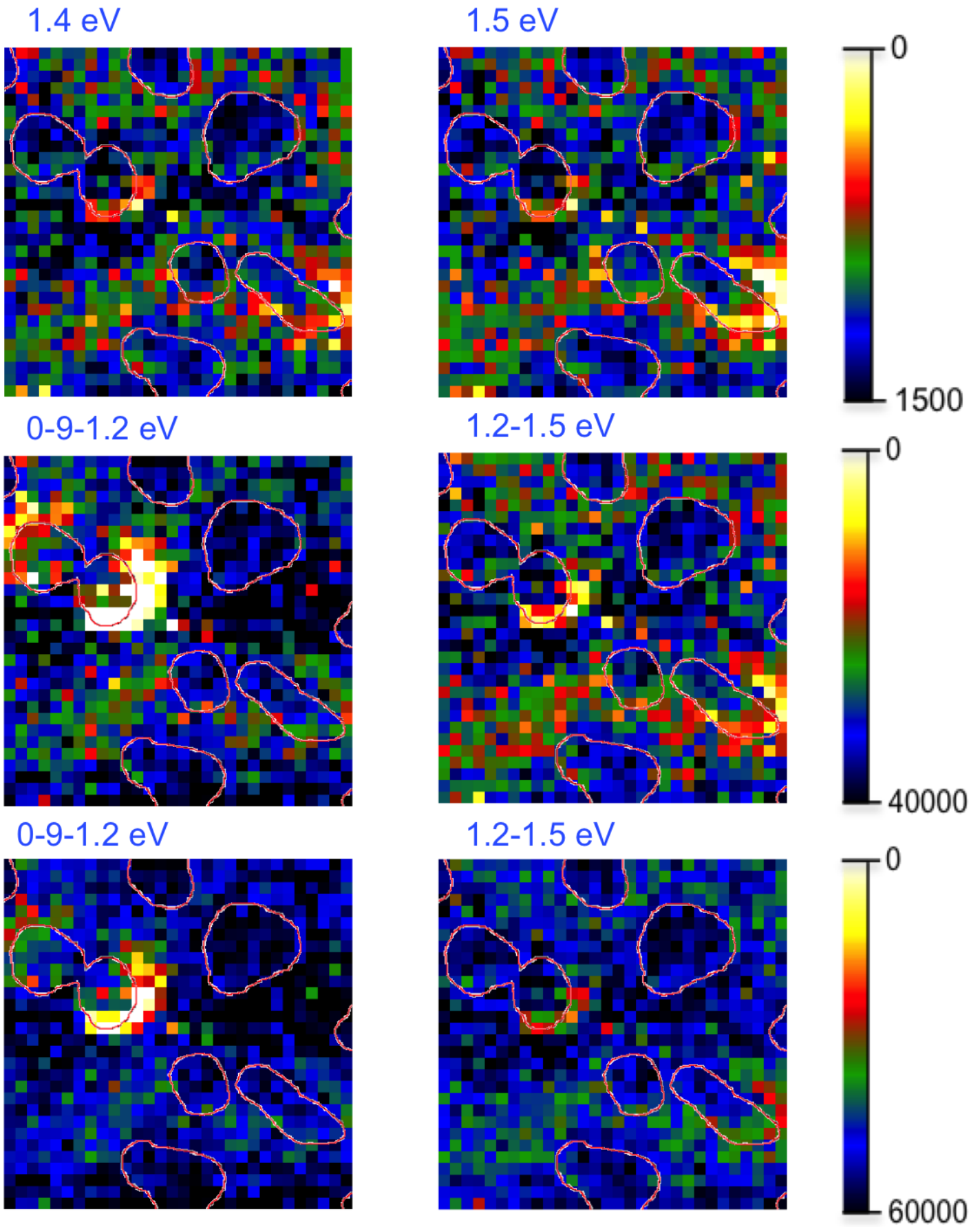
1.2 eV



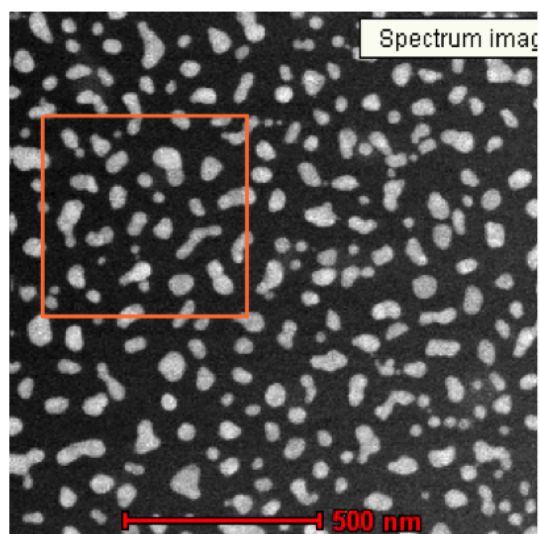
1.3 eV



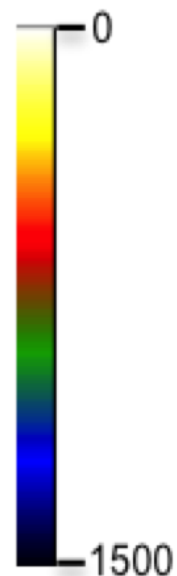
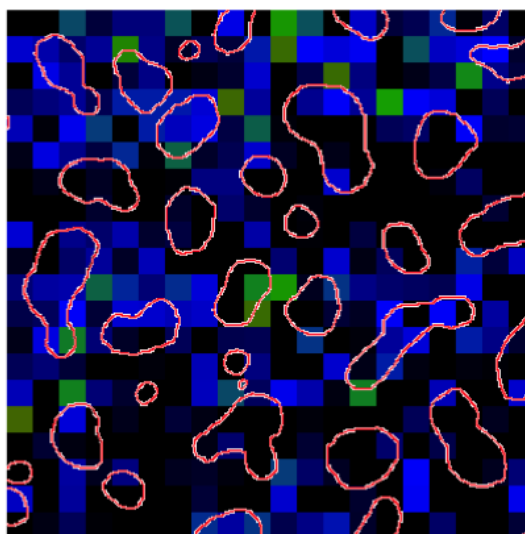
Zone 2-zoom



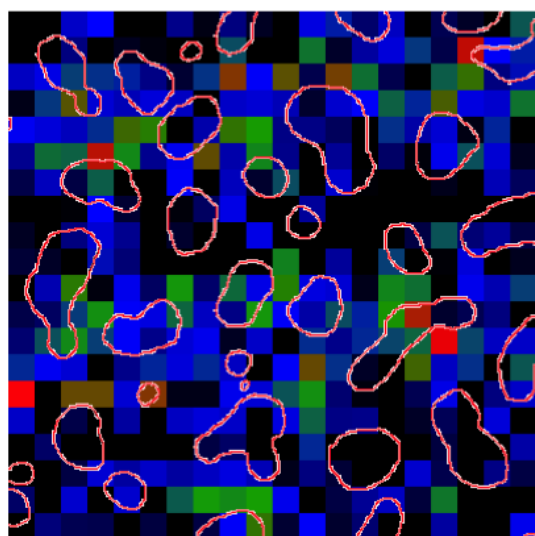
Zone 3



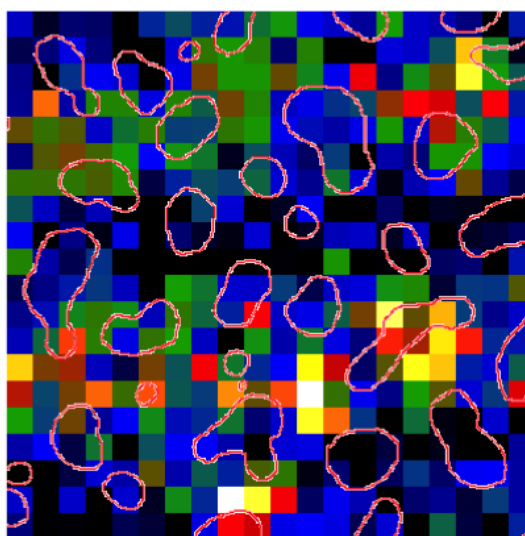
0.9 eV



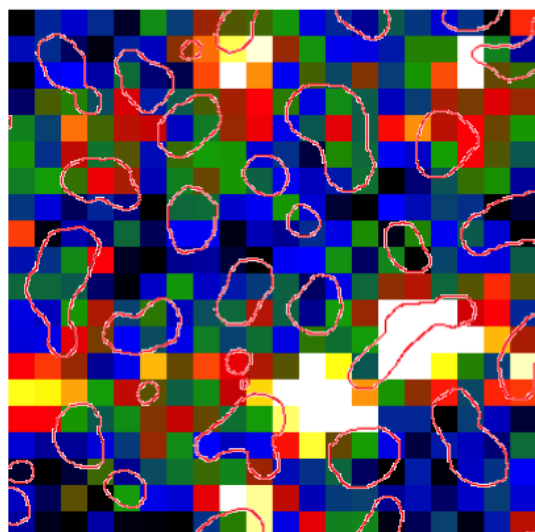
1.0 eV



1.1 eV

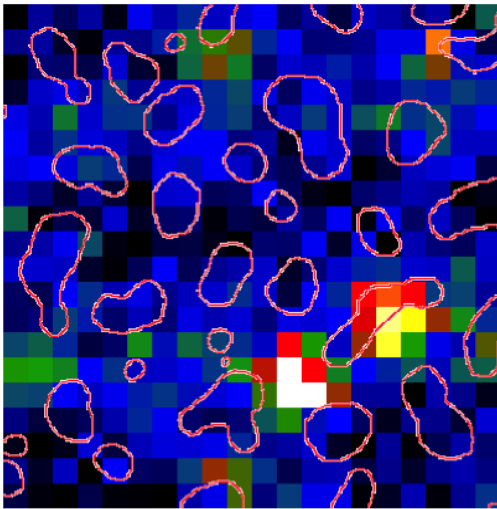


1.2 eV

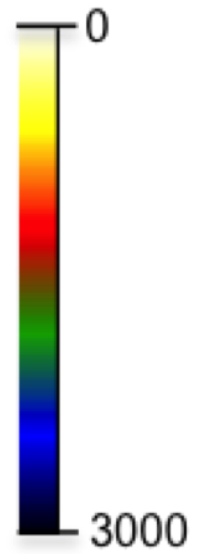
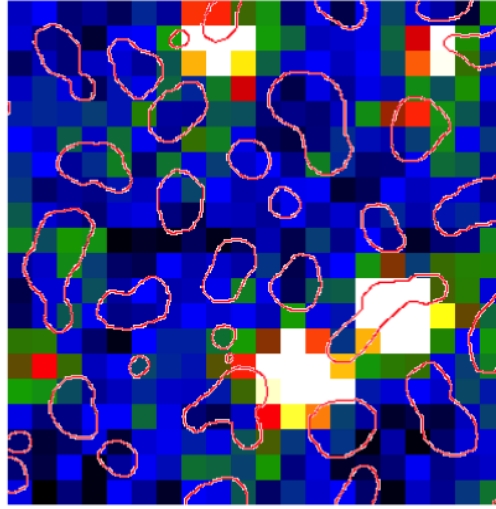


Zone 3

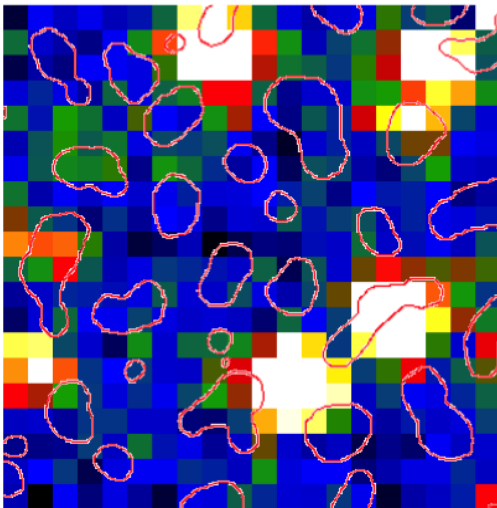
1.2 eV



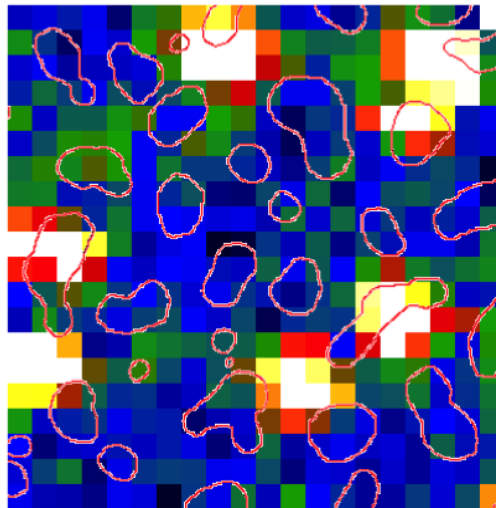
1.3 eV



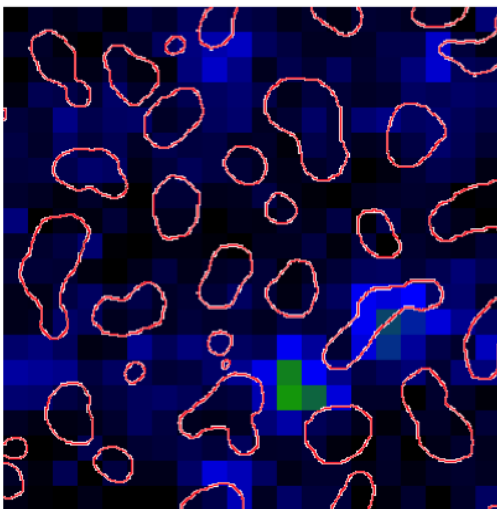
1.4 eV



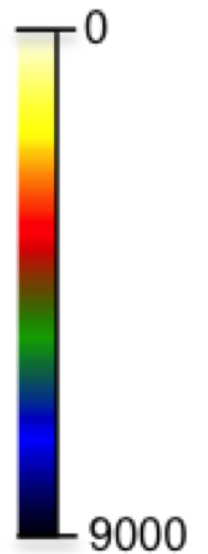
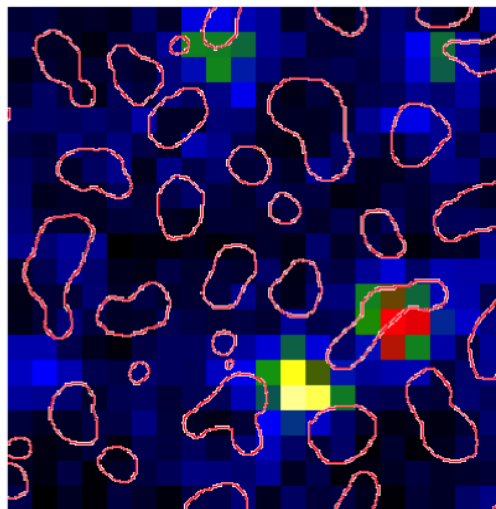
1.5 eV



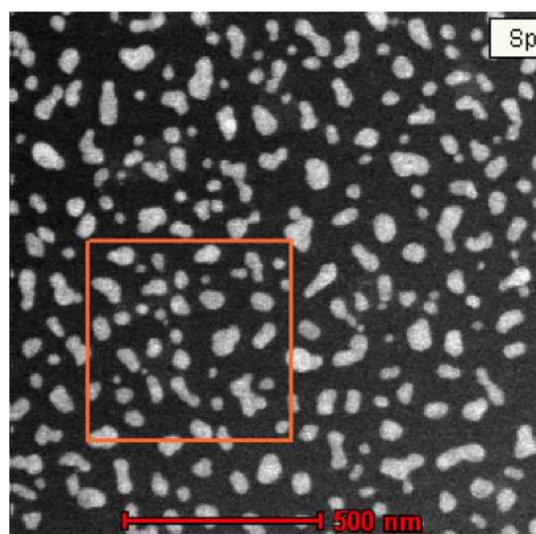
1.2 eV



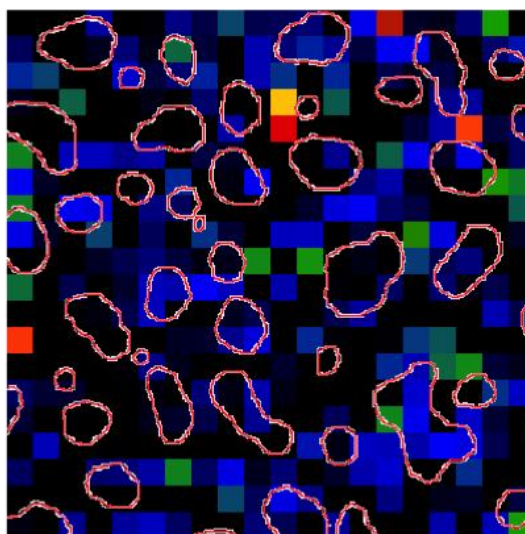
1.3 eV



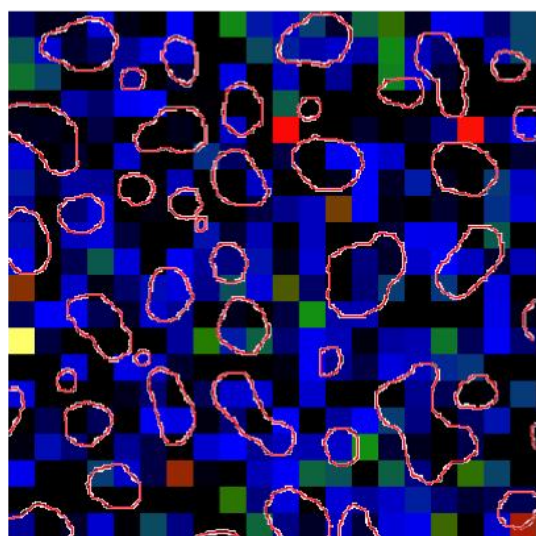
Zone 4



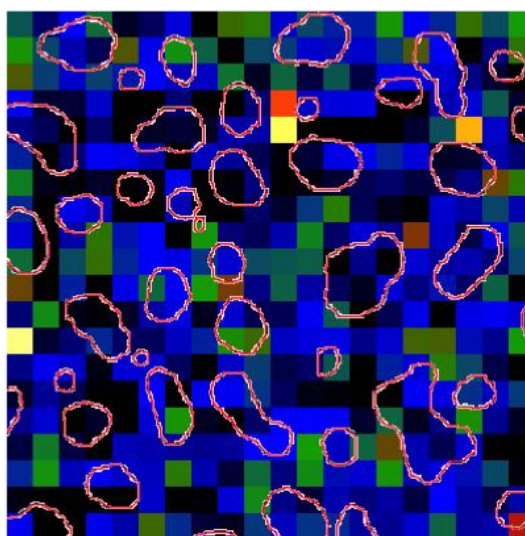
0.9 eV



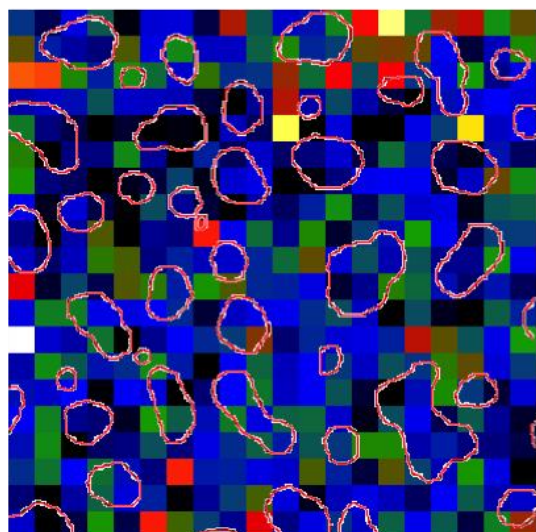
1.0 eV



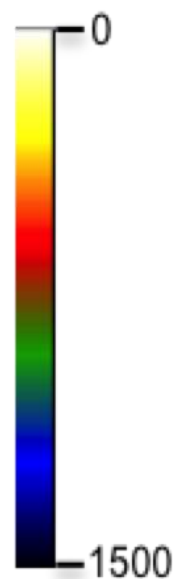
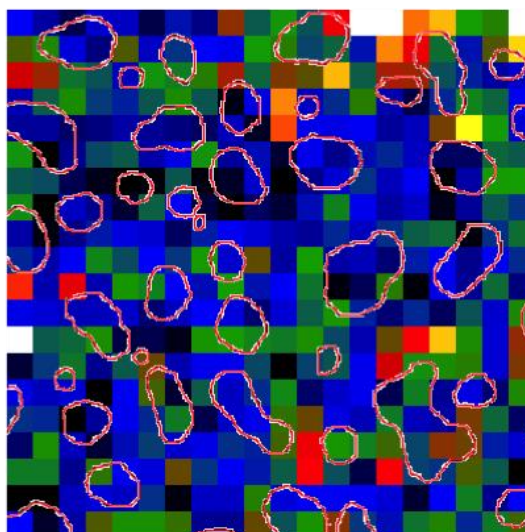
1.1 eV



1.2 eV

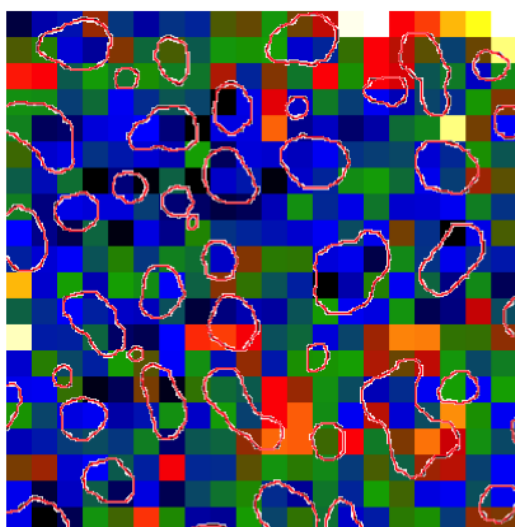


1.3 eV

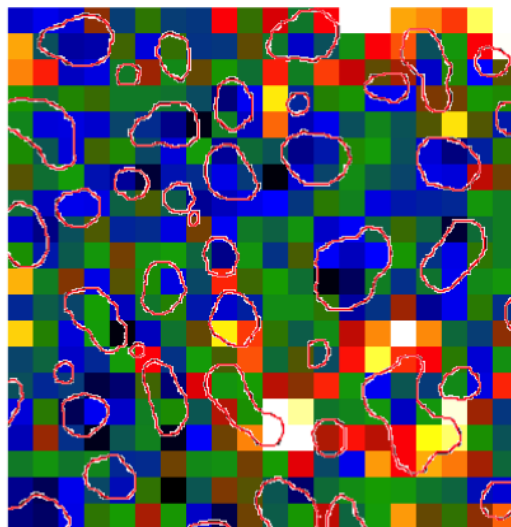


Zone 4

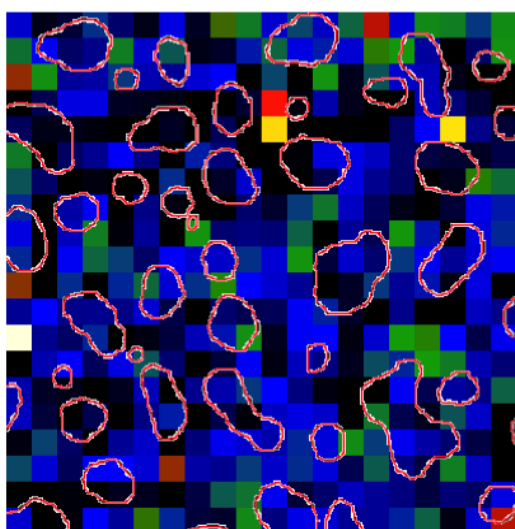
1.4 eV



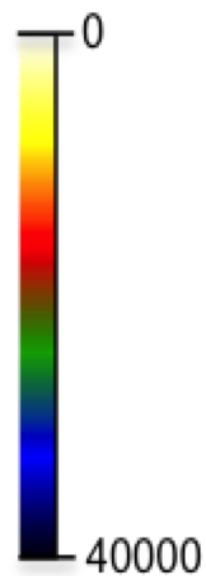
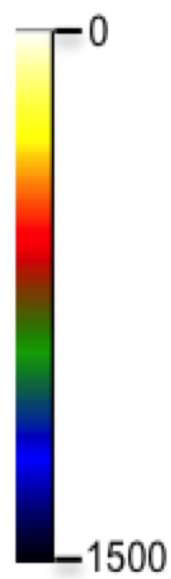
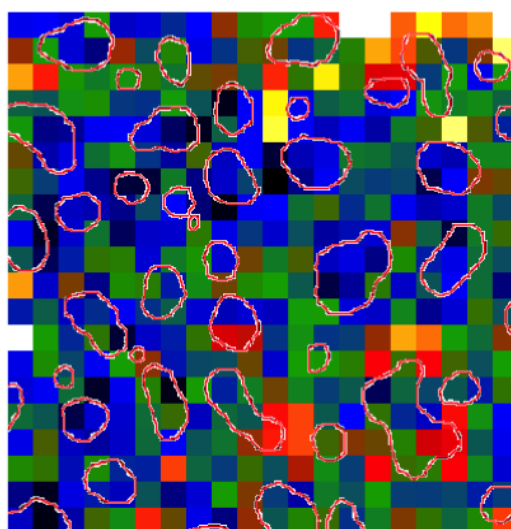
1.5 eV



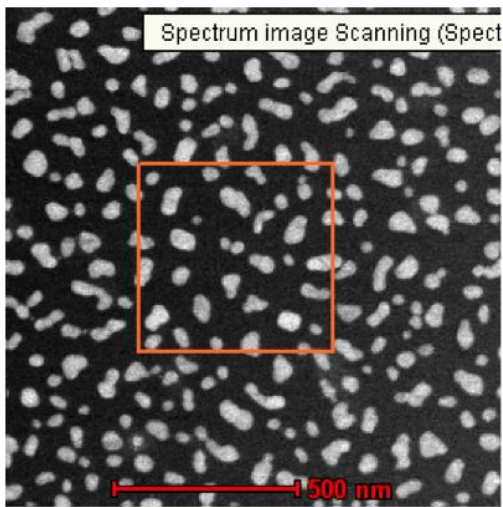
0.9-1.2 eV



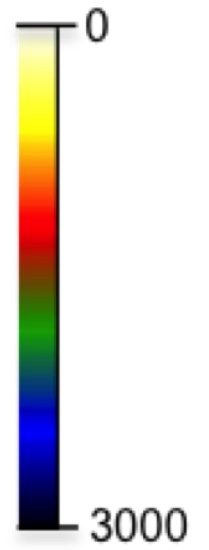
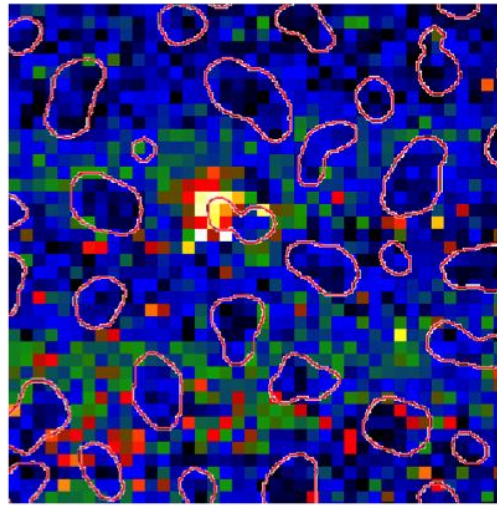
1.2-1.5 eV



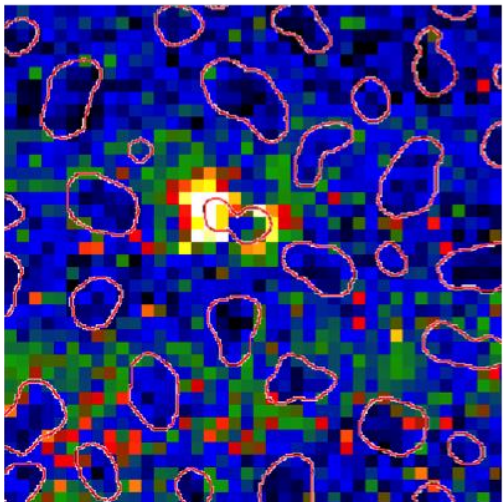
Zone 5



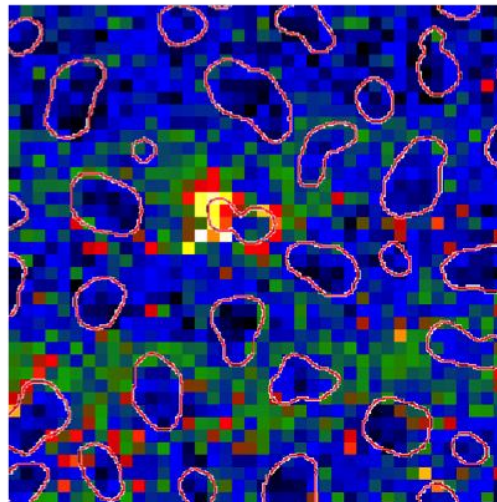
1.2 eV



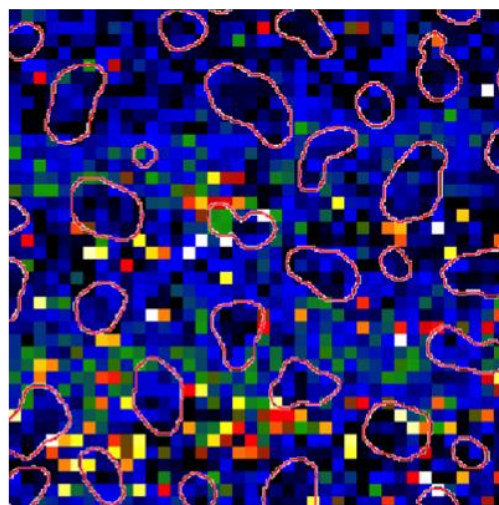
1.3 eV



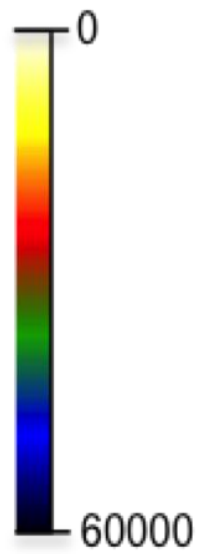
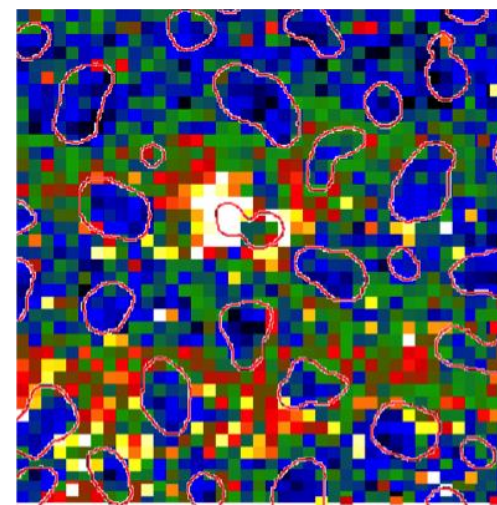
1.4 eV



0.9-1.2 eV

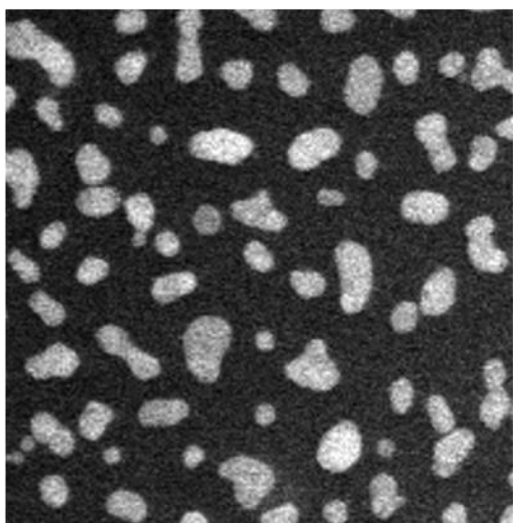


1.2-1.5 eV

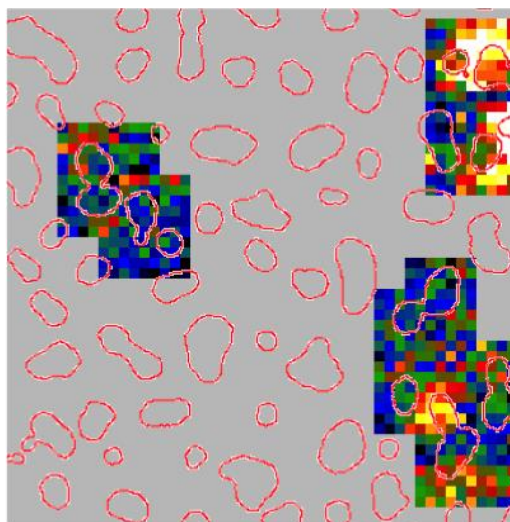


Zone 6

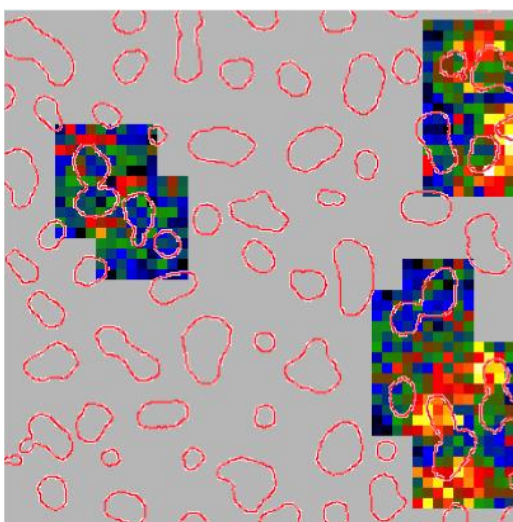
0.9 eV



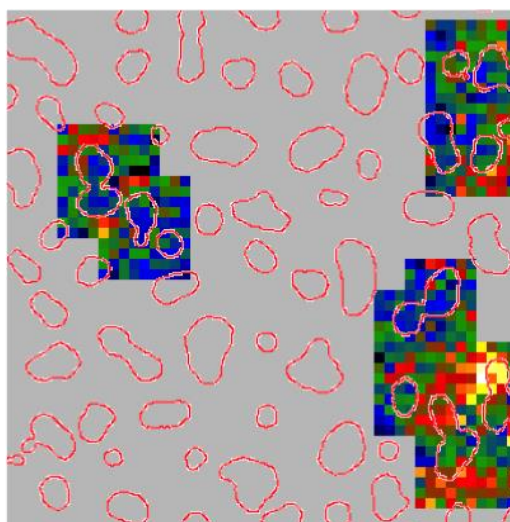
1.0 eV



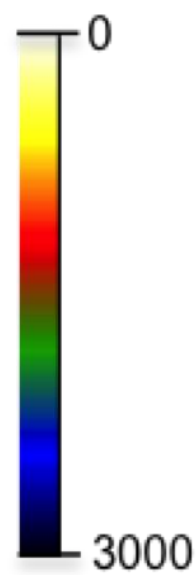
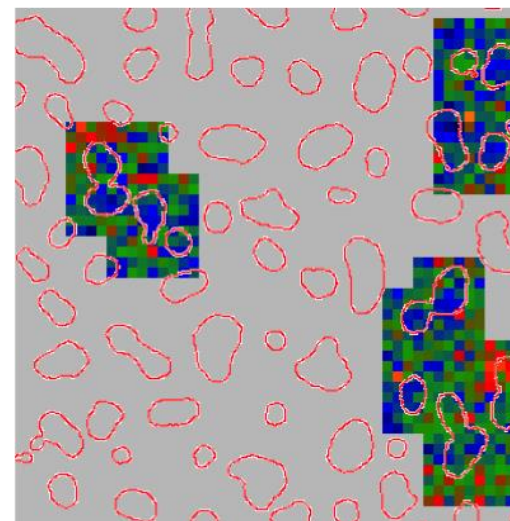
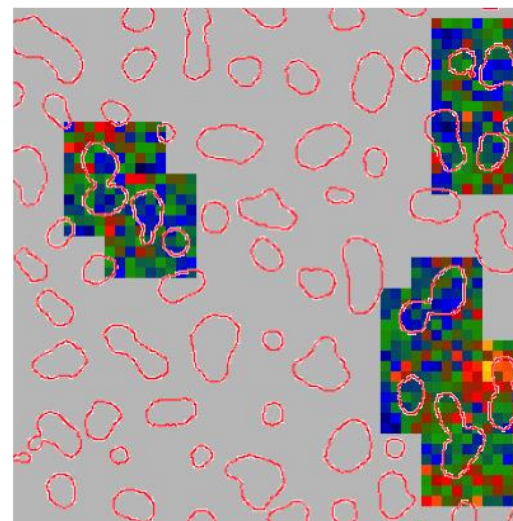
1.1 eV



1.2 eV

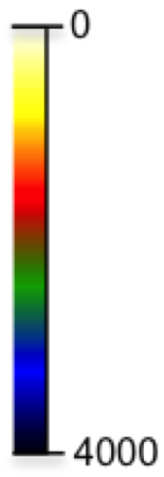
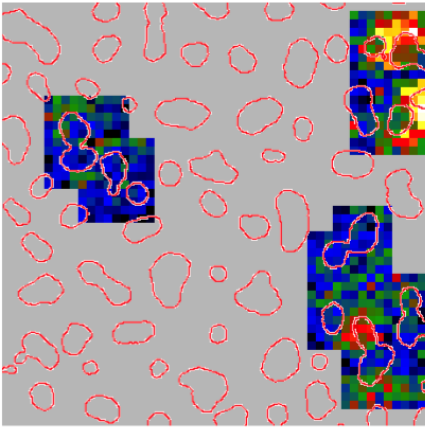


1.3 eV

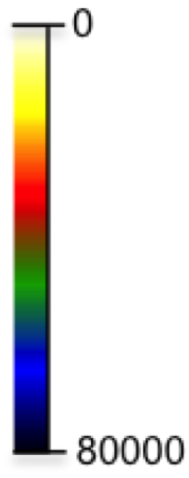
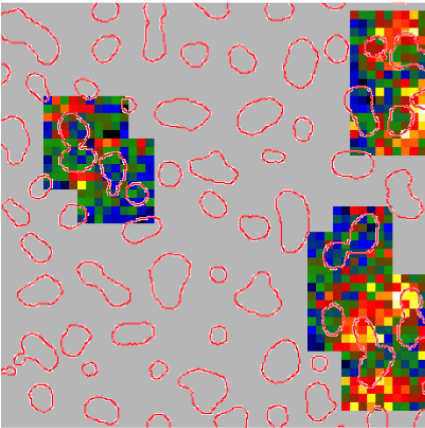


Zone 6

0.9 eV



0.9-1.2 eV



Publications

Related to this work

Photon absorption and photocurrent in solar cells below semiconductor bandgap due to electron photoemission from plasmonic nanoantennas.

A. Novitsky, A. V. Uskov, C. Gritti, I. E. Protsenko, B. E. Kardynał, A. V. Lavrinenko
Progress in Photovoltaics, DOI: 10.1002/pip.2278, (2012)

Photocurrent Enhancement with Photoemission from Metal Nanoparticles.

C. Gritti, A. Novitsky, R. Malureanu, A. Lavrinenko, B. Kardynał, A. Uskov
Part of: Proceedings of SPIE Photonics Europe (2012)

The manuscript of a paper including optical and electrical characterization of a-Si:H solar cells will be soon submitted.

Not related to this work

Origin of low quantum efficiency of photoluminescence of InP/ZnS nanocrystals

R. Shirazi, A. Kovacs, D. Dan Corell, C. Gritti, A. Thorseth, C. Dam-Hansen, P. M. Petersen, B. Kardynał

Journal of Luminescence, Volume 145, Pages 936–939 (2014)

A new method for obtaining transparent electrodes

R. Malureanu, M. Zalkovskij, Z. Song, C. Gritti, A. Andryeuskij, Q. He, L. Zhou, P. Uhd Jepsen, and A. V. Lavrinenko

Optics Express, Vol. 20, Issue 20, pp. 22770-22782 (2012)

Increased electron photoemission from plasmonic nanoparticles and photoemission enhanced solar cells

A. Novitsky, A. Uskov, C. Gritti, I. Protsenko, B. Kardynal, A. Lavrinenko

Part of: Proceedings of the Asia-Pacific Conference on Fundamental Problems of Opto-and Microelectronics (2011)

Embedded Porous Si Reflectors for Epitaxial Solar Cells: Stability, Optical Performance and Industrial Manufacturability

J. van Hoeymissen, C. Gritti, J. Deckers, H. Sivaramakrishnan Radhakrishnan, J. Poortmans

Part of: Proceedings of the European Photovoltaic Solar Energy Conference and Exhibition (2010)

Bibliography

- [1] J. Hansen, M. Sato, and R. Ruedy, "Perception of climate change.," *Proc. Natl. Acad. Sci. U. S. A.*, vol. 109, no. 37, pp. E2415–23, Sep. 2012.
- [2] M. Bender, T. Sowers, and E. Brook, "Gases in ice cores.," *Proc. Natl. Acad. Sci. U. S. A.*, vol. 94, no. 16, pp. 8343–9, Aug. 1997.
- [3] and R. A. T. Boden, G. Marland, "Global, Regional, and National Fossil-Fuel CO₂. Emissions in Trends, 2013," *Glob. Carbon Proj.*, no. November, 2013.
- [4] W. G. III, "Climate change 2014, mitigation of climate change," *Proc. Natl. Acad. Sci. U. S. A.*, vol. 5, 2014.
- [5] M. Moskovits, "Surface-enhanced spectroscopy," *Am. Phys. Soc.*, vol. 57, no. 3, pp. 783–826, 1985.
- [6] K. Kneipp, Y. Wang, H. Kneipp, L. Perelman, I. Itzkan, R. Dasari, and M. Feld, "Single Molecule Detection Using Surface-Enhanced Raman Scattering (SERS)," *Phys. Rev. Lett.*, vol. 78, no. 9, pp. 1667–1670, Mar. 1997.
- [7] S. Nie, "Probing Single Molecules and Single Nanoparticles by Surface-Enhanced Raman Scattering," *Science (80-.)*, vol. 275, no. 5303, pp. 1102–1106, Feb. 1997.
- [8] T. A. Taton, "Scanometric DNA Array Detection with Nanoparticle Probes," *Science (80-.)*, vol. 289, no. 5485, pp. 1757–1760, Sep. 2000.
- [9] S. Schultz, D. R. Smith, J. J. Mock, and D. A. Schultz, "Single-target molecule detection with nonbleaching multicolor optical immunolabels.," *Proc. Natl. Acad. Sci. U. S. A.*, vol. 97, no. 3, pp. 996–1001, Feb. 2000.
- [10] K. Li, M. I. Stockman, and D. J. Bergman, "Self-Similar Chain of Metal Nanospheres as an Efficient Nanolens," *Phys. Rev. Lett.*, vol. 91, no. 22, p. 227402, Nov. 2003.
- [11] T. Kalkbrenner, M. Ramstein, J. Mlynek, and V. Sandoghdar, "A single gold particle as a probe for apertureless scanning near-field optical microscopy," *J. Microsc.*, vol. 202, no. Pt 1, pp. 72–6, Apr. 2001.
- [12] X. Zhang and Z. Liu, "Superlenses to overcome the diffraction limit.," *Nat. Mater.*, vol. 7, no. 6, pp. 435–41, Jun. 2008.
- [13] H. Ditlbacher, J. R. Krenn, G. Schider, a. Leitner, and F. R. Aussenegg, "Two-dimensional optics with surface plasmon polaritons," *Appl. Phys. Lett.*, vol. 81, no. 10, p. 1762, 2002.
- [14] N. Engheta, "Circuits with light at nanoscales: optical nanocircuits inspired by metamaterials.," *Science*, vol. 317, no. 5845, pp. 1698–702, Sep. 2007.

- [15] H. A. Atwater and A. Polman, "Plasmonics for improved photovoltaic devices," *Nat. Mater.*, vol. 9, no. 3, pp. 205–13, Mar. 2010.
- [16] K. R. Catchpole and A. Polman, "Plasmonic solar cells," *Opt. Express*, vol. 16, no. 26, pp. 21793–800, Dec. 2008.
- [17] C. Rockstuhl and F. Lederer, "Photon management by metallic nanodiscs in thin film solar cells," *Appl. Phys. Lett.*, vol. 94, no. 21, p. 213102, 2009.
- [18] E. T. Yu, "Nanoplasmonics for photovoltaic applications," in *Chapter 11-Nanoplasmonics for Photovoltaics Applications*, 2010, pp. 391–421.
- [19] S. Pillai and M. A. Green, "Plasmonics for photovoltaic applications," *Sol. Energy Mater. Sol. Cells*, vol. 94, no. 9, pp. 1481–1486, Sep. 2010.
- [20] W. Rechberger, a. Hohenau, a. Leitner, J. R. Krenn, B. Lamprecht, and F. R. Aussenegg, "Optical properties of two interacting gold nanoparticles," *Opt. Commun.*, vol. 220, no. 1–3, pp. 137–141, May 2003.
- [21] B. Augu   and W. Barnes, "Collective Resonances in Gold Nanoparticle Arrays," *Phys. Rev. Lett.*, vol. 101, no. 14, p. 143902, Sep. 2008.
- [22] A. Shalav, B. S. Richards, and M. A. Green, "Luminescent layers for enhanced silicon solar cell performance: Up-conversion," *Sol. Energy Mater. Sol. Cells*, vol. 91, no. 9, pp. 829–842, May 2007.
- [23] M. Emziane and A. Sleiman, "Multi-junction solar cell designs," in *2011 IEEE GCC Conference and Exhibition (GCC)*, 2011, pp. 361–364.
- [24] A. Novitsky, A. V Uskov, C. Gritti, I. E. Protsenko, and B. E. Kardynal, "Photon absorption and photocurrent in solar cells below semiconductor bandgap due to electron photoemission from plasmonic nanoantennas," *Prog. Photovoltaics Res. Appl.*, vol. 1, no. 4, pp. 422–426, 2012.
- [25] S. A. Maier, *PLASMONICS: FUNDAMENTALS AND APPLICATIONS*. 2007.
- [26] D. R. C. Bohren, F. Huffman, *Absorption and Scattering of Light by Small Particles*. Wiley-VCH Verlag, 2004, pp. 82–129.
- [27] K. L. Kelly, E. Coronado, L. L. Zhao, and G. C. Schatz, "The Optical Properties of Metal Nanoparticles: The Influence of Size, Shape, and Dielectric Environment," *J. Phys. Chem. B*, vol. 107, pp. 668–677, 2003.
- [28] "Ashcroft,_Neil_W,_Mermin,_David_N_-_Solid_State_Physics.pdf." .
- [29] S. L. McCall, P. M. Platzman, and P. A. Wolff, "Surface enhanced Raman scattering," *Phys. Lett.*, vol. 77, no. 5, pp. 381–383, 1980.
- [30] A. M. Glass, P. F. Liao, J. G. Bergman, and D. H. Olson, "Interaction of metal particles with adsorbed dye molecules: absorption and luminescence," *Opt. Express*, vol. 5, no. 9, pp. 368–370, 1980.

- [31] Z. Zhu, C. Mao, and R. Yang, "Surface-enhanced Raman scattering of Ru(II) homo- and heterolytic complexes with 2,2'-bipyridine and 1,1'-biisoquinoline in Aqueous Silver Sol," *J. Raman Spectrosc.*, vol. 24, no. December 1992, pp. 221–226, 1993.
- [32] O. Stenzel, A. Stendal, and K. Voigtsberger, "Enhancement of the photovoltaic conversion efficiency of copper phthalocyanine thin film devices by incorporation of metal clusters," *Sol. Energy Mater. Sol. Cells*, vol. 37, pp. 337–348, 1995.
- [33] M. Westphalen, U. Kreibig, J. Rostalski, H. Lu, and D. Meissner, "Metal cluster enhanced organic solar cells," *Sol. Energy Mater. Sol. Cells*, vol. 61, pp. 97–105, 2000.
- [34] C. Wen, K. Ishikawa, M. Kishima, and K. Yamada, "Effects of silver particles on the photovoltaic properties of dye-sensitized TiO₂ thin films," *Sol. Energy Mater. Sol. Cells*, vol. 61, pp. 3–15, 2000.
- [35] S. Link and M. A. El-Sayed, "Spectral Properties and Relaxation Dynamics of Surface Plasmon Electronic Oscillations in Gold and Silver Nanodots and Nanorods," *J. Phys. Chem. B*, vol. 103, no. 1, pp. 8410–8426, 1999.
- [36] S. Link and M. A. El-Sayed, "Shape and size dependence of radiative, non-radiative and photothermal properties of gold nanocrystals," *Int. Rev. Phys. Chem.*, vol. 19, no. 3, pp. 409–453, Jul. 2000.
- [37] A. Furube, L. Du, K. Hara, R. Katoh, and M. Tachiya, "Ultrafast plasmon-induced electron transfer from gold nanodots into TiO₂ nanoparticles," *J. Am. Chem. Soc.*, vol. 129, no. 48, pp. 14852–3, Dec. 2007.
- [38] Y. Nishijima, K. Ueno, Y. Yokota, K. Murakoshi, and H. Misawa, "Plasmon-Assisted Photocurrent Generation from Visible to Near-Infrared Wavelength Using a Au-Nanorods/TiO₂ Electrode," *J. Phys. Chem. Lett.*, vol. 1, no. 13, pp. 2031–2036, Jul. 2010.
- [39] K. Nazeeruddin, P. Péchy, and M. Gratzel, "Efficient panchromatic sensitization of nanocrystalline TiO₂ films by a black dye based on a Trithiocyanato-Ruthenium complex," *Chem. Commun.*, vol. 18, pp. 1705–1706, 1997.
- [40] M. Gratzel, "Photoelectrochemical cells," *Nature*, vol. 414, no. 6861, pp. 338–344, 2001.
- [41] Y. Bai, Y. Cao, J. Zhang, M. Wang, R. Li, P. Wang, S. M. Zakeeruddin, and M. Grätzel, "High-performance dye-sensitized solar cells based on solvent-free electrolytes produced from eutectic melts," *Nat. Mater.*, vol. 7, no. 8, pp. 626–30, Aug. 2008.
- [42] E. W. McFarland and J. Tang, "A photovoltaic device structure based on internal electron emission," *Nature*, vol. 421, no. 6923, pp. 616–8, Feb. 2003.
- [43] F. Hallermann, C. Rockstuhl, S. Fahr, G. Seifert, S. Wackerow, H. Graener, G. V. Plessen, and F. Lederer, "On the use of localized plasmon polaritons in solar cells," *Phys. Status Solidi*, vol. 205, no. 12, pp. 2844–2861, Dec. 2008.
- [44] K. Nakayama, K. Tanabe, and H. a. Atwater, "Plasmonic nanoparticle enhanced light absorption in GaAs solar cells," *Appl. Phys. Lett.*, vol. 93, no. 12, p. 121904, 2008.

- [45] G.-W. Shu, W.-C. Liao, C.-L. Hsu, J.-Y. Lee, I.-J. Hsu, J.-L. Shen, M.-D. Yang, C.-H. Wu, Y.-C. Lee, and W.-C. Chou, "Enhanced Conversion Efficiency of GaAs Solar Cells Using Ag Nanoparticles," *Adv. Sci. Lett.*, vol. 3, no. 4, pp. 368–372, Dec. 2010.
- [46] S. Wu, "Absorption enhancement in thin-film silicon solar cells by two-dimensional periodic nanopatterns," *J. Nanophotonics*, vol. 4, no. 1, p. 043515, Aug. 2010.
- [47] T. L. Temple and D. M. Bagnall, "Optical properties of gold and aluminium nanoparticles for silicon solar cell applications," *J. Appl. Phys.*, vol. 109, no. 8, p. 084343, 2011.
- [48] T. L. Temple and D. M. Bagnall, "Broadband scattering of the solar spectrum by spherical metal nanoparticles," *Prog. Photovoltaics*, vol. 21, no. 4, pp. 600–611, 2012.
- [49] A. Paris, A. Vaccari, A. Calà Lesina, E. Serra, and L. Calliari, "Plasmonic Scattering by Metal Nanoparticles for Solar Cells," *Plasmonics*, vol. 7, no. 3, pp. 525–534, Mar. 2012.
- [50] S. Morawiec, M. J. Mendes, S. Mirabella, F. Simone, F. Priolo, and I. Crupi, "Self-assembled silver nanoparticles for plasmon-enhanced solar cell back reflectors: correlation between structural and optical properties," *Nanotechnology*, vol. 24, no. 26, p. 265601, Jul. 2013.
- [51] J. J. Mock, M. Barbic, D. R. Smith, D. a. Schultz, and S. Schultz, "Shape effects in plasmon resonance of individual colloidal silver nanoparticles," *J. Chem. Phys.*, vol. 116, no. 15, p. 6755, 2002.
- [52] T. K. Sau, A. L. Rogach, F. Jäckel, T. a Klar, and J. Feldmann, "Properties and applications of colloidal nonspherical noble metal nanoparticles," *Adv. Mater.*, vol. 22, no. 16, pp. 1805–25, Apr. 2010.
- [53] A. Pors, A. V. Uskov, M. Willatzen, and I. E. Protsenko, "Control of the input efficiency of photons into solar cells with plasmonic nanoparticles," *Opt. Commun.*, vol. 284, no. 8, pp. 2226–2229, Apr. 2011.
- [54] B. Auguié and W. L. Barnes, "Diffractive coupling in gold nanoparticle arrays and the effect of disorder," *Opt. Lett.*, vol. 34, no. 4, pp. 401–3, Feb. 2009.
- [55] D. A. Genov, A. K. Sarychev, V. M. Shalaev, and A. Wei, "Resonant Field Enhancements from Metal Nanoparticle," *Nano Lett.*, vol. 4, no. 1, pp. 153–158, 2004.
- [56] R. Santbergen, R. Liang, and M. Zeman, "A-Si:H solar cells with embedded silver nanoparticles," *2010 35th IEEE Photovolt. Spec. Conf.*, pp. 000748–000753, Jun. 2010.
- [57] Z. Ouyang, X. Zhao, S. Varlamov, Y. Tao, J. Wong, and S. Pillai, "Nanoparticle-enhanced light trapping in thin-film silicon solar cells," *Prog. Photovoltaics Res. Appl.*, no. July, pp. 917–926, 2011.
- [58] S. Fahr, C. Rockstuhl, and F. Lederer, "Metallic nanoparticles as intermediate reflectors in tandem solar cells," *Appl. Phys. Lett.*, vol. 95, no. 12, p. 121105, 2009.
- [59] A. Pinchuk, G. Von Plessen, and U. Kreibig, "Influence of interband electronic transitions on the optical absorption in metallic nanoparticles," *J. Phys. D. Appl. Phys.*, vol. 37, no. 22, pp. 3133–3139, Nov. 2004.

- [60] X. Chen, B. Jia, J. K. Saha, B. Cai, N. Stokes, Q. Qiao, Y. Wang, Z. Shi, and M. Gu, "Broadband enhancement in thin-film amorphous silicon solar cells enabled by nucleated silver nanoparticles," *Nano Lett.*, vol. 12, no. 5, pp. 2187–92, May 2012.
- [61] X. Chen, Y. Chen, J. Dai, M. Yan, D. Zhao, Q. Li, and M. Qiu, "Ordered Au nanocrystals on a substrate formed by light-induced rapid annealing," *Nanoscale*, pp. 1756–1762, 2014.
- [62] T. R. Jensen, M. D. Malinsky, C. L. Haynes, and R. P. Van Duyne, "Nanosphere Lithography: Tunable Localized Surface Plasmon Resonance Spectra of Silver Nanoparticles," *J. Phys. Chem. B*, vol. 104, no. 45, pp. 10549–10556, Nov. 2000.
- [63] C. L. Tan, S. J. Jang, and Y. T. Lee, "Localized surface plasmon resonance with broadband ultralow reflectivity from metal nanoparticles on glass and silicon subwavelength structures," vol. 20, no. 16, pp. 461–467, 2012.
- [64] C. Simovski, D. Morits, P. Voroshilov, M. Guzhva, P. Belov, and Y. Kivshar, "Enhanced efficiency of light-trapping nanoantenna arrays for thin-film solar cells," *Opt. Express*, vol. 21, no. S4, pp. 122–126, Mar. 2013.
- [65] M. Kirkengen, J. Bergli, and Y. M. Galperin, "Direct generation of charge carriers in c-Si solar cells due to embedded nanoparticles," *J. Appl. Phys.*, vol. 102, no. 9, p. 093713, 2007.
- [66] E. Moulin, P. Luo, B. Pieters, J. Sukmanowski, J. Kirchhoff, W. Reetz, T. Müller, R. Carius, F.-X. Royer, and H. Stiebig, "Photoresponse enhancement in the near infrared wavelength range of ultrathin amorphous silicon photosensitive devices by integration of silver nanoparticles," *Appl. Phys. Lett.*, vol. 95, no. 3, p. 033505, 2009.
- [67] P. Q. Luo, E. Moulin, J. Sukmanowski, F. X. Royer, X. M. Dou, and H. Stiebig, "Enhanced infrared response of ultra thin amorphous silicon photosensitive devices with Ag nanoparticles," *Thin Solid Films*, vol. 517, no. 23, pp. 6256–6259, Oct. 2009.
- [68] M. Fukuda, T. Aihara, K. Yamaguchi, Y. Y. Ling, K. Miyaji, and M. Tohyama, "Light detection enhanced by surface plasmon resonance in metal film," *Appl. Phys. Lett.*, vol. 96, no. 15, p. 153107, 2010.
- [69] M. W. Knight, H. Sobhani, P. Nordlander, and N. J. Halas, "Photodetection with active optical antennas," *Science*, vol. 332, no. 6030, pp. 702–4, May 2011.
- [70] F. Lükermann, U. Heinzmann, and H. Stiebig, "Plasmon induced NIR response of thin-film a-Si:H solar cells," vol. 8471, no. 1, p. 84710S, Oct. 2012.
- [71] E. Antoine Moulin, U. Wilhelm Paetzold, B. Elger Pieters, W. Reetz, and R. Carius, "Plasmon-induced photoexcitation of 'hot' electrons and 'hot' holes in amorphous silicon photosensitive devices containing silver nanoparticles," *J. Appl. Phys.*, vol. 113, no. 14, p. 144501, 2013.
- [72] E. V. Vashchenko, T. a. Vartanyan, and F. Hubenthal, "Photoconductivity of Silver Nanoparticle Ensembles on Quartz Glass (SiO₂) Supports Assisted by Localized Surface Plasmon Excitations," *Plasmonics*, vol. 8, no. 2, pp. 1265–1271, Mar. 2013.

- [73] P. Royer, J. L. Bijeon, J. P. Goudonnet, T. Inagaki, and E. T. Arakawa, "Optical absorbance of silver oblate particles," *Surf. Sci.*, vol. 217, pp. 384–402, 1989.
- [74] J. Kottmann, O. Martin, D. Smith, and S. Schultz, "Plasmon resonances of silver nanowires with a nonregular cross section," *Phys. Rev. B*, vol. 64, no. 23, p. 235402, Nov. 2001.
- [75] and Y. R. S. G. T. Boyd, Th. Rasing, J. R. R. Leite, "Local-field enhancement on rough surfaces of metals, semimetals, and semiconductors with the use of optical second-harmonic generation," *Phys. Rev. B*, vol. 30, no. 2, 1984.
- [76] E. Sánchez, L. Novotny, and X. Xie, "Near-Field Fluorescence Microscopy Based on Two-Photon Excitation with Metal Tips," *Phys. Rev. Lett.*, vol. 82, no. 20, pp. 4014–4017, May 1999.
- [77] J. Krenn, a. Dereux, J. Weeber, E. Bourillot, Y. Lacroute, J. Goudonnet, G. Schider, W. Gotschy, a. Leitner, F. Aussenegg, and C. Girard, "Squeezing the Optical Near-Field Zone by Plasmon Coupling of Metallic Nanoparticles," *Phys. Rev. Lett.*, vol. 82, no. 12, pp. 2590–2593, Mar. 1999.
- [78] P. Etchegoin, L. F. Cohen, H. Hartigan, R. J. C. Brown, M. J. T. Milton, and J. C. Gallop, "Electromagnetic contribution to surface enhanced Raman scattering revisited," *J. Chem. Phys.*, vol. 119, no. 10, p. 5281, 2003.
- [79] E. M. Hicks, S. Zou, G. C. Schatz, K. G. Spears, R. P. Van Duyne, L. Gunnarsson, T. Rindzevicius, B. Kasemo, and M. Käll, "Controlling plasmon line shapes through diffractive coupling in linear arrays of cylindrical nanoparticles fabricated by electron beam lithography.," *Nano Lett.*, vol. 5, no. 6, pp. 1065–70, Jun. 2005.
- [80] B. P. Rand, P. Peumans, and S. R. Forrest, "Long-range absorption enhancement in organic tandem thin-film solar cells containing silver nanoclusters," *J. Appl. Phys.*, vol. 96, no. 12, p. 7519, 2004.
- [81] T. Yang and K. B. Crozier, "Surface plasmon coupling in periodic metallic nanoparticle structures: a semi-analytical model," *Opt. Express*, vol. 16, no. 8, pp. 13070–9, Aug. 2008.
- [82] B. S. Simpkins, J. P. Long, O. J. Glembocki, J. Guo, J. D. Caldwell, and J. C. Owrutsky, "Pitch-dependent resonances and near-field coupling in infrared nanoantenna arrays.," *Opt. Express*, vol. 20, no. 25, pp. 27725–39, Dec. 2012.
- [83] S. Zou, N. Janel, and G. C. Schatz, "Silver nanoparticle array structures that produce remarkably narrow plasmon lineshapes.," *J. Chem. Phys.*, vol. 120, no. 23, pp. 10871–5, Jun. 2004.
- [84] V. A. Markel, "Divergence of dipole sums and the nature of non-Lorentzian exponentially narrow resonances in one-dimensional periodic arrays of nanospheres," *J. Phys. B At. Mol. Opt. Phys.*, vol. 38, no. 7, pp. L115–L121, Apr. 2005.
- [85] V. Kravets, F. Schedin, and A. Grigorenko, "Extremely Narrow Plasmon Resonances Based on Diffraction Coupling of Localized Plasmons in Arrays of Metallic Nanoparticles," *Phys. Rev. Lett.*, vol. 101, no. 8, p. 087403, Aug. 2008.
- [86] M. Meier, a. Wokaun, and P. F. Liao, "Enhanced fields on rough surfaces: dipolar interactions among particles of sizes exceeding the Rayleigh limit," *J. Opt. Soc. Am. B*, vol. 2, no. 6, p. 931, Jun. 1985.

- [87] B. Lamprecht, G. Schider, R. Lechner, H. Ditlbacher, J. Krenn, a Leitner, and F. Aussenegg, "Metal nanoparticle gratings: influence of dipolar particle interaction on the plasmon resonance," *Phys. Rev. Lett.*, vol. 84, no. 20, pp. 4721–4, May 2000.
- [88] B. Luk'yanchuk, N. I. Zheludev, S. a Maier, N. J. Halas, P. Nordlander, H. Giessen, and C. T. Chong, "The Fano resonance in plasmonic nanostructures and metamaterials.," *Nat. Mater.*, vol. 9, no. 9, pp. 707–15, Sep. 2010.
- [89] J. D. Caldwell, O. J. Glembocki, F. J. Bezares, M. I. Kariniemi, J. T. Niinistö, T. T. Hatanpää, R. W. Rendell, M. Ukaegbu, M. K. Ritala, S. M. Prokes, C. M. Hosten, M. a Leskelä, and R. Kasica, "Large-area plasmonic hot-spot arrays: sub-2 nm interparticle separations with plasma-enhanced atomic layer deposition of Ag on periodic arrays of Si nanopillars.," *Opt. Express*, vol. 19, no. 27, pp. 26056–64, Dec. 2011.
- [90] E. Hao and G. C. Schatz, "Electromagnetic fields around silver nanoparticles and dimers.," *J. Chem. Phys.*, vol. 120, no. 1, pp. 357–66, Jan. 2004.
- [91] A. L. Lereu, G. Sanchez-Mosteiro, P. Ghenuche, R. Quidant, and N. F. van Hulst, "Individual gold dimers investigated by far- and near-field imaging.," *J. Microsc.*, vol. 229, no. Pt 2, pp. 254–8, Mar. 2008.
- [92] R. a. Ismail, a. K. Ali, and K. I. Hasson, "Characteristics of a silicon Schottky photodetector produced from colloidal gold nanoparticles," *Micro Nano Lett.*, vol. 7, no. 6, p. 536, 2012.
- [93] T. Okamoto and I. Yamaguchi, "Optical Absorption Study of the Surface Plasmon Resonance in Gold Nanoparticles Immobilized onto a Gold Substrate by Self-Assembly Technique," *J. Phys. Chem. B*, vol. 107, no. 38, pp. 10321–10324, Sep. 2003.
- [94] F. J. García de Abajo, "Colloquium: Light scattering by particle and hole arrays," *Rev. Mod. Phys.*, vol. 79, no. 4, pp. 1267–1290, Oct. 2007.
- [95] Y. Nishijima, L. Rosa, and S. Juodkazis, "Surface plasmon resonances in periodic and random patterns of gold nano-disks for broadband light harvesting," *Opt. Express*, vol. 20, no. 10, May 2012.
- [96] U. W. Paetzold, M. Smeets, M. Meier, K. Bittkau, T. Merdzhanova, V. Smirnov, D. Michaelis, C. Waechter, R. Carius, and U. Rau, "Disorder improves nanophotonic light trapping in thin-film solar cells," *Appl. Phys. Lett.*, vol. 104, no. 13, p. 131102, Mar. 2014.
- [97] M. A. Green, K. Emery, Y. Hishikawa, W. Warta, and E. D. Dunlop, "Solar cell efficiency tables (version 44)," *Prog. Photovoltaics*, vol. 22, no. 7, pp. 701–710, 2014.
- [98] C. Gritti, A. Novitsky, R. Malureanu, a. V. Lavrinenko, a. V. Uskov, and B. Kardynal, "Absorption enhancement in metal nanoparticles for photoemission current for solar cells," in *SPIE*, 2012, vol. 8438, p. 84380K–84380K–9.
- [99] A. C. I. H. Baca A.G., *Fabrication of GaAs devices*. Institution of Electrical Engineers, 2005, p. Chapter 6.

- [100] M. a. Green and R. B. Godfrey, "MIS solar cell—General theory and new experimental results for silicon," *Appl. Phys. Lett.*, vol. 29, no. 9, p. 610, 1976.
- [101] J. A. W. Co and M. Street, "Spectroscopic ellipsometry characterization of indium tin oxide film microstructure and optical constants," pp. 394–397, 1998.
- [102] O. S. Jackson, WB, Kelso SM, Tsai CC, Allen JW, "ENERGY-DEPENDENCE OF THE OPTICAL MATRIX ELEMENT IN HYDROGENATED AMORPHOUS AND CRYSTALLINE SILICON," *Phys. Rev. B*, vol. 31, no. 8, pp. 5187 – 5198, 1985.
- [103] H. Stiebig, A. Kreisel, K. Winz, N. Schultz, C. Beneking, T. Eickhoff, H. Wagner, and M. Meer, "Spectral response modelling of a-Si:H solar cells using accurate light absorption profiles," in *Proceedings of 1994 IEEE 1st World Conference on Photovoltaic Energy Conversion - WCPEC (A Joint Conference of PVSC, PVSEC and PSEC)*, 1994, vol. 1, pp. 603–606.
- [104] N. K. Yoshida S., Yoshino M., Kitahara S., Seki K., Katayama S., Nabeshima K. and K. M. Yamada A., "Improvement of a-Si/a-Si double junction solar cells by utilizing the ZnO/Ag rear contact," in *11th E.C. Photovoltaic Solar Energy Conference*, 1992, pp. 590–593.
- [105] S. N. and W. H. Beneking C., Rech B., Eickhoff T., Michael Y.G., "Preparation and Light Stability of a-Si/a-Si Stacked Solar Cells," in *In Proceedings of the 12th EC PVSEC, Amsterdam*, 1994, pp. 683–686.
- [106] P. B. Johnson and R. W. Christy, "Optical constants of the noble metals," *Phys. Rev. B*, vol. 6, no. 12, 1972.
- [107] V. Zaporozhtchenko, T. Strunskus, K. Behnke, C. . Bechtolsheim, a Thran, and F. Faupel, "Formation of metal–polymer interfaces by metal evaporation: influence of deposition parameters and defects," *Microelectron. Eng.*, vol. 50, no. 1–4, pp. 465–471, Jan. 2000.
- [108] W. Alberth, "Chemical (Electroless)Nickel Plating," *GALVANOTECHNIK*, vol. 70, no. 6, pp. 502–505, 1979.
- [109] Y. Okinaka and M. Hoshino, "Some recent topics in gold plating for electronics applications," *Gold Bull.*, vol. 31, no. 1, pp. 3–13, Mar. 1998.
- [110] H. J. B. Mallory G.O., *Electroless plating : Fundamentals and applications*, no. September. Technology & Engineering, 1990.
- [111] Y. O. Sato J., Kato M., Otani H., Homma T., Okinaka Y., Osaka T., "Substrate (Ni)-catalyzed electroless gold deposition from a noncyanide bath containing thiosulfate and sulfite," *J. Electrochem. Soc.*, vol. 149, no. 3, pp. C168–72, 2002.
- [112] M. Kato, J. Sato, H. Otani, T. Homma, Y. Okinaka, T. Osaka, and O. Yoshioka, "Substrate (Ni)-Catalyzed Electroless Gold Deposition from a Noncyanide Bath Containing Thiosulfate and Sulfite," *J. Electrochem. Soc.*, vol. 149, no. 3, p. C164, 2002.
- [113] S. P. C. Oskam G., Long J. G., Natarajan A., "Electrochemical deposition of metal onto silicon," *J. Phys. D (Applied Physics)*, vol. 31, no. 16, pp. 1927 – 1949, 1998.

- [114] L. Xu, K. Zhou, H. Xu, H. Zhang, L. Huang, J. Liao, A. Xu, N. Gu, H. Shen, and J. Liu, "Copper thin coating deposition on natural pollen particles," *Appl. Surf. Sci.*, vol. 183, no. 1–2, pp. 58–61, Nov. 2001.
- [115] A. N. Shipway, E. Katz, and I. Willner, "Nanoparticle arrays on surfaces for electronic, optical, and sensor applications.," *Chemphyschem*, vol. 1, no. 1, pp. 18–52, Aug. 2000.
- [116] D. van Noort and C.-F. Mandenius, "Porous gold surfaces for biosensor applications," *Biosens. Bioelectron.*, vol. 15, no. 3–4, pp. 203–209, Jun. 2000.
- [117] L. C. Kacer Petr, "Structure effects in hydrogenation reactions on noble metal catalysts," *Appl. Phys. A*, vol. 229, no. 5, pp. 193–216, 2002.
- [118] G. Ling, J. He, and L. Huang, "Size control of silver nanoparticles deposited on silica dielectric spheres by electroless plating technique," *J. Mater. Sci.*, vol. 39, no. 8, pp. 2955–2957, Apr. 2004.
- [119] L. A. Porter, H. C. Choi, A. E. Ribbe, and J. M. Buriak, "Controlled Electroless Deposition of Noble Metal Nanoparticle Films on Germanium Surfaces," *Nano Lett.*, vol. 2, no. 10, pp. 1067–1071, 2002.
- [120] W. Ye, Y. Chang, C. Ma, B. Jia, G. Cao, and C. Wang, "Electrochemical investigation of the surface energy: Effect of the HF concentration on electroless silver deposition onto p-Si (111)," *Appl. Surf. Sci.*, vol. 253, no. 7, pp. 3419–3424, Jan. 2007.
- [121] X. Wan, Q. K. Wang, P. H. Wangyang, and H. Tao, "Roles of Ag in fabricating Si nanowires by the electroless chemical etching technique," *J. Nanoparticle Res.*, vol. 14, no. 4, p. 784, Mar. 2012.
- [122] N. Chitvoranund, S. Jiemsirilers, and D. P. Kashima, "Effects of surface treatments on adhesion of silver film on glass substrate fabricated by electroless plating Glass slide Preparation," *J. Aust. Ceram. Soc.*, vol. 49, pp. 62–69, 2013.
- [123] E. Moulin, P. Luo, B. Pieters, J. Sukmanowski, J. Kirchhoff, W. Reetz, T. Müller, R. Carius, F.-X. Royer, and H. Stiebig, "Photoresponse enhancement in the near infrared wavelength range of ultrathin amorphous silicon photosensitive devices by integration of silver nanoparticles," *Appl. Phys. Lett.*, vol. 95, no. 3, p. 033505, 2009.
- [124] A. L. Koh, K. Bao, I. Khan, W. E. Smith, G. Kothleitner, K. P. Nordlander, S. A. Maier, and D. W. Mccomb, "Electron Energy-Loss Spectroscopy Silver Nanoparticles and Dimers: Influence of Beam Damage and Mapping of Dark Modes," *ACS Nano*, vol. 3, no. 10, pp. 3015–3022, 2009.
- [125] H. Raether, *Excitation of plasmons and interband transitions by electrons*. Springer, 1980.
- [126] S. Lazar, G. a Botton, and H. W. Zandbergen, "Enhancement of resolution in core-loss and low-loss spectroscopy in a monochromated microscope.," *Ultramicroscopy*, vol. 106, no. 11–12, pp. 1091–103, 2006.
- [127] J. Nelayah, M. Kociak, O. Stéphan, F. J. García de Abajo, M. Tencé, L. Henrard, D. Taverna, I. Pastoriza-Santos, L. M. Liz-Marzán, and C. Colliex, "Mapping surface plasmons on a single metallic nanoparticle," *Nat. Phys.*, vol. 3, no. 5, pp. 348–353, Apr. 2007.

- [128] M.-W. Chu, V. Myroshnychenko, C. H. Chen, J.-P. Deng, C.-Y. Mou, and F. J. García de Abajo, "Probing bright and dark surface-plasmon modes in individual and coupled noble metal nanoparticles using an electron beam.," *Nano Lett.*, vol. 9, no. 1, pp. 399–404, Jan. 2009.
- [129] F. J. García de Abajo, "Optical excitations in electron microscopy," *Rev. Mod. Phys.*, vol. 82, no. 1, pp. 209–275, 2010.
- [130] F. Ouyang, P. E. Batson, and M. Isaacson, "Quantum size effects in the surface-plasmon excitation of small metallic particles by electron-energy-loss spectroscopy," *Phys. Rev. B*, vol. 46, no. 23, pp. 421–425, 1992.
- [131] C. Kittel, *Quantum Theory of Solids*. John Wiley & Sons, 1987.
- [132] T. L. Ferrell, R. J. Warmack, and V. E. Anderson, "Analytical calculation of stopping power for isolated small spheres," *Phys. Rev. B*, vol. 35, no. 14, pp. 7365–7371, May 1987.
- [133] D. Ugarte, C. Colliex, and P. Trebbia, "Surface- and interface-plasmon modes on small semiconducting spheres.," *Phys. Rev. B. Condens. Matter*, vol. 45, no. 8, pp. 4332–4343, Feb. 1992.
- [134] K. C. Mamola, R. J. Warmack, and T. L. Ferrell, "Surface-plasmon excitation by electrons in microlithographically produced channels," *Phys. Rev. B*, vol. 35, no. 6, 1987.
- [135] F. J. García de Abajo, "Nonlocal Effects in the Plasmons of Strongly Interacting Nanoparticles, Dimers, and Waveguides," *J. Phys. Chem. C*, vol. 112, pp. 17983–17987, 2008.
- [136] R. H. Ritchie and A. L. Marusak, "The surface plasmon dispersion relation for an electron gas," *Surf. Interface Anal.*, vol. 4, pp. 234–240, 1966.
- [137] R. Ruppin, "Surface modes of two spheres," *Phys. Rev. B*, vol. 26, no. 6, pp. 3440–3444, 1982.
- [138] M. Schmeits and L. Dambly, "Fast-electron scattering by bispherical surface-plasmon modes," *Phys. Status Solidi*, vol. 44, no. 23, 1991.
- [139] N. Zabala, a. Rivacoba, and P. Echenique, "Coupling effects in the excitations by an external electron beam near close particles," *Phys. Rev. B*, vol. 56, no. 12, pp. 7623–7635, Sep. 1997.
- [140] P. Nordlander, C. Oubre, E. Prodan, K. Li, and M. I. Stockman, "Plasmon Hybridization in Nanoparticle Dimers," *Nano Lett.*, vol. 4, no. 5, pp. 899–903, May 2004.
- [141] M. Pelton, *Introduction to metal-nanoparticle plasmonics*. John Wiley, 2013.
- [142] F. J. García de Abajo, "Relativistic description of valence energy losses in the interaction of fast electrons with clusters of dielectrics: Multiple-scattering approach," *Phys. Rev. B*, vol. 60, no. 8, 1999.
- [143] M. Schmeits, "Surface-plasmon coupling in cylindrical pores," *Phys. Rev. B*, vol. 39, no. 11, 1989.
- [144] F. García de Abajo and a. Howie, "Retarded field calculation of electron energy loss in inhomogeneous dielectrics," *Phys. Rev. B*, vol. 65, no. 11, p. 115418, Mar. 2002.

- [145] A. Manjavacas and F. J. García de Abajo, "Robust Plasmon Waveguides in Strongly Interacting Nanowire Arrays," *Nano Lett.*, vol. 9, no. 4, pp. 1285–1289, 2009.
- [146] H. Xu, E. Bjerneld, M. Käll, and L. Börjesson, "Spectroscopy of Single Hemoglobin Molecules by Surface Enhanced Raman Scattering," *Phys. Rev. Lett.*, vol. 83, no. 21, pp. 4357–4360, Nov. 1999.
- [147] K. Kneipp, Y. Wang, H. Kneipp, L. Perelman, I. Itzkan, R. Dasari, and M. Feld, "Single Molecule Detection Using Surface-Enhanced Raman Scattering (SERS)," *Phys. Rev. Lett.*, vol. 78, no. 9, pp. 1667–1670, Mar. 1997.
- [148] T. Atay, J.-H. Song, and A. V. Nurmikko, "Strongly Interacting Plasmon Nanoparticle Pairs: From Dipole–Dipole Interaction to Conductively Coupled Regime," *Nano Lett.*, vol. 4, no. 9, pp. 1627–1631, Sep. 2004.
- [149] G. Toscano, S. Raza, J. Antti-Pekka, N. A. Mortensen, and M. Wubs, "Modified field enhancement and extinction by plasmonic nanowire dimers due to nonlocal response," *Opt. Express*, vol. 20, no. 4, Jan. 2012.
- [150] J. Zuloaga, E. Prodan, and P. Nordlander, "Quantum description of the plasmon resonances of a nanoparticle dimer.," *Nano Lett.*, vol. 9, no. 2, pp. 887–91, Feb. 2009.
- [151] I. Romero, J. Aizpurua, G. W. Bryant, and F. J. García De Abajo, "Plasmons in nearly touching metallic nanoparticles: singular response in the limit of touching dimers.," *Opt. Express*, vol. 14, no. 21, pp. 9988–99, Oct. 2006.
- [152] M. N'Gom, J. Ringnalda, J. F. Mansfield, A. Agarwal, N. Kotov, N. J. Zaluzec, and T. B. Norris, "Single particle plasmon spectroscopy of silver nanowires and gold nanorods.," *Nano Lett.*, vol. 8, no. 10, pp. 3200–4, Oct. 2008.
- [153] H. Duan, A. I. Fernández-Domínguez, M. Bosman, S. a Maier, and J. K. W. Yang, "Nanoplasmonics: classical down to the nanometer scale.," *Nano Lett.*, vol. 12, no. 3, pp. 1683–9, Mar. 2012.
- [154] A. Yurtsever, R. M. van der Veen, and A. H. Zewail, "Subparticle ultrafast spectrum imaging in 4D electron microscopy.," *Science*, vol. 335, no. 6064, pp. 59–64, Jan. 2012.
- [155] K. J. Savage, M. M. Hawkeye, R. Esteban, A. G. Borisov, J. Aizpurua, and J. J. Baumberg, "Revealing the quantum regime in tunnelling plasmonics.," *Nature*, vol. 491, no. 7425, pp. 574–7, Nov. 2012.
- [156] J. a Scholl, A. García-Etxarri, A. L. Koh, and J. a Dionne, "Observation of quantum tunneling between two plasmonic nanoparticles.," *Nano Lett.*, vol. 13, no. 2, pp. 564–9, Feb. 2013.
- [157] S. Kadkhodazadeh, J. B. Wagner, H. Kneipp, and K. Kneipp, "Coexistence of classical and quantum plasmonics in large plasmonic structures with subnanometer gaps," *Appl. Phys. Lett.*, vol. 103, no. 8, p. 083103, 2013.
- [158] R. Esteban, A. G. Borisov, P. Nordlander, and J. Aizpurua, "Bridging quantum and classical plasmonics with a quantum-corrected model.," *Nat. Commun.*, vol. 3, no. May, p. 825, Jan. 2012.

- [159] P. E. Batson, a Reyes-Coronado, R. G. Barrera, a Rivacoba, P. M. Echenique, and J. Aizpurua, "Plasmonic nanobilliards: controlling nanoparticle movement using forces induced by swift electrons.," *Nano Lett.*, vol. 11, no. 8, pp. 3388–93, Aug. 2011.
- [160] N. Mirsaleh-kohan, V. Iberi, P. D. Simmons, N. W. Bigelow, A. Vaschillo, M. M. Rowland, M. D. Best, S. J. Pennycook, D. J. Masiello, B. S. Guiton, and J. P. Camden, "Single-Molecule Surface-Enhanced Raman Scattering: Can STEM/ EELS Image Electromagnetic Hot Spots?," *J. Phys. Chem. Lett.*, vol. 3, pp. 2303–2309, 2012.
- [161] K. Fukutani, M. Kanbe, W. Futako, B. Kaplan, T. Kamiya, and C. M. Fortmann, "Band gap tuning of a-Si : H from 1 . 55 eV to 2 . 10 eV by intentionally promoting structural relaxation," *J. Non. Cryst. Solids*, vol. 227–230, P, pp. 63–67, 1998.
- [162] S. Hayashi, K. Kozaru, and K. Yamamoto, "Enhancement of photoelectric conversion efficiency by surface plasmon excitation: a test with an organic solar cell," *Solid State Commun.*, vol. 79, no. 9, pp. 763–767, 1991.
- [163] T. Kampen, a Schüller, D. R. . Zahn, B. Biel, J. Ortega, R. Pérez, and F. Flores, "Schottky contacts on passivated GaAs(100) surfaces: barrier height and reactivity," *Appl. Surf. Sci.*, vol. 234, no. 1–4, pp. 341–348, Jul. 2004.
- [164] N. A. Mortensen, S. Raza, M. Wubs, and S. I. Bozhevolnyi, "A generalized non-local optical response theory for plasmonic nanostructures," *Nat. Commun.*, vol. 5, 2014.